



JAEA-Conf 2012-001  
INDC(JPN)-197

**Proceedings of the 2011 Symposium on Nuclear Data**  
**November 16-17, 2011, Ricotti, Tokai, Japan**

(Eds.) Hideo HARADA, Kenji YOKOYAMA, Nobuyuki IWAMOTO  
Shoji NAKAMURA and Hiroyuki KOURA

Nuclear Science and Engineering Directorate

July 2012

Japan Atomic Energy Agency

日本原子力研究開発機構

JAEA-Conf

本レポートは独立行政法人日本原子力研究開発機構が不定期に発行する成果報告書です。  
本レポートの入手並びに著作権利用に関するお問い合わせは、下記あてにお問い合わせ下さい。  
なお、本レポートの全文は日本原子力研究開発機構ホームページ (<http://www.jaea.go.jp>)  
より発信されています。

独立行政法人日本原子力研究開発機構 研究技術情報部 研究技術情報課  
〒319-1195 茨城県那珂郡東海村白方白根 2 番地 4  
電話 029-282-6387, Fax 029-282-5920, E-mail:ird-support@jaea.go.jp

This report is issued irregularly by Japan Atomic Energy Agency  
Inquiries about availability and/or copyright of this report should be addressed to  
Intellectual Resources Section, Intellectual Resources Department,  
Japan Atomic Energy Agency  
2-4 Shirakata Shirane, Tokai-mura, Naka-gun, Ibaraki-ken 319-1195 Japan  
Tel +81-29-282-6387, Fax +81-29-282-5920, E-mail:ird-support@jaea.go.jp

© Japan Atomic Energy Agency, 2012

Proceedings of the 2011 Symposium on Nuclear Data  
November 16-17, 2011, Ricotti, Tokai, Japan

(Eds.) Hideo HARADA, Kenji YOKOYAMA, Nobuyuki IWAMOTO,  
Shoji NAKAMURA and Hiroyuki KOURA<sup>+</sup>

Nuclear Science and Engineering Directorate  
Japan Atomic Energy Agency  
Tokai-mura, Naka-gun, Ibaraki-ken

(Received May 18 , 2012)

The 2011 data symposium on nuclear data, organized by the Nuclear Data Division of Atomic Energy Society of Japan (AESJ) was held at Ricotti, Tokai, on Nov.16 and 17, 2011 in cooperation with Nuclear Science and Engineering Directorate of JAEA and North-Kanto Branch of AESJ. The symposium was devoted for discussions and presentations of current topics in the field of nuclear data such as nuclear accident and accident analysis code, innovative methods on nuclear data theory and measurements, and nuclear data applications, including 2 tutorial talks, NJOY99 and PHITS. Talks as well as posters presented at the symposium aroused lively discussions among 97 participants. This report contains 34 papers submitted from the oral and poster presenters.

**Keywords:** Nuclear Data Symposium 2011, Nuclear Accident, Accident Analysis Code, Measurement, Experimental Facilities, Theoretical Model, Nuclear Data Applications

---

<sup>+</sup> Advanced Science Research Center

Organizers: H. Harada (JAEA, Chair), K. Nakajima (Kyoto Univ., Vice-Chair), K. Kato (Hokkaido Univ.), G. Hirano (TEPSYS), J. Hori (Kyoto Univ.), I. Murata (Osaka Univ.), K. Yokoyama (JAEA), N. Iwamoto (JAEA), H. Koura (JAEA), S. Chiba (JAEA), S. Nakamura (JAEA), Y. Watanabe (Kyushu Univ.)

## 2011年度核データ研究会報告集

2011年11月16日～11月17日、テクノ交流館リコッティ、東海村

日本原子力研究開発機構 原子力基礎工学研究部門

(編)原田 秀郎、横山 賢治、岩本 信之、中村 詔司、小浦 寛之<sup>+</sup>

(2012年5月18日受理)

2011年度核データ研究会は、2011年11月16日から17日にかけて、東海村のテクノ交流館リコッティにて開催された。当研究会は日本原子力学会核データ部会の主催、日本原子力研究開発機構原子力基礎工学研究部門、及び日本原子力学会北関東支部の共催の下、原発事故と事故時解析コード、最新の核データ研究手法やその応用に関するトピックスが、多くの研究者の参加を得て議論された。また、NJOY99とPHITSに関するチュートリアルも行われた。参加総数は97名で、盛況のうちに全日程を終えた。本レポートは、同研究会における講演、及びポスター発表者から提出された34件の報告集である。

---

原子力科学研究所（駐在）：〒319-1195 茨城県那珂郡東海村白方白根2-4

<sup>+</sup> 日本原子力研究開発機構 先端基礎研究センター

2011年核データ研究会実行委員会：原田 秀郎（委員長、原子力機構）、中島 健（副委員長、京大）、加藤 幾芳（北大）、平野 豪（テプコシステムズ）、堀 順一（京大）、村田 勲（阪大）、横山 賢治（原子力機構）、岩本 信之（原子力機構）、小浦 寛之（原子力機構）、千葉 敏（原子力機構）、中村 詔司（原子力機構）、渡辺 幸信（九大）

## Contents

1. Program of 2011 Symposium on Nuclear Data .....	1
 <b>Papers presented at Oral sessions</b>	
2. What has happened at the Fukushima Dai-ichi nuclear power plant by the Great East Japan Earthquake? .....	5
Ken Nakajima (Kyoto Univ.)	
3. Severe accident analysis and related nuclear data .....	13
Kazufumi Tsujimoto (JAEA)	
4. High Temperature Gas-cooled Reactor (HTGR) with inherent safety features .....	15
Kazuhiko Kunitomi (JAEA)	
5. Fast Breeder Reactor core design study using JENDL-4.0 .....	21
Kazuya Ohgama (JAEA) <i>et al.</i>	
6. Nuclear Data in Radiation Protection Dosimetry .....	27
Daiki Satoh (JAEA)	
7. Solution for Pandemonium Problem in FP Decay Heat Summation Calculations ...	33
Tadashi Yoshida (Tokyo City Univ.) <i>et al.</i>	
8. Nuclear Data for Prediction of Isotope Generation and Depletion .....	39
Keisuke Okumura (JAEA)	
9. Estimation of average burnup of damaged fuels loaded in Fukushima Dai-ichi reactors by using the $^{134}\text{Cs}/^{137}\text{Cs}$ ratio method .....	45
Tomohiro Endo (Nagoya Univ.) <i>et al.</i>	
10. Present Status and Perspective of Neutron Cross Section Measurement in a Low Energy Region .....	53
Masayuki Igashira (Tokyo Inst. of Tech.)	
11. Present Status and Perspective on Intermediate Energy Nuclear Data Measurements	57
Yukinobu Watanabe (Kyushu Univ.)	
12. Surrogate Reactions .....	63
Satoshi Chiba (JAEA)	
13. Approach by the $\gamma$ -ray Strength Function Method .....	67
Hiroaki Utsunomiya (Konan Univ.)	
 <b>Papers presented at a Poster session</b>	
14. Activation analyses by deuteron beam loss at 5-9 MeV for the IFMIF/EVEDA accelerator .....	73
Sunao Maebara (JAEA) <i>et al.</i>	
15. Evaluation of energy reduction in main shielding materials for gamma-ray and neutron generated by deuteron beam at 5 MeV and 9 MeV .....	77
Hiroki Takahashi (JAEA) <i>et al.</i>	
16. $\gamma$ -ray strength function measurement on $^{181}\text{Ta}$ at ELBE .....	83
Ayano Makinaga (Hokkaido Univ.) <i>et al.</i>	

17. Development of the ORIGEN2 Library for Light Water Reactors Based on JENDL-4.0 .....	89
Keisuke Okumura (JAEA) <i>et al.</i>	
18. Evaluation of fragmentation cross-section energy dependence by thick target experiments .....	95
Tatsuhiko Ogawa (The Univ. of Tokyo) <i>et al.</i>	
19. Microscopic optical potentials for nucleon, deuteron, $^3\text{He}$ and $^4\text{He}$ .....	101
Guo Hairui (Kyusyu Univ.) <i>et al.</i>	
20. Low-Energy Nuclear Reactions of Light Nuclei .....	107
Masayuki Aikawa (Hokkaido Univ.) <i>et al.</i>	
21. Measurement of Neutron and Gamma-ray Yields on Thick Targets Bombarded with 12 MeV Protons .....	111
Masayuki Hagiwara (KEK) <i>et al.</i>	
22. Study on the Neutron Capture Cross Sections and Capture Gamma-ray Spectra of $^{93}\text{Nb}$ , $^{103}\text{Rh}$ and $^{115}\text{In}$ .....	117
Taihei Matsushashi (Tokyo Inst. of Tech.) <i>et al.</i>	
23. Analysis of Radioactivity of the Ground Surface Measured at the Fukushima-Daiichi Nuclear Power Plant Site .....	123
Go Chiba (Hokkaido Univ.)	
24. Design and Construction of A Thermal Column Using An Am-Be Neutron Source for BNCT Studies .....	129
Kazuyuki Harada (Osaka Univ.) <i>et al.</i>	
25. Measurement of $\gamma$ -ray-Production Double-Differential Cross Sections for 290 MeV/u Oxygen Ion Incidence .....	135
Haruhiko Uehara (Kyusyu Univ.) <i>et al.</i>	
26. Identification of High-Energy Levels in $^{147}\text{Ce}$ with a Total Absorption Clover Detector .....	141
Yosuke Shima (Nagoya Univ.) <i>et al.</i>	
27. Neutron Capture Cross Section of Palladium-107 in the Thermal-Neutron Energy Region .....	147
Shoji Nakamura (JAEA) <i>et al.</i>	
28. Study on neutron spectrometer for thermal to epithermal energy regions with an advanced multi-activation-foil method .....	153
Hiroyuki Kanasugi (Osaka Univ.) <i>et al.</i>	
29. Systematic Study on keV-neutron Capture Cross Sections and Capture Gamma-ray Spectra of Pd Isotopes .....	159
Kazushi Terada (Tokyo Inst. of Tech.) <i>et al.</i>	
30. Characterization Test of CdTe Detector Element Designed and Developed for BNCT-SPECT .....	165
Soichiro Nakamura (Osaka Univ.) <i>et al.</i>	
31. Critical Experiment with Thorium at KUCA .....	171
Takashi Fujii (Osaka Univ.) <i>et al.</i>	

32. Benchmark Test of JENDL-4.0 with TOF Experiments at Osaka Univ./OKTAVIAN .....	177
Yoshinari Kato (Tokai Univ.) <i>et al.</i>	
33. Self-shielding effect in unresolved resonance data in JENDL-4.0 .....	183
Chikara Konno (JAEA) <i>et al.</i>	
34. Angular distribution of light fragments for proton induced reaction at intermediate energies .....	189
Toshiya Sanami (KEK) <i>et al.</i>	
35. Sensitivity Analysis for Kyoto University Research Reactor Using JENDL-4.0 .....	195
Tadafumi Sano (Kyoto Univ.) <i>et al.</i>	

## 目次

1. 2011 年度核データ研究会 (NDS2011) プログラム .....	1
<b>口頭発表論文</b>	
2. 福島第一原発で何がおきたか .....	5
中島 健 (京大)	
3. シンビアアクシデント解析と関連する核データ .....	13
辻本 和文 (原子力機構)	
4. 固有安全性の高い高温ガス炉 .....	15
國富 一彦 (原子力機構)	
5. 高速炉炉心設計における JENDL-4.0 の適用性評価 .....	21
大釜 和也 (原子力機構)、等	
6. 放射線防護研究と核データ .....	27
佐藤 大樹 (原子力機構)	
7. FP 崩壊熱総和計算におけるパンデモニウム問題の解決 .....	33
吉田 正 (東京都市大)	
8. 核種生成量予測のための核データ .....	39
奥村 啓介 (原子力機構)	
9. $^{134}\text{Cs}/^{137}\text{Cs}$ 比法を用いた福島第一原発破損燃料の平均燃焼度の推定 .....	45
遠藤 知弘 (名大)、等	
10. 低エネルギー領域の核データ測定 .....	53
井頭 政之 (東工大)	
11. 中間エネルギー核データ測定の現状と展望 .....	57
渡辺 幸信 (九大)	
12. 代理反応 .....	63
千葉 敏 (原子力機構)	
13. ガンマ線強度関数法によるアプローチ .....	67
宇都宮 弘章 (甲南大)	
<b>ポスター発表論文</b>	
14. IFMIF/EVEDA 加速器における 5-9 MeV 重陽子イオンビーム損失による放射化解析 .....	73
前原 直 (原子力機構)、等	
15. 5MeV 及び MeV D+ビームによる $\gamma$ 線と中性子の遮蔽材によるエネルギー減衰の評価 .....	77
高橋 博樹 (原子力機構)、等	
16. ELBE 施設における $^{181}\text{Ta}$ のガンマ線強度関数の測定 .....	83
牧永 あや乃 (北大)、等	
17. JENDL-4.0 に基づく軽水炉用 ORIGEN 2 ライブラリの開発 .....	89
奥村 啓介 (原子力機構)、等	
18. 厚いターゲットを用いたフラグメンテーション断面積エネルギー依存性評価 .....	95
小川 達彦 (東大)、等	
19. 核子、重陽子、 $^3\text{He}$ 、 $^4\text{He}$ の微視的光学ポテンシャル .....	101
郭 海瑞 (九大)、等	

20. 軽い核での低エネルギー核反応 .....	107
合川 正幸 (北大)、等	
21. 陽子 12 MeV における厚いターゲットからの中性子・ $\gamma$ 線スペクトルの系統的測定 .	111
萩原 雅之 (高エネ機構)、等	
22. $^{93}\text{Nb}$ , $^{103}\text{Rh}$ 及び $^{115}\text{In}$ の中性子捕獲断面積および捕獲ガンマ線の研究 .....	117
松橋 泰平 (東工大)、等	
23. 福島第一原子力発電所内土壌の放射能データの解析 .....	123
千葉 豪 (北大)	
24. Am-Be 線源を用いた BNCT 研究用中性子サーマルカラムの設計および製作 .....	129
原田 和幸 (阪大)、等	
25. 290 MeV/u 酸素イオン入射ガンマ線生成断面積測定 .....	135
上原 春彦 (九大)、等	
26. 全吸収クローバー検出器を用いた $^{147}\text{Ce}$ の高エネルギー励起準位の同定 .....	141
嶋 洋佑 (名大)、等	
27. 熱中性子エネルギー領域におけるパラジウム 107 の断面積 .....	147
中村 詔司 (原子力機構)、等	
28. 多重箔法を用いた熱~ 熱外エネルギー中性子スペクトロメータの研究・開発 .....	153
金杉 浩幸 (阪大)、等	
29. Pd 同位体の keV 中性子捕獲断面積および捕獲ガンマ線スペクトルの系統的研究 ....	159
寺田 和司 (東工大)、等	
30. BNCT-SPECT のために設計・開発した CdTe 検出器の素子の特性試験 .....	165
中村 宗一郎 (阪大)、等	
31. KUCA における臨界実験 .....	171
藤井 貴志 (阪大)、等	
32. 大阪大学 OKTAVIAN TOF 実験による JENDL-4.0 ベンチマークテスト .....	177
加藤 祥成 (東海大)、等	
33. JENDL-4.0 の非分離共鳴データの自己遮蔽効果 .....	183
今野 力 (原子力機構)、等	
34. 中高エネルギーにおける陽子誘起反応からの軽核破砕片の角度分布 .....	189
佐波 俊哉 (高エネ機構)、等	
35. JENDL-4.0 を用いた京都大学研究用原子炉の感度解析 .....	195
佐野 忠史 (京大)、等	

This is a blank page.

# 1 Program of 2011 Symposium on Nuclear Data

Date : November 16,17, 2011

Venue : Techno Plaza Ricotti (Tokai-mura, Ibaraki-ken)

Host : Nuclear Data Division, Atomic Energy Society of Japan

Co-host : North Kanto Branch of Atomic Energy Society of Japan,  
Nuclear Science and Engineering Directorate of JAEA

## Nov. 16 (Wednesday)

**9:50 - 10:00**

1. Opening Address H. Harada (JAEA)

**10:00 – 11:30**

2. Nuclear Accident and Accident Analysis Code 【Chair: K. Kato (Hokkaido Univ.)】  
2.1 What has happened at the Fukushima Dai-ichi nuclear power plant by the Great East Japan  
Earthquake? [50+10] K. Nakajima (Kyoto Univ.)  
2.2 Severe accident analysis and related nuclear data [25+5] K. Tsujimoto (JAEA)

**11:30 – 12:20** Photo & Lunch

**12:20 – 14:20**

3. Poster presentation (Venue: Ricotti 1F Meeting Room3)

**14:20 – 14:30** Coffee Break

**14:30 – 16:00**

4. Next Nuclear Development and Radiation Protection 【Chair: G. Hirano (TEPSYS)】  
4.1 Inherent Safety Features of High Temperature Gas-cooled Reactor (HTGR) [25+5] K.Kunitomi (JAEA)  
4.2 Fast Breeder Reactor core design study using JENDL-4.0 [25+5] K. Ohgama (JAEA)  
4.3 Nuclear Data in Radiation Protection Dosimetry [25+5] D. Satoh (JAEA)

**16:00 - 16:15** Coffee Break

**16:15 – 17:15**

5. Tutorial-I 【Chair: S. Nakamura (JAEA)】  
Development of Cross Section Library by NJOY99 code K. Kosako (Shimizu Corp.)

**17:20 – 18:30** Convivial Gathering (Venue: Ricotti 1F Coffee Lounge)

## Nov. 17 (Thursday)

**9:10 – 10:40**

6. To What Extent Decay Heat and Activation Cross Section are Understood? 【Chair: T. Fukahori (JAEA)】  
6.1 Decay Heat [25+5] T. Yoshida (Tokyo City Univ.)

- 6.2 Nuclear Data for Prediction of Nuclide Generation and Depletion [25+5] K. Okumura (JAEA)  
6.3 Estimation of Average Burnup in Failed Fuel at the Fukushima No.1 Nuclear Power Plant  
by the Cs134/Cs137 Ratio Method [25+5] T. Endo (Nagoya Univ.)

**10:40 – 10:50** Coffee Break

**10:50 – 12:20**

7. Research Trend of Nuclear Data Measurements and Future Prospects 【Chair: T. Fukahori (JAEA)】  
7.1 Present Status and Perspective of Neutron Cross Section Measurement  
in a low energy region [25+5] M. Igashira (Tokyo Inst. Tech.)  
7.2 Present Status and Perspective on Intermediate Energy Nuclear Data Measurements [25+5]  
Y. Watanabe (Kyusyu Univ.)  
7.3 Surrogate Reaction [25+5] S. Chiba (JAEA)

**12:20 – 13:10** Lunch

**13:10 – 14:10**

8. Production of Nuclear Data by Innovative Nuclear Theory and Measurement  
【Chair: Y. Watanabe (Kyusyu Univ.)】  
8.1 Beta-decay Half-life of Se-79 by an Advanced Large Scale Shell Model Calculation [25+5]  
T. Ohtsuka (Tokyo Univ.)  
8.2 Approach by the g-ray Strength Function Method [25+5] H. Utsunomiya (Konan Univ.)

**14:10 – 14:15**

9. Poster Award Nuclear Data Division, AESJ

**14:15 – 14:20**

10. Closing Address K. Nakajima (Kyoto Univ.)

**14:20 – 14:30** Coffee Break

**14:30 – 17:30**

11. Tutorial-II  
Lecture of PHITS Y. Iwamoto (JAEA)

### Poster Presentation

Date : November 16 (Wednesday), 12:20 – 14:20 (Display 11:30 - )

Venue : Ricotti 1F Meeting Room-3

1. Activation analysis by deuteron beam loss at 5-9 MeV for the IFMIF/EVEDA accelerator  
S. Maebara (JAEA)
2. Evaluation of energy reduction in main shielding materials for gamma-ray and neutron generated  
by deuteron beam at 5 MeV and 9 MeV H. Takahashi (JAEA)
3. Gamma-ray strength function measurement on <sup>181</sup>Ta at ELBE A. Makinaga (Hokkaido Univ.)

4. Development of the ORIGEN2 Library for Light Water Reactors Based on JENDL-4.0  
K. Okumura (JAEA)
5. Evaluation of fragmentation cross-section energy dependence by thick target experiments  
T. Ogawa (Tokyo Univ.)
6. (Canceled)
7. Microscopic optical potentials for nucleon, deuteron,  $^3\text{He}$  and  $^4\text{He}$  H. R. Guo (Kyusyu Univ.)
8. Low-Energy Nuclear Reaction of Light Nuclei M. Aikawa (Hokkaido Univ.)
9. Systematic Measurement of Neutron and Gamma-ray Yields on Thick Targets Bombarded  
with 12 and 18 MeV Protons M. Hagiwara (KEK)
10. Study on the neutron capture cross sections and capture gamma-ray spectra  
of  $^{93}\text{Nb}$ ,  $^{103}\text{Rh}$  and  $^{115}\text{In}$  T. Matsushashi (Tokyo Inst. Tech.)
11. Analysis of radioactivity of the ground surface measured at the Fukushima-daiichi  
nuclear power plant site G. Chiba (Hokkaido Univ.)
12. Design and construction of a thermal column using an Am-Be neutron source for BNCT studies  
K. Harada (Osaka Univ.)
13. Measurement of  $\gamma$ -ray-Production Double-Differential Cross Section  
for 290 MeV/u Oxygen Ion Incidence H. Uehara (Kyusyu Univ.)
14. Identification of high-energy levels in  $^{147}\text{Ce}$  with a total absorption clover detector  
Y. Shima (Nagoya Univ.)
15. Neutron Capture Cross-Section of Palladium-107 in the Thermal-Neutron Energy Region  
S. Nakamura (JAEA)
16. Study on neutron spectrometer for thermal to epithermal energy regions  
with an advanced multi-activation-foil method H. Kanasugi (Osaka Univ.)
17. Systematic Study on keV-neutron Capture Cross Sections and Capture Gamma-ray Spectra  
of Pd Isotopes K. Terada (Tokyo Inst. Tech.)
18. Characterization Test of CdTe Detector Element Designed and Developed for BNCT-SPECT  
S. Nakamura (Osaka Univ.)
19. Critical Experiment with Thorium at KUCA T. Fujii (Osaka Univ.)
20. Benchmark Test of JENDL-4.0 with TOF Experiments at Osaka Univ./OKTAVIAN  
Y. Kato (Tokai Univ.)
21. Self-shielding effect in unresolved resonance data in JENDL-4.0 C. Konno (JAEA)
22. Angular distribution of light fragments for proton induced reaction at intermediate energies  
T. Sanami (KEK)
23. Sensitivity Analysis for Kyoto University Research Reactor Using JENDL-4.0  
T. Sano (Kyoto Univ.)

This is a blank page.

## 2 What has happened at the Fukushima Dai-ichi nuclear power plant by the Great East Japan Earthquake?

Ken Nakajima

Research Reactor Institute, Kyoto University  
Asashiro-Nishi 2-1010, Kumatori-cho, Sennan-gun,  
Osaka 590-0494, Japan  
e-mail: nakajima@rri.kyoto-u.ac.jp

### 1. Introduction

The greatest earthquake on record, which occurred on 11th March, 2011, and the large tsunami caused by the quake have hit the Fukushima Dai-ichi nuclear power plant of Tokyo Electric Power Company (TEPCO), and that resulted in the loss of all electric power (station blackout). Then, three reactors (units 1, 2 and 3) and four spent fuel storage pools (units 1 to 4) have lost the all cooling functions, and hence the cores melted down, followed by the hydrogen explosions in the reactor buildings. Consequently, a large amount of radioactive materials were released to the environment and contaminated the soil, water, foods, etc. More than hundred thousand residents evacuated from their hometowns. At present, seven months have passed, the accident is not yet terminated although the cooling systems for the reactors and pools are working well.

In this paper, the accident at the Fukushima Dai-ichi nuclear power plant is reviewed<sup>1,2)</sup>, and the lessons learned from the accident are discussed.

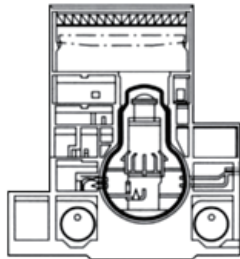
### 2. Outline of Fukushima Dai-ichi Nuclear Power Plant (NPP)

Fukushima Dai-ichi NPP consists of 6 nuclear reactors, Unit 1 to Unit 6. Specifications of each unit are shown in Table 1<sup>3)</sup>. As shown in the table, all the units started the commercial operation in 70's. Mark-I type primary containment vessel (PCV) was employed for the units 1 to 5, which has a torus-shape suppression chamber in the bottom and has a smaller volume than Mark-II type PCV employed for the unit 6 as shown in Fig. 1<sup>3)</sup>

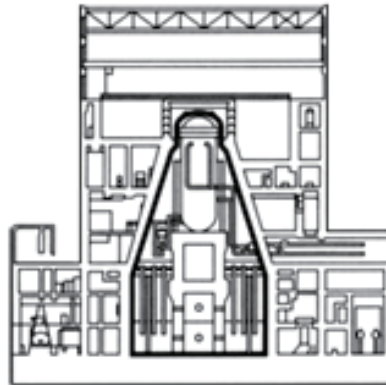
At the time earthquake occurred, three reactors of units 1 to 3 were operated and the other three reactors were shutdown for regulatory inspection. Besides the reactor core, each unit stored the nuclear fuels in the fuel pool located in the reactor building. The status of each unit before the accident is shown in Table 2.

Table 1 Specifications of Fukushima Dai-ichi Nuclear Power Plant<sup>3)</sup>

	Unit 1	Unit 2	Unit 3	Unit 4	Unit 5	Unit 6
Electric Output (MW)	460	784	784	784	784	1100
Thermal Output (MW)	1,380	2,381	2,381	2,381	2,381	3,293
Start-up of Commercial Operation	1971/3	1974/7	1976/3	1978/10	1978/4	1979/10
PCV Type	Mark I	Mark I	Mark I	Mark I	Mark I	Mark II



Mark-I



Mark-II

Fig. 1 Primary Containment Vessels<sup>3)</sup>

Table 2 Status of Fukushima Dai-ichi Nuclear Power Plant

		Status before the earthquake
Unit 1	Core	Full power operation (400 fuels = assemblies)
	Fuel pool	392 fuels (incl. 100 fresh fuels)
Unit 2	Core	Full power operation (548 fuels)
	Fuel pool	615 fuels (incl. 28 fresh fuels)
Unit 3	Core	Full power operation (548 fuels incl. 32 MOX fuels)
	Fuel pool	566 fuels (incl. 52 fresh fuels)
Unit 4	Core	Regular inspection (No fuel loaded, PCV filled with water)
	Fuel pool	1,535 fuels (incl. 204 fresh fuels)
Unit 5	Core	Regular inspection (RPV cover closed)
	Fuel pool	994 fuels (incl. 48 fresh fuels)
Unit 6	Core	Regular inspection (RPV cover closed)
	Fuel pool	940 fuels (incl. 64 fresh fuels)
Fuel pool for common use		6,375 fuels (after 19 months or more cooling)

### 3. Outline of Accident

#### 3.1 Influences of Earthquake and Tsunami

The earthquake with a moment magnitude ( $M_w$ ) 9.0 occurred at 14:46 on 11 March in the coast of Sanriku, and the seismic intensity of 6 upper on the Japanese scale was measured at the Fukushima Dai-ichi NPP site, about 180km far from the seismic center. The maximum observed ground motion at several units exceeded the designed value, and external power was lost due to the damage of facilities, such as line towers or transformers. However, all the operated reactors have shutdown successfully, the emergency diesel generators activated automatically, and no significant damage on the main equipments due to the quake are found currently.

Tsunami with about 15m height has attacked the NPP site at around 15:30, and damaged seawater pumps, emergency diesel generators, power panels, thus resulted in the loss of cooling function for the cores of units 1 to 3 and for the fuel pools of units 1 to 4. The emergency diesel generator for the unit 6 was only operable one after tsunami attacked and it could supply power to the units 6 and 5, then the fuels in these units could be cooled stable.

#### 3.2 Hydrogen explosions and Release of Radioactive Materials

Due to the lack of cooling function for the cores of units 1 to 3, the fuels in those cores became high temperature and hence the fuel rod cladding was damaged that caused the release of radioactive materials into the reactor pressure vessel (RPV). In addition, a large amount of hydrogen gas was produced in the RPV as a result of chemical reactions of the fuel cladding, made of zirconium, with water vapor (steam) at high temperature.

Then, gaseous radioactive materials and hydrogen gas flowed out to the PCV with steam through the safety relief valve and/or other leakage passes, and it increased the pressure of the PCV significantly. The operators had tried to conduct the PCV ventilation in order to avoid the breakdown of PCV. Although the decrease of the pressure was observed for the units 1 and 3 after the ventilations, no decrease was observed for the unit 2.

Finally, the explosions occurred in the unit 1 at 15:36 on 12<sup>th</sup> March, in the unit 3 at 11:01 on 14<sup>th</sup> March, and the upper part of each reactor building collapsed (Fig.2). Those explosions were thought to be caused by the accumulated hydrogen gas in the reactor building leaked from the PCV. In the morning of 15<sup>th</sup> March, the third explosion occurred at the reactor building of unit 4, where no fuel stored in the core. This explosion was estimated to be caused by the hydrogen gas flowed out from the unit 3 through the emergency gas treatment system which is connected to that of unit 4. For the unit 2, there observed no explosion, however, sudden pressure decrease was observed in the morning of 15<sup>th</sup> March, and high radiation level was recorded at the monitoring posts in the site, therefore, it was estimated that the breakdown of PCV occurred at this time.

Consequently a large amount of radioactive materials were released to the environment, and many residents had to evacuate. In the wide range of east Japan, the radioactive isotopes such as Iodine 131, Cesium 134 and 137 were detected and the contaminations of drinking water, agricultural crops, sea water, and so on were found.



Fig. 2 Reactor Buildings of Fukushima Dai-ichi NPP, Unit 1 (left) and Unit 2 (right)

### 3.3 Estimation of Fuel Damage

TEPCO has analyzed the plant (core) behavior of units 1 to 3 with the accident analysis code MAAP (Modular Accident Analysis Program) using the obtained information on the plant status<sup>4</sup>.

For the unit 1, the analyzed plant behavior, under the assumption that the IC (Isolation Condenser) did not work after the tsunami, was as follows:

The core water level decreased rapidly and reached to the top of active fuel level (TAF) in about 3 hours after the quake. One hour later, the fuel temperature exceeded 1,200°C, that is, the core damage has started. The total amount of hydrogen gas produced by the water-zirconium reaction was estimated as about 750kg. The water level continued to decrease and subsequently it reached to the bottom of active fuel level (BAF) in about 5 hours after the quake. Meanwhile, the RPV pressure increased to about 8MPa and it was kept due to the activation of safety relief valve. Fifteen hours after the quake, the pressure dropped suddenly to the lower level (less than 1MP) due to some reasons. All the fuel melted and moved to downwards, and then the most of fuel might reach to the bottom of the PCV, through the damaged bottom of RPV.

For the units 2 and 3, the RCIC (Reactor Core Isolation Cooling system) was operated for a while, therefore, the accident proceeded slower than the case of unit 1. The core water level reached to the TAF in about 75 hours after the quake for the unit 2, and in about 40 hours for the unit 3. Fuel was damaged and melted, however, some parts stayed in the core region and the rest moved to the lower plenum of RPV and/or the pedestal of PCV.

For the fuels in the pools, it was evaluated that they had no significant damage and kept cooled, by the visual observation and the measured data.

### 3.4 Recent Status

The operators have been struggling to cool the fuels in the cores and pools of units 1 to 4

with the help of domestic and international supports, and the situation improved gradually. In September, stable cooling could be achieved by using circulated-cooling systems for all cores and pools. Before the circulated-cooling system established, the water injecting to the core leaked out from PCV as high-level contaminated water and accumulated in the basement of the turbine building with huge volume and it leaked to the ocean partially. Presently, the contaminated water is collected and cleaned up, and re-uses as a coolant, then the volume of contaminated water decreases. On 16<sup>th</sup> December, the government has announced that the system became cold-shutdown phase, that is, the system became under control.

The release of radioactive materials has been decreasing since April as shown in Fig.3, and the contamination by the long-life isotopes Cesium 134 (half life: ca 2y) and 137 (30y) remains an issue. Although the effort to decontaminate has been conducted, it will take long time and high cost, since the target area is very large and the disposal method of radioactive wastes is not determined.

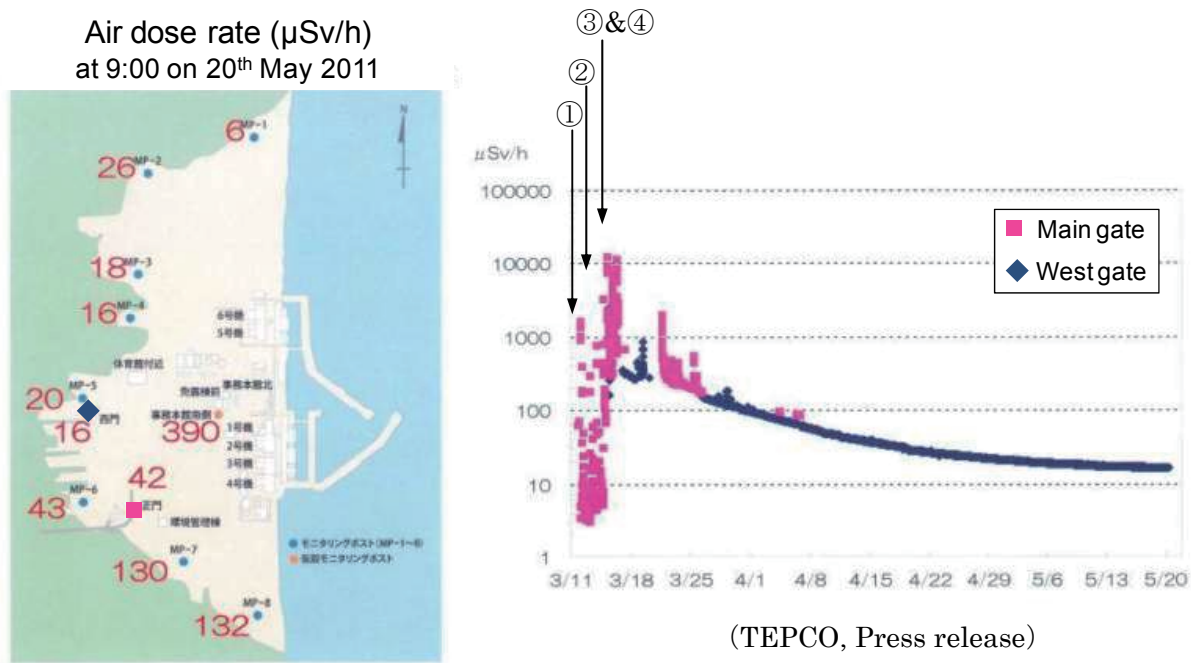


Fig. 3 Monitoring data (periphery of Fukushima Dai-ichi site)

The rapid increases of dose rate in the early period of the accident were caused by the following events, which resulted in the release of radioactive materials to the environment.

- ①Unit 1: Hydrogen explosion at 15:36, 3/12.
- ②Unit 3: Hydrogen explosion at 11:01, 3/14.
- ③Unit 4: Hydrogen explosion in the morning, 3/15.
- ④Unit 2: PCV pressure drop in the morning, 3/15.

#### 4. Lessons Learned

Since the accident is not yet terminated, it is too early to conclude the reasons and the lessons learned. In this section, author's personal impressions and opinions are shown as the lessons learned.

##### 4.1 On the station blackout

It can be said that the direct reason of the accident was the loss of cooling function caused by the loss of power supply (Station Blackout; SBO). In Japan, the electric power supply is very stable and reliable, and it will be recovered rapidly even if the blackout happens. This fact is also reflected into the safety design of the nuclear power plant. In the safety review guide<sup>1</sup>, "Review Guide for Safety Design of Light Water Nuclear Power Reactor Facilities<sup>5)</sup>," it is described that "The nuclear reactor facilities shall be designed that safe shutdown and proper cooling of the reactor after shutting down can be ensured in case of a short-term total AC power loss." In addition, in the commentary of the guideline, it is said that "No particular considerations are necessary against long-term total AC power loss because the repair of troubled power transmission line or emergency AC power system can be expected in such case." This guideline states that the Japanese nuclear power plants have no need to prepare against the long-term SBO.

The Nuclear Safety Commission (NSC) has determined to totally revise the safety review guides by reflecting the Fukushima accident in last June, and discussions in the subcommittees have been conducted.

##### 4.2 On the Emergency Preparedness<sup>6)</sup>

After the JCO-Tokai criticality accident, the Special Act of Emergency Preparedness for Nuclear Disaster was established for the following purposes:

- (1) To ensure swift initial activation,
- (2) To ensure close cooperation with the central government and local governments,
- (3) To enhance the emergency response by the central government, and
- (4) To clarify the responsibility of licensees.

According to the act, many kinds of facilities/equipments are prepared, such as the offsite centers, accident information gathering/evaluating tools, robotics machines for emergency, and so on. However, those facilities/equipments did not work well in the early stage of the present accident. For examples, the offsite center at Fukushima area was not functioned for first few days because that the power supply system was damaged by the quake, and after that the people had to evacuate from the center due to high radiation level. For the robotics

---

<sup>1</sup> Safety review guide is a guideline used for safety review that is determined by the Nuclear Safety Commission of Japan. There are guides for siting, designing, safety evaluation, dose objective, etc.

machines developed after the JCO accident did not work in this time because the machines were not well maintained due to the lack of financial support. Thus, it can be said that the emergency preparedness for nuclear disaster in Japan was unavailable for the “real” emergency. It is impossible to evaluate the impact of natural disaster exactly, and hence we have to prepare for the emergency that may exceed the evaluations and make a lot of practices on the premise that such emergency will really occur.

## 5. Conclusions

After the accident, the government has decided to reform the nuclear regulation system; to abolish the present regulatory bodies, NISA (Nuclear and Industrial Safety Agency) and NSC, and establish the new organization, the Nuclear Regulation Agency, as an external agency under the Ministry of the Environment. The NISA is a part of METI (Ministry of Economy, Trade and Industry). Since the METI is the ministry which drives forward the nuclear energy utilization, the independence of nuclear regulatory body from the METI has been emphasized widely before the accident. However, the most important matter for the safety of nuclear facilities is to foster the human resources in the variety of the fields, regulation, industry, research and development. For the safer world, we have to learn lessons from the present and past accidents and hand them on to the next generation.

## References

- 1) “Report of Japanese Government to the IAEA Ministerial Conference on Nuclear Safety – The Accident at TEPCO's Fukushima Nuclear Power Stations –,” Nuclear Emergency Response Headquarters, Government of Japan, June 2011.  
[http://www.kantei.go.jp/foreign/kan/topics/201106/iaea\\_houkokusho\\_e.html](http://www.kantei.go.jp/foreign/kan/topics/201106/iaea_houkokusho_e.html)
- 2) “Investigation Report on Accident of Fukushima Nuclear Power Plants (Interim Report),” Tokyo Electric Company, Dec. 2011. [in Japanese]  
<http://www.tepco.co.jp/cc/press/11120203-j.html>
- 3) Outline of Fukushima Dai-ich Nuclear Power Plant. [in Japanese]  
<http://www.tepco.co.jp/nu/f1-np/intro/outline/outline-j.html>  
[http://www.tepco.co.jp/nu/fukushima-np/outline\\_f1/index-j.html](http://www.tepco.co.jp/nu/fukushima-np/outline_f1/index-j.html)
- 4) Estimation of Core Damage for Units 1 to 3 of Fukushima Dai-ich Nuclear Power Plant. [in Japanese]  
[http://www.tepco.co.jp/nu/fukushima-np/images/handouts\\_111130\\_07-j.pdf](http://www.tepco.co.jp/nu/fukushima-np/images/handouts_111130_07-j.pdf)
- 5) “Review Guide for Safety Design of Light Water Nuclear Power Reactor Facilities,” JNESeL-RG-003 (2011). <http://www.jnes-elearning.org/contents/rg/JNESeL-RG-003.pdf>  
The original version (determined in 1990 by NSC) is in the following site. [in Japanese]

<http://www.nsc.go.jp/shinsashishin/pdf/1/si002.pdf>

- 6) Ken Nakajima, “Are the lessons of JCO criticality accident well applied? - For the nuclear accident management-,” Journal of the Atomic Energy Society of Japan, Vol. 53, No.9, p.628-632 (2011). [in Japanese]

### 3 Severe accident analysis and related nuclear data

Kazufumi Tsujimoto  
*Nuclear Transmutation Technology Group,*  
*Japan Atomic Energy Agency*  
tsujimoto.kazufumi@jaea.go.jp

The design of any nuclear power plant is impossible without safety evaluation. Analysis of design basis accident (DBA) considered to prove safety features of installed equipment to prevent accidents. On the other hand, analysis of severe accidents plays a very important role in risk assessments in order to reduce the probability of severe accidents with core melt to the level of  $10^{-6}$ /reactor-year or less. In comparison to DBA, the main differences for the modeling of severe accident are connected to the fact that the object of modeling itself is not well defined due to changes of geometrical factors, composition of the melt and its properties.

Typical system analysis codes for severe accidents are MELCOR (Methods for Estimation of Leakages and Consequences of Releases)<sup>1)</sup>, MAAP (Modular Accident Analysis Program)<sup>2)</sup>, and SCDAP/RELAP (SCDAP : Severe Core Damage Analysis Package)<sup>3,4)</sup>. They have been developed from different approaches and for different purposes. MELCOR was originally intended to be a probabilistic risk assessment tool. Latter versions of MELCOR contain significant modifications, including the addition of a large number of physics models. The initial objective for the MAAP code was to predict severe accidents, using simple models based on first principles. MAAP has been shown to produce credible results for several severe accident scenarios despite relatively coarse spatial mesh and run times two or three orders of magnitude shorter than those of MELCOR and SCDAP/RELAP5. SCDAP/RELAP5 began as a best estimate code with physics-based models.

MELCOR and SCDAP/RELAP5 are used by regulatory agencies and research institutes to evaluate several hypothetical severe accident events. MAAP is the most widely used by nuclear utilities and vendors because of its short run time and reduced requirements for code expertise. In the report for the accident of the Fukushima Nuclear Power Plants from Japanese government, the analysis results were presented. In the report, TEPCO carried out analysis and evaluation of reactor situation of Unit 1, Unit 2 and Unit 3 using MAAP, whose results are reported to NISA on May 23. NISA also carried out a crosscheck for validation of TEPCO's analysis by using other code, MELCOR.

Evaluations related to nuclear data in the analysis of severe accidents are as following; (1) core composition and source term, (2) decay heat, and (3) criticality. In the MELCOR code, there are some calculation models to estimate the source term and the decay heat. One of them is a method to use the ORIGEN code. However, it is impossible to consider the detailed distribution in the core. These

information will be needed for the detailed modeling of the core debris. Moreover, evaluation of the criticality is a remaining issue in the severe accident analysis for the nuclear power plant.

The possibility of the severe accident with core melt is considered as level of  $10^{-6}$ / reactor-year or less. In Japan, severe accident management has been considered as the independent efforts by the power company. The latest results from the research for the severe accidents and related phenomena were not timely reflected for the regulatory. However, we experienced three severe accidents past 50 years of nuclear power operation, TMI-2, Chernobyl, and Fukushima. We must learn the lessons from these accidents and make progress for the effort to get and reflect the latest knowledge.

#### References

- [1] Sandia National Laboratory, "MELCOR Computer Code Manuals, vol.1: Primer and Users Guide, Version 1.8.5", NUREG/CR-6119, Rev.2, 2001, Prepared by Sandia National Laboratories for the U.S. Nuclear Regulatory Commission, Office of Nuclear Regulatory Research.
- [2] "MAAP5-Modular Accident Analysis Program for LWR Power Plants", Fauske and Associates Inc., 2008.
- [3] L. J. Siefken, E.W.Coryell, E.A.Harvego, and J.K.Hohorst, "SCDAP/RELAP5/MOD 3.3 Code Manual, Code Architecture and Interface of Thermal-Hydraulic and Core Behavior Models", NUREG/CR-6150, vol.1, Rev.2, INEL-96/0422, 2001, Idaho National Engineering and Environmental Laboratory.
- [4] L. J. Siefken, E.W.Coryell, E.A.Harvego, and J.K.Hohorst, "SCDAP/RELAP5/MOD 3.3 Code Manual, Modeling of Reactor Core and Vessel Behavior During Severe Accidents", NUREG/CR-6150, vol.2, Rev.2, INEL-96/0422, 2001, Idaho National Engineering and Environmental Laboratory.

#### 4 High Temperature Gas-cooled Reactor (HTGR) with inherent safety features

Kazuhiko KUNITOMI

Nuclear Hydrogen and Heat Application Research Center

Japan Atomic Energy Agency

Oarai-machi, Ibraki-ken, 311-393, Japan

e-mail: [kunitomi.kazuhiko@jaea.go.jp](mailto:kunitomi.kazuhiko@jaea.go.jp)

Japan Atomic Energy Agency (JAEA) has long been developing the advanced technology of High Temperature Gas-cooled Reactor (HTGR) through the construction and operation of the High Temperature Engineering Test Reactor (HTTR) and the design of a future commercial HTGR system. After the Fukushima Daiichi Light Water Reactor accident the safety of nuclear reactors became far more important than before. Nuclear reactors with inherent safety features are expected to be replacement with existing nuclear reactors. The HTGR with outstanding inherent safety features is the best candidate to be deployed after the accident.

This paper describes inherent safety features of the Gas Turbine High Temperature Reactor (GTHTR) as a reference design of HTGR.

##### 1. Introduction

GTHTR series have been designed to meet demand increase of the electricity especially in developing countries, and to supply high temperature heat for chemical, petrochemical and steelmaking industries in advanced countries. It is expected to be a promising energy system to contribute to reduce CO<sub>2</sub> emission in 2020s. So far, several types of GTHTRs have been designed to meet requirements from various users. Standard one is a 600 MWth unit for electricity generation (GTHTR300)[1], the other options are a 600MWth unit for hydrogen production and electricity generation (GTHTR300C)[2] and a 50 MWth unit for electricity generation and district heating (GTHTR50C)[3].

Figure 1 shows the plant layout of the GTHTR300 which consists of three subsystem modules including the 600MWt prismatic reactor module, horizontal gas turbine generator (GTG) module, and vertical heat exchangers (HTX) module. Table 1 shows the major specification of the GTHTR300. The electricity output is closed to 280MW.

Safety features of this system are very attractive, considering that nuclear accidents widely damage environment around the reactor site and it takes more than a life long time to solve all the problems followed by the accident. Even in the worst accident, the reactor automatically stops due to negative feedback coefficient, a passive indirect core cooling system located outside of the Reactor Pressure Vessel

(RPV) cools the reactor core, and coated fuel particle contains fission products safely. Also beneficial point is that it can be placed in remote inland area or the desert because the amount of cooling water necessary for this system is very small. Due to these merits the GTHTR will expand the nuclear reactor site to Kazakhstan, Saudi Arabia etc. and tsunami free areas in Japan.

Table 1 Major specification of the GTHTR300

Reactor thermal power and electric power	600MWth/274MWe
Efficiency	45.8%
Reactor inlet and outlet temperature	587/850°C
Gas turbine inlet pressure	7 MPa
Gas turbine mass flowrate	439kg/s
Core height	8.4m
Inner and outer diameter of the core	3.6/5.5m
Fuel type	Pin-in-block type
Fuel enrichment	14wt%
Average power density	5.4 MW/m <sup>3</sup>
Reactor pressure vessel inner diameter	7.6m

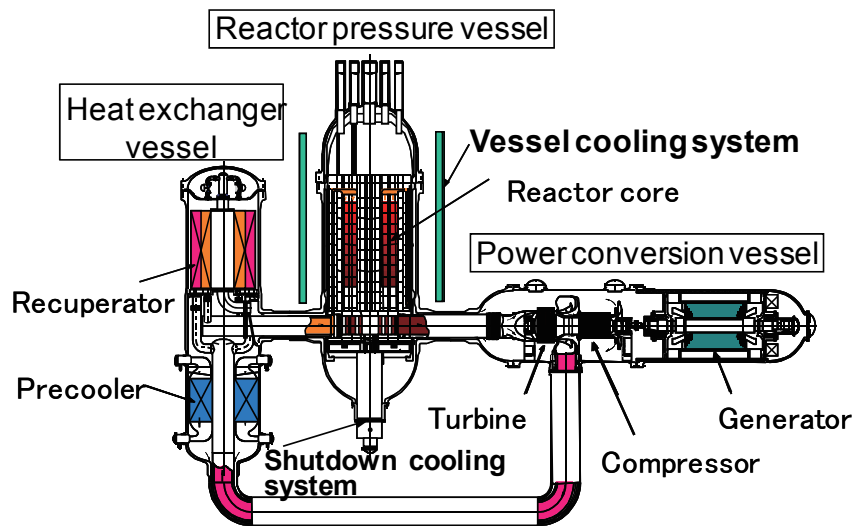


Figure 1 Plant layout of GTHTR300

## 2. Fundamental safety functions

### (1) Control of reactivity

The reactor is shut down safely and reliably from any operational state using the control rod system. Furthermore, the reserve shutdown system is provided, which is composed of boron-carbide/graphite ( $B_4C/C$ ) pellets. The power control and normal reactor shutdown of the GTHTR300 are achieved with 30 pairs of control rods. The control rod system can achieve subcriticality from any operational state and maintain subcriticality in the cold core conditions even when a pair of control rods sticks at the operational position. A pair of control rods is driven by one drive mechanism. The control rods are released from the drive mechanism and inserted by gravity when the reactor is scrammed. Even in the case that the control rod insertion fails, the reactor shuts down due to negative feedback characteristic of the core.

### (2) Removal of heat from the core

The GTHTR300 has two residual heat removal systems, vessel cooling system (VCS) and shutdown cooling system (SCS). The VCS is used as a residual heat removal system in all off-normal states. Even the case that forced circulation in the primary cooling circuit is not available due to a rupture of primary pipes or the case that no active system is working by station blackout, the VCS consisting of air ducts and cooling panels around the RPV induces air into the cooling panels by natural circulation and removes heat from the RPV. The VCS is classified as safety grade.

The SCS located under the reactor core (see Fig.1) cools the reactor core during off-normal transients or accidents in which the coolant flow boundary is intact. It speeds up cooling the core for safety-check and maintenance work. The SCS is not classified as safety grade because the VCS has a sufficient cooling capacity to keep the reactor core safe condition.

### (3) Containment of fission product

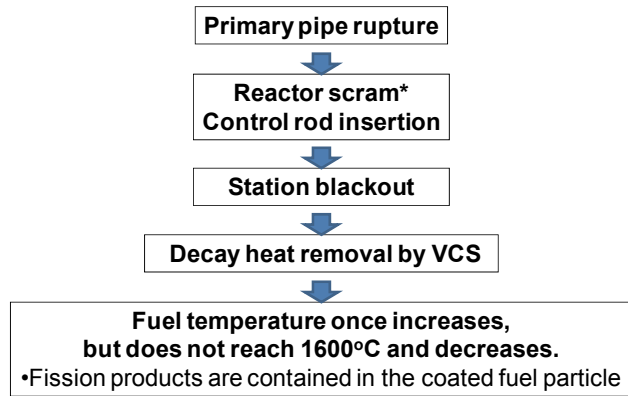
The GTHTR300 has multiple barriers to prevent fission product release into the environment, fuel coatings, the reactor pressure boundary, the confinement and the reactor building. The ceramic layers surrounding the fuel kernel act as the primary barrier for the fission product release. The integrity of these ceramic layers is sufficiently kept under 1600°C based on several experiments. The JAEA carried out irradiation tests and post irradiation tests up to 33000MWd/t before the HTTR operation and continues to carry out irradiation tests for the HTTR initial loading fuel up to 70000MWd/t. So far, the heating up tests after the irradiation proved that the integrity of the fuel can be sufficiently maintained under 1600°C. It also showed that the fuel failure rate in the range from 1600 to 1800°C is negligible small.

The GTHTR300 does not have a leak-tight pressure resistant steel containment vessel. In the case of the primary pipe rupture, the helium gas escaped from the primary circuit is released to the atmosphere through the confinement. Though fission products in the primary circuit and plated-out FPs on the surface of the pipe is immediately released into the atmosphere, the off-site radiation dose limit in such accident is under the limit

because initial fuel failure in manufacturing process, and failure in normal operation are very low, and the additional fuel failure by heat-up and oxidation after the occurrence of the accident is limited[4].

3. Safety evaluation of the worst accident

An accident initiated by a primary pipe rupture and the following station blackout was selected as the worst accident from the standpoints of heat removal of the fuel and containment of the fission products. The reactor core temperature transients during this accident were calculated by the thermal analysis code TAC-NC to examine the fuel integrity and its containment function. Figure 2 shows the accident sequence. The reactor power is shut down by the reactor scram. Even if the reactor scram fails, the reactor automatically shuts down due to negative feedback.



\* Even if the reactor scram fails, the reactor power automatically decreases due to negative feedback characteristic

Figure 2 Accident sequence

Figure 3 shows concept of an air-cooled VCS and heat flow from the core to the atmosphere. The core residual heat is transferred from the RPV to the cooling panels by radiation and natural convection in the core cavity. The cooling air in the cooling panels absorbs heat and flows out to the atmosphere. The driving force of the air circulation is temperature difference between the hot side and cold side of air.

Figure 4 shows the fuel temperature transients during this accident. The maximum fuel temperature closes to 1600°C at about 70 hours after the occurrence of the accident, however, it does not exceed the fuel temperature limit of 1600°C.

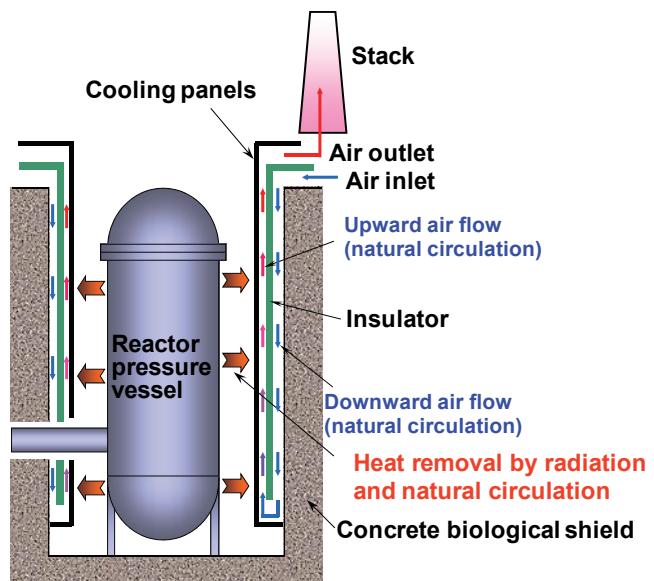


Figure 3 Heat removal by Vessel Cooling System

Also, the spent fuel temperature in the dry storage during the accident was evaluated. Fuel blocks are taken out from the core and contained into a rack. In this process, fuel rods are not removed from the fuel block so that the power density by their decay heat is kept at reasonable low level. The rack is installed in the dry storage and cooled by air. Air is circulated naturally and no air circulators are necessary shown in Fig 5.

Figure 6 shows the fuel temperature in the dry storage. The fuel temperature decreases gradually and is remained under the allowable temperature.

The evaluation revealed that the temperature of fuels in the core and spent fuel is kept under the allowable limit and no risk of FP release from the coated fuel particles.

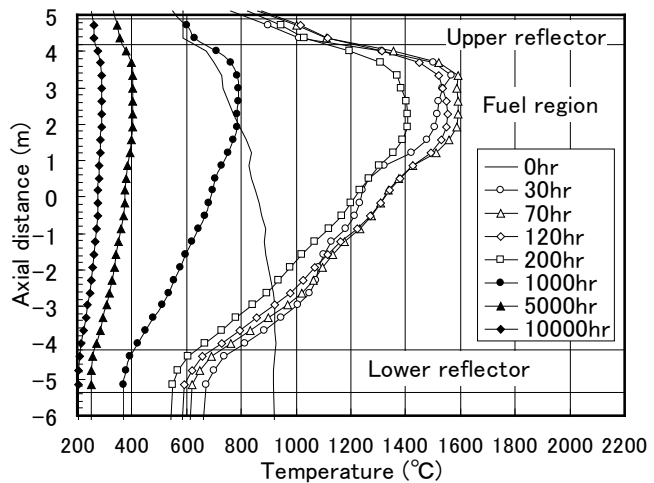


Figure 4 Temperature profile after occurrence of accident

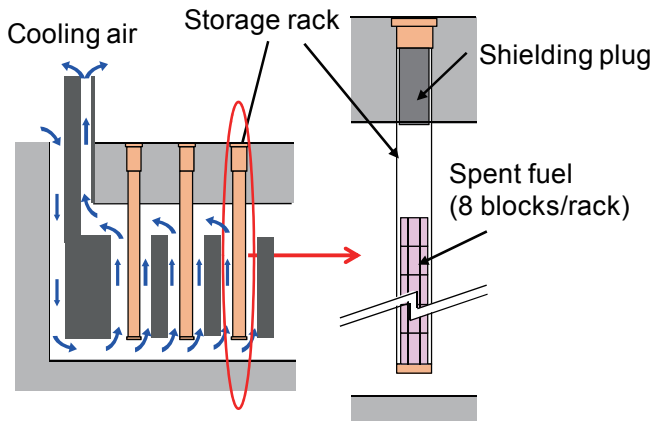


Figure 5 Dry spent fuel storage of GTHTR300

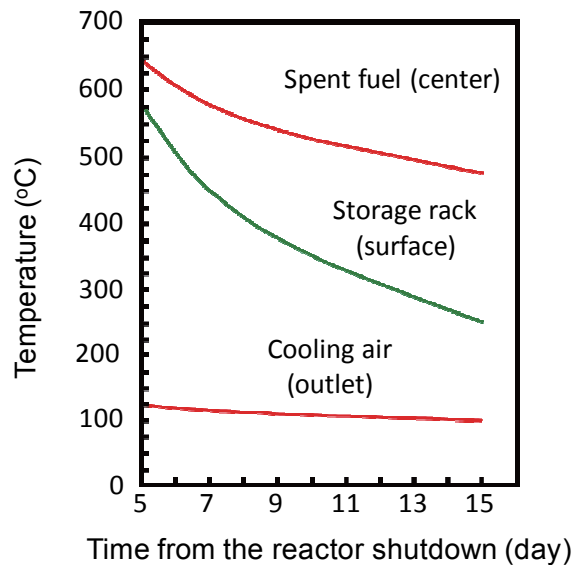


Figure 6 Temperature transient of spent fuel

#### 4. Conclusion

The inherent safety features of the HTGR were described by the design and safety evaluation of the GTHTR300. The containment function of the FP is kept during the worst accident such as a primary pipe rupture and the following station blackout. After the Higashi-Nihon earthquake, safety of the nuclear system is of prime concern to average population as well as nuclear experts. A super safe HTGR system to meet public requirements will be deployed from now on. The HTGR will live up to the requirements of public and safety authority as a super safe energy supply system in 2020s.

#### Reference

- [1] K. Kunitomi, et al., "Japan's future HTGR- the GTHTR300", Nucl. Eng. Design, 233, P309-327,(2004).
- [2] K. Kunitomi, et al., "Development of GTHTR300 Cogeneration for Hydrogen and Electricity Generation", ICAPP04, Pittsburgh, PA USA, June 13-17, (2004).
- [3] S. Sakaba, et al., "Examination on Small-Sized Cogeneration HTGR for Developing Countries", JAEA-Technology 2008-019, (2008).
- [4] K. Kunitomi, et al., "Evaluation on Fuel Oxidation during Depressurization Accident in GTHTR300", ICAPP05, Seoul, Korea, May15-19, (2005).

## 5 Fast Breeder Reactor core design study using JENDL-4.0

Kazuya OHGAMA, Shigeo OHKI and Tsutomu OKUBO  
*Advanced Nuclear System R&D Directorate, Japan Atomic Energy Agency*  
 4002, Narita-cho, O-arai-machi, Higashi-Ibaraki-gun,  
 Ibaraki Pref, 311-1393, Japan  
 e-mail: ohgama.kazuya@jaea.go.jp

The core characteristics of a sodium-cooled fast breeder reactor (FBR) with 750 MWe output were evaluated by using the fast reactor cross section set JFS-3-J4.0, which was generated by the new Japanese nuclear data library JENDL-4.0. The core characteristics were compared with those obtained by using the former fast reactor cross section set JFS-3-J3.3 in order to investigate differences between the both results. Effects on the core characteristics caused by differences of important reactions and nuclides in the cross section sets were analyzed.

## 1. Introduction

The new nuclear data library JENDL-4.0 was released in 2010.<sup>1)</sup> In this library, neutron reaction cross sections of important nuclides for the FBR core design including fission products and minor actinides (MA) were improved both in quality and quantity. In addition to that, neutron reaction cross sections of uranium and plutonium isotopes were reevaluated.

Benchmark testing for the new data library has been carried out by using a lot of integral data including criticality data and post irradiation test data for fast systems. It was confirmed that Calculation/Experiment (C/E) values have been considerably improved in JENDL-4.0 in comparison with those in JENDL-3.3, which is former version of nuclear data.<sup>2),3)</sup> Further, it was found that results obtained with JENDL-4.0 were slightly larger in the effective multiplication factor,  $k_{\text{eff}}$ , than those with JENDL-3.3 in middle- and large-size fast systems. For these reasons, adopting the JFS-3-J4.0 to the FBR core design is expected to improve accuracy of prediction of the core characteristics. In addition, it is also expected that there are beneficial changes such as decrease of Pu enrichment of fuel and improvement of reactivity control balance in core design due to slightly larger  $k_{\text{eff}}$  in the JENDL-4.0 results. In addition to these, other characteristics such as decay heat and heavy metal composition are expected to be influenced by improvement of nuclear data of MA nuclides.

In the present study, the core characteristics of a sodium-cooled fast breeder reactor (FBR) with 750 MWe output<sup>4)</sup> evaluated with JFS-3-J4.0 (JENDL-4.0) and JFS-3-J3.3 (JENDL-3.3) were compared. The core characteristics such as reactivity coefficients, MA composition and decay heat in spent fuel were evaluated with "Low-decontaminated TRU" composition which is expected to give relatively higher values of them than those with other compositions. On the other hand, reactivity control balance was confirmed with "High-decontaminated U-Pu" composition which causes higher burnup reactivity.<sup>5),6)</sup> The differences between the core characteristics evaluated by using the both libraries were investigated by a burnup sensitivity analysis.

## 2. Calculation

## (1) Core specifications and fuel compositions

The major specifications of the 750MWe FBR are listed in Table 1. Thermal and electric power outputs are 1765 and 750 MW, respectively. The core outlet and inlet temperatures are 550 and 395°C. The operation cycle length is set to 18 months, and the fuel exchange is performed with 6 batches. The driver core height is 100 cm. The upper and lower axial blanket lengths are 20 and 25 cm. The core equivalent diameter is 3.75m. The core contains 274 driver subassemblies and 27 control rods and is surrounded by the axial blanket fuel and one layer of radial blanket subassemblies (See Fig.1). The fuel compositions are listed in Table 2.

## (2) Methods

The major core characteristics of the 750 MWe FBR core with the high-decontaminated U-Pu fuel such as reactivity control balance, burnup reactivity and a breeding ratio were evaluated by a diffusion and burnup calculation in three-dimensional geometry with a 7-group cross section structure. Calculations of sodium void reactivity and a Doppler coefficient were performed in two-dimensional RZ core geometry with a 70-group cross section structure. The Pu enrichment was adjusted at the lowest percentage as long as the core reaches its criticality. Those calculations were performed with the both fast reactor cross section sets based on JENDL-4.0

and JENDL-3.3.

Table 1 750MWe sodium-cooled fast reactor

Item	Unit	Specification
Thermal Power Output	MWt	1765
Electric Power Output	MWe	750
Outlet/Inlet temperature	°C	550/395
Operational Cycle Length	Month	18
Refueling Batch (Core/Radial Blanket)	-	(6/6)
Core Height	cm	100
Axial Blanket Thickness (Upper/Lower)	cm	20/25
Core Equivalent Diameter	m	3.75

Table 2 Fuel composition

Nuclide	High-decontaminated U-Pu	Low-decontaminated TRU
	(wt%) <sup>*1</sup>	(wt%) <sup>*2</sup>
Pu-238	2.5	1.7
Pu-239	52.4	46.7
Pu-240	26.2	23.6
Pu-241	10.3	2.0
Pu-242	7.6	6.7
Np-237	0.0	6.2
Am-241	1.0	11.5
Am-243	0.0	1.4
Cm-244	0.0	0.2
Total	100.0	100.0
Pu/f/TRU	62.3	48.7
MA/TRU	1.0	19.3

<sup>\*1</sup> LWR UOX spent fuel composition (8years cooling).

<sup>\*2</sup> High burnup LWR UOX spent fuel composition (40 years cooling).

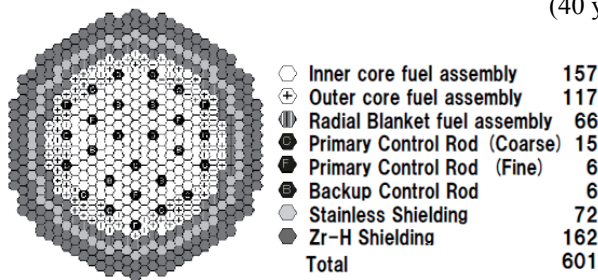


Fig.1 Core configuration

### 3. Results and discussion

#### 3.1 Low-decontaminated TRU fuel core

##### (1)Core characteristics

The major core characteristics of the 750 MWe FBR core with the low-decontaminated TRU fuel evaluated by using JENDL-4.0 and JENDL-3.3 are listed in Table 3.

In the calculation with JENDL-3.3, Pu enrichments of inner and outer core fuel were 18.4 and 24.7 wt% respectively. In the comparison of calculations with JENDL-3.3 and JENDL-4.0 based on the same Pu enrichments, there was almost no difference in burnup reactivity and breeding ratios, though the  $k_{eff}$  calculated with JENDL-4.0 was slightly higher than that with JENDL-3.3. In the calculations with the initial load core composition,  $k_{eff}$  with JENDL-4.0 was higher by about 1% than that with JENDL-3.3.

In another calculation with JENDL-4.0, Pu enrichments of inner and outer core fuel were adjusted to 18.1 and 23.7 wt %. Because of its lower Pu enrichments, it was found that relatively lower  $k_{eff}$ , a higher breeding ratio and lower burnup reactivity in the calculation with JENDL-4.0 than those in that with JENDL-3.3.

Table.3 Core characteristics of 750MWe SFR (Low-decontaminated TRU)

Item	Unit	JENDL-4.0		JENDL-3.3
Pu enrichment(Inner/Outer)	wt%	18.1/23.7	18.4/24.7	18.4/24.7
$k_{eff}$ (Max)	-	1.0100	1.0140 (1.0358) <sup>*1</sup>	1.0114 (1.0277) <sup>*1</sup>
Burnup reactivity	%Δk/kk'	0.81	0.93	0.92
Breeding ratio (Average)	-	1.149	1.133	1.132
Max Linear Heat Rate (Inner/Outer)	W/cm	382/383 <sup>*2</sup>	369/368 <sup>*2</sup>	369/368 <sup>*2</sup>
Sodium Void Reactivity	\$	6.5 <sup>*3</sup>	6.4 <sup>*3</sup>	6.2 <sup>*3</sup>
	%Δk/kk'	2.01x10 <sup>-2</sup>	1.99x10 <sup>-2</sup>	1.95x10 <sup>-2</sup>
Delayed Neutron Fraction	-	3.11x10 <sup>-3</sup>	3.10x10 <sup>-3</sup>	3.14x10 <sup>-3</sup>
Doppler coefficient	Tdk/dT	-4.08x10 <sup>-3</sup>	-4.03x10 <sup>-3</sup>	-3.96x10 <sup>-3</sup>

<sup>\*1</sup> Calculation for initial fuel load core.

<sup>\*2</sup> Calculation by a diffusion and burnup calculation in RZ core geometry with a 70-group cross section.

<sup>\*3</sup> No correction such as heterogeneous and mesh effects.

(2)Burnup sensitivity analysis

In order to investigate the differences of  $k_{eff}$  and sodium void coefficient calculated with JENDL-4.0 and JENDL-3.3 with the same Pu enrichments, a sensitivity analysis was performed.

Product of the burnup sensitivity coefficients and the relative differences between the both libraries provides the nuclide-and-reaction-wise information about differences of the core characteristics calculated with the both libraries.

Sensitivity coefficients of  $k_{eff}$  and sodium void coefficient of the core with the low-decontaminated TRU fuel were calculated with JENDL-3.3 by the use of a burnup sensitivity analysis code system based on the Generalized Perturbation theory.<sup>7)</sup> The 70-group nuclear data prepared from the both libraries were collapsed into 18-group structure by the use of neutron spectrum in the core central region of the reference core. Relative differences between the both libraries were derived from the 18-group data.

(a)Criticality

Sensitivity coefficients of  $k_{eff}$  were calculated for the initial load core with the low-decontaminated TRU fuel. It was confirmed that differences in fission and capture cross sections of Pu-239, the average number of neutrons per fission ( $\nu$ -value) of Pu-240, inelastic scattering cross section of U-238 and capture cross section of Am-241 were major contributors of increases of  $k_{eff}$  (See Fig.2).

Figure 3 shows an example of the sensitivity analysis of  $k_{eff}$ . The Sensitivity coefficients of  $\nu$ -value of Pu-240 were positive and relatively larger above  $10^5$ eV than other area due to its fission threshold. The  $\nu$ -value of Pu-240 of JENDL-4.0 is larger by about 2% than that of JENDL-3.3 in any region. So it is obvious that positive sensitivity coefficients and difference in  $\nu$ -value of Pu-240 provide positive contribution to  $k_{eff}$  in JENDL-4.0 calculation.

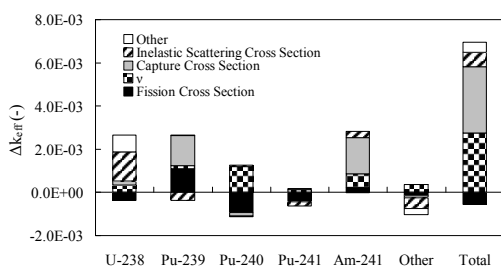


Fig.2 Sensitivity analysis of  $k_{eff}$

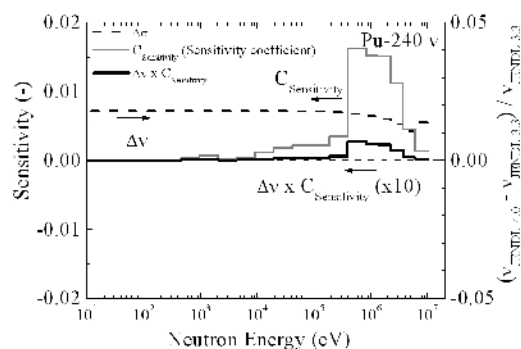


Fig.3 Effect to  $k_{eff}$  caused by difference in  $\nu$ -value of Pu-240

(b)Sodium void reactivity

Sodium void reactivity calculated with JENDL-4.0 based on the end of cycle burnup composition calculated with JENDL-3.3 was higher by 3% than that with JENDL-3.3. The differences in delayed neutron fractions contributed to the difference by 1%, and other contributions came from differences in other nuclear data such as fission, capture and inelastic scattering cross sections,  $\nu$ -value and so on.

A sensitivity analysis for sodium void reactivity was performed (See Fig.4). It was found that the differences in fission cross section and  $\nu$ -value of Pu-239, average cosine of scattering angle ( $\mu$ -average) and inelastic scattering cross section of U-238, and capture cross section of Pu-240 between JENDL-4.0 and JENDL-3.3 were major contributors of differences of the sodium void reactivity obtained in calculations using by the both libraries.

Energy distribution of sensitivity coefficients of sodium void reactivity is different from that of the  $k_{eff}$ . When void is induced in coolant sodium in the core region, neutron spectrum becomes harder. Thus, sensitivity coefficients below  $3 \times 10^3$ eV are strongly negative and coefficients above  $10^5$ eV are positive for fission cross sections and  $\nu$ -values of heavy metals. Because relative difference in  $\nu$ -value of Pu-239 had coincidentally similar energy distribution as its sensitivity coefficients, contribution of difference in  $\nu$ -value of Pu-239 became relatively large despite of small difference which hardly influenced  $k_{eff}$  (See Fig. 5).

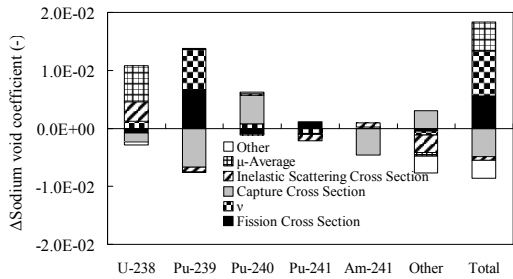


Fig.4 Sensitivity analysis of sodium void reactivity

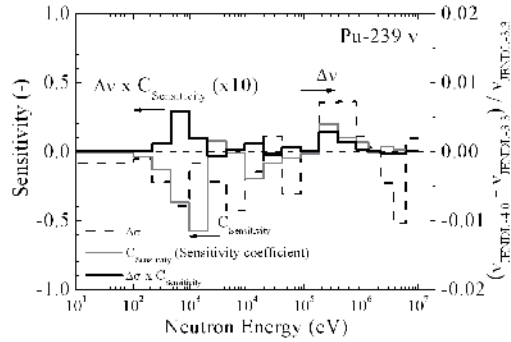


Fig.5 Effect to sodium void reactivity caused by difference in  $\nu$ -value of Pu-239

(3)MA composition

Figure 6 shows relative differences of TRU compositions of discharged spent fuel at mid plane of the core and the innermost part of the outer core region evaluated by a diffusion and burnup calculation with JENDL-4.0 and JENDL-3.3 with the same Pu enrichments. There was almost no difference in production of Pu-239, as it was confirmed that the breeding ratios obtained by using JENDL-4.0 and JENDL-3.3 based on the same Pu enrichments were identical (See Table 3). Regarding to nuclides which cause decay heat, the amount of Am-241 and Pu-238 in the spent fuel increased, and the amount of Cm-242 and Cm-244 decreased.

Figures 7 and 8 show the results of sensitivity analyses of production of Pu-238 and Am-241 by a diffusion and burnup calculation. Figures 9 and 10 illustrate reaction rate energy distribution concerning to production of those nuclides, which were evaluated by multiplying a 70-group cross section set and a 70-group normalized neutron spectrum in outer core region of reference core.

The difference in capture cross section of Pu-238 in  $5 \times 10^3 - 4 \times 10^6$  eV was major contributor of the increase of Pu-238 (See Fig.9). The difference in capture cross section of Am-241 in  $10^2 - 3 \times 10^5$  eV contributed to the increase of Am-241 (See Fig.10).

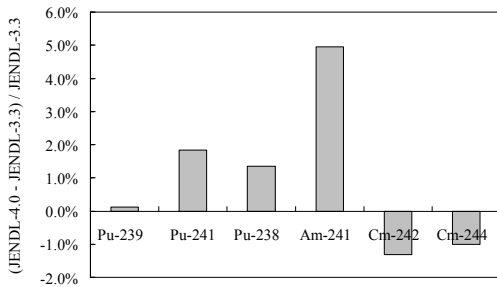


Fig.6 Differences of composition of major Nuclides in spent fuel in outer core region

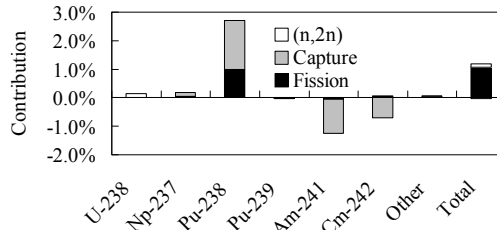


Fig.7 Sensitivity analysis of production of Pu-238

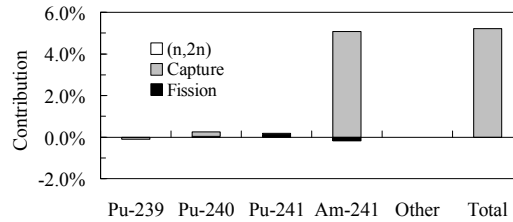


Fig.8 Sensitivity analysis of production of Am-241

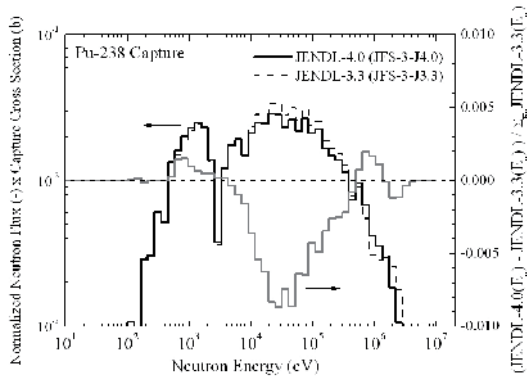


Fig.9 Pu-238 Neutron capture reaction rate

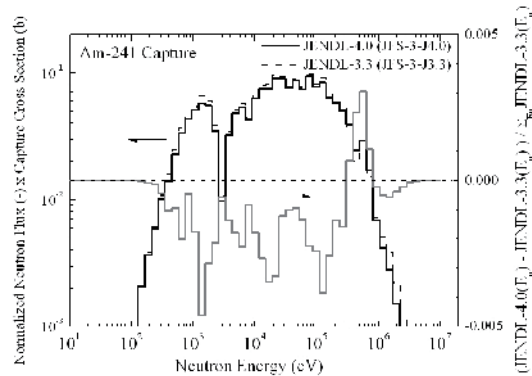


Fig.10 Am-241 Neutron capture reaction rate

(4) Decay heat

Figure 11 shows decay heat caused by heavy metal elements of outer core region (Same as above). In the calculations in the same Pu enrichments, the decay heat evaluated with JENDL-4.0 was smaller by about 1% at most until about a year passed since discharge of spent fuel, but became higher by about 2% at most than JENDL-3.3 after several decades of the discharge because of differences of amounts of MA nuclides. Curium-242, which was major contributor of decay heat within a year of the discharge, decreased about 1% in calculation with JENDL-4.0. After a year, Pu-238 and Cm-244 became major contributor, and then Pu-238, which has relatively longer half-life than Cm-244, was getting more dominant. Additionally, it was less significant than other nuclides, but Am-241, which increased by about 5% in the result calculated with JENDL-4.0, contribute to decay heat too.

In the calculation with JENDL-4.0 with the lower Pu enrichments, decay heat became lower by about 2% than JENDL-3.3 due to its lower MA inventory.

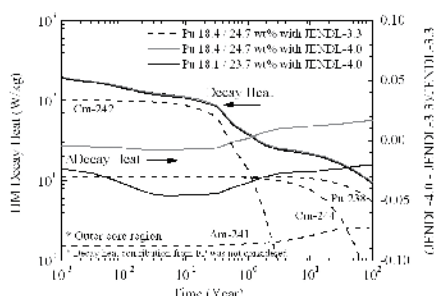


Fig.11 Decay heat of spent fuel in outer core region

3.2 High-decontaminated U-Pu fuel core

Table 4 shows the major core characteristics of the 750MWe FBR core with the high-decontaminated U-Pu fuel evaluated by using JENDL-4.0 and JENDL-3.3. Differences in Pu enrichments,  $k_{eff}$ , breeding ratios and burnup reactivity between calculations with the both libraries were similar to those with the low-decontaminated TRU fuel.

Reactivity control balance was listed in Table .5. The lower Pu enrichments of calculation with JENDL-4.0 made power defect and burnup loss lower. Because of this effect, the reactivity control balance was improved in primary control rod system (PCR). It was also beneficial in reduction of reactivity insertion in Control Rod (CR) withdrawal accident. Relatively lower power defect and burnup loss allowed PCR to stay upper position, which caused smaller amount of reactivity insertion when in CR withdrawal accident.

Table 4 Core characteristics of 750MWe SFR (High-decontaminated U- Pu)

Item	Unit	JENDL-4.0	JENDL-3.3
Pu enrichment(Inner/Outer)	wt%	18.1/24.8	18.5/25.2
$K_{eff}(\text{Max})$	-	1.0311	1.0333
Burnup reactivity	% $\Delta k/kk'$	2.55	2.72
Breeding ratio (Average)	-	1.095	1.082
Max Linear Heat Rate (Inner/Outer)	W/cm	419/419	425/424
Sodium Void Reactivity	\$	4.9	4.7
	% $\Delta k/kk'$	$1.69 \times 10^{-2}$	$1.63 \times 10^{-2}$
Delayed Neutron Fraction	-	$3.42 \times 10^{-3}$	$3.45 \times 10^{-3}$
Doppler coefficient	Tdk/dT	$-5.50 \times 10^{-3}$	$-5.46 \times 10^{-3}$

Table.5 Reactivity control balance

Item	Primary Control Rod		Backup Control Rod System	
	JENDL-4.0	JENDL-3.3	JENDL-4.0	JENDL-3.3
Total Excess Reactivity	4.5	4.7	0.8	0.8
Power defect and burnup loss	(3.5)	(3.7)	-	-
Temperature defect <sup>*1</sup>	(1.0)	(1.0) <sup>*4</sup>	(0.8)	(0.8) <sup>*4</sup>
Reactivity insertion in CR Withdrawal Accident <sup>*2</sup>	-	-	0.6	0.7
Control Rod Worth <sup>*3</sup>	6.0	6.1	1.5	1.5

<sup>\*1</sup> Reactivity difference between cold shut down and hot standby.

<sup>\*2</sup> Assumed that the most valuable PCR was pulled out accidentally.

<sup>\*3</sup> One rod stuck.

<sup>\*4</sup> Assumed the same value as evaluated by JENDL-4.0.

#### 4. Conclusions

There was no significant impact on the FBR core characteristics caused by differences in the both libraries. In the calculations with the same Pu enrichments with the initial fuel load core composition of the low-decontaminated TRU fuel,  $k_{\text{eff}}$  calculated with JENDL-4.0 became higher by about 1% than that with JENDL-3.3. It was confirmed that differences in fission and capture cross sections of Pu-239,  $\nu$ -value of Pu-240, inelastic scattering cross section of U-238 and capture cross section of Am-241 between JENDL-4.0 and JENDL-3.3 were major contributors of differences of the  $k_{\text{eff}}$  obtained in calculations using by the both libraries. The calculation with JENDL-4.0 could make the Pu enrichments lower than that with JENDL-3.3. It slightly improved the core characteristics such as burnup reactivity, a breeding ratio, decay heat and reactivity control balance.

In the calculations with the same Pu enrichments, the sodium void reactivity of the low-decontaminated TRU fuel core calculated with JENDL-4.0 became higher by about 3% than that with JENDL-3.3. It was found that differences in fission cross section and  $\nu$ -value of Pu-239,  $\mu$ -average and inelastic scattering cross section of U-238, and capture cross section of Pu-240 between JENDL-4.0 and JENDL-3.3 were major contributors of differences of the sodium void reactivity obtained by using the both libraries.

#### References

- 1) K. Shibata, O. Iwamoto, T. Nakagawa *et al.*, “JENDL-4.0: A New Library for Nuclear Science and Engineering”, *J. Nucl. Sci. Technol.*, **48**[1], 1-30 (2011).
- 2) K. Okumura, K. Sugino, G. Chiba *et al.*, “JENDL-4.0 Integral Testing for Fission System”, *J. Korean Phys. Soc.*, **59**[2], 1135-1140 (2011).
- 3) G. Chiba, K. Okumura, K. Sugino, *et al.*, “JENDL-4.0 Benchmarking for Fission Reactor Applications”, *J. Nucl. Sci. Technol.*, **48**[2], 172-187 (2011).
- 4) K. Aoto, N. Uto, Y. Sakamoto *et al.*, “Design study and R&D Progress on Japan Sodium-Cooled Fast Reactor”, *J. Nucl. Sci. Technol.*, **48**[4], 463-471 (2011).
- 5) K. Kawashima, S. Maruyama, S. Ohki *et al.*, “Fast reactor core design studies to cope with TRU fuel composition changes in the LWR-to-FBR transition period”, *Proc. Int. Conf. on Advances in Nuclear Power Reactors*, Tokyo, Japan, May. 10-14, 2009, 9288 (2009).
- 6) S. Maruyama, K. Kawashima, S. Ohki *et al.*, “Study on FBR Core Concepts for the LWR-to-FBR transition period,” *Proc. Int. Conf. on Advanced Nuclear Fuel Cycle; Sustainable Options & Industrial Perspectives*, Paris, France, Sep. 6-11, 2009, 1548-1556 (2009).
- 7) T. Takeda and T. Umamo, “Burnup sensitivity analysis in a fast breeder reactor—Part I: Sensitivity calculation method with generalized perturbation theory”, *Nucl. Sci. Eng.*, **91**, 1-10 (1985).

## 6 Nuclear Data in Radiation Protection Dosimetry

Daiki SATOH

Nuclear Science and Engineering Directorate, Japan Atomic Energy Agency

Tokai-mura, Naka-gun, Ibaraki-ken 319-1195 Japan

e-mail: satoh.daiki@jaea.go.jp

Nuclear data plays an important role for studies of radiation protection dosimetry. Accurate nuclear data lead us to reliable results on dosimetric calculations. In this paper, the application of nuclear data to radiation protection dosimetry is demonstrated with the calculation of dose conversion coefficients for radionuclides in the environment. A problem in reproduction of forward neutron spectra for proton incidence with high-energy nuclear data is also discussed.

### 1. Introduction

In a field of radiation protection dosimetry, nuclear data have been used for calculations of fluence, dose, and heat against mediums such as human body tissues, shielding walls, and the environment. Since the results of those calculations are applied to estimating a radiation safety for workers and the public, they are expected to be a high precision. Evaluated nuclear-data library is an indispensable tool for radiation protection dosimetry to ensure an accuracy of the dosimetric calculations.

In this paper, the author introduces the studies in radiation protection dosimetry performed with nuclear data. Advantages and problems are discussed with regards to the use of the current nuclear-data libraries. In Section 2, the evaluation of dose conversion coefficients for nuclides in the environment is described as an example of the nuclear data application to dosimetric calculations. The reliability of high-energy nuclear data for neutron production at most forward angles is discussed in Section 3, and a summary of this paper is given in Section 4.

### 2. Calculation of dose conversion coefficients for radionuclides distributed in the environment

Nuclear-data libraries are utilized for the evaluation of dose conversion coefficients for external exposure to photons and electrons emitted by radionuclides distributed in air, water, and soil. Under the condition that a lot of radioactive materials are released to the environment, external exposure to the environmental sources becomes a main pathway of exposures for the public. In order to estimate the radiation doses of the public, it is needed to evaluate the dose conversion coefficients for radionuclides distributed in the environment.

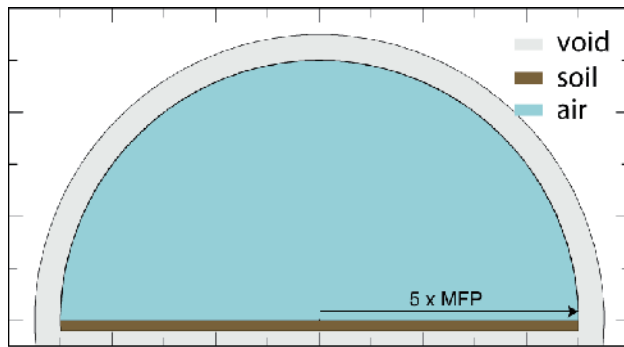


Fig.1 Calculation geometry in PHITS to reproduce the environment. The boundary radius of the geometry was set at five times of the mean free path (MFP) of the source photons.

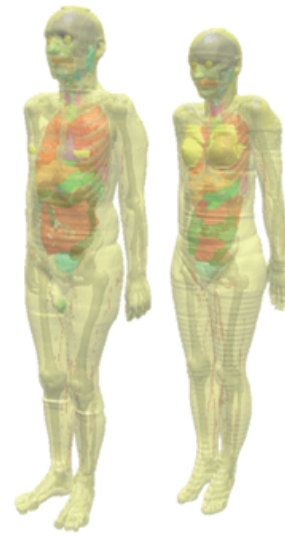


Fig. 2 Human models of adult male (left) and female (right) defined by ICRP.

The data sets of the dose conversion coefficients in the environmental radiation protection have been reported on the basis of previously developed dosimetric methodologies [1, 2]. However, some models and database used in the calculation are already obsolete. The data set must be updated with the latest nuclear data and more precise human models according to new recommendations of the International Commission on Radiological Protection (ICRP) [3]. The nuclear-data libraries for photons and electrons, *i.e.* MCPLIB04 [4] and EL03 [5] respectively, were used for the particle transport calculations in the environment. To reproduce the semi-infinite source in the environment, a large size of calculation geometry depicted in Fig. 1 was constructed on a Monte Carlo particle transport code PHITS [6]. The radius of the boundary of the calculation geometry was determined five times of a mean free path (MFP) of the photons depending on their energies, *e.g.* 650 m for 1.0 MeV photons. Because human models used in the dose calculation are exposed to the environmental radiation fields calculated here, the accuracy of the dose calculation strongly depends on the accuracy of the particle transport calculation. The use of nuclear-data libraries improves the accuracy of the particle transport in the environment.

Figure 2 shows the adult male and female models defined in the ICRP Publication 110 [7]. These human models were based on medical image data of real persons, and internal organs were segmented according to the images. The elemental compositions of organs and body tissues assigned to the models are consistent with the data given in the ICRP Publication 89 [8]. The human models were put in the radiation fields determined by the transport calculation in the environment. The organ doses were calculated by the photon and electron transport simulation inside the body. Figure 3 represents the organ doses from a 0.5-MeV photon source distributed uniformly to a depth of 0.5 cm in soil. Similar calculations were performed for 12 initial photon energies, from 10 keV to 10 MeV, to cover the energy range of the photons emitted from many artificial radionuclide sources. The effective doses for monoenergetic photons from the contaminated soil are shown in Fig. 4. The effective doses are increasing with the increase of the photon

energies.

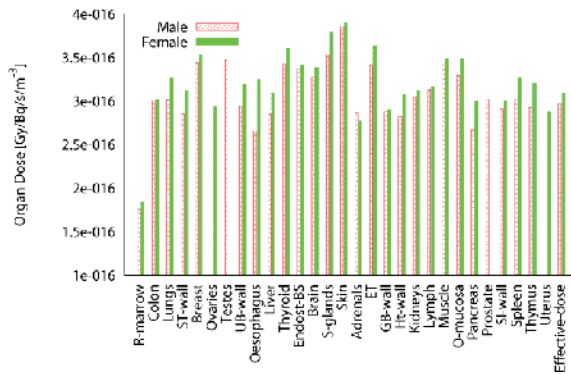


Fig. 3 Organ doses of adult male and female for 0.5-MeV photon source distributed uniformly to the depth of 0.5 cm in soil.

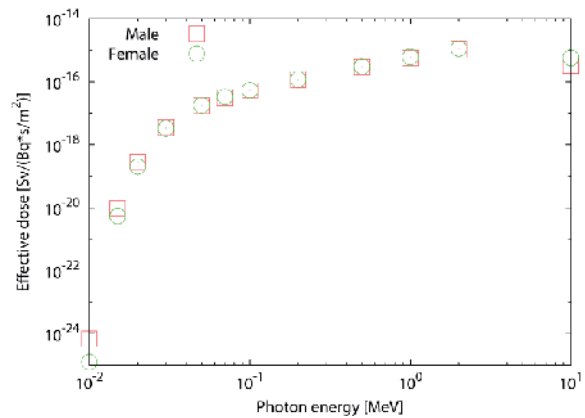


Fig. 4 Effective doses of adult male and female calculated for the photon sources distributed to the depth of 0.5 cm in soil.

The dose conversion coefficients for radionuclides in the environment were derived by using those for monoenergetic photons and the database of yields and energies of radiations emitted in nuclear decay of radionuclides. The nuclear decay data were taken from the ICRP Publication 107 [9]. The evaluation of the dose conversion coefficients is supported by the latest knowledge of both nuclear data and radiation protection dosimetry. The newly evaluated data set will be submitted to the ICRP to supersede the previous one.

### 3. Neutron-production cross sections at zero degrees in JENDL/HE

For a radiation protection at accelerator facilities, an appropriate shielding design is indispensable for reducing radiations outside the shielding wall and avoiding undesirable exposure for the public. In recent years, Monte Carlo particle transport simulations have been employed to the shielding design at accelerator facilities. Figure 5 shows an example of dose distributions at a proton therapy facility calculated by PHITS. The use of Monte Carlo transport code has an advantage to estimate the doses at once over the whole facility considering the radiation behavior in 3-dimensional space. While the high-energy nuclear-data library JENDL/HE [10] has often been used in these simulations, its prediction ability is not examined well for neutron production at most forward angles. The yield of spallation neutrons increases around the forward angles. It is very important for shielding design to predict the neutron spectra in this direction.

Figure 6 depicts the calculation results by JENDL/HE for neutron-production double differential cross sections at zero degrees from a carbon nucleus bombarded by 256-MeV protons



Fig. 5 Example of neutron-dose distribution calculated by PHITS for a typical proton therapy facility.

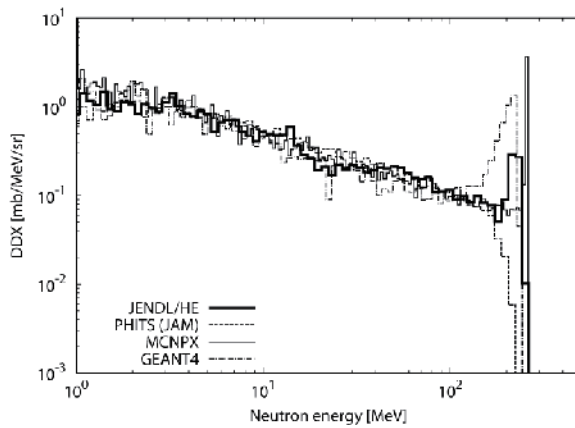


Fig. 6 Neutron-production double differential cross sections at zero degrees from carbon nucleus bombarded with 256-MeV protons.

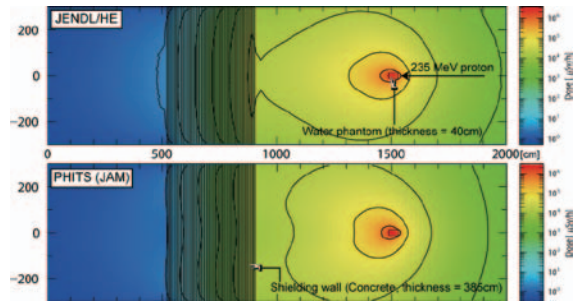


Fig. 7 Neutron-dose distributions calculated with JENDL/HE (upper) and JAM (lower) for 235-MeV proton incidence on a water phantom.

together with the results of theoretical models of PHITS (JAM [11]), MCNPX [12], and GEANT4 [13]. It is obvious from the figure that the results of the JENDL/HE and the theoretical models give quite different lines around a high-energy peak. The discrepancy among the results comes from a lack of experimental data to verify the nuclear data and models. This affects the prediction of neutron doses behind a shielding wall on a beam axis. Figure 7 demonstrates the neutron-dose distributions inside and outside a shielding wall calculated with JENDL/HE and JAM model in PHITS. In this calculation, 235-MeV protons were bombarded upon a 40-cm thick water phantom, and a 385-cm thick concrete wall was set downstream the phantom. The calculated doses for the neutrons emitted from the water phantom are distributed with different contour lines, especially at forward angles, due to the difference of the neutron-production cross sections at zero degrees. Behind the shielding wall, the neutron dose calculated with JENDL/HE is about three times larger than that with JAM. In order to improve the reliability of the high-energy nuclear data for very forward neutron production, experimental data to be dedicated to the verification of the nuclear data are strongly required. The author and his colleague plan to measure the neutron-production double differential cross sections around zero degrees. The data will be furnished to the nuclear data community.

#### 4. Summary

In radiation protection dosimetry, evaluated nuclear-data libraries are employed to keep the quality of dosimetric calculations. The dose conversion coefficients for radionuclides distributed in the environment were calculated by using nuclear data for reaction cross section, angular distribution, and decay scheme. Thanks to accurate nuclear data, the results were given with a good reliability.

Neutron-dose distribution at a proton therapy facility was calculated by a Monte Carlo transport code PHITS. Due to the difference of proton-induced neutron-production cross sections at most forward angles calculated by JENDL/HE and the other theoretical models, the calculation results of the neutron dose behind a shielding wall give a large discrepancy between JENDL/HE and the model. To solve this problem,

new cross-section measurement will be carried out.

Nuclear data are indispensable for radiation protection dosimetry, but some problems are still remained in the current nuclear-data libraries. Collaborations across the fields of nuclear data and radiation protection dosimetry would be important to sophisticate the nuclear data and improve the accuracy of dosimetric calculations.

### Acknowledgements

The present paper contains research results obtained by collaborations with colleagues. Especially, the author is grateful to Drs. A. Endo, H. Nakashima, and T. Shibata of JAEA for their cooperation.

### References

- [1] K. F. Eckerman and J. C. Ryman: "External Exposure to Radionuclides in Air, Water, and Soil," EPA-402-R-93-081 (1993).
- [2] K. Saito et al.: "Calculation of Organ Doses from Environmental Gamma Rays Using Human Phantoms and Monte Carlo Methods," GSF-Bericht 2/90 (1990).
- [3] International Commission on Radiological Protection: "The 2007 Recommendations of the International Commission on Radiological Protection," ICRP Publication 103 (2007).
- [4] M. C. White: "Photoatomic Data Library MCPLIB04: A New Photoatomic Library Based on Data from ENDF/B-VI Release 8," LA-UR-03-1019 (2003).
- [5] K. J. Adams: "Electron Upgrade for MCNP4B," LA-UR-00-3581 (2000).
- [6] K. Niita et al.: "PHITS: Particle and Heavy Ion Transport code System, Version 2.23," JAEA-Data/Code 2010-022 (2010).
- [7] International Commission on Radiological Protection: "Adult Reference Computational Phantoms," ICRP Publication 110 (2009).
- [8] International Commission on Radiological Protection: "Basic Anatomical and Physiological Data for Use in Radiological Protection," ICRP Publication 89 (2003).
- [9] International Commission on Radiological Protection: "Nuclear Decay Data for Dosimetric Calculations," ICRP Publication 107 (2008).
- [10] Y. Watanabe et al.: "Nuclear Data Evaluations for JENDL High-Energy File," AIP Conference Proceedings, Sept. 26- Oct. 1, 2004, Santa Fe, USA, p.326 (2005).
- [11] Y. Nara et al.: Phys. Rev., C61, 024901 (1999).
- [12] D. B. Pelowitz: "MCNPX User's Manual", LA-CP-07-1473 (2008).
- [13] S. Agostinelli et al.: Nucl. Instrum. Methods, A506, 250 (2003).

This is a blank page.

## 7 Solution for Pandemonium Problem in FP Decay Heat Summation Calculations

Tadashi YOSHIDA\*, Takayuki ARAI

*Tokyo City University, 1-28-1 Tamazutsumi, Setagaya-ku, Tokyo 158-8557*

\*E-mail: [88r9t9@bma.biglobe.ne.jp](mailto:88r9t9@bma.biglobe.ne.jp)

The decay schemes are of critical importance in the wide range of nuclear science and applications. Those for short-lived nuclides, however, are overlooking the  $\beta$ -feedings to highly excited states in their daughter nuclei. This defect, known as ‘*pandemonium*’ problem, inevitably biases the summation calculation of FP decay heat, leading to disagreement between the calculation and the sample-irradiation results. It is argued that the  $\beta$ -feeding obtained utilizing a total absorption gamma-ray spectrometer (TAGS) are free from the *pandemonium* problem. It is demonstrated that introducing the  $E_\beta$  and  $E_\gamma$  values obtained from the very recent  $\beta$ -feeding data measured by Algora *et al.* remarkably improves the decay heat summation calculation without any help of nuclear theories as had been carried out in Japan.

### 1. Introduction

Fission products (FPs) dominate the heat generation from a reactor core in the early stage after the termination of the fission chain-reactions in it. Though they are eventually taken over by the transuranic decay heat originated from the heavy nuclides such as Pu, Am and Cm, the transition from FP to these nuclides depends on the fuel-type and its burn-up history. In the present review we concentrate only on the FP decay heat which dominates the total decay heat for early several decades in the case of uranium fuels.

Generally speaking, there are two approaches to know the decay heat quantitatively. One is the sample-irradiation experiment, where a pure fissile sample, for example a highly enriched U-235, is irradiated (typically in an experimental reactor core). By measuring the  $\beta$ -ray and the  $\gamma$ -ray energies from the recovered irradiated-sample and, then, by integrating these energies one can get the total FP decay heat and its  $\beta$ -ray and the  $\gamma$ -ray components. In principle, this method gives us the true value of the decay heat from the specific sample used within the experimental uncertainty. In this sense, this kind of experimental data (hereafter, sample-irradiation data) is reliable and can be utilized as a benchmark.

In practice, however, we cannot see nor predict the decay heat of any real nuclear reactor, a PWR or a BWR, at a given instance after the reactor shutdown simply from the pure sample irradiation data. In the case of power reactors, the decay heat depends on the initial nuclide composition of the fuel, the operation and the burn-up histories, fuel position in the core, and the cooling time, namely, the lapse of time after the reactor shut-down. As we experienced in a tragic way at the Fukushima-Daiichi NPP on March 2011, the FP decay heat governs the fate of the damaged or even collapsed core in an accidental situation. One, and possibly the only one reliable and flexible method to predict the decay heat in any actual situation may be a so-called summation calculation based on reliable basic data; that is to say, the fission yields, the decay data and neutron cross-sections of all the FP nuclides involved. In the summation calculation of decay heat, the concentration of all the FP nuclides  $n_i(t)$ , where  $i$  stands for

each FP nuclide, are calculated from the initial fuel composition, the operation history of the reactor and the cooling time. The  $\beta$ -ray and the  $\gamma$ -ray components of the decay heat are calculated as  $\sum_{i=1}^N E_{\beta}^i \lambda_i n_i(t)$  and  $\sum_{i=1}^N E_{\gamma}^i \lambda_i n_i(t)$ , respectively. Here  $\lambda_i$  stands for the decay constant of the  $i$ -th nuclide and the total number of nuclide  $N$  is ranging from 800 to 1100, from  $^{67}_{24}\text{Cr}$  to  $^{192}_{70}\text{Yb}$  for example, depending on the nuclear data library used. The quantities  $E_{\beta}^i$  and  $E_{\gamma}^i$  are the average energies of the  $\beta$ - and the  $\gamma$ -rays per  $\beta$ -disintegration. The sum of the above two summations, or  $\sum_{i=1}^N (E_{\beta}^i + E_{\gamma}^i) \lambda_i n_i(t)$ , gives us the total decay heat. In the present paper, we specifically deal with the quantities  $E_{\beta}^i$  and  $E_{\gamma}^i$  specific to each individual nuclide. Other important items, e.g. the calculation of  $n_i(t)$  and fission yield, are out of scope of our review, though they also need critical review and extensive scrutiny.

At the end of this chapter, it would be better to add that both the sample-irradiation and the summation calculation are *experiment-based* methods. Even though it is called the summation *calculation*, it is based on the nuclide-wise experimental data, that is to say the decay scheme, of each individual FP nuclide with some exception. In the present review we concentrate only on these nuclear decay data for the summation calculations.

## 2. Average Energies of the $\beta$ - and the $\gamma$ -Rays per $\beta$ -Disintegration

### 2.1 Calculation of the Average Energies from Decay Scheme

Figure 1 is the decay scheme of  $^{106}\text{Tc}$  taken from the “Tables of Isotopes”<sup>1)</sup> just for a typical example of short-lived FP nuclide.

Usually the important quantities  $E_{\beta}^i$  and  $E_{\gamma}^i$ , where the index  $i$  stands for  $^{106}\text{Tc}$  in this case, are calculated from such decay scheme as this. As we see the percentage of the Curie-point energies per decay from this decay scheme, we can calculate the average  $\beta$ -ray energy. This can be done uniquely by, for example, introducing an approximation that the Fermi function for allowed transition can be applied to

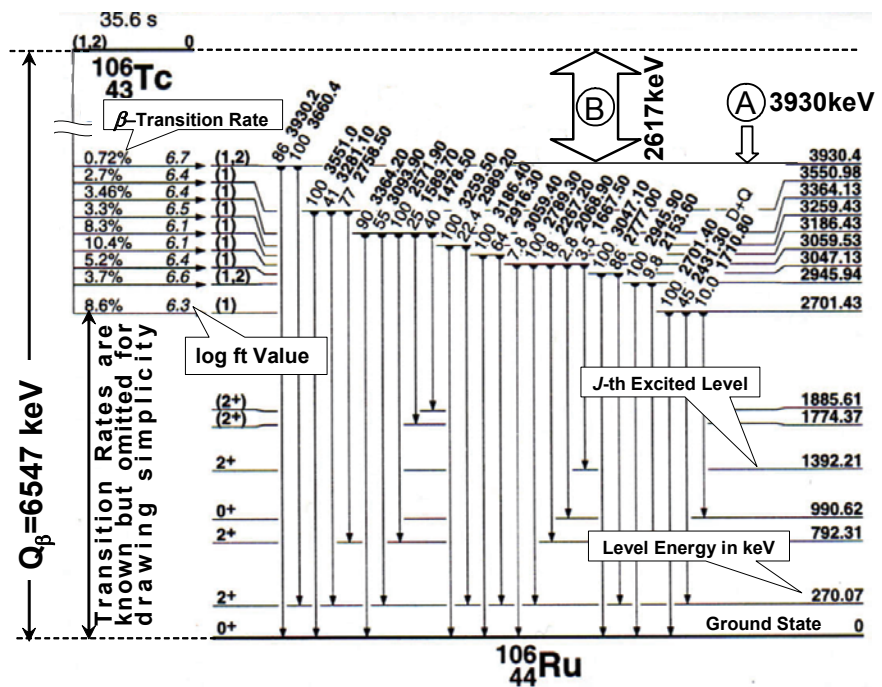


Fig. 1 Decay scheme of  $^{106}\text{Tc}$  as an example of short-lived FP

all the  $\beta$ -transitions shown here. This approximation may not introduce any noticeable error to the calculated average  $\beta$ -ray energy  $E^{i_\beta}$ . The  $j$ -th excited level thus formed by the  $\beta$ -transition is then de-excited into the ground immediately by emitting a single photon or by emitting several photons in a way of multi-step cascade. The point is that the total photon energies  $\varepsilon_j$  are the same in either cases, *single or cascades*. Further, in addition to  $E^{i_\beta}$ , we can obtain the average  $\gamma$ -ray energy  $E^{i_\gamma}$  by summing up  $\varepsilon_j$  over all the excited levels using the  $\beta$ -transition rate as the weighting function (see Fig. 1).

### 2.2 Pandemonium Problem of Decay Schemes

In this section we scrutinize Fig. 1 more carefully. The highest level of the daughter nuclide  $^{106}\text{Ru}$  (A) lies at 3930 keV and no  $\beta^-$  transition is given above here up to 6547 KeV (B) ( $=Q_\beta$ ; the highest

energy energetically accessible from the parent by  $\beta$ -transition; see the left-bottom of Fig.2). This *desert* of the energy range from 3930 to 6547 keV occupies 40 % of the whole range to which the  $\beta^-$  transition is accessible energetically. Please find the symbol  $\approx$  in the vertical or energy axis indicating the axis is curtailed in-between to save the blank space. The presence of this *desert* is not acceptable from the theoretical point of view. In the Gross Theory of  $\beta$ -Decay<sup>2)</sup>, the log ft value, or the nuclear matrix element, increases along with the excitation energy up to  $Q_\beta$  measured from the daughter's

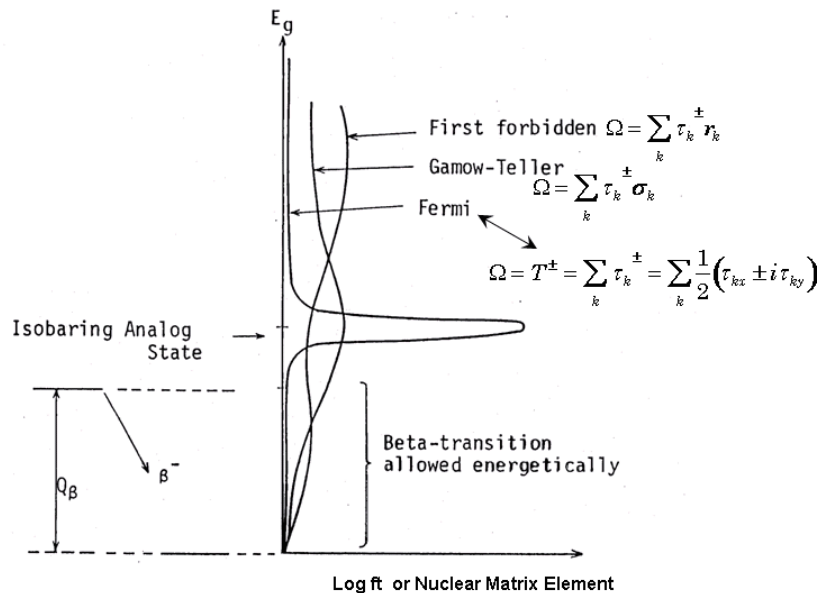


Fig.2 Simplified behavior of the nuclear matrix element for types of the  $\beta$ -transition ( $\Omega$  stands for transition operator)

ground state (in our case  $Q_\beta=6547$  keV) as is simplified and illustrated in Fig.2. In the neutron-rich FP nuclide such as  $^{106}\text{Tc}$  in Fig. 1 has a common tendency that the Fermi and the Gamow-Teller transition increase toward the isobaric analog state which is situated highly above  $Q_\beta$ , the highest daughter's excitation energy energetically accessible. Here we do not relate the forbidden transitions because of their relative less importance in our present problem.

The existence of the *desert* mentioned above suggests that the  $\beta$ -transition to highly excited states may possibly be missed in the process of high-resolution  $\gamma$ -ray detection and construction of decay scheme from the detected  $\gamma$ -rays, which are known as the *unplaced gammas*. These two kind of possible defects of the current decay schemes of highly  $Q_\beta$ -valued or short-lived nuclides were first warned by Hardy *et al.*<sup>2)</sup> and they named this *pandemonium* problem. In principle we should better think that most of the decay schemes of short-lived FP nuclides suffer from the pandemonium problem.

As an important conclusion of this Chapter, it can be said that averaged  $\beta$ -ray energy  $E^i_\beta$  calculated from any *pandemonium-suffered* decay-scheme is overvalued in comparison with the true value, because the large energy  $\beta$ -rays are counted too much in *pandemonium* nuclides such as  $^{106}\text{Tc}$  studied here as an example. On the contrary, the averaged  $\gamma$ -ray energy  $E^i_\gamma$  is underestimated.

### 3. Struggle with Pandemonium Problem

#### 3.1 Theoretical Approach

After the TMI accident occurred in 1979, efforts toward precise and reliable decay-heat prediction was accelerated both in the areas of the sample-irradiation experiment and the summation-calculation data basis as we saw briefly in Introduction. The nuclear data libraries for summation calculation (hereafter, simply library) were produced almost at the same time in Japan (JNDC FP Decay Data Library<sup>4</sup>), in the US (ENDF/B-IV) and in Europe (UKFPDD-2) around 1980, in all of which the newest decay schemes available at that time were fully utilized. But, in spite of the big anticipation, the summation calculations based on all the three libraries badly failed to reproduce the sample irradiation experiments. In reality the  $\beta$ -ray component of decay heat was overestimated and, *vice versa*, the  $\gamma$ -ray component was seriously underestimated just in accordance with the conclusion of Chapter 2. In the case of JNDC (Japanese Nuclear Data Committee), the Decay Heat Working Group succeeded in circumventing the pandemonium problem by introducing the gross theory of  $\beta$ -decay<sup>2</sup>. A typical result is shown in Fig. 3 which is taken from an old paper published in 1981<sup>5</sup>. In order to save the space, only the  $\gamma$ -ray component is shown here, namely, the underestimation case by the pandemonium problem.

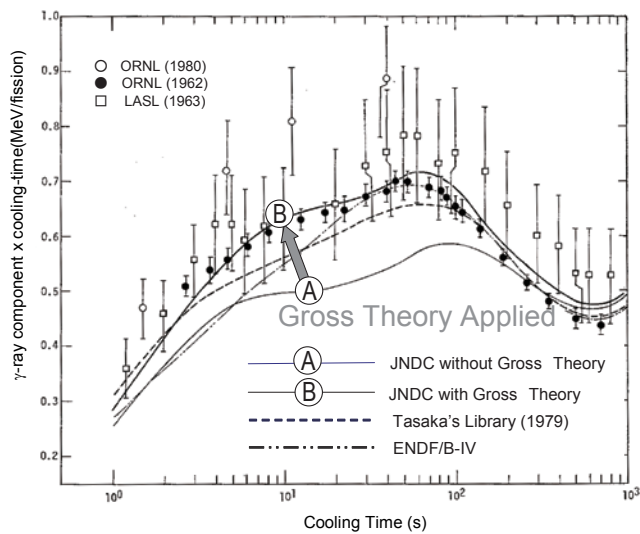


Fig.3 Calculated decay heat by JNDC before and after the introduction of nuclear theory ( $\gamma$ -ray component after a fission burst in  $^{235}\text{U}$ )

#### 3.2 Experimental Approach

In 1990's, the total absorption gamma-ray spectrometer (TAGS) was first introduced by Greenwood *et al.*<sup>6</sup> to measure the  $\beta$ -feed for 45 short-lived FP nuclides starting from  $^{89}\text{Rb}$  to  $^{158}\text{Eu}$ . In a lower energy region where the positions of excited levels are precisely known, they provides the beta-feeding, or  $\beta$ -transition probability, to each of it. Above this energy region they gives the sum of the  $\beta$ -feeds to all the level included in a energy bin which have a width of 100 keV and, then, a lot of energy bins thoroughly cover the whole energy range up to  $Q_\beta$  (measured from the ground state of the daughter) where the  $\beta$ -transition is energetically permitted.

It is interesting to see the pandemonium problem in the light of their data. Figure 4 shows the  $E^i_\beta$  and  $E^i_\gamma$  values divided by  $Q_\beta$ . Here it is worthy noting that the relation  $Q^i_\beta = E^i_\beta + E^i_\gamma + E^i_\nu$  is

exactly satisfied in each nuclide  $i$ , where the average neutrino energy  $E^i_\nu$  has nothing to do with the nuclear decay heat. Neutrino does not interact with the material on earth. In this figure, though each radial axis corresponds to a nuclide, its name is not indicated because here we are interested only in the overall behavior of  $E_\beta/Q_\beta$  and  $E_\gamma/Q_\beta$  of short-lived FPs in connection with their pandemonium problem. In reality, almost all the average  $\beta$ -ray energies calculated from ENSDF, namely the decay-schemes based on high-resolution  $\gamma$ -ray measurements, are overvalued (left) in accordance with the description up to here in the present paper. On the contrary, most of the average  $\gamma$ -ray energies calculated from ENSDF are too small (right) as far as TAGS is giving reliable data. It should be noted that there are several nuclides where both of  $E_\beta/Q_\beta$  and  $E_\gamma/Q_\beta$  are large or are small at the same time. In these cases a careful check is needed together with re-evaluation of the  $Q_\beta$ -value itself.

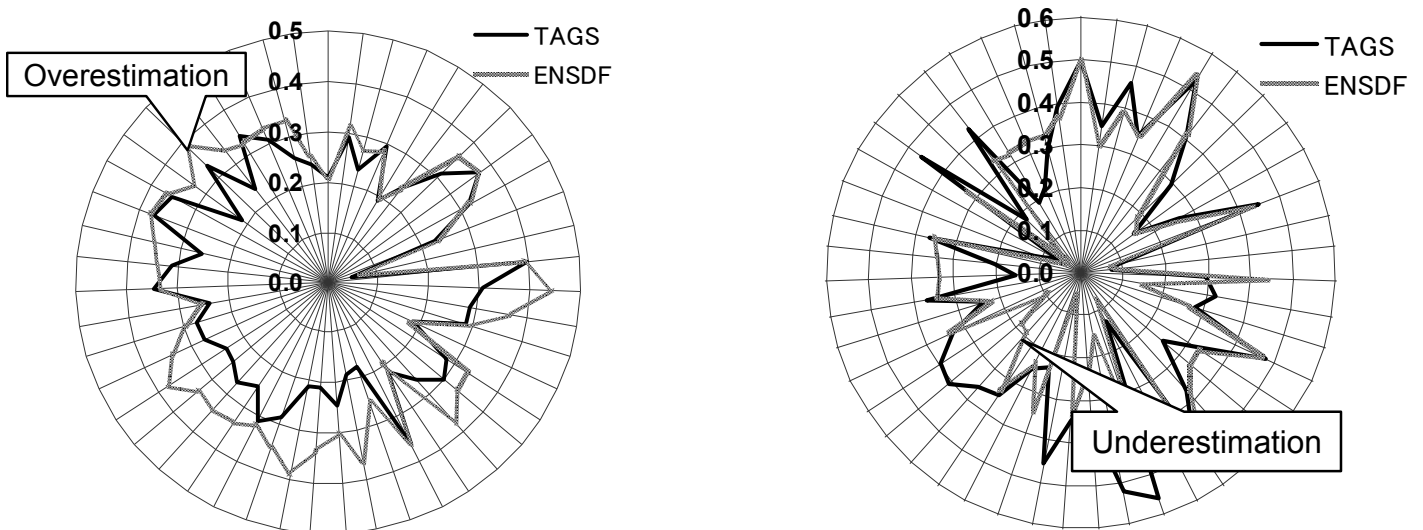


Fig.4 Average  $E^i_\beta / Q^i_\beta$  (left) and  $E^i_\gamma / Q^i_\beta$  (right) values of 45 nuclides from the US TAGS measurement by Greenwood et al. <sup>6)</sup> and the values calculated from ENSDF

Figure 5 shows the result of the latest TAGS measurement led by Algora and Tain *et al*<sup>7)</sup> (Polar Project). In this case ENSDF overvalues  $E^i_\beta / Q^i_\beta$  (left) and undervalues  $E^i_\beta / Q^i_\gamma$  (right) for all the pandemonium nuclides persistently. In this sense, reliability of TAGS measurements seems improved in a decade.

#### 4 Conclusion

Effect of introducing the TAGS data to the ENSDF-based decay-heat calculation (here we used JEFF3-1) is shown in Fig.6. We can follow the three curves as follows. ① start with ENSDF-equivalent JEFF3-1 → ② replace the  $E_\beta$  and  $E_\gamma$  for 6 nuclides of Fig5 taken by the European TAGS group<sup>7)</sup> → ③ replace the  $E_\beta$  and  $E_\gamma$  for 45 nuclides of Fig.4 by the US TAGS group<sup>6)</sup>. Then, we finally obtained good agreement between the summation calcu-

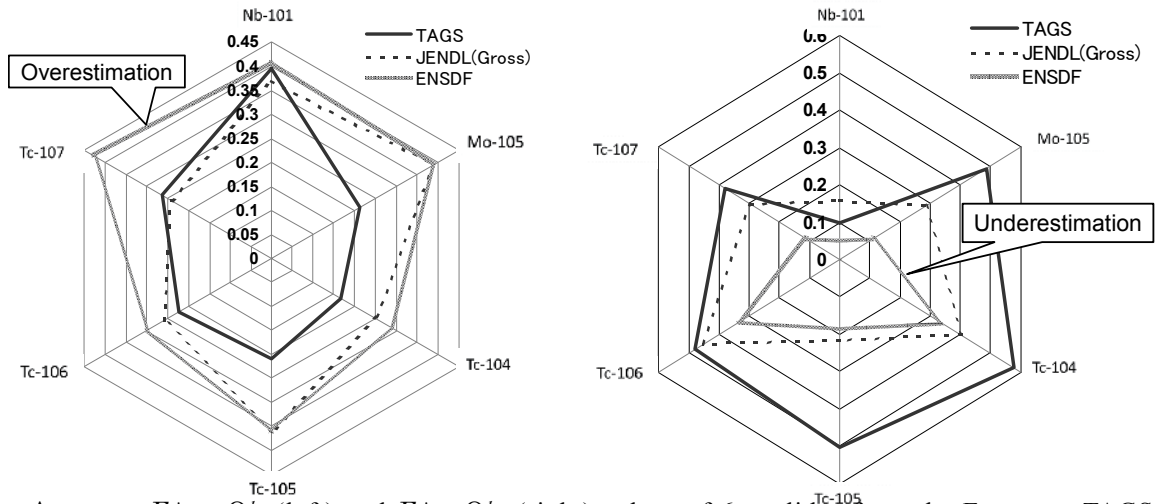


Fig.5 Average  $E_{\beta}^i / Q_{\beta}^i$  (left) and  $E_{\gamma}^i / Q_{\gamma}^i$  (right) values of 6 nuclides from the European TAGS (Polar Project) measured by Algora et al. <sup>7)</sup> and the values calculated from ENSDF

lation based on TAGS and the sample-irradiation experiments. In this sense, we could solve the pandemonium problem with the TAGS data especially those from the Jyväskylä

measurement<sup>7)</sup>. Though the number of nuclide from Jyväskylä is small (only 6) in comparison with 45 of the US TAGS<sup>6)</sup>, the contribution to the present improvement from the former is fairly larger. This comes from the fact that former had carefully carried out on the basis of preliminary survey in detail about the priority of the nuclides to be measured<sup>8)</sup>.

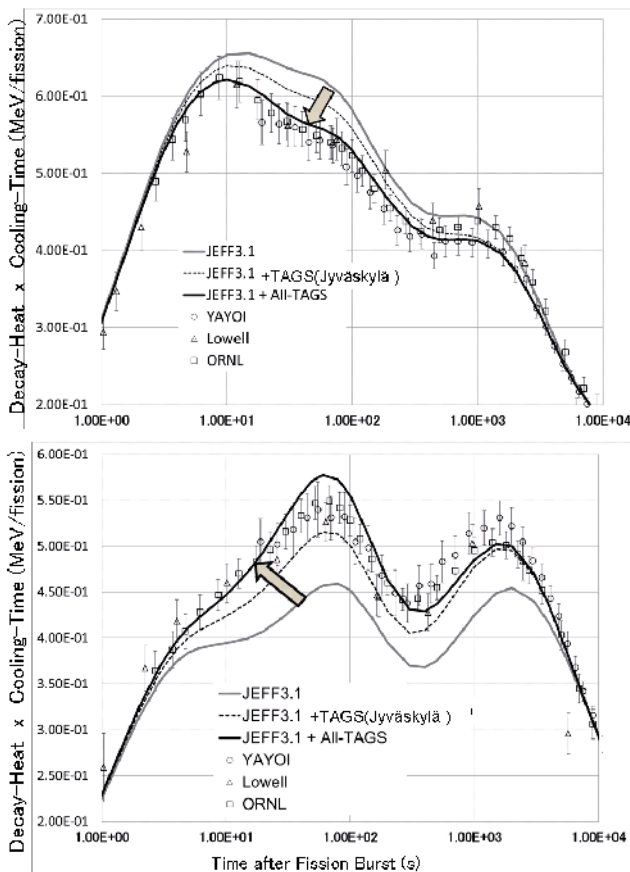


Fig.6 Effect of introducing TAGS data to the ENSDF based decay Data File (JEFF3-1); Decay heat of <sup>239</sup>Pu after a fission burst

### Reference

- 1) Tables of Isotopes, 8<sup>th</sup> Ed, Wiley & Sons
- 2) K.Takahashi et al., Atom. Data and Nucl. Data Tables, **12**, 101 (1973) and references therein
- 3) J.C.Hardy, et al: *Phys. Lett.*, **71B**, 307 (1977)
- 4) K.Tasaka et al., JAERI 1287 (1983)
- 5) T.Yoshida, R.Nakashima, *J. Nucl. Sci. Technol.*: **18**[6], 393 (1981)
- 6) R.C.Greenwood et al: *Nucl. Instr. and Meth.*, **A390**, 95(1997)
- 7) A. Algora et al., *Phys. Rev. Lett.*, 105, 202501 (2010)
- 8) NEA/WPEC-Report, Vol. 25, OECD(2007)

## 8 Nuclear Data for Prediction of Isotope Generation and Depletion

Keisuke OKUMURA

Nuclear Science and Engineering Directorate, Japan Atomic Energy Agency  
 Tokai-mura, Naka-gun, Ibaraki-ken 319-1195 Japan  
 e-mail: okumura.keisuke@jaea.go.jp

Data libraries for neutron transport and burn-up calculations are produced on the basis of JENDL-4.0. Accurate prediction of isotope generation and depletion for LWR fuels are achieved by using the data libraries.

### 1. Calculation scheme of Isotope Generation and Depletion

For the calculation of isotope generation and depletion, we have to prepare burn-up chain model as shown in Fig.1, where generation paths of each isotope are described.

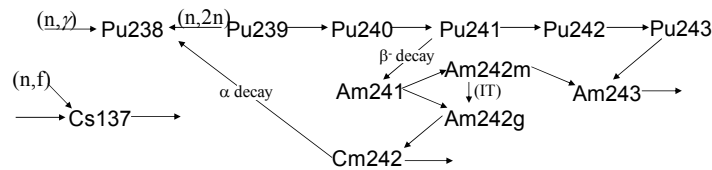


Fig.1 Example of burn-up chain model

Then, the time change of atomic number density ( $N$ ) for nuclide ( $i$ ) is expressed by the following burn-up equation,

$$\frac{dN^i}{dt} = \sum_{j \neq i} f^{j \rightarrow i} \lambda^j N^j + \sum_{k \neq i} \sum_x g_x^{k \rightarrow i} \int R_x^k(E) dE + \sum_{l \neq i} \gamma^{l \rightarrow i} F^l - \left\{ \lambda^i N^i + \int R_a^i(E) dE \right\}, \quad (1)$$

where,  $i, j, k, l$ : identification numbers of nuclides in the chain mode,  $f$ : branching decay fraction,  $\lambda$ : decay constant,  $g$ : yield fraction by transmutation (e.g. isomeric ratio),  $R_x(E)$ : energy-dependent reaction rate for reaction type  $x$ ,  $\gamma$ : fission product (FP) yield,  $F$ : energy-integrated fission reaction rate. By solving a system of the above differential equations for all nuclides in the chain model, we can get burn-up change of fuel compositions in atomic reactors. Therefore, for accurate prediction of the fuel compositions, accurate nuclear data are necessary for the parameters in Eq.(1), that is, branching decay fractions, half-lives, isomeric ratios, FP yields and neutron-induced cross sections, especially for  $(n, \gamma)$ ,  $(n, f)$  and  $(n, 2n)$  reactions.

The treatment of the reaction rate in Eq.(1) depends on burn-up calculation codes. For example, the reaction rate is accurately calculated by Eq.(2) in MVP-BURN[1], which is a burn-up calculation code using a continuous-energy Monte Carlo code MVP[2]. On the other hand, the reaction rate is approximated by Eq.(3) in the neutron transport calculation codes based on the multi-group method, such as

SRAC2006[3] and its improved version MOSRA-SRAC[4]

$$\int R_x^i(E)dE \equiv N^i \int \sigma_x^i(E)\Phi(E)dE \quad (2)$$

In the case of the burn-up calculation codes with no function of neutron spectrum calculation such as ORIGEN2[5], the reaction rate is given by Eq.(4) by using one-group flux  $\langle \Phi \rangle$  and one-group cross section  $\langle \sigma_x^i \rangle$ .

$$\int R_x^i(E)dE \approx N^i \langle \sigma_x^i \rangle \langle \Phi \rangle, \quad (4)$$

According to Eq.(5), the one-group cross-section is prospectively prepared by using the multi-group effective cross section and the neutron spectrum obtained by the neutron transport calculation for a typical fuel model in the assumed reactor condition.

$$\langle \sigma_x^i \rangle = \frac{\sum_g \sigma_{x,g}^i \Phi_g}{\sum_g \Phi_g} \quad (5)$$

## 2. Data Libraries for Neutron Transport and Burn-up Calculations based on JENDL-4.0

In order to enable neutron transport and burn-up calculations with JENDL-4.0[6], neutron cross section libraries available for several codes are produced from JENDL-4.0 as shown in Table 1.

Table 1 Neutron cross section libraries based on JENDL-4.0 for neutron transport and burn-up calculations

Name of library	Available codes	Energy structure
MVPLib_nJ40[7]	MVP, MVP-BURN	continuous-energy
FSXLIB-J40	MCNP[8], PHITS[9]	continuous-energy
SRACLIB-JDL40	SRAC2006, SWAT[10]	107-group
MSRACLIB-J40	MOSRA-SRAC	200-group
MATXSLIB-J40	Several Sn codes via TRANSX[11]	199-group (neutron) 42-group (photon)
ORLIBJ40[12]	ORIGEN2	one-group

A set of new burn-up chain data based on JENDL-4.0 (ChainJ40)[13] is also prepared for the burn-up calculations with MVP-BURN, SRAC2006 and MOSRA-SRAC. The chain data includes burn-up chain model, branching decay fractions, isomeric ratios, FP yields and half-lives. These data are mainly taken from JENDL-4.0 except for half-lives, which are employed from ENSDF[14] revised at Oct. 2008 and from recent literatures for long-lived FPs (Se-79 and Sn-126). As shown in Fig.2, the half-lives of Se-79 and Sn-126 have been unclear during the last two decades. The ChainJ40 employed the recent measured values by Bienvenu *et al.* [15,16].

For the ORIGEN2 library ORLIBJ40, the branching decay fractions, isomeric ratios, FP yields and half-lives are given in the same way as ChainJ40. The one-group cross sections for important nuclides are generated [12] by using MOSRA-SRAC, ChainJ40 and MSRACLIB-J40.

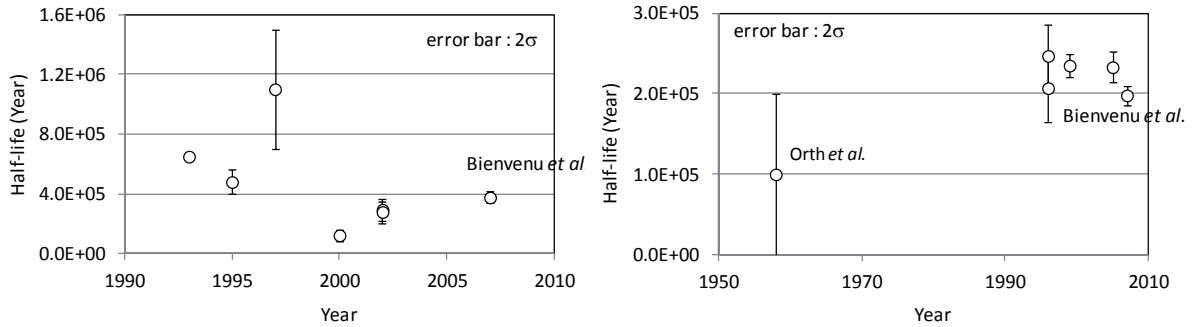


Fig.2 Measured half-lives of Se-79 (left) and Sn-126 (right)

### 3. Post Irradiation Analyses with JENDL-4.0 for LWR Spent Fuels

As part of integral test[17] of JENDL-4.0, a post-irradiation examination analysis was performed for a sample fuel (SF97-4 in Fig.3) irradiated in a Japanese PWR (Takahama-3). The sample was cut out from near the center of the fuel rod, which had the highest burn-up among the irradiated sample rods. The <sup>235</sup>U enrichment of SF97-4 was 4.1 wt% and it had been irradiated up to 47 GWd/t. After about 4 years of cooling, isotopic compositions were determined by radiochemical analyses[18].

A cell burn-up calculation was carried out with MVP-BURN and with the nuclear data based on JENDL-4.0 (MVPLib\_nJ40 and ChainJ40). The power and boron histories in Fig.3 were considered in the calculation.

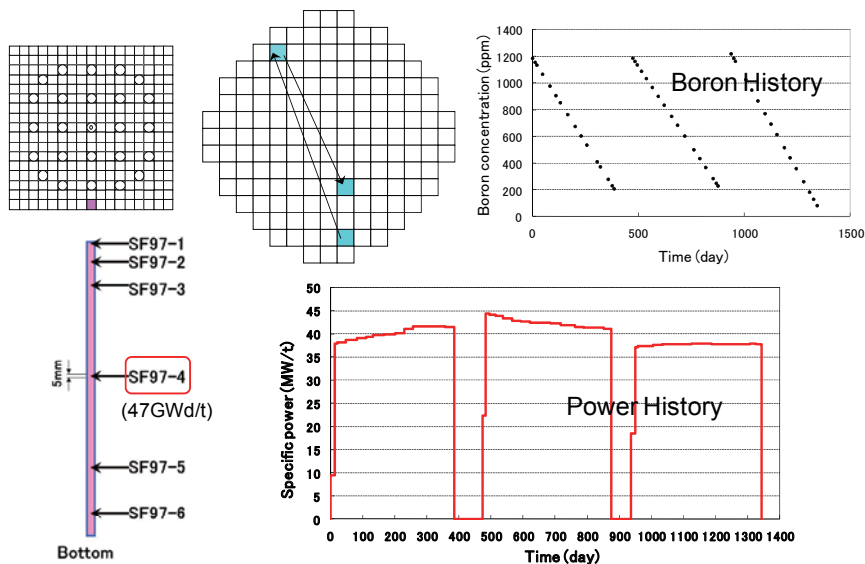


Fig. 3 Position and irradiation history of SF97-4 in Takahama-3 PIE

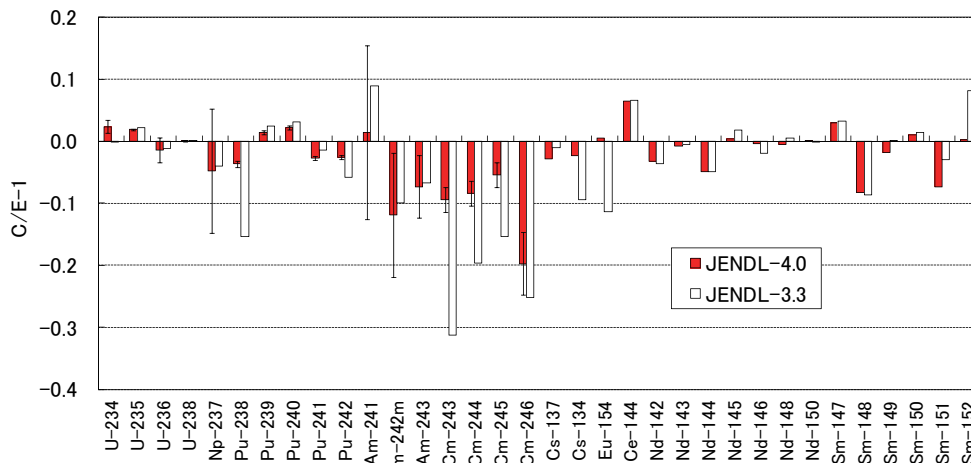


Fig. 4 Irradiation history of SF97-4 in Takahama-3 PIE

Figure 4 shows the deviations of calculated results from measured ones (C/E-1) for the atomic number densities of measured nuclides. We can see drastic improvements for minor actinides (e.g. Pu-238, Am and Cm isotopes) and FPs sensitive to cross sections (e.g. Cs-134, Eu-154, Sm-151, Sm-152) as compared with the results of JENDL-3.3[19], where FP yields are based on JENDL/FPD-2000[20]. The improvements are mainly owing to updating of the capture cross sections in JENDL-4.0 for Np-237, Am and Cm isotopes, Cs-133, Eu-154, Sm-152. Similar improvements are achieved also in the PIE analysis using ORIGEN2 with the ORLIBJ40 library[21].

#### 4. Post Irradiation Examination Analyses for LLFPs

Se-79 is one of the important nuclides for long-term safety assessment of a geological disposal of high level vitrified waste. Then, MVP-BURN with the JENDL-4.0 library (MVPlib\_nJ40 and ChainJ40) was applied to PIEs including assay data of Se-79[22]. They are PIEs for sample fuels irradiated in Cooper (BWR) and those in Calvert-Cliffs-1 (PWR) performed by PNL[23], and the recent PIE for a sample fuel irradiated in Ohi-1 (PWR) performed by JAEA[24]. The experimental values of PNL-PIEs were taken from the database SFCOMPO[25].

Figure 5 shows the burn-up dependences of calculated values and experimental ones for the concentrations of Se-79 in the sample fuels. The experimental value and the calculated one show a good agreement for the PIE of Ohi-1 (JAEA-PIE) at 44.9 GWd/t. On the other hand, there are large discrepancies between the experimental values and calculated ones for PNL-PIEs; the averaged C/E value is 5.5.

In the PNL-PIEs, concentration of Se-79 was measured by liquid scintillation counter after chemical separation. Therefore, the experimental value is originally reported in the unit of Bq/MTU. After that, it was converted to the reevaluated experimental value in kg/MTU, for the compilation of SFCOMPO, using a half-life value smaller than the recent one. Since all burn-up calculations are performed using atomic number densities, accurate half-life is necessary to compare with the experimental values of PNL-PIEs. On the other hand, half-life is not necessary for the experimental value of JAEA-PIE, because the concentration of Se-79 was directly measured by ICP-QMS. In Fig.5(b), the experimental values of Se-79 for PNL-PIEs are modified; the measured values in PNL-PIEs are converted with the recent half-life of Se-79 by Bienvenu *et al.* (2007). As a result, the averaged C/E for 15 samples in PNL-PIEs is 0.92±0.15

(2 $\sigma$ ), which is consistent with the C/E value (1.07 $\pm$ 0.29) obtained from JAEA-PIE.

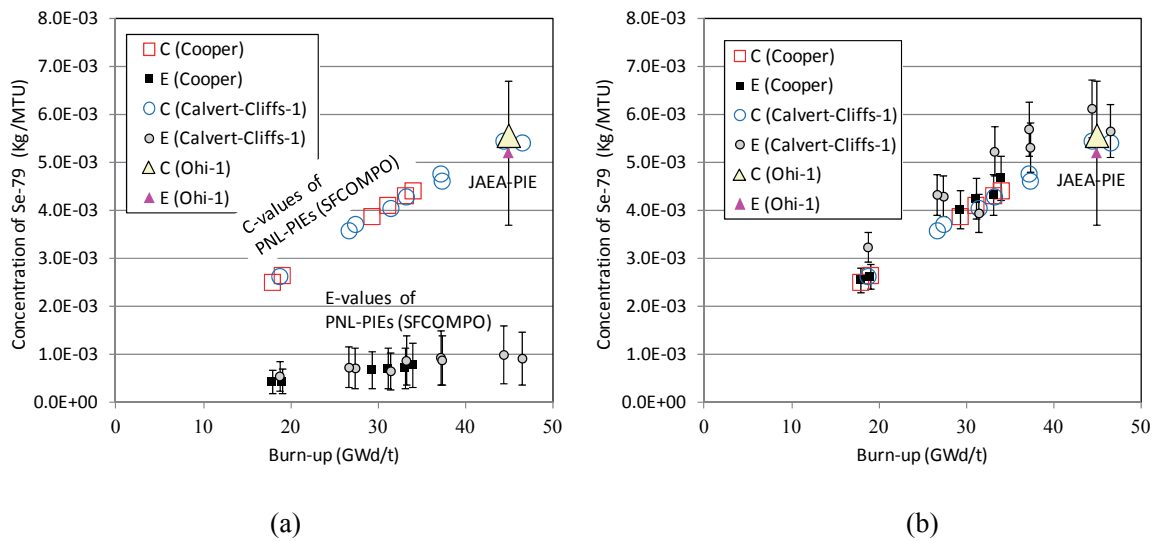


Fig. 5 Experimental and calculated values for Se-79

- (a) E-values of Cooper and Calvert-Cliffs-1 are taken from SFCOMPO,
- (b) E-values of Cooper and Calvert-Cliffs-1 are modified with the recent half-life of Se-79.

### 5. Conclusion

Data libraries for neutron transport and burn-up calculations are produced on the basis of JENDL-4.0. Accurate prediction of isotope generation and depletion for LWR fuels are confirmed by PIE analyses with the data libraries. Compared with the old data libraries based on JENDL-3.3, drastic improvements are achieved for the prediction of LWR spent fuel compositions especially for MAs (Np, Am, Cm isotopes) and FPs (Cs-134, Eu-154, Sm-151, Sm-152), which are sensitive to cross sections. It is also found that the recent data for half-life of Se-79 improves the prediction of Se-79 radioactivity, which is important for long-term safety assessment of a geological disposal of high level vitrified waste.

### References

- [1] K. Okumura, T. Mori, M. Nakagawa and K. Kaneko: "Validation of a Continuous-Energy Monte Carlo Burn-up Code MVP-BURN and Its Application to Analysis of Post Irradiation Experiment," J. Nucl. Sci. Technol., 37[2], pp.128-138 (2000).
- [2] Y. Nagaya, T. Mori, K. Okumura and M. Nakagawa: "MVP/GMVP II: General Purpose Monte Carlo Codes for Neutron and Photon Transport Calculations based on Continuous Energy and Multigroup Methods," JAERI 1348 (2005).
- [3] K. Okumura, T. Kugo, K. Kaneko and K. Tsuchihashi: "SRAC2006 : A Comprehensive Neutronics Calculation Code System," JAEA-Data/Code 2007-004 (2007).
- [4] K. Okumura, T. Kugo, H. Nakano, *et al.*: "Development of Modular Reactor Analysis Code System MOSRA", 2008 annual meeting of the Atomic Energy Society of Japan (2008).
- [5] A.G. Croff: "ORIGEN2: A Versatile Computer Code for Calculating the Nuclide Compositions and Characteristics of Nuclear Materials," Nucl. Technol. 62, 335 (1983).
- [6] K. Shibata, O. Iwamoto, T. Nakagawa, *et al.*: "JENDL-4.0: A New Library for Nuclear Science and

- Engineering,” J. Nucl. Sci. Technol. 48[1], 1 (2011).
- [7] K. Okumura and Y. Nagaya, “Production of Neutron Cross Section Library Based on JENDL-4.0 to Continuous-energy Monte Carlo Code MVP and Its Application to Criticality Analysis of Benchmark Problems in the ICSBEP Handbook,” JAEA-Data/Code 2011-010 (2011).
- [8] X-5 Monte Carlo Team: “MCNP - A General Monte Carlo N-Particle Transport Code, Version 5,” LA-UR-03-1987 (2003).
- [9] K. Niita, N. Matsuda, Y. Iwamoto, *et al.*: “PHITS: Particle and Heavy Ion Transport code System, Version 2.23,” JAEA-Data/Code 2010-022 (2010).
- [10] K. Suyama, T. Kiyosumi and H. Mochizuki, “Revised SWAT - Integrated Burn-up Calculation Code System -,” JAERI-Data/Code 2000-027 (2000).
- [11] R.E. MacFarlane: “TRANSX2: A Code for Interfacing MATXS Cross-Section Libraries to Nuclear Transport Codes,” LA-12312-MS (1992).
- [12] K. Okumura, K. Sugino, K. Kojima, T. Jin, T. Okamoto and J. Katakura, “A Set of ORIGEN2 Cross Section Libraries based on JENDL-4.0: ORLIBJ40,” to be appeared in JAEA-Data/Code (2012).
- [13] K. Okumura, K. Kojima and T. Okamoto: “Development of the Burn-up Chain Data ChainJ40 based on JENDL-4.0”, 2012 annual meeting of the Atomic Energy Society of Japan (2012).
- [14] National Nuclear Data Center: “Evaluated Nuclear Structure Data File (ENSDF), <http://www.nndc.bnl.gov/>.
- [15] P. Bienvenu, P. Cassette, G. Andreoletti *et al.*: “A new determination of  $^{79}\text{Se}$  half-life,” Appl. Radiat. Isot., 65, 355 (2007).
- [16] P. Bienvenu, L. Ferreux, G. Andreoletti *et al.*: “Determination of  $^{126}\text{Sn}$  half-life from ICP-MS and gamma spectrometry measurements,” Radiochim. Acta, 97, 687 (2009).
- [17] G. Chiba, K. Okumura, K. Sugino, *et al.* : “JENDL-4.0 Benchmarking for Fission Reactor Applications”, J. Nucl. Sci. Technol. 48[2], 172 (2011).
- [18] Y. Nakahara, K. Suyama, T. Suzaki (Eds.): “Technical Development on Burn-up Credit for Spent LWR Fuels,” JAERI-Tech 2000-071 (2000).
- [19] K. Shibata, T. Kawano, T. Nakagawa,*et al.*: “Japanese Evaluated Nuclear Data Library Version 3 Revision-3: JENDL-3.3,” J. Nucl. Sci. Technol., 39, 1125 (2002).
- [20] J. Katakura, T. Yoshida, K. Oyamatsu and T. Tachibana: “JENDL FP Decay Data File 2000,” JAERI 1343 (2001).
- [21] K. Okumura, K. Kojima and T. Okamoto, “Development of the ORIGEN2 Library for Light Water Reactors Based on JENDL-4.0,” Proc of the 2011 Symposium on Nuclear Data, Nov. 16,17, Tokai-mura, Japan, 2011.
- [22] K. Okumura, S. Asai, Y. Hanzawa, *et al.*: “Analyses of Assay Data of LWR Spent Nuclear Fuels with a Continuous-Energy Monte Carlo Code MVP and JENDL-4.0 for Inventory Estimation of  $^{79}\text{Se}$ ,  $^{99}\text{Tc}$ ,  $^{126}\text{Sn}$ , and  $^{135}\text{Cs}$ ,” Progr. in Nucl. Sci. and Technol., 2, 369 (2011).
- [23] R. J. Guenther, D. E. Blahnik, T. K. Campbell *et al.*: “Characterization of Spent Fuel Approved Testing Material,” ATM-103/-104/-105/-106, Pacific Northwest Laboratory, PNL-5109-103 (1988), -104 (1991), -105 (1991), -106 (1988).
- [24] S. Asai, Y. Hanzawa, K. Okumura, *et al.*: “Determination of  $^{79}\text{Se}$  and  $^{135}\text{Cs}$  in Spent Nuclear Fuel for Inventory Estimation of High-Level Radioactive Wastes,” J. Nucl. Sci. Technol., 48[5], 851 (2011).
- [25] H. Mochizuki, K. Suyama, Y. Nomura, H. Okuno, Spent Fuel Composition Database System on WWW - SFCOMPO on WWW Ver.2 -, JAERI-Data/Code 2001-020, Japan Atomic Energy Research Institute (JAERI) (2001), [in Japanese].

## 9 Estimation of average burnup of damaged fuels loaded in Fukushima Dai-ichi reactors by using the $^{134}\text{Cs}/^{137}\text{Cs}$ ratio method

Tomohiro Endo, Shunsuke Sato, Akio Yamamoto

Department of Materials, Physics and Energy Engineering Graduate School of Engineering,

Nagoya University, Furo-cho, Chikusa-ku, Nagoya-shi, 464-8603, Japan

e-mail: t-endo@nucl.nagoya-u.ac.jp

Average burnup of damaged fuels loaded in Fukushima Dai-ichi reactors is estimated by using the  $^{134}\text{Cs}/^{137}\text{Cs}$  ratio method for actually measured radioactivities of  $^{134}\text{Cs}$  and  $^{137}\text{Cs}$  in contaminated soils within the range of 100 km from the Fukushima Dai-ichi nuclear power plants. The numerical analysis of radioactivity ratio of  $^{134}\text{Cs}/^{137}\text{Cs}$  is carried out by two deterministic codes (SRAC2006/PIJ, SCALE6.0/TRITON) and a Monte Carlo code (MVP-BURN). Moreover, the void fraction effect for  $^{134}\text{Cs}/^{137}\text{Cs}$  ratio is also investigated with two recent evaluated nuclear data libraries (JENDL-4.0, ENDF-B/VII.0). As a result, the measured  $^{134}\text{Cs}/^{137}\text{Cs}$  ratio from the contaminated soil is  $0.996\pm 0.07$  as of March 11th, 2011. By using the  $^{134}\text{Cs}/^{137}\text{Cs}$  ratio method, the estimated burnup of Fukushima Dai-ichi units 1, 2, and 3 is approximately  $17.2\pm 1.5$  [GWd/t] in the present research.

### 1. Introduction

At 14:46, March 11th, 2011, the M9.0 earthquake followed by tsunami hit the Tohoku area. In Fukushima Dai-ichi nuclear power plants, station blackout accompanied with loss of cooling capability and loss of ultimate heat sink was caused by excessive tsunami that was generated by the earthquake. Consequently, it resulted in severe core damages in Fukushima Dai-ichi units 1, 2, and 3. Confinement capabilities (RPV, CV) were partially damaged, thereby radioactive nuclides released to the environment. From the view point of health effects due to radioactive nuclides released from Fukushima Dai-ichi reactors, it is very important to comprehend isotopic compositions of radioactive nuclides released to the environment, especially for the isotopes that have not been surveyed. The estimation of burnup of damaged fuels loaded in Fukushima Dai-ichi reactors enables us to evaluate the isotopic compositions. Moreover, the estimated burnup can be utilized for burnup credit to safely discharge fuel-debris in each core.

For this purpose, in the present research, average burnup of damaged fuels is estimated by using the  $^{134}\text{Cs}/^{137}\text{Cs}$  ratio method<sup>1,2)</sup> for actually measured radioactivities of  $^{134}\text{Cs}$  and  $^{137}\text{Cs}$  in contaminated soils within the range of 100km from the Fukushima Dai-ichi nuclear power plants, published by the Ministry of Education, Culture, Sports, Science & Technology (MEXT) in Japan<sup>3)</sup>.

## 2. Numerical analysis for the radioactivity ratio of $^{134}\text{Cs}/^{137}\text{Cs}$

The burnup dependency of the radioactivity ratio of  $^{134}\text{Cs}/^{137}\text{Cs}$  is evaluated by unit-cell depletion calculation by deterministic codes (SRAC2006/PIJ<sup>4)</sup> and SCALE6.0/TRITON<sup>5)</sup>) and a Monte Carlo code (MVP-BURN<sup>6)</sup>), with recent evaluated nuclear data libraries (JENDL-4.0<sup>7)</sup> and ENDF-B.VII.0<sup>8)</sup>). Detail information about nuclear fuels loaded in Fukushima Dai-ichi reactors is classified due to proprietary data:  $^{235}\text{U}$ , Pu, and Gd enrichment/content splitting in  $\text{UO}_2$  and MOX assemblies; core loading pattern; distributions and histories of power, void fraction (VF), and temperature in each cycle. Therefore, the simple calculation model is used in the present research. The calculation geometry is unit fuel pin cell geometry for  $\text{UO}_2$  (8×8  $\text{UO}_2$ , 9×9-A, 9×9-B) and MOX (8×8) fuels. And assembly-averaged values of  $^{235}\text{U}$  enrichment and Pu content, and core-averaged specific power are used as input values of depletion calculation.

Firstly, the numerical results of three calculation codes (SRAC2006/PIJ, SCALE6.0/TRITON, and MVP-BURN) are compared, on the condition that assembly-averaged VF is 40% and ENDF-B.VII.0 library are used. In the depletion calculation of SRAC2006/PIJ and MVP-BURN, the most detailed burnup chain data (th2cm6fp193bp6T) is used; however, it is noted that the used burnup chain data is previous data, *i.e.*, the recent burnup chain data based on JENDL-4.0 (ChainJ40<sup>9)</sup>) is not used in the present research. In the SCALE6.0/TRITON, the depletion calculation is executed by ORIGEN-S<sup>10)</sup> based on the microscopic cross-sections created by the two-dimensional transport calculation code, NEWT<sup>11)</sup>. For example, Fig. 1 shows the numerical results of  $^{134}\text{Cs}/^{137}\text{Cs}$  ratio for 9×9-B fuel. As shown in Fig. 1, in the case of the same evaluated nuclear data library, numerical results of  $^{134}\text{Cs}/^{137}\text{Cs}$  ratio are almost same among these three calculation codes.

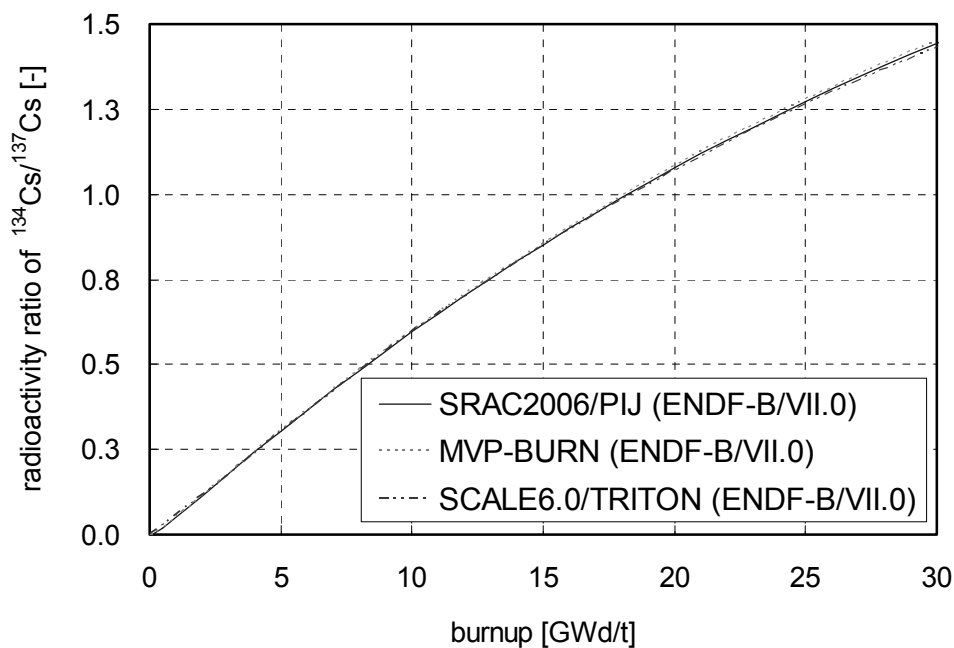


Fig. 1 Comparison of  $^{134}\text{Cs}/^{137}\text{Cs}$  ratio among calculation codes

Secondly, by using SRAC2006/PIJ with JENDL-4.0 and ENDF-B.VII.0, VF effects for  $^{134}\text{Cs}/^{137}\text{Cs}$  ratio are investigated under the core-averaged specific power. Lower VF value of moderator makes neutron spectrum softer. As shown in Fig. 2, lower VF value results in lower  $^{134}\text{Cs}/^{137}\text{Cs}$  ratio because of the softer neutron spectrum. The difference of  $^{134}\text{Cs}/^{137}\text{Cs}$  ratio between VF=0% and 70% is approximately 0.3 at 30 [GWd/t]. It is noted that the difference due to evaluated nuclear data libraries is relatively smaller than that of VF effects, *i.e.*, the difference between JENDL-4.0 and ENDF-B.VII.0 is approximately 0.05 at 30 [GWd/t].

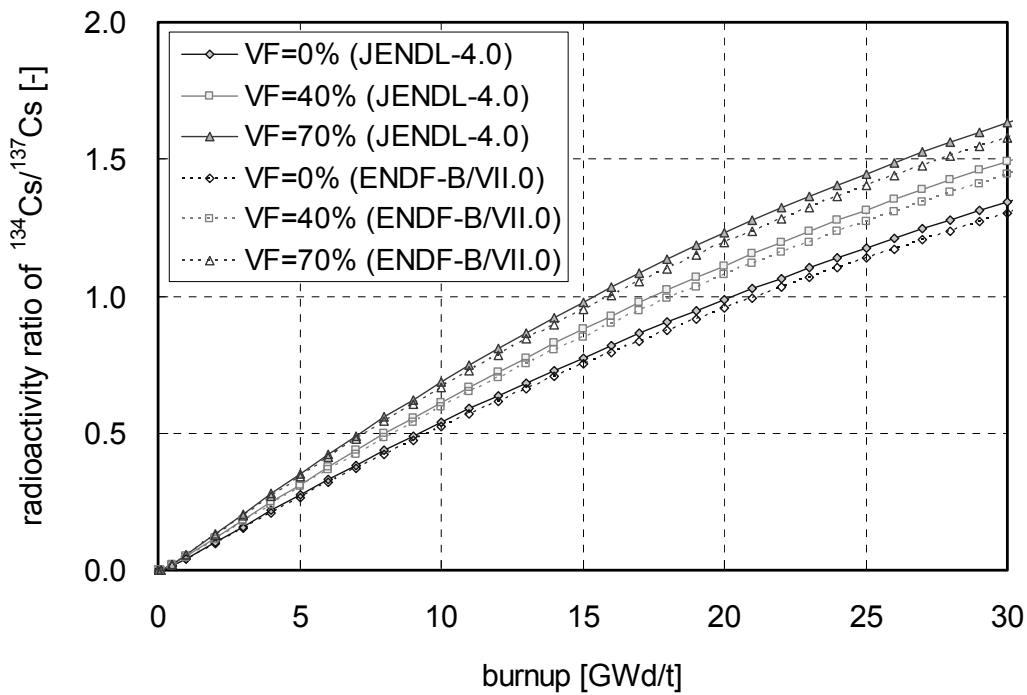


Fig. 2 Comparison of  $^{134}\text{Cs}/^{137}\text{Cs}$  ratio for 0, 40, 70% void fractions

Finally, based on the numerical results of radioactivities  $^{134}\text{Cs}$  and  $^{137}\text{Cs}$  for unit-cell depletion calculations by SRAC2006/PIJ with JENDL-4.0, the weighted-means of  $^{134}\text{Cs}/^{137}\text{Cs}$  ratio for Fukushima Dai-ichi units 1-3 are obtained by weighting the radioactivities of  $^{134}\text{Cs}$  and  $^{137}\text{Cs}$  by the loaded heavy metal weights for corresponding cores. Consequently, if the fuel burnup is approximated by cubic function of the weighted-averages of  $^{134}\text{Cs}/^{137}\text{Cs}$  ratio, the following estimation formula is obtained in the present research:

$$B(x) \approx \begin{cases} 18.04 \times x - 0.8321 \times x^2 + 3.162 \times x^3 & (\text{VF} = 0\%) \\ 15.94 \times x - 1.409 \times x^2 + 2.779 \times x^3 & (\text{VF} = 40\%) \\ 14.36 \times x - 1.785 \times x^2 + 2.676 \times x^3 & (\text{VF} = 70\%), \end{cases} \quad (1)$$

where  $B(x)$  is fuel burnup [GWd/t] and  $x$  indicates the radioactivity ratio of  $^{134}\text{Cs}/^{137}\text{Cs}$ .

### 3. Estimation of fuel burnup based on the measured radioactivity ratio of $^{134}\text{Cs}/^{137}\text{Cs}$ from contaminated soils

Based on the measured radioactivities of  $^{134}\text{Cs}$  and  $^{137}\text{Cs}$  in contaminated soils within the range of 100 km from the Fukushima Dai-ichi nuclear power plants<sup>3)</sup>, the frequency distribution of  $^{134}\text{Cs}/^{137}\text{Cs}$  ratio is analyzed, as shown in Fig. 3. As a result, the measured  $^{134}\text{Cs}/^{137}\text{Cs}$  ratio from the contaminated soil is  $0.996\pm 0.07$  as of March 11th, 2011, where 0.07 is standard deviation ( $1\sigma$ ) for the analyzed frequency distribution of  $^{134}\text{Cs}/^{137}\text{Cs}$  ratio.

Using the Eq. (1) for the measured  $^{134}\text{Cs}/^{137}\text{Cs}$  ratio, if it is assumed that typical VF=40% in BWR core, the estimated burnup of Fukushima Dai-ichi units 1-3 is approximately  $17.2\pm 1.5$  [GWd/t], where the deviation of 1.5 is simply estimated by the error propagation for the standard deviation of the measured  $^{134}\text{Cs}/^{137}\text{Cs}$  ratio. According to the alarm recording data that includes numerical summaries of BWR plant process computer<sup>12-14)</sup>, the core average burnup values for Fukushima unit 1, 2, and 3 as of March 11, 2011 are 25.8, 23.2, and 21.8 [GWd/t], respectively. Thus, the estimated burnup  $17.2\pm 1.5$  [GWd/t] by  $^{134}\text{Cs}/^{137}\text{Cs}$  ratio is nearly equal but slightly lower than that of core average burnup values recorded in the alarm recording data. One of the reasons for this discrepancy would be core meltdown process<sup>15)</sup>. Namely, the damages of fuel assemblies in the core progressed from the center to the peripheral region of the core, thereby the averaged burnup of damaged fuel is lower than that of core averaged value, since fuel assemblies loaded in peripheral region are typically forth- or fifth-burned fuel assemblies, *i.e.*, the fuel burnup in the peripheral region of core is relatively high compared with central region. For another reason, once-burned fuel assemblies, which have relatively high power density due to burnout of burnable poison, may be highly damaged.

### 4. Conclusion

In the present research, the average burnup of damaged fuels were estimated as  $17.2\pm 1.5$  [GWd/t] by using the  $^{134}\text{Cs}/^{137}\text{Cs}$  ratio method based on actually measured radioactivities of  $^{134}\text{Cs}$  and  $^{137}\text{Cs}$  in contaminated soils. The numerical results of SRAC2006/PIJ, SCALE6.0/TRITON, and MVP-BURN are almost the same evaluation values of  $^{134}\text{Cs}/^{137}\text{Cs}$  ratio with same evaluated nuclear data library, ENDF-B/VII.0. The void fraction effect in depletion calculation has a major impact on  $^{134}\text{Cs}/^{137}\text{Cs}$  ratio compared with the differences between JENDL-4.0 and ENDF-B/VII.0. More precise evaluation of burnup of damaged fuels requires more detail information about fuel assemblies' data loaded in Fukushima Dai-ichi reactors, especially, histories and distributions of the specific power and the void fraction are strongly desired.

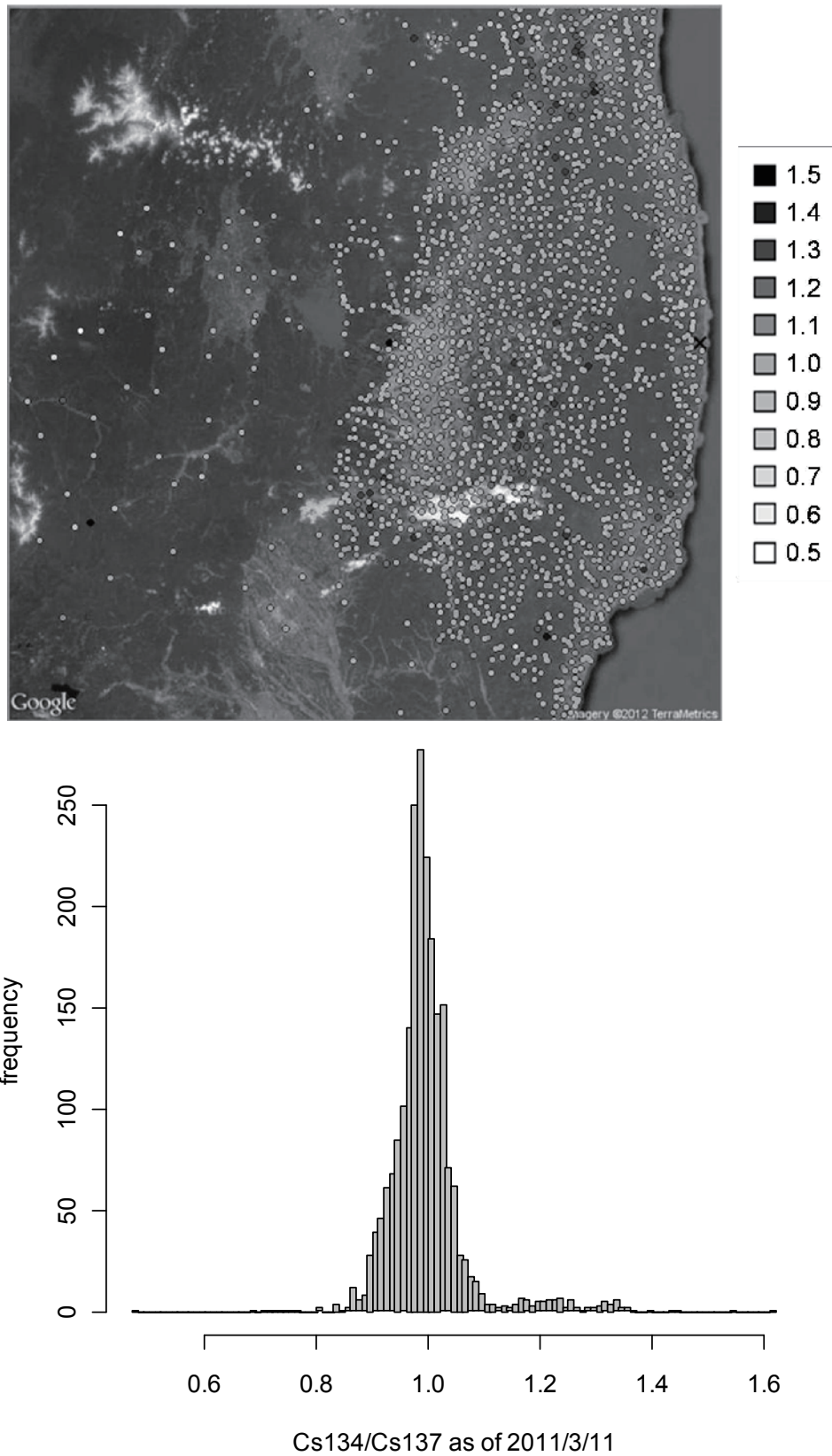


**Fig. 3** Frequency distribution of  $^{134}\text{Cs}/^{137}\text{Cs}$  ratio in contaminated soils within the range of 100 km from the Fukushima Dai-ichi nuclear power plants

## Acknowledgements

The authors sincerely thank all of researchers that are involved in the measurement and analysis of radiation dose and radioactive-contamination map project supported by the Ministry of Education, Culture, Sports, Science & Technology (MEXT) in Japan.

## References

- [1] E. M. Pazukhin, A. A. Borovoi, "The ratio of plutonium isotopes depending on the burnup of the fuel from the fourth block of the Chernobyl nuclear power plant," *Radiochemistry*, **45**[2], 209-210 (2003).
- [2] V. D. Kuriny, Yu. A. Ivanov, V. A. Kashparov, *et al.*, "Particle-associated Chernobyl fall-out in the local and intermediate zones," *Ann. Nucl. Energy*, **20**[6], 415-420 (1993).
- [3] Nuclide analysis for soils ( $^{134}\text{Cs}$  and  $^{137}\text{Cs}$ ),  
[http://www.mext.go.jp/b\\_menu/shingi/chousa/gijyutu/017/shiryo/\\_icsFiles/afldfile/2011/09/02/1310688\\_1.pdf](http://www.mext.go.jp/b_menu/shingi/chousa/gijyutu/017/shiryo/_icsFiles/afldfile/2011/09/02/1310688_1.pdf), MEXT (2011). [in Japanese]
- [4] K. Okumura, T. Kugo, K. Kaneko, *et al.*, "SRAC2006 : A comprehensive neutronics calculation code system," JAEA-Data/Code 2007-004 (2007).
- [5] M. D. DeHart, "TRITON: A two-dimensional transport and depletion module for characterization of spent nuclear fuel," Oak Ridge National Laboratory, ORNL/TM-2005/39 Version 6 Vol. I, Sect. T1.
- [6] K. Okumura, T. Mori, M. Nakagawa, *et al.*, "Validation of a continuous energy Monte Carlo burn-up code MVP-BURN and its application to analysis of post irradiation experiment," *J. Nucl. Sci. Technol.*, **37**[2], 128-138, (2000).
- [7] K. Shibata, O. Iwamoto, T. Nakagawa, *et al.*, "JENDL-4.0: A new library for nuclear science and engineering," *J. Nucl. Sci. and Technol.*, **48**[1], 1-30 (2011).
- [8] M. B. Chadwick, P. Oblozinsky, M. Herman, *et al.*, "ENDF/B-VII.0: Next generation evaluated nuclear data library for nuclear science and technology," *Nuclear Data Sheets*, **107**[12], 2931-3060 (2006).
- [9] K. Okumura, S. Asai, Y. Hanzawa, *et al.*, "Analyses of assay data of LWR spent nuclear fuels with a continuous-energy Monte Carlo code MVP and JENDL-4.0 for inventory estimation of  $^{79}\text{Se}$ ,  $^{99}\text{Tc}$ ,  $^{126}\text{Sn}$  and  $^{135}\text{Cs}$ ," *Progr. in Nucl. Sci. and Technol.*, **2**, 369-374 (2011).
- [10] I. C. Gauld, O. W. Hermann, and R. M. Westfall, "ORIGEN-S: SCALE system module to calculate fuel depletion, actinide transmutation, fission product buildup and decay, and associated radiation source terms," Oak Ridge National Laboratory, ORNL/TM-2005/39, Version 6 Vol. II, Sect. F7.
- [11] M. D. DeHart, "NEWT: A new transport algorithm for two-dimensional discrete ordinates analysis in non-orthogonal geometries," Oak Ridge National Laboratory, ORNL/TM-2005/39, Version 6 Vol. II, Sect. F21.
- [12] Alarm recording data at Fukushima Dai-ichi unit 1,  
[http://www.tepco.co.jp/nu/fukushima-np/plant-data/fl\\_3\\_Keihou1.pdf](http://www.tepco.co.jp/nu/fukushima-np/plant-data/fl_3_Keihou1.pdf), TEPCO, (2011). [in Japanese]
- [13] Alarm recording data at Fukushima Dai-ichi unit 2,

- [http://www.tepco.co.jp/nu/fukushima-np/plant-data/fl\\_3\\_Keihou2.pdf](http://www.tepco.co.jp/nu/fukushima-np/plant-data/fl_3_Keihou2.pdf), TEPCO, (2011). [in Japanese]
- [14] Alarm recording data at Fukushima Dai-ichi unit 3,  
[http://www.tepco.co.jp/nu/fukushima-np/plant-data/fl\\_3\\_Keihou3.pdf](http://www.tepco.co.jp/nu/fukushima-np/plant-data/fl_3_Keihou3.pdf), TEPCO, (2011). [in Japanese]
- [15] Evaluation report about core conditions due to the nuclear power plant disaster for Fukushima Dai-ichi units 1, 2, 3, JNES-RE-2011-0002, (2011). [in Japanese]

This is a blank page.

## **10 Present Status and Perspective of Neutron Cross Section Measurement in a Low Energy Region**

Masayuki IGASHIRA

Research Laboratory for Nuclear Reactors, Tokyo Institute of Technology

2-12-1-N1-26 O-okayama, Meguro-ku, Tokyo 152-8550, Japan

E-mail: iga@nr.titech.ac.jp

There are several facilities with intense spallation neutron sources in the world, and some of them are being utilized for neutron cross section measurement in a low energy region. In the present paper, characteristics of those facilities are described and comparison among them is made. Recent research activities at those facilities are also presented. Moreover, the perspective of those activities, especially those at J-PARC/MLF, is described.

### **1. Introduction**

Neutron cross section data in a low energy region are important for a variety of research fields. In particular, neutron capture cross section data below 1 MeV for Long-Lived Fission Products (LLFPs) and Minor Actinides (MAs) are very important for the R&D of innovative nuclear energy systems. Those for LLFPs in the keV region are also important for the study on the s-process of nucleosynthesis in stars.

There are several facilities with intense spallation neutron sources in the world, and some of them, e.g. LANCE, n\_TOF and J-PARC/MLF, are being utilized for neutron cross section measurement in a low energy region. In the present paper, characteristics of those facilities are described and comparison among them is made. Recent research activities at those facilities are also presented. Moreover, the perspective of those activities, especially those at J-PARC/MLF, is described.

### **2. Spallation Neutron Facilities (SNFs)**

Material and Life Sciences Experimental Facilities (MLF) at Japan Proton Accelerator Research Complex (J-PARC) use a 3 GeV proton beam (25 Hz) and a Hg target with liquid hydrogen moderators. A typical beam power was 200 kW before terrible earthquakes on March 11, 2011.

Los Alamos Neutron Science Center (LANSCE) has Weapon Neutron Research

Facility (WNR) and Lujan Center. WNR uses a 0.8 GeV proton beam and a W target without moderator. On the other hand, Lujan Center uses a W target with water moderators. Their nominal beam power is 80 kW.

The n\_TOF at CERN (European Organization for Nuclear Research) uses a 20 GeV proton beam and a Pb target without moderator. Its nominal beam power is 9 kW.

Spallation Neutron Source (SNS) at Oak Ridge National Laboratory (ORNL) uses a 1 GeV proton beam and a W target, but it has no beam line for neutron cross section measurement.

Figure 1 compares neutron fluxes at typical sample positions at J-PARC/MLF (ANNRI; 200 kW), LANSCE (DANCE at Lujan Center; 80 kW), and n\_TOF (9 kW)[1]. The distances, L, from the neutron source to the sample position are 21.5, 20, 185 m, respectively. As seen from Fig. 1, the neutron flux at ANNRI is much higher than those at the other facilities.

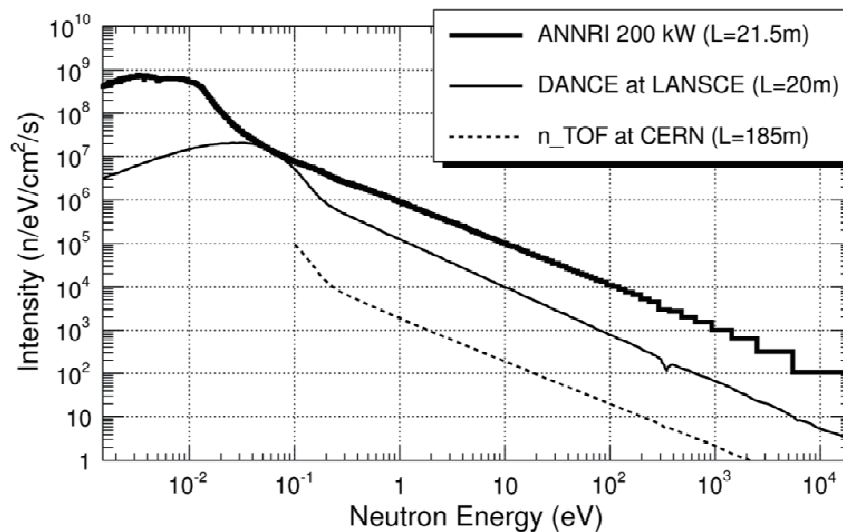


Fig. 1 Neutron fluxes at typical sample positions[1]

Accurate Neutron-Nucleus Reaction Measurement Instrument (ANNRI)[2] was installed in the beam line 04 of MLF of J-PARC in a Nuclear Data Project. Figure 2 shows vertical and horizontal cross sections of ANNRI[1]. ANNRI has two experimental areas. A 4 $\pi$  Ge spectrometer is installed at 21.5 m from the neutron source in the upstream area, and an NaI(Tl) spectrometer is installed at 27 m in the downstream area.

The Detector for Advanced Neutron Capture Experiments (DANCE)[3] is installed in Lujan Center. DANCE is a 4 $\pi$  spectrometer which consists of 160 BaF<sub>2</sub> detectors. Germanium Array for Neutron-Induced Excitations (GEANIE)[4] and Fast Neutron Induced Neutron and Gamma Ray Observer (FIGARO)[5] are installed in WNR.

The n\_TOF[6] also has a 4 $\pi$  spectrometer which consists of 42 BaF<sub>2</sub> detectors.

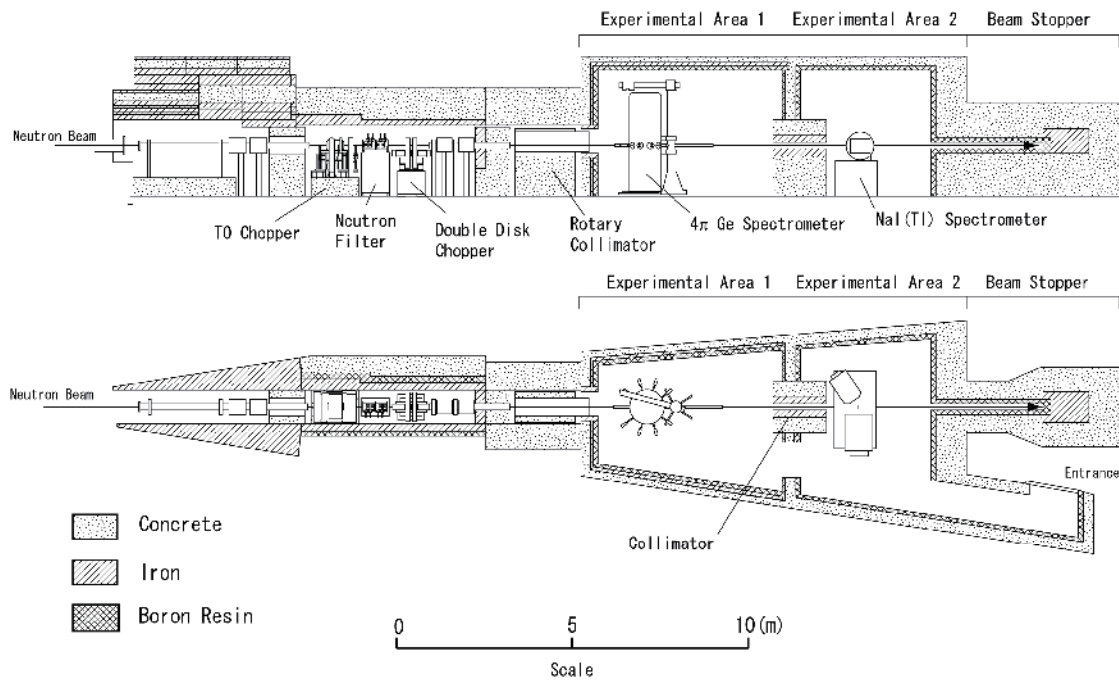


Fig. 2 Vertical (top) and horizontal (bottom) cross sections of ANNRI[1]

### 3. Cross Section Measurements at SNFs

Capture cross sections of LLFPs and MAs are being measured at ANNRI. Nuclear fuel (Th, U, Pu) and unsealed radio isotopes are not usable in MLF. Therefore, all samples are contained in a case made of aluminum or titanium. The measurements for  $^{93}\text{Zr}$ ,  $^{99}\text{Tc}$ ,  $^{107}\text{Pd}$ ,  $^{129}\text{I}$ ,  $^{237}\text{Np}$ ,  $^{241}\text{Am}$ ,  $^{243}\text{Am}$ ,  $^{244}\text{Cm}$ , and  $^{246}\text{Cm}$  were performed before the earthquakes. As for  $^{244}\text{Cm}$  and  $^{246}\text{Cm}$ , the measurements at ANNRI were the first ones with an accelerator neutron source.

At LANSCE, measurements of capture, fission and inelastic cross sections for a variety of nuclides are being performed. At n\_TOF, measurements of capture and fission cross sections for LLFPs and MAs are being performed.

### 4. Perspective of Measurements at J-PARC/MLF

ANNRI was dedicated to the project until March, 2010. After the project, the Ministry of Education, Culture, Sports, Science and Technology of Japan (MEXT) approved the usage of ANNRI for studies on (1) Nuclear Energy Systems, (2) Nucleosynthesis in the Universe, and (3) Nuclide-Quantification: practically, ANNRI is available to worldwide users. We expect ANNRI will be used for a variety of research fields.

### Acknowledgements

The present study includes the result of “Study on nuclear data by using a high intensity pulsed neutron source for advanced nuclear system” entrusted to Hokkaido

University by the Ministry of Education, Culture, Sports, Science and Technology of Japan (MEXT).

### References

- [1] K. Kino et al., *Nucl. Instr. and Meth. Phys. Res. A*, **626-627**, 58-66 (2011).
- [2] M. Igashira, Y. Kiyonagi, M. Oshima, *Nucl. Instr. and Meth. Phys. Res. A*. **600**, 332-334 (2009).
- [3] <http://lansce.lanl.gov/lujan/instruments/DANCE/pdfs/DANCE.pdf>
- [4] <http://geanie.lanl.gov/>
- [5] R. O. Nelson, *Journal of the Korean Physical Society*, **59**, 1558-1562 (2011).
- [6] CERN/INTC-O-011, INTC-2002-037, CERN-SL-2002-053 ECT (<http://pceet075.cern.ch/> "CERN n\_TOF Facility: Performance Report")

## 11 Present Status and Perspective on Intermediate Energy Nuclear Data Measurements

Yukinobu WATANABE

Department of Advanced Energy Engineering Science, Kyushu University,  
 Kasuga, Fukuoka 816-8580, Japan  
 e-mail: watanabe@aees.kyushu-u.ac.jp

Recent domestic and international activities of intermediate energy nuclear data measurements are overviewed. A strategy meeting on nuclear data research was held in June 2011 at RCNP, Osaka University in order to discuss the needs of intermediate energy nuclear data in various applications and proposals of new measurements among domestic researchers in universities, national institutes, and industries. Based on the summary, future perspectives on intermediate energy nuclear data measurements are remarked.

### 1. Introduction

There have been increasing needs of intermediate and high energy nuclear data in various applications such as accelerator-driven transmutation systems, particle radiation therapy, radioisotope production, space development, etc., as illustrated in Fig.1. These applications require not only neutron data but also charged-particle data, particularly proton data, in particle transport and activation calculations.

The activities on high-energy nuclear data evaluation have so far been undertaken all over the world, and have produced some available nuclear data libraries, such as general purpose libraries : JENDL/HE-2007[1], ENDF/B-VII.0[2], JEFF-3.1.1[3], and TENDL-2010[4], One of the recent topics on high-energy nuclear data evaluation is the FENDL-3 project [5] organized at IAEA for fusion applications to IFMIF and also for design studies of DEMO. The energy range of incident particles (neutron, proton, and deuteron) will be extended up to 150 MeV to comply fully with the requirements of the IFMIF design.

Experimental data are not necessarily enough in the intermediate energy range above 20 MeV, and further measurements are required to provide the data necessary for various applications and also to establish reliable theoretical models for cross section evaluation. In June 2011, a nuclear data research strategy meeting was held at RCNP (Research Center for Nuclear Physics), Osaka University to discuss the needs of intermediate energy nuclear data in various applications and proposals of new measurements among domestic researchers in universities, national institutes, and industries. In this report, recent domestic and international activities of cross section measurements are overviewed, and some perspectives based on the summary of the research strategy meeting are given.

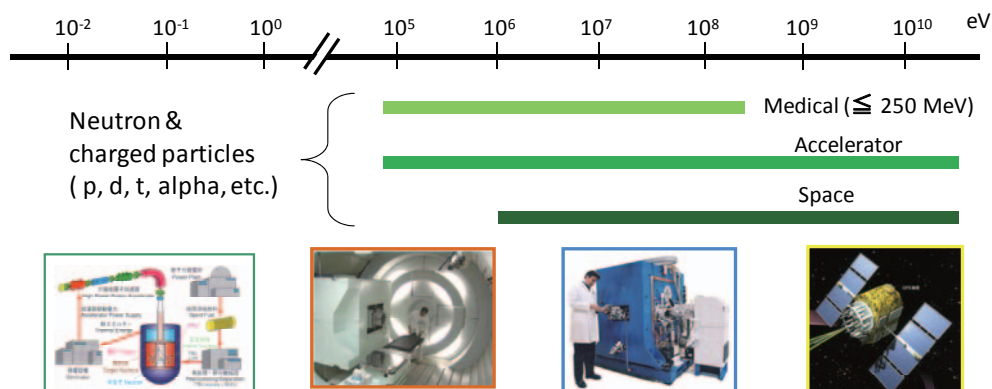


Fig.1 Schematic illustration of the needs of intermediate and high energy nuclear data

2. Domestic activities on intermediate energy nuclear data measurements

Several cross section measurements are now in progress in Japan as listed in Table 1. One of the major experimental facilities is RCNP, Osaka University. A schematic drawing of the facility is shown in Fig.2, indicating the experimental halls which are utilized in the cross section measurements listed in Table.1.

T. Sanami et al. [6,7,8] have been carrying out systematic measurements of double-differential fragment production cross sections for proton-induced reactions on C, O, N, Al, Ti, Cu and Ta using proton beams of 40 to 80 MeV at NIRS and proton beams of 140 to 300 MeV at RCNP using a Bragg curve counter. They have analyzed the measured data using reaction models implemented in PHITS [9] and clarified that the models underestimate the high energy parts of forward emission spectra. Systematic trends on the experimental spectral shape and the effect of Coulomb barrier are being investigated.

Table 1. Nuclear data measurements at domestic accelerator facilities

Measured data	Representative person	Facility	References
Fragment production DDXs from proton-induced reactions	T. Sanami (KEK)	RCNP* NIRS**	[6,7,8]
Neutron elastic scattering cross sections	D. Satoh (JAEA)	RCNP	[11]
Monoenergetic neutron energy spectra	Y. Iwamoto (JAEA)	RCNP	[10]
Neutron-induced nuclear production cross sections	H. Yashima (Kyoto U)	RCNP	[12]
Neutron production DDXs from heavy-ion interactions	N. Shigyo (Kyushu U)	NIRS	[13,14,15,16]

\*) RCNP: Research Center for Nuclear Physics, Osaka University

\*\*\*) NIRS: National Institute of Radiological Sciences

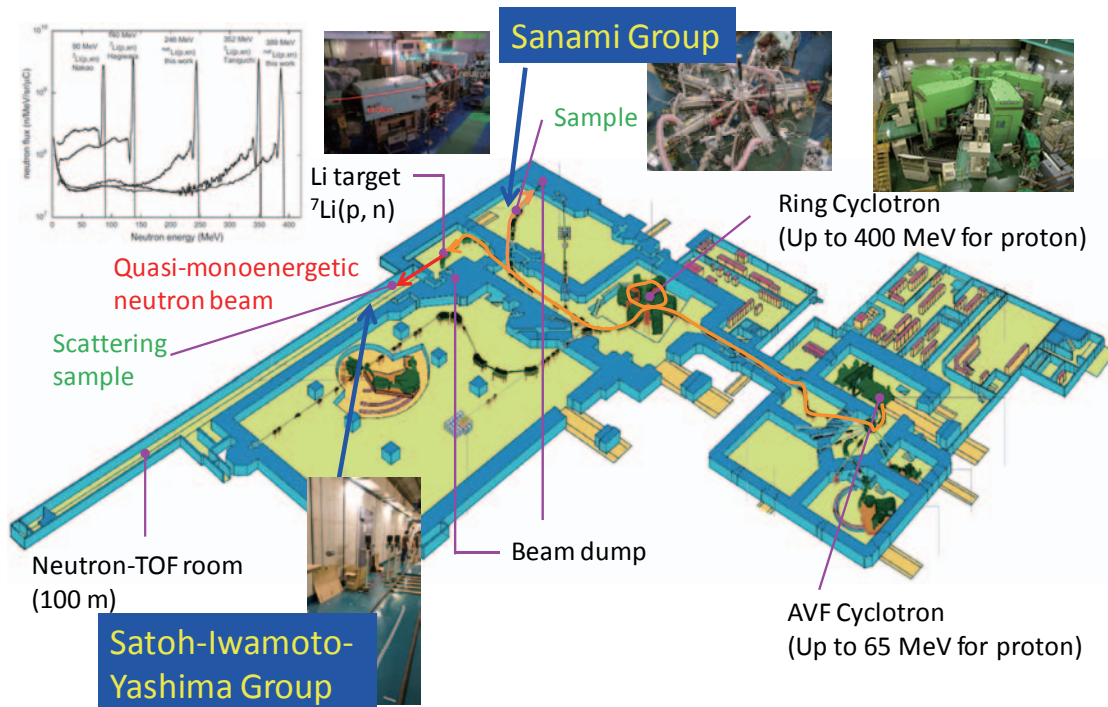


Fig.2 Nuclear data measurement activities at RCNP, Osaka University

At RCNP, high-quality quasi-monoenergetic neutron beams produced from the Li(p,n) reaction are available in the energy range of 100 to 400 MeV. Y. Iwamoto et al. [10] have measured systematically the energy spectra at 140, 200, 246, and 389 MeV. The data are useful for measurements of neutron-induced reactions as well as response measurements of various neutron detectors. Using the neutron beams, differential neutron elastic scattering cross sections for C, Al, Pb have been measured by D. Satoh et al.[11] using quasi-monoenergetic neutrons of 134, 200, and 300 MeV at the n-TOF room. The conventional TOF technique with an NE213 detector was used. The preliminary result is shown in Fig.3. The data will be useful for determination of reliable neutron optical potential. Also, H. Yashima et al.[12] made a systematic measurement of isotope production cross sections for Co and Bi using an activation method.

A research team of N. Shigyo et al. [13,14,15,16] has been intensively measuring DDXs of neutrons produced by interaction of 290 MeV/u C or O beam with C, O, and N at the HIMAC facility, NIRS. One of the measurements is compared with PHITS prediction in Fig.4. The measured data will serve as benchmark data for validation and improvement of the reaction models used in the dose estimation in heavy-ion therapy.

Two research groups in Kyushu University are actively involved in nuclear data measurements at foreign facilities within international collaboration framework. Y. Uozumi et al [19] started a systematic measurement of DDXs of 280 MeV ( $\pi^+$ ,p'x) and ( $\pi^+$ ,dx) reactions on C at PSI. Also they plan to measure DDXs of (n,dx) and (n, $\alpha$ x) reactions in the high energy region at n\_TOF facility, CERN. Y. Watanabe et al.[20,21,22] have measured DDXs of light ions (p,d,t, $^3$ He, and  $\alpha$ ) produced from C, O, and Si bombarded by 175-MeV quasi mono-energetic neutrons at the TSL neutron beam facility in Uppsala University, Sweden. The data of Si was successfully used for validation of the reaction models employed in the simulation of single event effects in microelectronic devices.

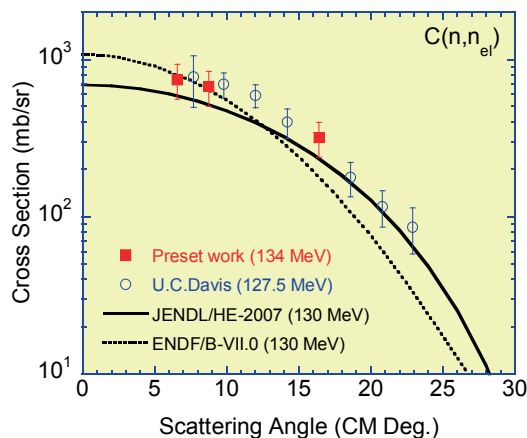


Fig.3 Neutron elastic scattering from C at 134 MeV [11,17]

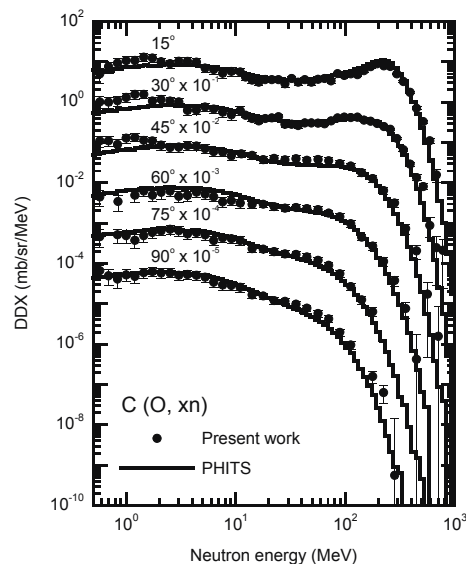


Fig.4 Double differential cross sections of C(O,xn) reaction at 290 MeV/u [13,18]

### 3. Topics on international activities: NFS and KoRIA

Two projects are overviewed as the examples of international activities related to intermediate energy nuclear data measurements: NFS (Neutrons For Science) at SPIRAL2 project[23,24], GANIL, France and KoRIA (Korea Rare Isotope Accelerator) in Korea.

The SPIRAL2 project aims at delivering high intensities of rare isotope beams by the ISOL (Isotope Separation On-Line) method, or by direct irradiation and by in-flight techniques. It is expected to contribute to fundamental research in nuclear physics as well as multidisciplinary researches in various fields of science and engineering requiring high neutron fluxes. The NFS is a neutron facility at SPIRAL2 and is composed of a neutron beam in a Time-Of-Flight area, an irradiation box (p and d induced reactions), and an irradiation cell for interdisciplinary research at SPIRAL2. The intensive neutron beams with white and quasi-monoenergetic spectra in the 1 to 40 MeV range will be produced using 40 MeV deuterons and 33 MeV protons (the maximum current is 5 mA), respectively: the (d,n) reaction with thick Be or C target for white neutrons and the Li(p,n) reaction for quasi-monoenergetic neutrons. Note that the white neutron spectrum is similar to that of IFMIF using the Li(d,n) reaction. Nuclear data measurements at NFS are now planned in the following topics: fission reactors of new generation, fusion technology, hybrid reactors (ADS), validation of nuclear model codes, nuclear medicine, development and characterization of new detectors, and irradiation of chips and electronics structures, etc. The first experiment is scheduled in the fall of 2012.

In Korea, conceptual design of the KoRIA project is in progress. The Korean nuclear data community has a plan to utilize KoRIA for the following nuclear data production [25] :

- Neutron data for fusion device or GEN-VI using fast neutrons produced by proton and deuteron beams from the cyclotron of KoRIA or using a spallation neutron source
- Nuclear data for waste transmutation using in-flight and ISOL facilities
- Nuclear data from surrogate reactions using heavy ion sources.

Their first priority is given to nuclear data measurements using fast neutrons. Fast neutron nuclear data are essential in developing fast reactors, fusion reactors and accelerator-driven systems. They plan to measure the fast neutron cross sections for important elements in the fuel and structural materials of the above-mentioned systems.

### 4. Nuclear data research strategy meeting at RCNP

We had a nuclear data research strategy meeting in June 2011 at RCNP, Osaka University, and discussed the needs of intermediate-energy nuclear data in various applications and proposals of new measurements among domestic researchers in universities, national institutes, and industries. About 40 participants took part in the meeting and total 24 presentations were included. They are categorized as follows:

- Nuclear data activities
- PHITS and nuclear reaction models
- Energy applications (ADS, Innovative reactors, and fusion device)
- Medical applications (Particle therapy and RI production)
- Radiation effects of semiconductor devices and materials
- Nuclear data measurements

In the meeting, the present status of nuclear data required in various applications (mainly, energy, medical, and material) was reviewed. We discussed what data will be crucial in these applications and the possibility of cross section measurements at RCNP as well.

Further information on this meeting is available in the report written by Y. Iwamoto who is one of the organizers [26] and in the web page (<http://www.rcnp.osaka-u.ac.jp/~nuc-data/>) prepared by the meeting organizers.

## 5. Summary and perspective

In this report, recent domestic and international activities of intermediate energy nuclear data measurements were reviewed. Also, the nuclear data research strategy meeting held at RCNP was briefly overviewed. Finally, I summarize my future perspectives on intermediate energy nuclear data measurements as follows:

- Systematic measurements will be still required towards improvement of nuclear reaction theories and models over wide ranges of target mass number and incident energy. The strategy should be discussed among our community with international collaboration, particularly with Asian countries, in consideration.
- Exclusive data , e.g., (p,pn) , may be important for more stringent comparison between theoretical model calculations, because multi-particle emission plays a crucial role in intermediate energy nuclear reactions.
- Cooperation with researchers in experimental nuclear physics will be increasingly necessary to plan and carry out new measurements at domestic accelerator facilities such as RCNP, RIBF@RIKEN, HIMAC@NIRS, etc.
- Close collaboration with application fields will be crucial to understand the impact of our measured data and improved reaction models on the applications and to find new needs of intermediate energy nuclear data.

## Acknowledgements

I would like to thank Y. Iwamoto, Y. Uozumi, N. Shigyo, T. Sanami, D. Satoh, and H. Yashima for their cooperation on preparation for my presentation and valuable discussion about intermediate energy nuclear data measurements.

## References

- [1] Y. Watanabe, et al., Journal of Korean Physics Society **59**, 1040-1045 (2011).
- [2] M.B. Chadwick, et al., Nuclear Data Sheets **107**, 2931-3117 (2006).
- [3] A.J. Koning, et al., Proc. Int. Conf. on Nuclear Data for Science and Technology (ND2007), Nice, France, April 22-27, 2007, EDP Sciences, 721-726 (2008).
- [4] A.J. Koning and D. Rochman, <http://www.talys.eu/tendl-2010/>.
- [5] FENDL-3, <http://www-nds.iaea.org/fendl3/>.
- [6] T.Sanami, et al., Proceedings of the 2010 Symposium on Nuclear Data, JAEA-Conf 2011-002, 59-64 (2011).
- [7] T.Sanami, et al., Journal of Korean Physics Society **59**, 1805-1808 (2011).
- [8] M.Hagiwara, et al., to be submitted to Journal of Nucl. Sci. Technol. (2011).
- [9] K. Niita, et al., PHITS: Particle and Heavy Ion Transport code System, Version 2.23, JAEA-Data/Code 2010-022 (2010).
- [10] Y. Iwamoto, et al., Nucl. Instr. and Methods A **629**, 43-49 (2011).
- [11] D. Satoh, et al., Radiation Measurements **45**, 1159-1162 (2011).
- [12] H. Yashima, et al., Proc. Radiochim. Acta **1**, 135-139 (2011).
- [13] D. Moriguchi, et al., JAEA-Conf 2011-002, 141 – 146 (2011).
- [14] D. Moriguchi, et al., Journal of the Korean Physical Society **59**, 1789-1792, (2011).

- [15] D. Satoh, et al., Journal of the Korean Physical Society **59**, 1741-1744, (2011).
- [16] D. Satoh, et al., Nucl. Instr. and Methods A **644**, 59-67, (2011).
- [17] D. Satoh, private communication (2011).
- [18] N. Shigyo, private communication (2011).
- [19] Y. Uozumi, private communication (2011).
- [20] M. Hayashi, et al., Proc. Int. Conf. on Nuclear Data for Science and Technology (ND2007), Nice, France, April 22-27, 2007, EDP Sciences, 1091-1094 (2008).
- [21] S. Hirayama, et al., Journal of Korean Physics Society **59**, 1447-1450 (2011).
- [22] S. Hirayama, et al., Proceedings of the 2010 Symposium on Nuclear Data, JAEA-Conf 2011-002, 125-130 (2011).
- [23] M. Lewitowicz, Acta Physica Polonica B **40**, 811-813 (2009).
- [24] SPIRAL2, <http://pro.ganil-spiral2.eu/spiral2>.
- [25] Y.O. Lee, Proceedings of the 2010 Symposium on Nuclear Data, JAEA-Conf 2011-002, 71-75 (2011).
- [26] Y. Iwamoto, Nuclear Data News **100**, 14-21 (2011) in Japanese:  
<http://wwwndc.jaea.go.jp/JNDC/ND-news/No100.html>.

## 12 Surrogate Reactions

Satoshi CHIBA

Advanced Science Research Center, Japan Atomic Energy Agency

Tokai-mura, Naka-gun, Ibaraki-ken 319-1195 Japan

e-mail: chiba.satoshi@jaea.go.jp

Status of research in the surrogate method based on heavy-ion as well as light-ion projectiles carried out at JAEA in collaboration with other organizations is described.

### 1. Introduction

Direct measurements of neutron cross sections of unstable nuclei relevant to nuclear energy and other applications normally face difficulty. Thus, a lot of important data still remain unmeasured in the minor-actinide and fission product regions. Recently, surrogate method is actively applied to measure neutron cross sections indirectly using available targets<sup>1,2)</sup>. However, physical foundation of the surrogate method is not established yet. The problem lies in the fact that the spin and parity distributions of the nuclei populated by the surrogate reactions are (very probably) different from those of the neutron-induced reactions, while the decay branching ratios are sensitive to the spin-parity values in the energy range of our interest.

In this paper, status of a JAEA-based activity on the surrogate method and its physical justification will be explained briefly.

### 2. Status of experimental apparatus

Our experimental apparatus consists of 1) a capture setup consisting of Compton-suppressed LaBr<sub>3</sub>(Ce) scintillators to measure decay gamma-rays from the populated compound nuclei, and 2) a fission setup including 4 multi-wire proportional counters (MWPCs). A photograph of them is given in Fig. 1. Both of them contain an array of silicon  $\Delta E$ -E counter to detect charged particles emitted as projectiles. We also plan to locate several neutron counters around the Fission setup to detect fission neutrons in coincidence with the fission fragments observed by the MWPCs. Unfortunately, due to an intervention by the Great Japan Earthquake, there is no new data to show here from the previous report<sup>3)</sup>.

### 3. Status of theoretical works

Theory is important to determine experimental conditions to deduce correct neutron cross sections from the results of surrogate experiments. So far, we have published 5 papers<sup>4-8)</sup>. The theory developed is as follows. Firstly, we have shown in which condition the difference of the spin and parity distributions between desired neutron-induced reactions and surrogate reactions can be compensated if we carry out

surrogate "ratio" method (SRM)<sup>4</sup>. In this paper, it was assumed that surrogate reactions carried out for 2 nascent nuclei having similar nuclear structure employed in SRM should populate similar spin-parity distributions. This assumption was verified by successive papers<sup>6,7</sup>. Ref. [6] explains our model to describe the whole process of the surrogate reactions in terms of a semi-classical model. On the contrary, ref.[7] describes our attempt to calculate the populated spin distribution by the coupled discretized-continuum channels method, a fully quantum mechanical model. Both approaches have shown that the assumption of Ref. [4], equivalence of the spin distributions in SRM, is indeed correct. Ref. [8] proposes some spin-dependent observables infer the populated spin distributions. Ref. [5] deals with a microscopic structure of oxygen isotopes which will be used in our surrogate experiments.

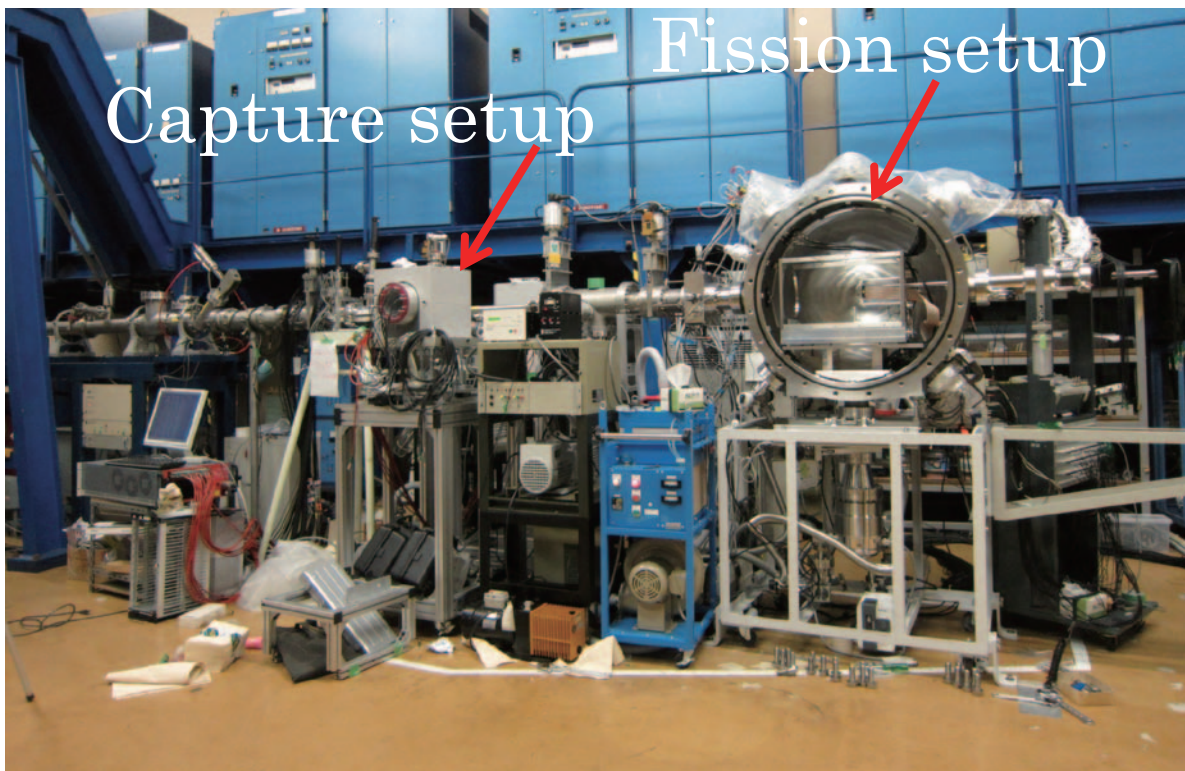


**Fig.1** Photograph of our apparatus. The Capture setup denotes a set of photon counters based on Compton-suppressed  $\text{LaBr}_3(\text{Ce})$  scintillators. The Fission setup designates a set of MWPCs. Both are equipped with  $\Delta E$ - $E$  silicon detectors.

#### 4. Summary

We have prepared experimental apparatus and theoretical backgrounds for surrogate method to determine neutron cross sections of unstable or rare nuclei. The project started under financial support from MEXT. I wish to comment that some variations of the method, such as the inverse kinematics, projectile fragmentation and even some other methods would be possible as a surrogate method and in some cases they would be very useful. We are working on the direction as well.

## Acknowledgments

The present paper contains research results obtained by my colleagues. Especially, the author is grateful to Dr. K. Ogata of Kyushu University, Drs. K. Nishio and Y. Aritomo of JAEA for a close collaboration. Present study includes the result of "Development of a Novel Technique for Measurement of Nuclear Data Influencing the Design of Advanced Fast Reactors" entrusted to Japan Atomic Energy Agency (JAEA) by the Ministry of Education, Culture, Sports, Science and Technology of Japan (MEXT).

## References

- 1) G. Kessedjian et al., *Phys. Lett. B* **692**, 297(2010).
- 2) N.D. Scielze et al., *Phys. Rev.* **C81**, 034608(2010).
- 3) S. Chiba, "Research in Surrogate Reactions at JAEA", JAEA-Conf 2011-002, pp35-40 (2011).
- 4) S. Chiba and O. Iwamoto, "Verification of the Surrogate Ratio Method", *Phys. Rev.* **C81**, 044604-1-6(2010)
- 5) Y. Utsuno and S. Chiba, "Multi-particle multi-hole states around  $^{16}\text{O}$  and correlation-energy effect on the shell gap", *Phys. Rev.* **C83**, 021301(R)-1-5(2011).
- 6) Y. Aritomo, S. Chiba and K. Nishio, "Dynamical model of surrogate reactions", *Phys. Rev.* **C84**, 024602-1-10(2011).
- 7) K. Ogata, S. Hashimoto and S. Chiba, "Three-Body Model Calculation of Spin Distribution in Two-Nucleon Transfer Reaction", *J. Nucl. Sci. Technol.* **48**, 1337-1342(2011).
- 8) S. Chiba, O. Iwamoto and Y. Aritomo, "Spin-dependent observables in surrogate reactions", *Phys. Rev.* **C84**, 054602-1-5(2011).

This is a blank page.

## 13 Approach by the $\gamma$ -ray Strength Function Method

Hiroaki UTSUNOMIYA

Department of Physics, Konan University,  
Okamoto 8-9-1, Higashinada, Kobe 658-8501, Japan  
e-mail: [hiro@konan-u.ac.jp](mailto:hiro@konan-u.ac.jp)

Stephane GORIELY

Institut d'Astronomie et d'Astrophysique, Université Libre de Bruxelles,  
Campus de la Plaine, CP-226, 1050 Brussels, Belgium  
e-mail: [sgoriely@astro.ulb.ac.be](mailto:sgoriely@astro.ulb.ac.be)

Hideo HARADA and Nobuyuki IWAMOTO

Japan Atomic Energy Agency, Tokai, Naka-gun, Ibaraki 319-1195, Japan

Radiative neutron capture cross sections for unstable nuclei are of current interest to nuclear engineering and nuclear astrophysics. An indirect method alternative to the surrogate reaction technique has been devised to determine radiative neutron capture cross sections for unstable nuclei along the valley of  $\beta$ -stability. This method called the  $\gamma$ -ray strength function ( $\gamma$ SF) method follows the Hauser-Feshbach model and is based on a statistical nuclear quantity ( $\gamma$ SF) that interconnects radiative neutron capture and photoneutron emission within the statistical model. The method was applied to several unstable nuclei such as  $^{79}\text{Se}$ ,  $^{93,95}\text{Zr}$ ,  $^{107}\text{Pd}$ , and  $^{121,123}\text{Sn}$ . This method, when combined with Coulomb dissociation experiments at the RIKEN-RIBF, offers a versatile application to unstable nuclei not only along but far from the valley of  $\beta$ -stability.

### 1. Introduction

Radiative neutron capture cross sections are basic nuclear data in both nuclear engineering and nuclear astrophysics. While  $(n,\gamma)$  cross sections for stable nuclei have been systematically measured and well documented [1], measurements for unstable

nuclei are a challenge to experimentalist. The development of high-intensity neutron beams at new generation facilities, n-TOF at CERN, DANCE at LANSCE, FRANZ in Frankfurt, and MLF at J-PARC, aims at measuring  $(n,\gamma)$  cross sections for unstable nuclei along the valley of  $\beta$ -stability. However, direct measurements are rather limited to a small number of nuclei with relatively long half-lives (less radioactivity) by the availability of irradiation samples.

The surrogate reaction technique [2] has been developed at the Lawrence Livermore National Laboratory as an indirect method of determining  $(n,\gamma)$  cross sections for unstable nuclei. This method may, however, suffer from complications associated with the reaction mechanism, for example, a mismatching in the spin distribution between the compound nuclear reaction and surrogate reaction.

We have devised an alternative method based on the  $\gamma$ -ray strength function, which interconnects radiative neutron capture and photoneutron emission within the statistical model. This method referred to as the  $\gamma$ -ray strength function method ( $\gamma$ SF method) has a potential applicability to unstable nuclei not only along the valley of  $\beta$ -stability but far from stability in conjunction with Coulomb dissociation experiments.

## 2. The $\gamma$ -ray strength function method and applications

The  $\gamma$ -ray strength function method follows the statistical model of radiative neutron capture in the formation of a compound nucleus and its decay. The method is described in detail in Ref. [3].

The Hauser-Feshbach model cross section of radiative neutron capture is formulated in terms of the  $\gamma$ -ray and neutron transmission coefficients. Since the  $\gamma$ -ray transmission coefficient is much smaller than the neutron transmission coefficient, the radiative capture cross section is sensitive to the  $\gamma$ -ray transmission coefficient, being rather insensitive to a choice of neutron optical potential for the neutron transmission coefficient.

Neutron capture states at the excitation energy  $E$  undergo  $\gamma$  transition to either experimentally-unresolved high-density states or low-lying discrete states with multipolarity  $X\lambda$  ( $X=E$  or  $M$ ,  $\lambda=1,2, \dots$ ). The transition strength is determined by the downward  $\gamma$ -ray strength function ( $\gamma$ SF) with  $X\lambda$  for a given  $\gamma$ -ray energy ( $\epsilon$ ) and the nuclear level density (NLD) at the excitation energy of  $E-\epsilon$ . Note that  $\epsilon$  is less than or equal to the neutron separation energy ( $S_n$ ).

The  $\gamma$ SF method aims at providing experimental constraints on the  $\gamma$ SF, while NLD is constrained by experimental data such as low-lying discrete states and neutron resonance spacings whenever they are available. The NLD is a source of uncertainties in the present method. The uncertainty is typically 30-40 % with the experimental constraint, whereas the uncertainty becomes large without experimental constraints.

The  $\gamma$ SF of direct relevance to radiative neutron capture is primarily low-lying E1 strength in the tail of GDR. In addition, extra strengths known as pygmy dipole and M1 resonances exist around neutron threshold typically in the region of 6 - 10 MeV. The  $\gamma$ SF has been actively investigated by photoneutron cross section measurements for stable nuclei with real photons in the energy region above  $S_n$  and by the nuclear resonance fluorescence below  $S_n$ . Coulomb dissociation/excitation can be used to investigate the  $\gamma$ SF for unstable nuclei.

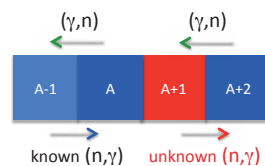


Figure 1. Simplest case for an application of the  $\gamma$ SF method

Figure 1 depicts a simplest case that shows how the  $\gamma$ SF method proceeds to determine radiative neutron capture cross section for a radioactive nucleus,  $^{A+1}\text{X}$ . The method follows three steps.

- Step 1: The first step of the  $\gamma$ SF method is to measure photoneutron cross sections for neighboring stable nuclei,  $^A\text{X}$  and  $^{A+2}\text{X}$  to determine their  $\gamma$ SFs above  $S_n$ .
- Step 2: The second step is to extrapolate the  $\gamma$ SF for  $^A\text{X}$  obtained in Step 1 to low-energy region below  $S_n$  by models and justify the extrapolation by reproducing known  $(n,\gamma)$  cross sections for  $^{A-1}\text{X}$ .
- Step 3: The third step is to extrapolate the  $\gamma$ SF for  $^{A+2}\text{X}$  with the same model justified in Step 2 and calculate  $(n,\gamma)$  cross sections for a radioactive nucleus,  $^{A+1}\text{X}$ .

The  $\gamma$ SF obtained in Step 1 is the upward  $\gamma$ -ray strength function, which is equivalent to the downward quantity according to the Brink Hypothesis [4]. It is remarked that we do not a priori rely on the Brink Hypothesis of the equality of the downward and upward

$\gamma$ SF. The finite temperature dependence can be taken into account for the downward  $\gamma$ SF separately.

In an application to the Sn case [5], we have measured photoneutron cross sections for  $^{116,117,118,119,120,122,124}\text{Sn}$  in Step 1 and used existing data of radiative neutron capture cross sections for  $^{116,117,118,119}\text{Sn}$  for justification in Step 2. Figure 2 shows photoneutron cross sections for  $^{117}\text{Sn}$ . Also shown in the figure are the standard Lorentzian model [6] and Skyrme Hartree-Fock Bogoliubov (HFB) plus quasiparticle random-phase approximation model (QRPA) [7] of the primary E1  $\gamma$ SF. While the Lorentzian model fits the data, the HFB+QRPA model strongly underestimates the data near neutron threshold. The underestimate of the HFB+QRPA model is compensated by the presence of a pygmy dipole resonance (PDR) indicated by the nuclear resonance fluorescence experiment for  $^{116,124}\text{Sn}$  [8] and  $\alpha$ - $\gamma$  coincidence measurements for  $^{124}\text{Sn}$  [9].

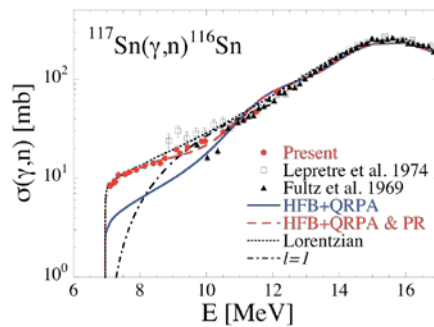


Figure 2. Photoneutron cross sections for  $^{117}\text{Sn}$ .

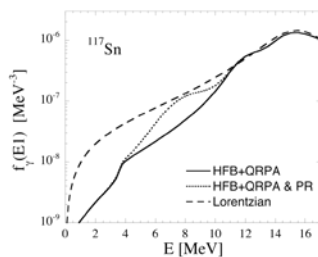


Figure 3.  $\gamma$ -ray strength function for  $^{117}\text{Sn}$ .

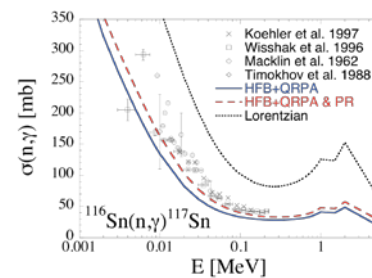


Figure 4. Radiative neutron capture cross sections for  $^{116}\text{Sn}$ .

Figure 3 shows the  $\gamma$ SF for  $^{117}\text{Sn}$  extrapolated below  $S_n$  by the Lorentzian model (dashed line) and the HFB+QRPA model (solid line) of the primary E1 strength. The PDR is parametrized in the Gaussian shape with the resonance energy  $E_o \sim 8.5$  MeV, the

width  $\Gamma \sim 2.0$  MeV, and the peak cross section  $\sigma_0 \sim 7$  mb. The total strength of the PDR amounts to  $\sim 1\%$  of the Thomas-Reiche-Kuhn (TRK) sum rule. The HFB+QRPA primary E1 strength supplemented with extra PDR strength now reproduces  $(\gamma, n)$  cross sections for  $^{117}\text{Sn}$ . Apparently the Lorentzian model has more strengths in the low-energy region than the HFB+QRPA model with PDR.

Figure 4 shows  $(n, \gamma)$  cross sections for  $^{116}\text{Sn}$  calculated by using the Lorentzian model and the HFB+QRPA model with PDR. The HFB+QRPA with PDR reasonably reproduces the experimental data for  $^{116}\text{Sn}$  [10-13], while the Lorentzian model strongly overestimates the data. The extrapolated  $\gamma$ SFs for  $^{118,119,122}\text{Sn}$  were compared with those obtained with the Oslo method [14,15]. The agreement with the Oslo data is satisfactory.

Figure 5 shows  $(n, \gamma)$  cross sections for  $^{121}\text{Sn}$  and  $^{123}\text{Sn}$  in comparison with those compiled in JENDL [16], ENDF/B [17], and JEFF libraries [18]. Note that the NLDs for both nuclei are constrained only by low-lying level schemes because of a lack of data of s-wave neutron resonance spacings. The uncertainty stemming from the unknown NLD was estimated based on the model of Ref. [19]; it is typically 30 % for  $^{121}\text{Sn}$  and as large as a factor of 2 for  $^{123}\text{Sn}$ .

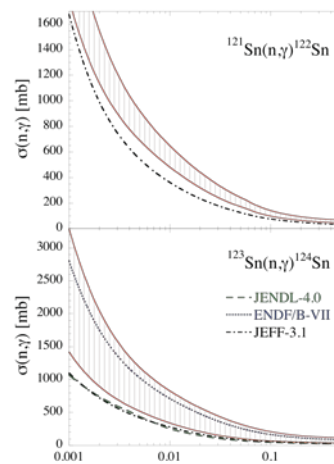


Figure 5. Radiative neutron capture cross sections for  $^{121}\text{Sn}$  and  $^{123}\text{Sn}$ .

### 3. The versatility and future perspectives

With the  $\gamma$ SF method, one can indirectly determine  $A(n, \gamma)B$  cross sections for unstable nuclei along the valley of  $\beta$ -stability. The method requires measurements of  $(\gamma, n)$  cross sections for a nucleus B that is formed by the  $(n, \gamma)$  reaction of interest. The photoneutron

cross section for stable nuclei has been measured by using real photons. However, if the nucleus B is unstable, one has to use not real but virtual photons for photodissociation, that is, Coulomb dissociation. In the astrophysical applications, there are many such cases even along the valley of  $\beta$ -stability. According to the latest compilations of the s-process nucleosynthesis [20], one can find 11 s-process branching nuclei like  $^{170}\text{Tm}$  (0.352 yr) for which radiative neutron capture forms unstable nuclei like  $^{171}\text{Tm}$  (1.921 yr). Furthermore, both A and B nuclei are obviously unstable in the r-process nucleosynthesis. For the versatile applications of the  $\gamma$ SF method, Coulomb dissociation experiments are indispensable. The research opportunity for Coulomb dissociation of unstable nuclei with the mass number 100 – 200 in the neutron channel is foreseen at RIKEN-RIBF and GSI.

This work is supported by the JSPS-FNRS bilateral program between Konan University and ULB. S.G. acknowledges support from FNRS.

## References

1. Z. Bao *et al.*, *At. Data Nucl. Data Tables*, **76**, 70 (2000).
2. C. Forssén *et al.*, *Phys. Rev.* **C75**, 055807 (2007).
3. H. Utsunomiya *et al.*, *Phys. Rev.* **C82**, 064610 (2010).
4. D.M. Brink, Ph.D thesis, Oxford University, 1955.
5. H. Utsunomiya *et al.*, *Phys. Rev.* **C85**, 055805 (2011).
6. R. Capote *et al.*, *Nuclear Data Sheets*, **110**, 3107 (2009).
7. S. Goriely, E. Khan, M. Samyn, *Nucl. Phys.* **A739**, 331 (2004).
8. K. Govaert *et al.*, *Phys. Rev.* **C57**, 2229 (1998).
9. J. Endres *et al.*, *Phys. Rev. Lett.* **105**, 212503 (2010).
10. P.E. Koehler *et al.*, in *Proceedings of the International Conference on Nuclear Data for Science and Technology, Trieste 1997*, edited by G. Reffo, A. Ventura, and G. Grandi (Italian Physical Society, Bologna, Italy, 1997), Vol.2, p.1581.
11. K. Wisshak *et al.*, *Phys. Rev.* **C54**, 1451 (1996).
12. R.L. Macklin, T. Inada, J.H. Gibbons, *Nature* **194**, 1272 (1962).
13. V.M. Timokhov *et al.*, *Yad. Fiz.* **50**, 609 (1988).
14. H.K. Toft *et al.*, *Phys. Rev.* **C81**, 064311 (2010).
15. H.K. Toft *et al.*, *Phys. Rev.* **C83**, 044320 (2011).
16. K. Shibata *et al.*, *J. Nucl. Sci. Technol.*, **48**, 1 (2011).
17. M.B. Chadwick *et al.*, *Nucl. Data Sheets*, **102**, 2931 (2006).
18. A. Santamarina, D. Bernard, Y. Rugama, JEFF Report 22 (2009).
19. A.J. Koning, S. Hilaire, S. Goriely, *Nucl. Phys.* **A810**, 13 (2008).
20. F. Käppeler *et al.*, *Rev. Mod. Phys.* **83**, 157 (2011).

## 14 Activation analyses by deuteron beam loss at 5-9MeV for the IFMIF/EVEDA accelerator

Sunao MAEBARA<sup>a</sup>, Hiroki Takahashi<sup>a</sup>, Hironao Sakaki<sup>b</sup>, Keiichi Hirabayashi<sup>c</sup>, Kosuke Hidaka<sup>c</sup>,  
Nobuhiro Shigyo<sup>c</sup>, Yukinobu Watanabe<sup>d</sup> and Kenshi Sagara<sup>e</sup>

<sup>a</sup> IFMIF Development Group, Directorates of Fusion Energy Research, JAEA

<sup>b</sup> Photo Medical Research Center, JAEA

<sup>c</sup> Department of Applied Quantum Physics and Nuclear Engineering, Kyushu University

<sup>d</sup> Department of Advanced Energy Engineering Science, Kyushu University

<sup>e</sup> Department of Physics, Kyushu University

e-mail: maebara.sunao@jaea.go.jp

The activation due to beam loss or stopping of deuterons is critical to achieve successful beam operation, and the analyses as for isotope productions in the accelerator structural materials, Cu, SS316, Fe, etc., are indispensable for safety assessment. For this purpose, deuteron induced thick target neutron yield at 5MeV and 9MeV were measured, since there was no experimental data for Cu(d,nx) reaction in the range of 5-9MeV. The experimental data are used as a source term in neutron transportation, and isotope productions are evaluated by PHITS code. It is found that the isotope productions of Co60 and Cu62 in the copper, Mn54, Mn56 and Fe59 in the iron, and Mn54, Mn56, Fe59, Co57, Co58, Co60 and Ni57 in the stainless steel are dominant for effective dose rate. It suggests that maintenance works cannot be started immediately after deuteron beam operation. Due to deuteron beam loss of 5MeV-1 $\mu$ A and 9MeV-1 $\mu$ A are also evaluated in the 1m-long transmission line model. As for Co60 in copper by the beam loss of 5MeV-1 $\mu$ A, it is found to be approximately a one-56<sup>th</sup> value of that by the 9MeV-1 $\mu$ A.

Keywords: Activation, Deuteron, Beam-loss, PHITS, IFMIF/EVEDA accelerator

### 1. Introduction

The International Fusion Materials Irradiation Facility (IFMIF) [1-3] has been conceived as an intense 14MeV neutron-source for a demonstration fusion reactor materials development next to the International Thermonuclear Experimental Reactor (ITER). The IFMIF provides an irradiation volume of 0.5 liters with a neutron flux of 10<sup>18</sup> n/m<sup>2</sup>/s or more using the neutron-generating D-Li stripping reaction. The required damage production rates for iron base specimens are 50dpa/y in an irradiation volume of 0.1 liters and 20dpa/y in volume of 0.5 liters. In the top-level requirements of IFMIF accelerator system, a 40MeV deuteron beam with a current of 250mA has to be injected into liquid lithium flow, being realized by two independent beam lines of 125mA each. Furthermore, accelerator system availability of 88% or more with CW operation mode is required.

For providing materials to make a decision of IFMIF construction, Engineering Validation and Engineering Design Activities (EVEDA) under the Broader Approach (BA) agreement have been started in June 2007. In order to validate the most critical part of such an accelerator system development, the acceleration tests up to 9MeV by employing the deuteron beam of 125 mA, are planned at the BA site in Rokkasho, Aomori, Japan [4].

For domestic safety review, activation analysis and shielding analysis including sky shine are indispensable for the accelerator prototype. The activation is caused by beam loss in beam line, and neutrons generated and transported from the 9MeV-125mA beam dump. This article in the first step for activation analyses, presents i) isotope productions by the beam loss of 9MeV-1 $\mu$ A for typical structural materials of Copper, Iron and Stainless Steel in a simple model by nucleon-meson cascade calculation, excluding time-decay of half-life time, and ii) isotope productions in a beam transmission line of 1m-long for the beam loss of 5MeV-1 $\mu$ A and a 9MeV-1 $\mu$ A, which is made of copper material, using the same calculation of i).

### 2. Isotope Production in Cu, Fe and SS316

Since there is no experimental data of Cu(d,nx) reaction in the range of 5-9 MeV, deuteron induced thick target neutron yield at 5 and 9MeV were measured in collaboration with Kyushu University using Tandem accelerator in 2009-2010[5-6]. An example of the neutron angular distributions in the angular range of 0°, 60° and 120° at a

9MeV deuteron beam is shown in Fig.1. A 0.2 mm thick copper was used as a target, and the average beam current of 10nA was injected into the target.

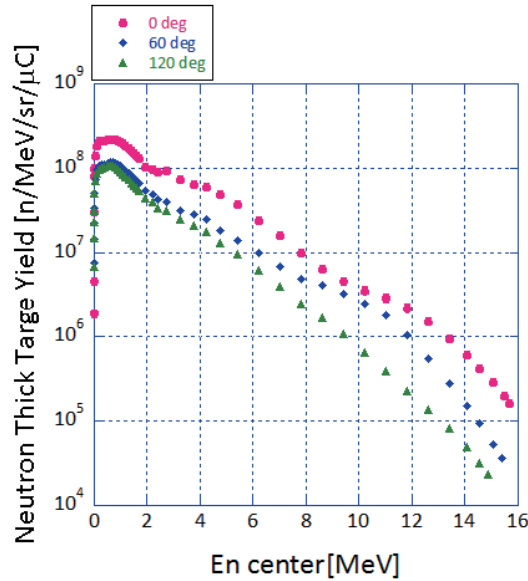


Fig.1 Neutron energy distributions produced at the angles of 0°, 60° and 90° with 9MeV deuteron beam bombarding the copper.

For the neutron distribution in all direction, the measured energy spectra at angles, 0°, 15°, 30°, 45°, 60°, 75°, 90°, 120° and 140°, are used for a source term, and this source term is set for a point source in activation analysis. A spherical shape using the diameter of 50mm and the thickness of 5mm is selected for a simple structural model. In the center, this source is set. The material components of copper, iron and stainless steel are indicated in Table 1. As for nuclear reaction with each material component, the JENDL 4.0 is used for nuclear cross-section library. Isotopic productions with 9MeV-1μA deuteron bombarding copper, iron and stainless steel are evaluated by PHITS code. The isotopic productions in materials are obtained by nucleon-meson cascade calculation.

Table 1. Material components of Cu, Fe and SUS316

Copper	Iron	Stainless steel
<sup>63</sup> Cu: 69.1%	<sup>54</sup> Fe:5.8%	<sup>56</sup> Fe:5.06e-2*
<sup>65</sup> Cu:30.9%	<sup>56</sup> Fe:91.7%	<sup>52</sup> Cr:1.35e-2*
	<sup>57</sup> Fe:2.2%	<sup>58</sup> Ni:6.83e-3*
	<sup>58</sup> Fe:0.3%	<sup>62</sup> Ni:3.45e-3*
		<sup>54</sup> Fe:3.34e-3*
		<sup>60</sup> Ni:2.55e-3*
		Mo(nat):1.24e-3* etc.,

\*Unit [10<sup>24</sup> atoms/cm<sup>3</sup>]

In the Accelerator Prototype, commissioning tests for several years are planned, and the net accelerator tests with a 9MeV-125mA CW operation are going to be within a few months. Therefore, isotope productions having the half life of shorter than 30 days, are dominant for the maintenance works and the decommissioning.

In these analysis results, it is found that the isotope productions in half-life time of shorter than 5.0x10<sup>8</sup>year; Co60, Co62, Ni63, Ni65, Cu62, Cu64 and Cu66 in the copper material, the Cr51, Mn54, Mn56, Mn57, Fe55 and Fe59 in the iron, and H3, Si31, Cr51, Cr55, Mn53, Mn54, Mn56, Mn57, Fe55, Fe59, Co57, Co58, Co60, Co61, Ni57, Ni59, Ni63, Ni65, Cu64, Cu66, Mo93, Mo99 and Mo104 in the stainless steel are produced to be in the range of 1x10<sup>3</sup>-1x10<sup>7</sup>[n/sec]; 1kBq-10MBq level.

For these isotopic productions by the 9MeV deuteron beam, it is found that Co60 and Cu62 in the copper, Mn54, Mn56 and Fe59 in the iron, and Mn54, Mn56, Fe59, Co57, Co58, Co60 and Ni57 in the stainless steel are dominant for effective dose rate, since these productions have a high specific gamma constant of higher than  $0.1[\mu\text{Svh}^{-1}\text{MBq}^{-1}\text{m}^2]$ .

Cu62, Mn56 and Ni57 have the half-life time of 9.74m, 2.579h and 35.6h, respectively. In initial stage after the beam operation during 7days, it is inferred a person cannot approach six days ( $=35.6\text{hx}4$ ) at least for maintenance works. Because Fe59 and Co58 have the half-life time of 44.5d and 70.86d, these productions are important for de-commissioning after the IFMIF/EVEDA accelerator tests. The use of stainless steel at least as accelerator structural materials has to be avoided as much as possible even if it is planning for the Accelerator Prototype.

For the IFMIF accelerator (life time of 20-30years) in future, isotope productions of Co60 (5.27y) and Zn65 (244.3d) in the copper, Mn54 (312.1d), Fe55 (2.73y), Fe59, Co57 (271.7d), Co60 in the iron, and Mn54, Fe59, Co57, Co58, Co60 in the stainless steel are key isotopes, since these isotope productions have the life time in the range of 40days-5.27years. Because copper and iron are indispensable for accelerator structural materials in drift tubes and magnetic coils, periodic exchanges or component developments including shielding are indispensable. For stainless steel material, the use of aluminum material has to be considered instead of it.

### 3. Activation in a beam transmission line

Isotope productions due to 5MeV-1 $\mu\text{A}$  and 9MeV-1 $\mu\text{A}$  are evaluated in a beam transmission line. For the beam transmission line, copper material which has the dimension of a 1m-long, a 50mm-radius and a thickness of 5mm, is assumed. A cylindrical shape using the diameter of 50mm and the thickness of 5 $\mu\text{m}$  in the 1m-long is set for a source term. Example of experimental data of Cu(d,nx) reaction at a 5MeV and 9MeV deuteron beam in the energy spectra at angles of 0° and 60° is indicated in Fig.2. In comparing with the 9MeV neutron yield, the yield at 5MeV deuteron beam falls more than 1-order or more, and it is also to be 12 MeV for the maximum neutron energy.

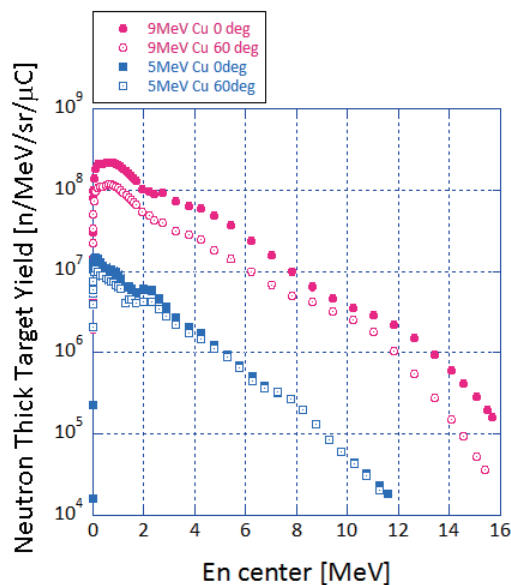


Fig. 2 Experimental data of Cu(d,nx) reaction at a 5MeV and 9MeV deuteron beam

Table 2 indicates isotope productions in the 1m-long transmission line due to the 5MeV and the 9MeV deuteron with 1 $\mu\text{A}$ , respectively. The Cu62 due to the beam loss of 5MeV-1 $\mu\text{A}$ , is lower by 4-order or more, it is not a 2-order level, than the value of 9MeV-1 $\mu\text{A}$ . This means that the Cu62 production is strongly dependent on the neutron yield profile of the 9MeV-1 $\mu\text{A}$  from 12MeV to 16MeV in Fig.2. For the isotope production in copper due to the 5MeV-1 $\mu\text{A}$ , therefore, it is indicated that main Co60 is dominant for the effective dose rate at the beam loss of 1 $\mu\text{A}$ . However, the Cu62 by the 5MeV-1 $\mu\text{A}$  may not be neglected, since a beam loss of more than a few100 $\mu\text{A}$  is considerable at beam-selectors in the post-RFQ linac. For the Co60 by the 5MeV-1 $\mu\text{A}$ , it is to be

$3.45 \times 10^3$  [n/s], and it is approximately a one-56<sup>th</sup> value of that by the 9MeV-1 $\mu$ A. For the effective dose rate due to the isotope productions only by the 9MeV-1 $\mu$ A, it can be roughly evaluated to be a few  $\mu$ Sv/hm<sup>2</sup> level by the productions in Table 2 and the specific gamma constant of 0.1 [ $\mu$ Svh<sup>-1</sup>MBq<sup>-1</sup>m<sup>2</sup>] level, but it has to be evaluated by a total integration of main isotope productions taking account of each half-life time. The detail evaluation is in progress using DCHAIN code [7] for the next step.

Table 2. Main isotope productions in a 1m-long transmission line, made of copper, due to deuteron beam loss of 5MeV-1 $\mu$ A and 9MeV-1 $\mu$ A

	Isotope production [n/s]		Half-life time
	5MeV-1 $\mu$ A	9MeV-1 $\mu$ A	
Co60	$3.45 \times 10^3$	$1.77 \times 10^5$	5.27y.
Co62	$7.85 \times 10^1$	$1.07 \times 10^4$	13.21m.
Ni63	$3.59 \times 10^5$	$8.23 \times 10^6$	101.1y.
Ni65	$5.29 \times 10^3$	$1.75 \times 10^5$	2.517h
Cu62	$2.69 \times 10^1$	$3.65 \times 10^5$	9.74m.
Cu64	$2.96 \times 10^5$	$5.46 \times 10^6$	12.7h.
Cu66	$5.66 \times 10^4$	$9.59 \times 10^5$	5.12m.

## Conclusion

For the deuteron beam loss of 9MeV-1 $\mu$ A using a simple model, it is found that Co60 and Cu62 in the copper, Mn54, Mn56 and Fe59 in the iron, and Mn54, Mn56, Fe59, Co57, Co58, Co60 and Ni57 in the stainless steel are dominant for effective dose rate. In initial stage after the beam operation during 7days, it is inferred a person cannot approach six days (=35.6hx4) at least for maintenance works, by Cu62, Mn56 and Ni57. For the de-commissioning after the accelerator tests, Fe59 and Co58 are critical issues. It suggested that the use of stainless steel at least as accelerator structural materials has to be avoided as much as possible even if it is planning for the Accelerator Prototype.

For the Co60 production by the 5MeV-1 $\mu$ A in the 1m-long transmission line model, it is found to be approximately a one-56<sup>th</sup> value of that by the 9MeV-1 $\mu$ A. For the effective dose rate due to isotope productions only by the beam loss of 9MeV-1 $\mu$ A, it is roughly evaluated to be a few  $\mu$ Sv/hm<sup>2</sup> using the specific gamma constant, but it has to be evaluated by a total integration of main isotope productions taking account of each half-life time. The detail evaluation of the total integration including time-decay is in progress using DCHAIN code.

## Acknowledgments

The authors would like to express their thanks to Drs. T. Fukahori, H. Nakashima, Y. Iwamoto and Y. Sakamoto of Nuclear Science and Engineering Directorate in JAEA, for their advice about nuclear-data and appropriate analysis models. We also would like to acknowledge Dr. K. Niita, Director of Research center of Research Organization for Information Science & Technology (RIST), for his continuous support of PHITS code.

## References

- [1] IFMIF-CDA Team (Ed.) M. Martone, IFMIF Conceptual Design Activity Final Report, ENEA Frascati Report, RT/ERG/FUS/96/17 (1996).
- [2] T. Kondo, IFMIF, its facility concept and technology, *Journal of Nuclear Materials*, 258-263, p47-55(1998).
- [3] T. F. Shannon, Conceptual design of the international fusion materials irradiation facility (IFMIF), *Journal of Nuclear Materials*, 258-263, p106-112(1998).
- [4] A. Mosnier et al., The accelerator prototype of the IFMIF/EVEDA project, Proceedings of 1<sup>st</sup> Int. Particle Accelerator Conf. (IPAC10), MOPEC056, p588-590(2010).
- [5] N. Shigyo et al., Measurement of Deuteron Induced Thick Target Neutron Yields at 9 MeV, *Journal of the Korean Physical Society*, Vol. 59, No. 2, p1725-1728(2011).
- [6] K. Hirabayashi et al., Measurement of deuteron induced thick target neutron yields at 5MeV and 9MeV, JAEA-Conf 2011-2, p113-118(2011).
- [7] T. Kai et al., DCHAIN-SP 2001: High energy particle induced radioactivity calculation code, JAERI-Data/Code 2001-016(2001).

## 15 Evaluation of energy reduction in main shielding materials for gamma-ray and neutron generated by deuteron beam at 5MeV and 9MeV

Hiroki TAKAHASHI<sup>1\*</sup>, Sunao MAEBARA<sup>2</sup>, Hironao SAKAKI<sup>3</sup>, Keiichi HIRABAYASHI<sup>4</sup>,  
Kosuke HIDAKA<sup>4</sup>, Nobuhiro SHIGYO<sup>4</sup>, Yukinobu WATANABE<sup>5</sup>, Kenshi SAGARA<sup>6</sup>

*1. Directorates of Fusion Energy Research, Japan Atomic Energy Agency (JAEA),  
Rokkasho-mura, Aomori 039-3212, Japan*

*2. Directorates of Fusion Energy Research, JAEA, Tokai-mura, Naka-gun, Ibaraki 319-1195, Japan*

*3. Photo Medical Research Center, JAEA, Kizugawa Kyoto 619-0215, Japan*

*4. Department of Applied Quantum Physics and Nuclear Engineering, Kyushu University,  
Fukuoka 819-0395, Japan*

*5. Department of Advanced Energy Engineering Science, Kyushu University, Fukuoka 816-8580, Japan*

*6. Department of Physics, Kyushu University, Fukuoka 812-8581, Japan*

\*E-mail: takahashi.hiroki@jaea.go.jp

The Engineering Validation of the IFMIF/EVEDA accelerator prototype is planning at the BA site in Rokkasho. The commissioning will be planned at the 125 mA deuteron beam of the 5 MeV for RFQ and the 9 MeV injected Beam Dump. The design of local shield for Beam Dump (BD) is now in progress.

To design the local shield for RFQ commissioning, the reduction of neutron and photon energies throughout the main shielding materials (concrete, polyethylene) is evaluated by PHITS code, using the 5 MeV and 9 MeV experimental data of neutron source spectra. In this article, the decay effect of each material and thickness of layer is presented in details.

### 1. Introduction

The IFMIF/EVEDA prototype accelerator is planned by employing the deuteron beam of 125 mA at the BA site in Rokkasho. The prototype accelerator mainly consists of an injector, a RFQ linac (0.1-5.0 MeV), a superconducting RF linac (SRF linac: 5.0-9.0 MeV) and a beam dump (BD) [1].

For radiation protection, it is important to suppress gamma-rays and neutrons which are produced by collisions of BD with deuteron beams at 5MeV and 9MeV by using main shielding materials (concrete, polyethylene, etc.).

To understand the decay effects, energy reduction for the gamma-rays and neutrons are evaluated by PHITS code. For a source term in neutron transportation, deuteron induced thick target yield of Cu(d, nx) reaction at 5 MeV and 9 MeV measured in collaboration with Kyushu University [2] is used. The experimental data which is neutron generation in case of 1  $\mu$ C irradiated to copper are used. And, the

JENDL 4.0 is used for nuclear cross-section library.

## 2. IFMIF/EVEDA Accelerator

### 2.1 Accelerator Building and Beam Dump

The IFMIF/EVEDA accelerator building in Rokkasho site has the total area of 2019.5m<sup>2</sup>, and the accelerator vault has the inside area of W: 8.0m x D: 41.5m x H: 7.0m. The vault is surrounded by concrete walls of 150 cm-thickness.

A BD is required stopping the deuteron beam with maximum power of 1.125 MW in the CW operation mode. A selection of the beam facing materials has to take into account the neutron production and the activation level as well as the thermal stresses. In the present design, a cone-shaped copper with 0.5 cm-thickness is used, and it is surrounded by the water tank of a 50 cm-radius and the iron cylinder of a 25 cm-radius. (Fig. 1)

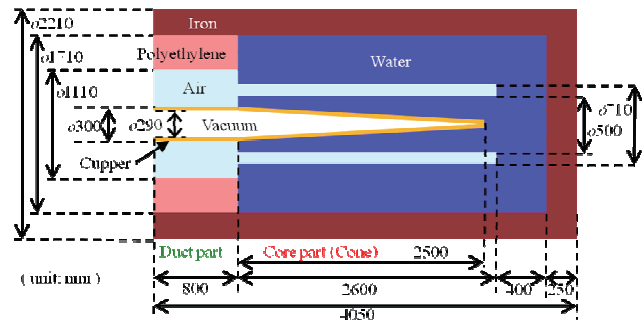


Figure 1: Design of beam dump

For a draft design of Low Power Beam Dump (LPBD) at 5 MeV beam, a cylindrical-shaped copper with a few cm-thickness is used, and it is surrounded by the local shield (Fig. 2).

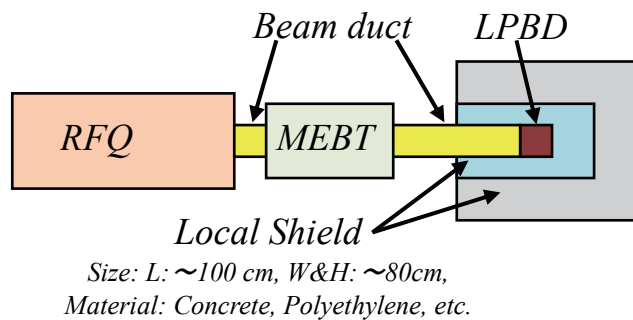


Figure 2: Draft design of local shield for 5 MeV beam

### 2.2 Local Shield

A local shield (LS) for 9 MeV beam is needed. On the other hand, a local shield for 5MeV beam is also needed for RFQ commissioning. The use of concrete and polyethylene are considered as main materials for LS. The main purpose of LS around the BD is to stop neutron back scattering from BD by injecting the 9 MeV-125 mA deuteron beam. For the RFQ commissioning, it is also important to suppress neutron and gamma-ray generated by 5 MeV deuteron beam injected to LPBD.

For the LS around the BD, the concrete of 60 cm-thickness and the polyethylene of 20 cm-thickness and an additional local shield for back scattering by beam duct are indispensable. This additional LS consists 2 concrete boards of 30 cm-thickness and a polyethylene board of 20 cm-thickness (Fig. 3). In this case, it is to be 10<sup>-1</sup> μSv/h level at the out of accelerator vault, and it is smaller than the limit value of radiation safety by two orders [3].

On the other hand, the design of this shield has just started. Then, for the efficient design by using the result of 9 MeV beam, it is important to clear difference of neutron and gamma-ray generated by deuteron

beam with the energy of between 5 MeV and 9 MeV.

### 3. Analysis

To analyze the energy reduction of gamma-rays and neutrons in main materials, the simple spherical model is used for analysis.

A point source which has the neutron angular distribution is used as shown in Fig. 4. The neutron point source is located in the center, and the total number of  $1.35 \times 10^{10}$  [n] by a 9MeV-1 $\mu$ C deuteron beam is emitted. The concrete and polyethylene are considered as the main materials for LS and each material is located around the point source. In this analysis, the thickness (it means “r” in Fig. 4.) of concrete is set every 30 cm from 30 to 300 cm and the thickness of polyethylene is set every 10 cm from 10 cm to 90 cm. As for concrete components, the 0.56Wt% for hydrogen concentration adopted in ITER design is employed, and the concrete density of 2.1g/cm<sup>3</sup> (instead of 2.3 for ITER) is used to consider a safety margin for required environmental assessment.

### 4. Calculations

Figure 5 shows neutron and photon number at the angle of 60° with 240 cm radius concrete layer (r = 240 in Fig. 4). In 9 MeV deuteron beam, the fluxes of neutron and photon for 1 MeV energy are to be  $10^4$ [n] level and  $10^2$ [n] level, respectively. In 5 MeV beam, the fluxes for same energy are each  $10^3$ [n] level and  $10^1$ [n] level, respectively. The maximum neutrons are reduced to 8 MeV and 7 MeV, respectively, but the maximum photon energies are to be same energies of 11 MeV. For the flux difference of neutron, it is found to be about  $10^1$ -order, but photon is same energy.

In Fig. 6, neutron and photon numbers at the same detector position with 20 cm radius polyethylene layer are indicated (r = 20 in Fig. 4). This shows that neutron and photon fluxes for 5 MeV case are lower than 9 MeV case about  $10^1$ -order.

Decay effects by the thickness of concrete and polyethylene are shown in Fig. 7 (1) and (2). The decay effects at the 9 MeV and 5 MeV have same characteristics. It is found that the neutron flux is

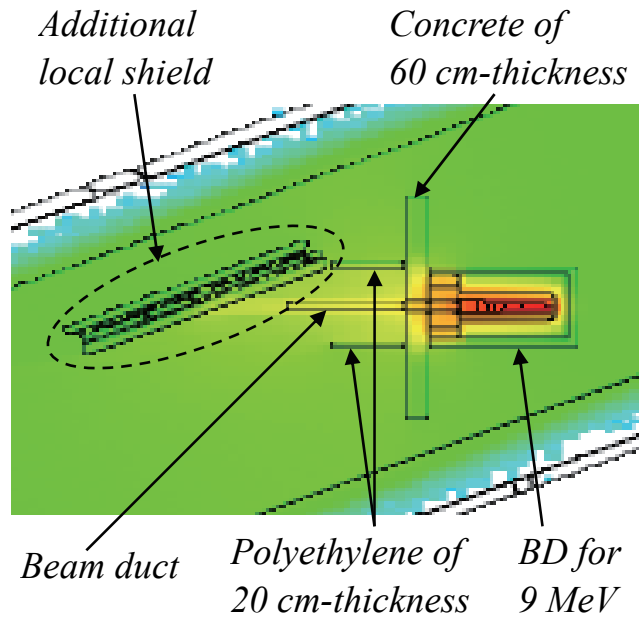
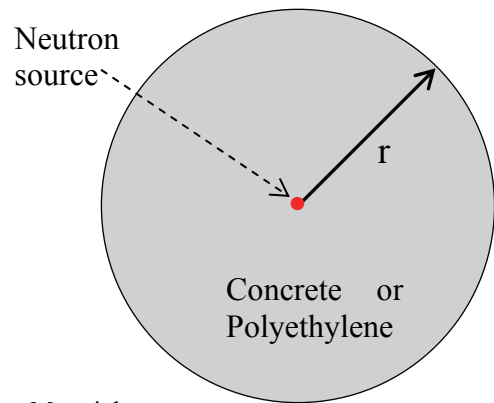


Figure 3: Design of local shield for 9 MeV beam



Material:  
 Concrete, r = 30, 60, ..., 300 cm  
 Polyethylene, r = 10, 20, ..., 90 cm

Figure 4: Spherical model

decreased by the 3-order for 120 cm-thickness of concrete shield, and by the 1-order for a 20 cm-thickness of polyethylene shield.

On the other hand, for the “Result of LS for 9MeV beam (BD)”, the concrete of 210 cm-thickness (150 cm + 60 cm) and the polyethylene of 20 cm-thickness, it is enough to shield for 9 MeV beam, because it is to be  $10^{-1}$   $\mu\text{Sv/h}$  level for the effective dose rate at the out of accelerator vault. In the 9 MeV neutron in Fig. 7 (1), the flux corresponding to concrete of 210 cm-thickness is to be found about  $1.5 \times 10^2$  [n]. To obtain the equivalent or less value by the 5 MeV neutron, it is found that a concrete of about 165 cm-thickness is needed at least for the LS for RFQ commissioning in Fig. 7 (1). Then, in this article, 180 cm-thickness is employed from values used in analysis of concrete. In the same way, it is also found that the polyethylene of about 5 cm-thickness has the enough shielding for RFQ commissioning in Fig. 7 (2) and 10 cm-thickness is employed from used values.

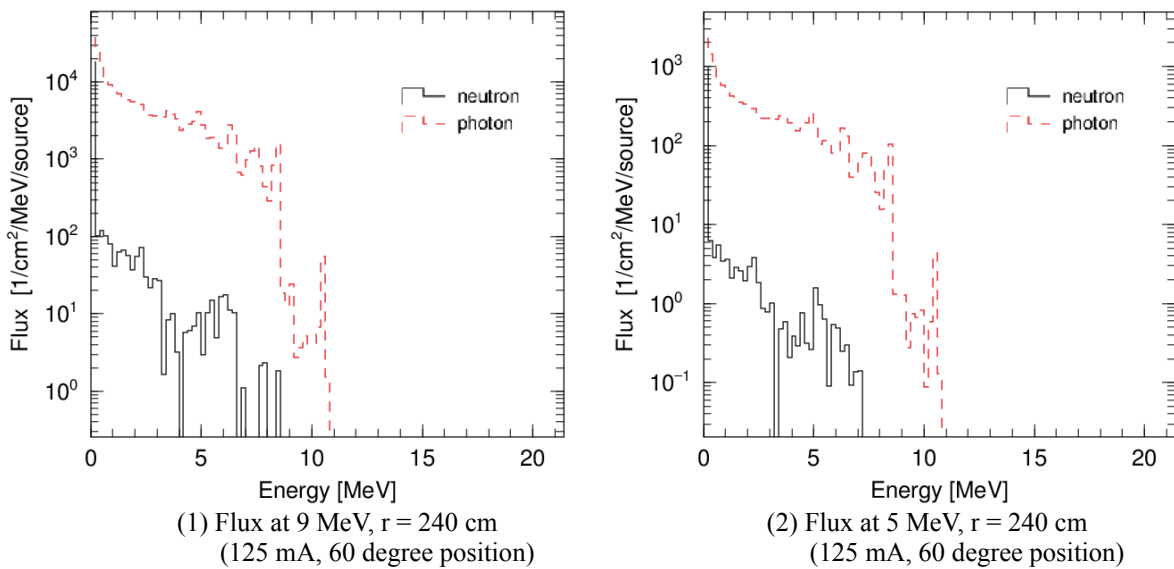


Figure 5: Difference of 9 MeV and 5 MeV (concrete)

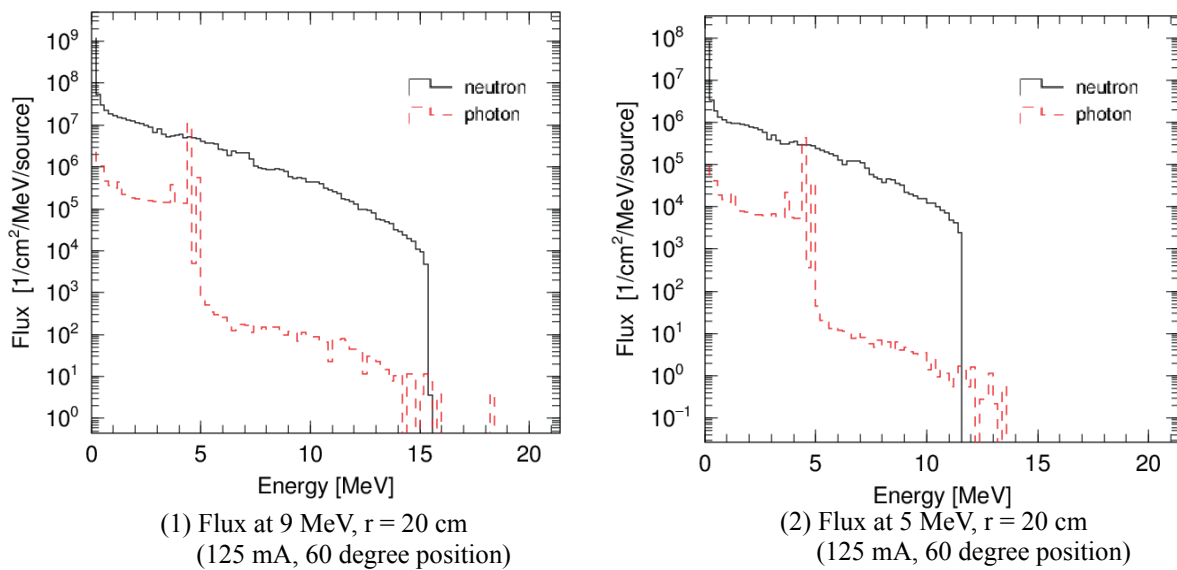


Figure 6: Difference of 9 MeV and 5 MeV (polyethylene)

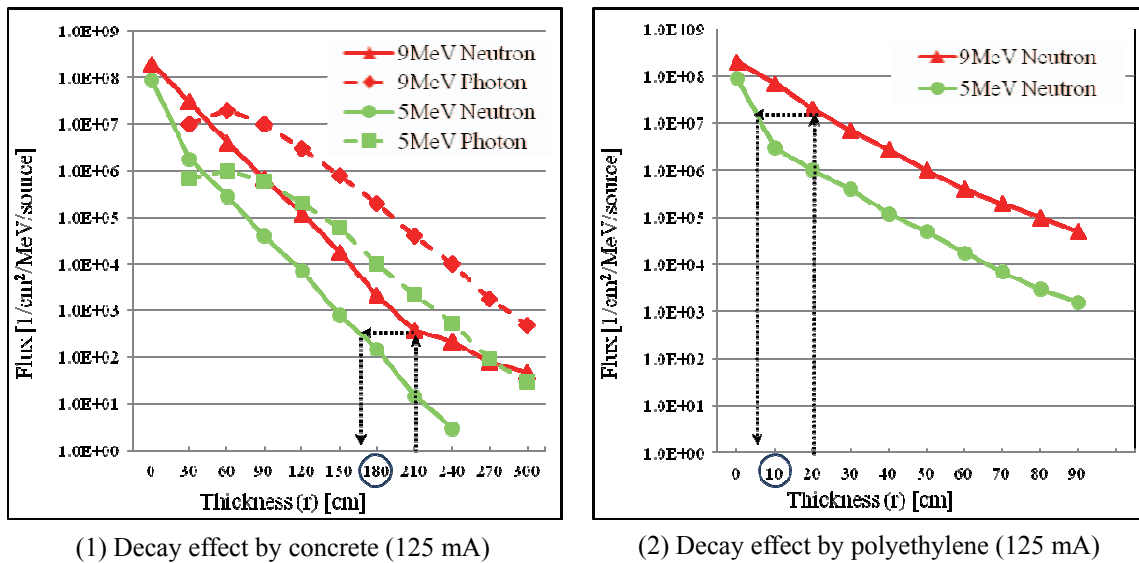


Figure 7: Decay effects at the 9 MeV and 5 MeV

**5. Conclusion**

In the simple spherical model using two kinds of materials (Concrete and Polyethylene), the decay effects of gamma-ray and neutron by the 5 MeV and 9 MeV deuteron beam are evaluated. At the results, the difference due to the deuteron beam energy are cleared, (1) neutron and photon fluxes generated by 5 MeV deuteron beam are lower than fluxes by the 9 MeV beam to be about 1-order in their materials and their decay effect with similar rate are indicated in each material, and (2) for a LS of RFQ commissioning by 5 MeV deuteron beam, it is found that a usage of the concrete of 180 cm-thickness (accelerator vault: 150 cm-thickness and local shield: 30 cm-thickness) and polyethylene of 10 cm-thickness are satisfied with the limit value of radiation safety.

References

[1] A. Mosnier et al., MOPEC056, Proceedings of 1st International Particle Accelerator Conference (2010)  
 [2] N. Shigyo et.al., Journal of the Korean Physical Society, Vol. 59, No. 2, August 2011, pp. 1725-1728.  
 [3] H. Takahashi et al., The 10th International Symposium on Fusion and Nuclear Technology, 2011, Portland, Oregon, USA, will be published.

This is a blank page.

## 16 $\gamma$ -ray strength function measurement on $^{181}\text{Ta}$ at ELBE

A. Makinaga<sup>1</sup>, R. Schwengner<sup>2</sup>, R. Massarczyk<sup>2</sup>, M. Anders<sup>2</sup>, R. Beyer<sup>2</sup>,  
R. Hannaske<sup>2</sup>, M. Kempe<sup>2</sup>, T. Kögler<sup>2</sup>, M. Röder<sup>2</sup>, K. Schmidt<sup>2</sup>, A. R. Junghans<sup>2</sup>,  
D. Bemmerer<sup>2</sup>, A. Wagner<sup>2</sup>

<sup>1</sup>Meme Media Laboratory, Hokkaido University, N10W8 Sapporo, 060-0810, Japan

<sup>2</sup>Institut für Strahlenphysik, Helmholtz Zentrum Dresden Rossendorf, 01314 Dresden, Germany

\*E-mail: [makinaga@nucl.sci.hokudai.ac.jp](mailto:makinaga@nucl.sci.hokudai.ac.jp)

$\gamma$ -ray strength function has been actively studied by using Nuclear Resonance Fluorescence (NRF) technique for applications in nuclear technologies as well as the astrophysics [1-5]. To develop the model calculation, photoabsorption cross sections were measured for  $^{181}\text{Ta}$  immediately below the neutron separation energy using bremsstrahlung beams produced at the electron accelerator ELBE of Helmholtz Zentrum Dresden-Rossendorf with an electron beam of 10.5 MeV electron kinetic energy. The measured spectra were analyzed with the statistical method of  $\gamma$ -ray cascades to obtain the intensities of the ground-state transitions and their branching ratios. We found some extra enhancement of electric dipole strength in the energy range from 4 to 8 MeV which may be related with pygmy dipole resonance. The present  $^{181}\text{Ta}(\gamma,\gamma')^{181}\text{Ta}$  cross sections are combined with  $^{181}\text{Ta}(\gamma,n)^{180}\text{Ta}$  cross sections and compared with results of the TALYS code. Such an experimental information helps to improve the  $\gamma$ -ray strength function which directly influences the abundance of p-process production in the Universe.

### 1 Introduction

The origin of the odd-odd nuclei  $^{180}\text{Ta}$  and  $^{138}\text{La}$  have been investigated over the last 40 years [6-15], because of their unsolved problems of production mechanism. In general, the typical p-process temperature is  $1.7 < T_9 [\text{K}] < 3.3$  which corresponds to the neutron separation energy. In this photon bath, nuclei are thermally populated between the ground state and excited states. In the statistical model, the calculation of the stellar reaction rate, which is the sum of the photodisintegration rates from all states, weighted by the Boltzmann factor, needs the transmission coefficients and nuclear level densities (NLD) of photons and any particles. Typically, it is known that the transmission coefficient for E1  $\gamma$ -rays from excited nuclei is directly related to the E1  $\gamma$ -ray strength function (GSF). In the case of a photo-neutron reaction with  $\gamma$ -ray energy  $E$ , the E1  $\gamma$ -ray transmission coefficient  $T(E)$  contributes to a nucleus in the ground-state. On the other hand, a nucleus in an excited state with energy  $\varepsilon$  has a transmission coefficient  $T(E-\varepsilon)$ . Thus, the E1 GSF below the neutron-separation energy  $S_n$  is effective to the photo-neutron reaction for excited nuclei. In addition, an enhancement of E1 strength below and above  $S_n$  is found in recent experiments [4, 16]. Such extra strength causes the stellar reaction rate to increase largely.

In previous work, we measured  $(\gamma,n)$  cross sections for  $^{181}\text{Ta}$  [13, 15],  $^{139}\text{La}$  [14],  $^{93}\text{Nb}$  [17] with laser Compton scattering (LCS)  $\gamma$ -ray beam at AIST (Advanced Industrial Science and Technology) and  $(\gamma,\gamma')$  cross section for  $^{139}\text{La}$  [4]. In this work, to test the model calculation, photon-scattering cross sections were measured for  $^{181}\text{Ta}$  up to the neutron separation energy with bremsstrahlung facility ELBE at Helmholtz Zentrum Dresden-Rossendorf.

In this paper, we show the experimental procedure of the photon scattering experiment below  $S_n$  at

ELBE and photo-neutron experiment above  $S_n$  at AIST.

## 2 Photon scattering experiment at ELBE

Photon scattering cross section  $\sigma_{\gamma f}(E_R)$  can be measured via  $\gamma$  ray transition from given excitation level  $E_R$  and de-excitation to a level  $E_f$  in the target. In case of non-overlapping resonances, photon scattering is described to process via a compound nucleus reaction with uncorrelated channels  $f$  characterized by the partial width  $\Gamma_f$  so photon-scattering cross section  $\sigma_{\gamma f}(E_R)$  can be described as:

$$\sigma_{\gamma f}(E_R) = \sigma_{\gamma}(E_R) \frac{\Gamma_f}{\Gamma} \quad (1)$$

Where, all partial widths contribute to the total level width  $\Gamma = \sum \Gamma_f$

$$I_S = \int_0^{\infty} \sigma_{\gamma\gamma}(E) dE = \frac{2J_R+1}{2J_0+1} \left( \frac{\pi \hbar c}{E_R} \right)^2 \Gamma_0 \frac{\Gamma_f}{\Gamma} \quad (2)$$

Where,  $I_S$  is the integral of scattering cross section for the level R and  $\Gamma_f$  is the partial width for a transition from R to a level f. Measured intensity of  $\gamma$ -rays emitted to the ground state at  $E_{\gamma} = E_R$  with an angle  $\theta$  can be expressed as:

$$I_{\gamma}(E_{\gamma}, \theta) = I_S(E_R) \Phi(E_R) \varepsilon(E_{\gamma}) N_{at} W(\theta) \frac{\Delta\Omega}{4\pi} \quad (3)$$

Where,  $N_{at}$  is number of the target nuclei per unit area,  $\varepsilon(E_{\gamma})$  is the absolute full-energy peak efficiency at  $E_{\gamma}$ ,  $\Phi(E_R)$  is the absolute photon flux at  $E_R$ ,  $W(\theta)$  is the angular correlation of this transition, and  $\Delta\Omega$  is solid angle for the detector.

If electron energy is high enough above a particular level, the experiments with bremsstrahlung lead to the possibility of the population of a level by a feeding transition from a higher-lying level. Such feeding increases the intensity of the transition to the ground state from the considered resonance R. The intensity of the transition to the ground state becomes a superposition of the rate of elastic scattering and the intensity of the transitions feeding level R. The cross-section integral  $I_{s+f}$  can be expressed as:

$$\begin{aligned} I_{s+f} &= \int_0^{\infty} \sigma_{\gamma\gamma}(E) dE + \sum_{i>R} \sigma_{\gamma i} \frac{\Gamma_0}{\Gamma} dE \\ &= \frac{2J_R+1}{2J_0+1} \left( \frac{\pi \hbar c}{E_R} \right)^2 \frac{\Gamma_0^2}{\Gamma} + \sum_{i>R} \frac{\Phi(E_i)}{\Phi(E_R)} \frac{2J_i+1}{2J_0+1} \left( \frac{\pi \hbar c}{E_i} \right)^2 \Gamma_0^i \frac{\Gamma_R^i}{\Gamma^i} \frac{\Gamma_0}{\Gamma} \end{aligned} \quad (4)$$

Where, summation over  $i>R$  is that the energy  $E_i$  of a level which feeds the considered resonance R is higher than the energy  $E_R$  of this resonance.  $\Gamma_i$ ,  $\Gamma_0$ , and  $\Gamma_R$  are the total width of the level  $E_i$ , the partial width of the transition to the ground state and the partial width of the transition to the level R, respectively.

### 2.1 Experimental setup

Photon-scattering cross section measurement on  $^{181}\text{Ta}$  was performed at the superconducting electron accelerator ELBE of the Research Center Dresden-Rossendorf. Bremsstrahlung was produced by hitting 7  $\mu$  m niobium radiator with electron beams of 10.5 MeV electron kinetic energy and average currents of 500  $\mu$  A. Produced Bremsstrahlung was collimated by an Al collimator with a length of 2.6 m and an opening angle of 5 mrad. A 10 cm length of cylindrical Al absorber was placed between the radiator and the collimator to reduce the low-energy part of the bremsstrahlung spectrum. The scattered photon was measured with four 100% HPGe detectors surrounded by BGO escape-suppression shields. Two Ge detectors were placed vertically at 90 degrees relative to the photon-beam direction. The other two Ge detector placed at 127 degrees were used to reduce angular

distributions of the  $\gamma$ -ray. To deduce the low-energy part of background photons absorbers of 8 mm Pb plus 3 mm Cu were placed in front of the detectors at 127 degrees and 13 mm Pb plus 3 mm Cu were used for the detectors at 90 degrees. Spectra of photons for  $^{181}\text{Ta}$  was measured for 110 h. A natural  $^{181}\text{Ta}$  (99.9%) target of 2.17g was irradiated with Bremsstrahlung.  $^{11}\text{B}$  (99.5%, 337.9 mg) was also used to determine the photon flux. Further experimental details can be found in the literature [2, 16].

## 2.2 Data analysis

Absolute efficiency of the HPGe detector was determined by using  $^{137}\text{Cs}$  and  $^{226}\text{Ra}$  as calibration sources and simulated with the GEANT4 code. Absolute photon flux was determined by using the known five integrated scattering cross sections of transition in  $^{11}\text{B}$  (2124 keV, 4445 keV, 5020 keV, 7286 keV, 8920 keV) and simulation code GEANT4 (Fig.1). So photon flux is formulated as:

$$\Phi_Y^{\text{cal}}(E_Y) = \frac{A_T^{\text{cal}}(\theta, t_{\text{live}})}{\varepsilon(E_Y, \theta) N_T^{\text{cal}} I_{s,t}^{\text{cal}} W(\theta) t_{\text{live}} S} \left[ \frac{1}{\text{s}\cdot\text{eV}} \right] \quad (5)$$

Where,  $A_T^{\text{cal}}(\theta, t_{\text{live}})$  is the number of photon at total peak area,  $\varepsilon(E_Y, \theta)$  is detection efficiency of HPGe detectors,  $W(\theta)$  is angular correlation,  $I_{s,t}^{\text{cal}}$  is the integrated scattering cross section for  $^{11}\text{B}$ ,  $S$  is the projected area of the target per  $\text{cm}^2$ .  $N_T^{\text{cal}}$  is the number of target nuclei which is expressed by  $N_T^{\text{cal}} = (M^{\text{cal}}/m_{\text{mol}}^{\text{cal}}) \cdot (N_A/S)$  [ $\text{cm}^{-2}$ ].

In photon-scattering experiment, experimental spectrum includes the contribution of inelastic and cascade transition. To obtain the intensities of the ground-state transitions and their branching ratio, Monte Carlo code for the simulation of  $\gamma$ -ray cascade is used. The simulation code is based on the nuclear statistical model. In the simulation, BSFG (back-shifted Fermi gas) model is used for level density. The level density parameter and the back-shift energy for  $^{181}\text{Ta}$  are taken from ref. [18]. The Wigner distribution is used for the nearest-neighbor spacing. The parameters for E1  $\gamma$ -strength function was taken from RIPL-2 [19]. The Porter-Thomas distribution is used for the fluctuations of the partial decay widths. Inelastic scattering correction scheme is described more detail in the literature [2, 20].

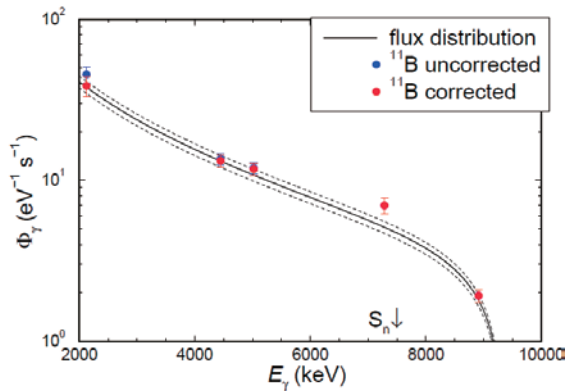


Fig.1 Photon flux and energy distribution

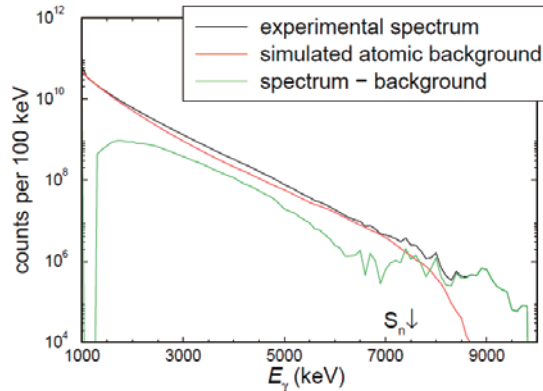


Fig.2 Scattered photon spectrum measured by HPGe detectors.

### 3 Photoneutron experiment at AIST

#### 3.1 Experimental procedure

The photoneutron cross sections were measured for  $^{139}\text{La}$  [14],  $^{181}\text{Ta}$  [13, 15],  $^{93}\text{Nb}$  [17] at Advanced Industrial Science and Technology (AIST). The detailed experimental procedure is described in [4, 13-15, 17]. Detailed description for  $^{139}\text{La}$  and  $^{181}\text{Ta}$  are shown in the literature [14, 13, 15]. We give only a brief description of  $^{93}\text{Nb}$  here.

$^{93}\text{Nb}$  metallic target, which has a thickness of 0.4 cm and surface density of  $3.43 \text{ g/cm}^2$ , was irradiated with a laser Compton scattering (LCS)  $\gamma$ -ray beam. The LCS  $\gamma$  ray beam was produced in head-on collisions of laser photons from a Nd:YLF Q-switch laser (wavelength= 527 nm) at a frequency of 1kHz with relativistic electrons in the storage ring TERAS. The electron beam energy was changed at 12 different energies from 507 MeV to 630 MeV. LCS  $\gamma$  rays were collimated 2 mm in diameter with 20 cm thick lead collimator. The energy distribution of the LCS  $\gamma$  rays was measured with a 120% high purity germanium (HPGe) detector. The energy spectrum of LCS  $\gamma$  rays were determined with the Monte Carlo code EGS4[21]. The photon beam flux was measured with NaI(Tl) detector (8-in. diameter times 12-in. length). The number of photons measured with NaI(Tl) detector was determined by  $\sum_i N_p(E_i)E_i / [\sum_i N_s(E_i)E_i / \sum_i N_s(E_i)]$ , where,  $N_p$  shows the events of the pileup spectrum and  $N_s$  means the event of the single event spectrum. The denominator represents the average pulse height of the single photon spectrum, while the numerator represents the average pulse height of the pileup spectrum  $[\sum_i N_p(E_i) / \sum_i N_p(E_i)]$  times the total number of the  $\gamma$ -ray beam pulses  $[\sum_i N_p(E_i)]$ .

Neutrons are counted with the  $4\pi$ -type neutron detector consisting of double rings of eight (Inner ring), eight (Outer ring)  $^3\text{He}$  proportional counters(EURISYS MESURES 96NH45) coaxially embedded in a polyethylene moderator at the distances of 7.0 and 10.0 cm from the beam axis, respectively. Background neutrons are identified as a time-independent component in a moderation-time distribution. The average energy of neutrons is determined by the ring ratio, which is the ratio of the number of neutrons detected by the inner ring and outer ring [Fig3:Right]. The efficiencies of the neutron detector are calibrated with a standard  $^{252}\text{Cf}$  source and calculated as a function of neutron energy with the Monte Carlo simulation code MCNP [22].

#### 3.2 Data analysis

The number of reactions induced by the photons in the target region  $x \sim x+dx$  is  $dY(x) = N_\gamma e^{-\mu x} \rho_t \sigma dx$ , where  $N_\gamma$  is the number of incident photons,  $\mu$  is the linear attenuation coefficient of photons in the target material,  $\rho_t$  is the number of target nuclei per unit volume, and  $\sigma$  is the photoreaction cross section. Integrating up to the target thickness  $t$  yields  $Y=N_\gamma \sigma N_t f$ , where  $N_t$  is the number of target nuclei per unit area, and  $f = (1-e^{-\mu t})/(\mu t)$ . So, the cross section for  $(\gamma,n)$  reaction is given by

$$\sigma(E_\gamma) = \frac{n_n}{N_t N_\gamma(E_\gamma) f \epsilon_n} \quad (6)$$

Note that  $Y=n_n/\epsilon_n$ , where  $n_n$  is the number of detected neutrons and  $\epsilon_n$  the neutron detection efficiency. Because we use the non-monochromatic  $\gamma$  rays,  $N_\gamma(E_\gamma)\sigma(E_\gamma)$  must be replaced by the integral  $\int_{S_n} n_\gamma(E)\sigma(E)dE$ , where  $n_\gamma(E)$  is the photon energy distribution, so that

$$\int_{S_n} n_\gamma(E)\sigma(E)dE = \frac{n_n}{N_t f \epsilon_n} \quad (7)$$

To determine the cross section at a given representative energy, Taylor expansion method or least

square method are used [14].

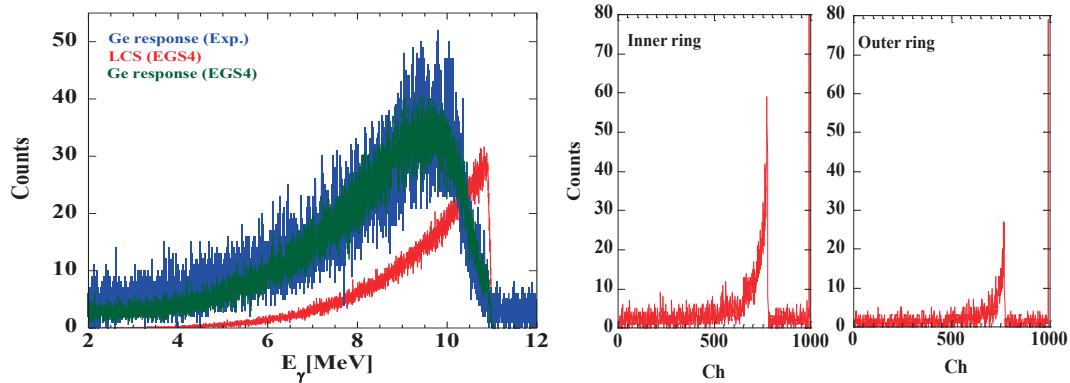


Fig.3 Left) Energy distribution of LCS  $\gamma$  rays measured with the HPGe. Blue line shows the experimental spectrum and green line shows the simulation of response function for HPGe with EGS4. Red line shows the simulated LCS  $\gamma$  ray energy distribution. Right) TAC spectrums for neutron detector system.

#### 4 Result

The left panel of Fig.4 shows the absorption cross section deduced from the present  $^{181}\text{Ta}(\gamma,\gamma')$  experiment combined with  $^{181}\text{Ta}(\gamma,n)$  data. One sees that the two data sets connect smoothly. We can also see the fine structure in the  $^{181}\text{Ta}(\gamma,\gamma')$  cross sections and can not explain this feature with TALYS code. Below the neutron separation energy for  $^{139}\text{La}$ , extra enhancement of  $(\gamma,\gamma')$  cross section which called pygmy resonance can be observed [Fig.4:Middle]. On the other hand, we analyzed the  $^{93}\text{Nb}(\gamma,n)$  cross sections and compared with the previous result [Fig.4:Right]. We note that behavior of the  $^{93}\text{Nb}(\gamma,n)$  cross sections and  $^{93}\text{Nb}(\gamma,\gamma')$  cross sections are also attracted increasing attention from astrophysics field.

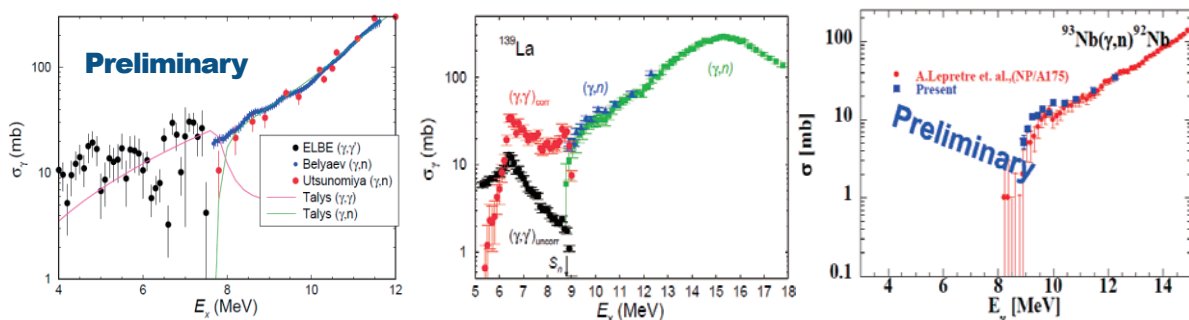


Fig.4 Left) Black circle data shows the present result of  $^{181}\text{Ta}(\gamma,\gamma')$  cross sections. Middle) Red circle data shows the result of  $^{139}\text{La}(\gamma,\gamma')$  cross sections. Right) Blue data is the present result of  $^{93}\text{Nb}(\gamma,n)$  cross sections

#### 5 Summary

Photon-scattering cross sections for  $^{181}\text{Ta}$  were measured at bremsstrahlung facility ELBE of the Research Center Dresden-Rossendorf at an electron kinetic energy of 10.5 MeV. The experimental data was analyzed with Monte Carlo simulation of  $\gamma$ -ray cascade to obtain the intensities of the ground-state transitions and their branching ratios. The comparison with photo-neutron data shows a smooth connection between the data of the two different experiments. We also show the previous result of  $^{139}\text{La}(\gamma,\gamma')$ ,  $^{93}\text{Nb}(\gamma,n)$  cross sections. In the future,

detailed theoretical evaluations are needed.

## Acknowledgments

We thank the staff of the ELBE accelerator for their cooperation during the experiments. We also thank to H. Utsunomiya for his teaching in the early stage of this research for photoneutron experiment at AIST. A. M also thanks Prof. K. Kato (Hokkaido Univ.) and Dr. N. Otsuka (IAEA) for their discussion of nuclear data. This work was supported by Helmholtz Zentrum Dresden – Rossendorf, Hokkaido University and IAEA.

## Reference

- [1] M. Arnould, S. Goriely, *Phys. Rep.* **384**, 1(2003).
- [2] G. Rusev, R. Schwengner, F. Dönau, M. Erhard, E. Grosse, A. R. Junghans, K. Kosev, K. D. Schilling, A. Wagner, F. Bečvář, and M. Krčička, *Phys. Rev. C* **77**, 064321 (2008).
- [3] R. Schwengner, R. Massarczyk, B. A. Brown, R. Beyer, F. Dönau, M. Erhard, E. Grosse, A. R. Junghans, K. Kosev, C. Nair, G. Rusev, K. D. Schilling, and A. Wagner, *Phys. Rev. C* **81**, 054315 (2010).
- [4] A. Makinaga, R. Schwengner, G. Rusev, F. Dönau, S. Frauendorf, D. Bemmerer, R. Beyer, P. Crespo, M. Erhard, A. R. Junghans, J. Klug, K. Kosev, C. Nair, K. D. Schilling, and A. Wagner, *Phys. Rev. C* **82**, 024314 (2010).
- [5] R. Hajima, T. Hayakawa, N. Kikuzawa and E. Minehara, *J. Nucl. Sci. Technol.* **45**, 441 (2008).
- [6] H. Beer and R. A. Ward, *Nature (London)* **291**, 308 (1981).
- [7] K. Yokoi and K. Takahashi, *Nature (London)* **305**, 198 (1983).
- [8] S.E. Woosley and W. M. Howard, *Astrophys. J. Suppl.* **36**, 285 (1978).
- [9] S.E. Woosley, D. H. Hartmann, R. D. Hoffmann, and W. C. Haxton, *Astrophys. J.* **356**, 272 (1990).
- [10] A. Heger, E. Kolbe, W. C. Haxton, K. Langanke, G. Martinez-Pinedo, and S. E. Woosley, *Phys. Lett. B* **606**, 258 (2005).
- [11] T. Hayakawa, T. Shizuma, T. Kajino, K. Ogawa, and H. Nakada, *Phys. Rev. C* **77**, 065802 (2008).
- [12] Myung-Ki Cheoun, Eunja Ha, T. Hayakawa, T. Kajino, and S. Chiba, *Phys. Rev. C* **82**, 035504 (2010).
- [13] H. Utsunomiya, H. Akimune, S. Goko, M. Ohta, H. Ueda, T. Yamagata, and K. Yamasaki, H. Ohgaki, H. Toyokawa, Y.-W. Lui, T. Hayakawa, T. Shizuma, E. Khan, S. Goriely, *Phys. Rev. C* **67**, 015807 (2003).
- [14] H. Utsunomiya, A. Makinaga, S. Goko, T. Kaihori, H. Akimune, T. Yamagata, M. Ohta, H. Toyokawa, S. Müller, Y.-W. Lui, and S. Goriely, *Phys. Rev. C* **74**, 025806 (2006).
- [15] S. Goko, H. Utsunomiya, S. Goriely, A. Makinaga, T. Kaihori, S. Hohara, H. Akimune, T. Yamagata, Y.-W. Lui, H. Toyokawa, A. J. Koning, and S. Hilaire, *Phys. Rev. Lett.* **96**, 192501 (2006).
- [16] R. Schwengner, G. Rusev, N. Benouaret, R. Beyer, M. Erhard, E. Grosse, A. R. Junghans, J. Klug, K. Kosev, L. Kostov, C. Nair, N. Nankov, K. D. Schilling, and A. Wagner, *Phys. Rev. C* **76**, 034321 (2007).
- [17] A. Makinaga, Master dissertation, Konan University, 2005  
<http://www.phys.konan-u.ac.jp/~makinaga/pdf/makinaga-master.pdf>
- [18] T. von Egidy and D. Bucurescu, *Phys. Rev. C* **72**, 044311 (2005).
- [19] <http://www.nds.iaea.org/RIPL2/>.
- [20] G. Rusev, PhD dissertation, Technische Universität Dresden, 2007  
(Wissenschaftlich-Technische Berichte, FZD-478, 2007); <https://www.fzd.de/publications/010008.pdf>.
- [21] W. R. Nelson, H. Hirayama, and W. O. Roger, *The EGS4 Code Systems*, SLAC-Report-265, 1985
- [22] K. Y. Hara, H. Utsunomiya, S. Goko, H. Akimune, T. Yamagata, and M. Ohta, *Phys. Rev. D* **68**, 072001 (2003).

## 17 Development of the ORIGEN2 Library for Light Water Reactors Based on JENDL-4.0

Keisuke OKUMURA, Kensuke KOJIMA and Tsutomu OKAMOTO  
Nuclear Science and Engineering Directorate, Japan Atomic Energy Agency  
Tokai-mura, Naka-gun, Ibaraki-ken 319-1195 Japan  
e-mail: okumura.keisuke@jaea.go.jp

A set of ORIGEN2 library for light water reactors was newly developed based on JENDL-4.0. High performance of the library was confirmed by comparison with assay data of LWR spent fuels.

### 1. Introduction

Accurate prediction of spent fuel composition is essential for the estimations of criticality, radioactivity, decay heat, toxicity, etc, in the facilities to treat spent fuels. In Japan, the ORIGEN2 code[1] has been widely used for the prediction of Light Water Reactor (LWR) fuel compositions. In order to improve the prediction accuracy, a set of new ORIGEN2 library (ORLIBJ40) was produced by using recent nuclear data based on JENDL-4.0[2] which was released in May 2010.

### 2. Production of ORLIBJ40

The ORIGEN2 library contains data such as energy-condensed neutron induced cross sections, fission yields, half-lives, branching ratios and photon data. These are replaced with the following data. The replacement of the branching ratios and photon data was carried out in the past work[3] by using JENDL FP Decay Data file (JENDL/FPD-2000)[4]. The data of the fission yields are updated with those in JENDL-4.0.

Since the data of half-lives are not updated in JENDL-4.0, they are employed from the recent Evaluated Nuclear Structure Data File (ENSDF revised as of Oct. 2008)[5] except for Se-79 and Sn-126. For these two nuclides, more recent values are employed from literatures; they are  $(3.77 \pm 0.19) \times 10^5$  y[6] and  $(1.98 \pm 0.06) \times 10^5$  y[7], respectively. This is because their half-lives have been unclear during the last two decades and because their values affect results of PIE analyses significantly[8].

Figure 1 shows the procedure to produce the energy-condensed (one-group) cross sections for ORLIBJ40. First, a cell burn-up calculation is carried out for the target LWR fuel model by

using a neutron transport calculation code MOSRA-SRAC[9] and its cross section library with 200-energy-group structure generated from JENDL-4.0. As a result, we obtain burn-up dependent neutron spectra and effective one-group cross sections of  $(n,\gamma)$ ,  $(n,f)$ ,  $(n,p)$ ,  $(n,\alpha)$ ,  $(n,2n)$ ,  $(n,3n)$  reactions for 28 heavy nuclides and 198 fission products, which are included in the burn-up chain model of MOSRA-SRAC (th2cm6fp198bp8T\_J40 in ChainJ40)[10]. For other nuclides which have cross section data in JENDL-4.0 or alternative JEFF-3.1/A[11], one group cross sections are produced by energy-condensations of infinite dilution cross sections from JENDL-4.0 or JEFF-3.1/A with the neutron spectrum obtained in the MOSRA-SRAC calculation at the representative burn-up (30GWd/t). As for the remaining nuclides, original library data of the ORIGEN2 code are employed.

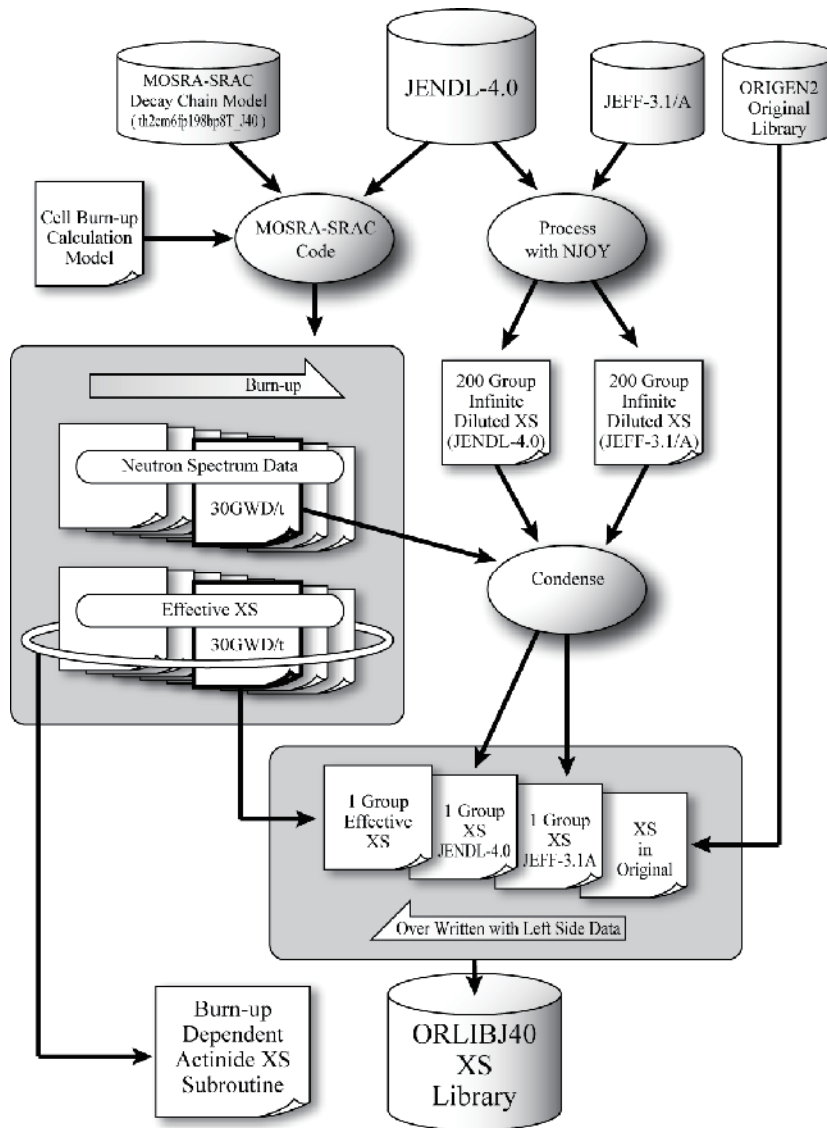


Fig.1 Procedure to produce ORLIBJ40 cross section library

Among the effective one-group cross sections, 20 sets of the cross sections for important actinides (Table 1) are treated as burn-up dependent ones, whose values are contained in the data statements in the ORIGEN2 subroutine program.

Table 1 Burn-up dependent actinides cross sections (0~80GWd/t)

$^{234}\text{U}(n,\gamma)$ , $^{235}\text{U}(n,\gamma)$ , $^{235}\text{U}(n,f)$ , $^{236}\text{U}(n,\gamma)$ , $^{238}\text{U}(n,\gamma)$
$^{237}\text{Np}(n,\gamma)$
$^{238}\text{Pu}(n,\gamma)$ , $^{238}\text{Pu}(n,f)$ , $^{239}\text{Pu}(n,\gamma)$ , $^{240}\text{Pu}(n,\gamma)$ , $^{241}\text{Pu}(n,\gamma)$ , $^{241}\text{Pu}(n,f)$ , $^{242}\text{Pu}(n,\gamma)$
$^{241}\text{Am}(n,\gamma)$ , $^{241}\text{Am}(n,\gamma)^{242m}\text{Am}$ , $^{243}\text{Am}(n,\gamma)$ , $^{243}\text{Am}(n,\gamma)^{244m}\text{Am}$ ,
$^{242}\text{Cm}(n,\gamma)$ , $^{244}\text{Cm}(n,\gamma)$

In this way, 24 sets of cross section libraries shown in Table 2 are prepared for typical  $\text{UO}_2$  or MOX fuels of PWR and BWR.

Table 2 List of cross section libraries for LWR fuels in ORLIBJ40

Library name	Fuel model	ORIGEN2 library index number (NLIB)			
		5	6	7	12
PWR34J40	PWR 17*17, U-235 Enrichment:3.4wt%	700	701	702	43
PWR41J40	PWR 17*17, U-235 Enrichment:4.1wt%	703	704	705	44
PWR47J40	PWR 17*17, U-235 Enrichment:4.7wt%	706	707	708	45
BS100J40	BWR STEP-I, 0% Void	709	710	711	46
BS140J40	BWR STEP-I, 40% Void	712	713	714	47
BS170J40	BWR STEP-I, 70% Void	715	716	717	48
BS200J40	BWR STEP-II, 0% Void	718	719	720	49
BS240J40	BWR STEP-II, 40% Void	721	722	723	50
BS270J40	BWR STEP-II, 70% Void	724	725	726	51
BS300J40	BWR STEP-III, 0% Void	727	728	729	52
BS340J40	BWR STEP-III, 40% Void	730	731	732	53
BS370J40	BWR STEP-III, 70% Void	733	734	735	54
BS2M040SJ40	BWR STEP-II, 0% Void, MOX Pu 4wt%, Standard Pu Compo.	900	901	902	83
BS2M044LJ40	BWR STEP-II, 40% Void, MOX Pu 4wt%, Low Pu Compo.	903	904	905	84
BS2M044SJ40	BWR STEP-II, 40% Void, MOX Pu 4wt%, Standard Pu Compo.	906	907	908	85
BS2M044HJ40	BWR STEP-II, 40% Void, MOX Pu 4wt%, High Pu Compo.	909	910	911	86
BS2M047SJ40	BWR STEP-II, 70% Void, MOX Pu 4wt%, Standard Pu Compo.	912	913	914	87
BS2M084SJ40	BWR STEP-II, 40% Void, MOX Pu 8wt%, Standard Pu Compo.	915	916	917	88
BS2M134SJ40	BWR STEP-II, 40% Void, MOX Pu 13wt%, Standard Pu Compo.	918	919	920	89
PWRM0113J40	PWR 17*17, MOX Pu 13wt%, Pu Vector : 1	921	922	923	90
PWRM0205J40	PWR 17*17, MOX Pu 5wt%, Pu Vector : 2	924	925	926	91
PWRM0210J40	PWR 17*17, MOX Pu 10wt%, Pu Vector : 2	927	928	929	92
PWRM0213J40	PWR 17*17, MOX Pu 13wt%, Pu Vector : 2	930	931	932	93
PWRM0305J40	PWR 17*17, MOX Pu 5wt%, Pu Vector : 3	933	934	935	94

NLIB(5): ID number of light nuclide cross-section library, NLIB(6): ID number of actinides cross-section library, NLIB(7): ID number of FP cross-section library, NLIB(12): ID number of variable actinides cross-section library

### 3. Post-Irradiation Examination Analyses with ORLIBJ40

ORLIBJ40 was first validated by application to the Post-Irradiation Examination (PIE) analysis of a sample fuel named SF97-4 discharged from a Japanese PWR (Takahama-3). The <sup>235</sup>U enrichment of SF97-4 was 4.1 wt% and it was irradiated up to 47 GWd/t. After about 4 years cooling, isotopic compositions were determined by radiochemical analysis[12].

In the ORIGEN2 calculation, a library data “PWR41J40” was employed from ORLIBJ40. For comparison with existing libraries, burn-up calculations were carried out with the original library “PWRUE” attached in the ORIGEN2 code and with a library “PWR41J33” produced from JENDL-3.3.

Figure 2 shows deviations (C/E-1) of calculated results from assay data in weight per initial metallic uranium (kg/MTU). ORLIBJ40 gives good agreements with experimental data within 10% except for Cm-246(22%). Compared with ORLIBJ33, results of minor actinides (Np, Am, Cm isotopes) and fission products (Eu, Sm isotopes) are drastically improved. This is owing to updating of capture cross sections of these nuclides[13].

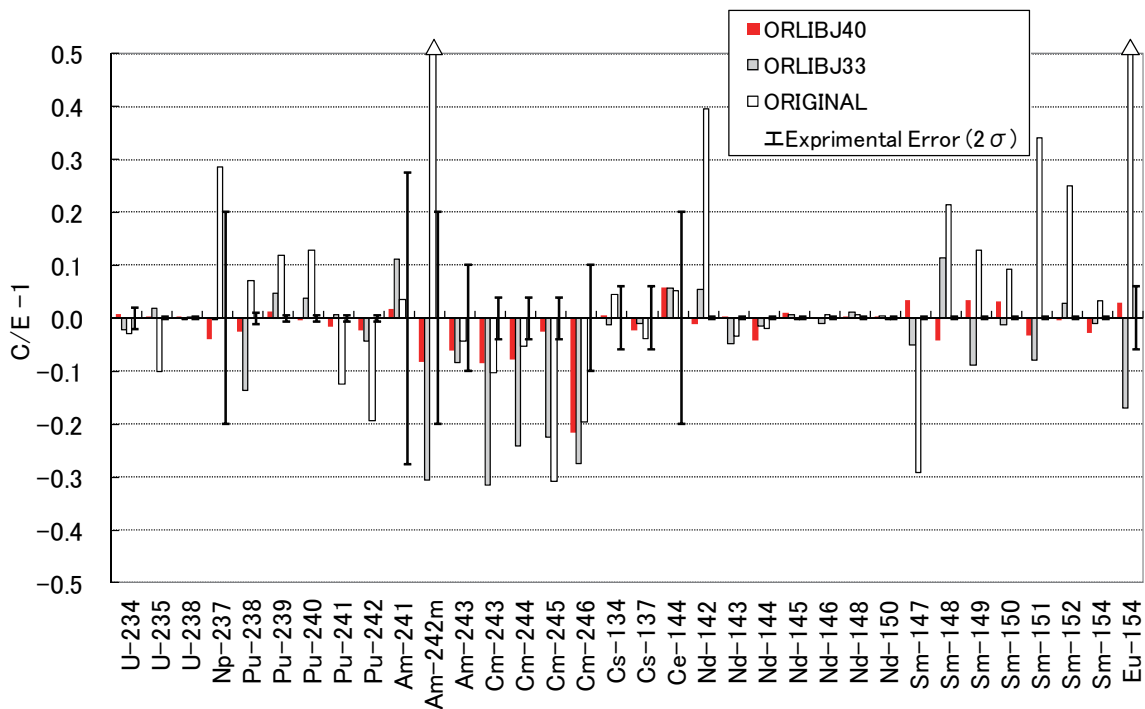


Fig. 2 Difference between ORIGEN2 calculation value (C) and Experimental value (E) for LWR spent fuel composition (kg/MTU)

Se-79 is one of the essential nuclides for long-term safety assessment of a geological disposal of the high-level radioactive vitrified wastes. To confirm applicability of ORLIBJ40 for inventory estimation of Se-79, it was applied to analyses of PIEs including assay data of

Se-79. They are PIEs for the sample fuels irradiated in Cooper (7×7 type BWR in USA) [14], Calvert-Cliffs-1 (14×14 type PWR in USA) [14], and Ohi-1(17×17 type PWR in Japan)[15].

Table 3 shows the averaged C/E for measured values in each PIE. Here, the measured value in the Ohi-1 PIE is given by weight (kg/MTU) while others are given by radioactivity (Bq/MTU). This is due to difference of analytical methods, i.e. mass spectrometry and radioactivity measurement. As shown in Table 3, ORLIBJ40 gives excellent results for all PIEs compared with the original ORIGEN2 library. The large overestimation observed in the results with the original library for Cooper and Calvert-Cliffs-1 PIEs is mainly due to too small half-life value in the original library.

Table 3 Results of PIEs for Se-79

PIE Data	Meassurment item	Number of fuel samples	Original Lib. <C/E>	ORLIBJ40 <C/E>
Cooper	Radioactivity (Bq/MTU)	6	7.5±0.3 <sup>a</sup>	0.98±0.05 <sup>a</sup>
Calvert-Cliffs-1	Radioactivity (Bq/MTU)	9	6.9±1.4 <sup>a</sup>	0.88±0.14 <sup>a</sup>
Ohi-1	Mass (kg/MTU)	1	1.49±0.12 <sup>b</sup>	1.07±0.29 <sup>b</sup>

a: standard deviation of C/E values (2σ)

b: experimental error (2σ)

#### 4. Conclusion

A set of new ORIGEN2 library (ORLIBJ40) for light water reactors was developed by using a neutron transport calculation code MOSRA-SRAC and recent nuclear data JENDL-4.0, etc. The library was validated by post-irradiation examination analyses of LWR spent fuels. As a result, compared with existing libraries, drastic improvements were confirmed on prediction accuracy of spent fuel compositions especially for minor actinides (Np, Am, Cm isotopes), fission products sensitive to cross sections (Eu, Sm isotopes), and for long-lived fission product (Se-79) which is important for long-term safety assessment of a geological disposal of high level vitrified waste.

#### References

- [1] A.G. Croff: "ORIGEN2: A Versatile Computer Code for Calculating the Nuclide Compositions and Characteristics of Nuclear Materials," Nucl. Technol. 62, 335 (1983).
- [2] K. Shibata, O. Iwamoto, T. Nakagawa, N. Iwamoto, A. Ichihara, S. Kunieda, S. Chiba, K. Furutaka, N. Otuka, T. Ohsawa, T. Murata, H. Matsunobu, A. Zukeran, S. Kamada and J. Katakura: "JENDL-4.0: A New Library for Nuclear Science and Engineering," J. Nucl. Sci. Technol. 48[1], 1 (2011).
- [3] J. Katakura and H. Yanagisawa: "Photon and Decay Data Libraries for ORIGEN2 Code Based on JENDL FP Decay Data File 2000," JAERI-Data/Code 2002-021 (2002).

- [4] J. Katakura, T. Yoshida, K. Oyamatsu and T. Tachibana: "JENDL FP Decay Data File 2000," JAERI 1343 (2001).
- [5] National Nuclear Data Center, "Evaluated Nuclear Structure Data File (ENSDF), <http://www.nndc.bnl.gov/>.
- [6] P. Bienvenu, P. Cassette, G. Andreoletti et al.: "A new determination of <sup>79</sup>Se half-life," *Appl. Radiat. Isot.*, 65, 355 (2007).
- [7] P. Bienvenu, L. Ferreux, G. Andreoletti et al.: "Determination of <sup>126</sup>Sn half-life from ICP-MS and gamma spectrometry measurements," *Radiochim. Acta*, 97, 687 (2009).
- [8] K. Okumura, S. Asai, Y. Hanzawa, et al.: "Analyses of Assay Data of LWR Spent Nuclear Fuels with a Continuous-Energy Monte Carlo Code MVP and JENDL-4.0 for Inventory Estimation of <sup>79</sup>Se, <sup>99</sup>Tc, <sup>126</sup>Sn, and <sup>135</sup>Cs," *Progr. in Nucl. Sci. and Technol.*, 2,369 (2011).
- [9] K. Okumura, T. Kugo, H. Nakano, et al.: "Development of Modular Reactor Analysis Code System MOSRA", 2008 annual meeting of the Atomic Energy Society of Japan (2009).
- [10] K. Okumura, K. Kojima and T. Okamoto: "Development of the Burn-up Chain Data ChainJ40 Based on JENDL-4.0," 2011 annual meeting of the Atomic Energy Society of Japan (2012).
- [11] J-Ch Sublet, A J Koning, R A Forrest and J Kopecky: "The JEFF-3.0/A Neutron Activation File - EAF-2003 into ENDF-6 format -," JEFDOC-982 (2003).
- [12] Y. Nakahara, K. Suyama, T. Suzaki (Eds.): "Technical Development on Burn-up Credit for Spent LWR Fuels," JAERI-Tech 2000-071 (2000).
- [13] G. Chiba, K. Okumura, K. Sugino, et al. : "JENDL-4.0 Benchmarking for Fission Reactor Applications", *J. Nucl. Sci. Technol.* 48[2], 172 (2011).
- [14] R. J. Guenther, D. E. Blahnik, T. K. Campbell et al.: "Characterization of Spent Fuel Approved Testing Material," ATM-103/-104/-105/-106, Pacific Northwest Laboratory, PNL-5109-103 (1988), -104 (1991), -105 (1991), -106 (1988).
- [15] S. Asai, Y. Hanzawa, K. Okumura, et al.: "Determination of <sup>79</sup>Se and <sup>135</sup>Cs in Spent Nuclear Fuel for Inventory Estimation of High-Level Radioactive Wastes," *J. Nucl. Sci. Technol.*, 48[5], 851 (2011).

## 18 Evaluation of fragmentation cross-section energy dependence by thick target experiments

Tatsuhiko Ogawa<sup>a</sup>, Mikhail N. Morev<sup>b</sup>, Takeshi Iimoto<sup>c</sup>, Toshiso Kosako<sup>d</sup>

<sup>a</sup> Department of Nuclear Engineering and Management, Graduate School of Engineering,  
The University of Tokyo, Hongo, Bunkyo-ku, Tokyo 113-8654, Japan, ogawa@n.t.u-tokyo.ac.jp

<sup>b</sup> Department of Fuel Cycle Facilities Safety, Laboratory of Radioactive Wastes, Science and Engineering  
Center for Nuclear and Radiation Safety, d.2/8, korp. 5, ul. Malaya Krasnoselskaya, Moscow, 107140, Russia,  
morev@secnrs.ru

<sup>c</sup> Division of Environment Health and Safety, University of Tokyo, Hongo, Bunkyo-ku, Tokyo 113-8654, Japan,  
iimoto.takeshi@mail.u-tokyo.ac.jp

<sup>d</sup> Nuclear Professional School, Graduate School of Engineering, University of Tokyo, Shirakata-shirane, Tokai,  
Ibaraki 319-1188, Japan, kosako@nuclear.jp

*An experimental method to measure fragmentation cross-sections of nucleus-nucleus reactions as functions of energy is proposed. In order to validate this method, it was applied to the fragment yields in a thick carbon target irradiated by 500 MeV/u <sup>56</sup>Fe ions calculated by FLUKA and compared with the excitation function of Fe(C,x)X cross-sections directly calculated by FLUKA. The shape of obtained excitation functions agree in a limited energy range, however, the cross-sections are underestimated or overestimated by a factor of three depending on the energy. The disagreement is attributed to fragmentation reactions of fragmented projectiles.*

### I. Introduction

Heavy ion accelerators are becoming more and more important in the field of material science, biology, etc. The importance is particularly growing in cancer therapy. Many hospital-based intermediate energy (a few hundreds of MeV/u) heavy ion accelerators are operated or constructed for application in cancer radiation therapy worldwide<sup>1</sup>. One of the key issues in the application of intermediate or high energy heavy ions is fragmentation reactions. In heavy ion radiotherapy, fragments of primary ions are transmitted beyond the range of primary ions giving undesired dose to healthy tissues. Fragments of target materials irradiated by heavy ions bring about external exposure to workers during operation and to the public after disposal. Therefore, fragmentation reaction is a key of safety in application of high energy heavy ions.

A lot of experiments to measure fragmentation cross-sections in the respect to mass yield and charge distribution have been published<sup>2-7</sup>. However, few data on energy dependence of fragmentation reaction cross-sections are available<sup>8-9</sup>. The stacked-foil method is commonly used to obtain fragmentation cross-section as a function of energy in interactions of protons with various materials<sup>10</sup>. Unfortunately, stacked-foil method cannot be directly applied to experiments with high-energy heavy ions. The major problem is activation by secondary particles (protons, neutrons, etc.), which rapidly grows with the increase of the energy and the atomic number of the projectile. Also, the range of the projectile fragments and target recoil is rather long; they travel far from the interaction point or even escape the target that additionally decreases applicability of the method.

In this study we develop a method to measure fragmentation reaction cross-sections as continuous functions of energy using a modified stacked foil method (hereafter, the method is referred to as the stacked foil deconvolution method (SFD)). In order to validate SFD, it was applied to the depth profile of the fragments inside a thick carbon target irradiated with 500MeV/u <sup>56</sup>Fe ions simulated with FLUKA<sup>11,12</sup>. Obtained excitation functions were compared with the cross-sections directly calculated by FLUKA.

### II. Method

#### II.A. Theoretical basis of SFD

In fragmentation reactions, the part of the nucleus involved to the collision with another nucleus is called a participant while the rest is called a spectator. Because the projectile spectator does not directly interact with the target nucleus, the momentum of nucleons in the projectile spectator is mostly conserved. In addition, the stopping power of the projectile fragments is also smaller than that of the projectiles. Furthermore, in a target bombarded by mono-energetic ion beam, projectile beam is quasi-mono-energetic at an arbitrary depth because of little statistical fluctuation of stopping power. Given that projectiles and fragments have no energy straggling,

fragmentation of fragmented projectiles does not form nucleus (i.e., reaction loss is considered, however, reaction ‘gain’ is not considered.) and the momentum of the nucleons in the projectile spectators is completely conserved before and after fragmentation, the energy of the projectile at fragmentation reaction  $E_r$  satisfies Eq. (1).

$$z = \int_{E_r}^{E_0} \frac{1}{s_{A_p, Z_p}(E)} dE + \int_0^{E_r} \frac{1}{s_{A_f, Z_f}(E)} dE \quad (1)$$

where  $z$  is the distance from the upstream surface of the target to the point where the fragment is stopped,  $E_0$  is the primary ion energy per nucleon,  $E_r$  is the energy of the primary ion per nucleon at the fragmentation reaction, which is assumed to be equal to the fragment energy per nucleon at interaction.  $s_{AZ}(E)$  is the stopping power of the target for nucleus with mass number  $A$ , charge  $Z$  and energy per nucleon  $E$ ,  $A_p$ ,  $Z_p$ ,  $A_f$  and  $Z_f$  are the projectile mass number, projectile charge, fragment mass number and fragment charge, respectively. Thus  $z$  is expressed as an implicit function of  $E_r$ .

By using  $z(E)$ , the fragment depth profile can be converted to a fragmentation reaction depth profile as illustrated in Fig. 1. This conversion is expressed as Eq. (2).

$$R_{A_f, Z_f}(z') \text{Exp} \left( -n \int_0^{e_r} \sigma_{l, A_f, Z_f}(E) \frac{1}{s_{A_f, Z_f}(E)} dE \right) \frac{dz'}{dE_r} dE_r = \int_{z(e_r)}^{z(e_r+dE)} N_{A_f, Z_f}(z) dz \quad (2)$$

where  $R_{A_f, Z_f}(z)$  is the number of reactions to produce a fragment with mass number  $A_f$ , charge  $Z_f$  at a depth of  $z$ ,  $n$  is the atomic density of the target material,  $\sigma_{l, A_f, Z_f}(E)$  is the total fragmentation cross-section of a nucleus with energy  $E$ , mass number  $A_f$  and charge  $Z_f$  in the target material.  $N_{A_f, Z_f}(z)$  is the number of nuclei with mass number  $A_f$  and charge  $Z_f$  stopped at a depth of  $z$ .

By definition,  $R$  is defined as Eq. (3).

$$R_{A_f, Z_f}(z') dz' = n \int_0^{E_0} \sigma_{A_f, Z_f}(E) \phi(E, z') dz' dE \quad (3)$$

where  $\sigma_{A_f, Z_f}(E)$  is the fragmentation reaction cross-section to produce fragment with mass number  $A_f$  and charge  $Z_f$  from the projectile in the target and  $\phi(E, z)$  is the fluence of the projectile with energy  $E$  at a depth of  $z$ . Once depth profile of projectile fragments  $N_{A_f, Z_f}(z)$  is given, the excitation function of fragmentation cross-section  $\sigma_{A_f, Z_f}(E)$  is obtained by solving Eq. (2) and Eq. (3).

It should be noted that SFD is not adequate for the projectile fragments lighter than or as heavy as the target nuclei because they are produced as not only as projectile fragment but also as target fragment, which is not anticipated.

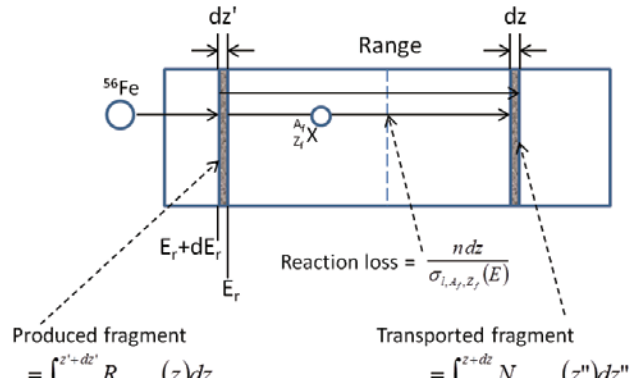


Fig.1 Schematic diagram of conversion from the obtained fragment yield to fragmentation reaction yield

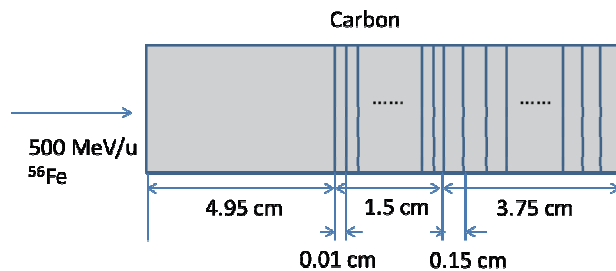


Fig.2 Schematic drawing of the simulated system. The system was built as a cylindrically symmetric system about the  $^{56}\text{Fe}$  beam axis.

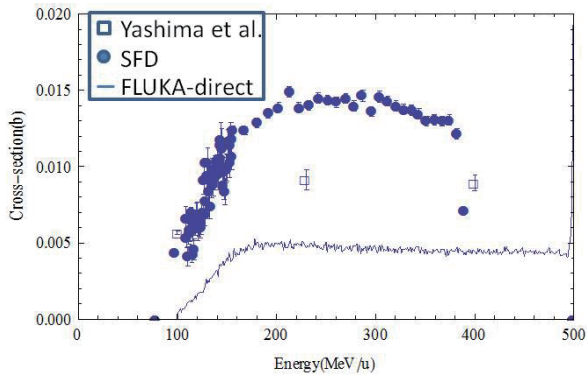


Fig.3 Excitation functions of  $^{56}\text{Fe}(\text{C},\text{x})^{24}\text{Na}$  obtained by SFD, that directly calculated by FLUKA and cross-section data provided by Yashima *et al.*..

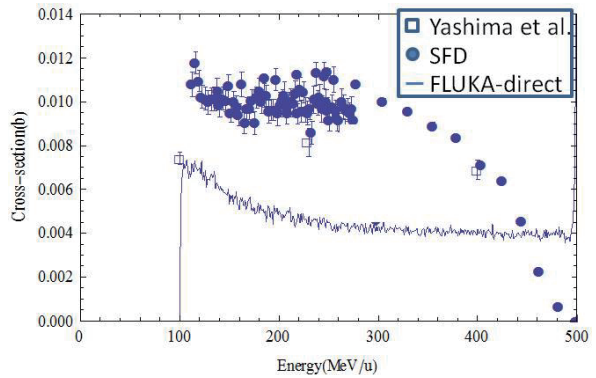


Fig.4 Excitation functions of  $^{56}\text{Fe}(\text{C},\text{x})^{42}\text{K}$  obtained by SFD, that directly calculated by FLUKA and cross-section data provided by Yashima *et al.*..

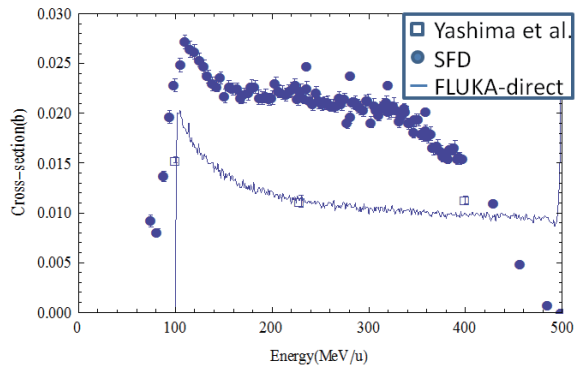


Fig.5 Excitation functions of  $^{56}\text{Fe}(\text{C},\text{x})^{46}\text{Sc}$  obtained by SFD, that directly calculated by FLUKA and cross-section data provided by Yashima *et al.*..

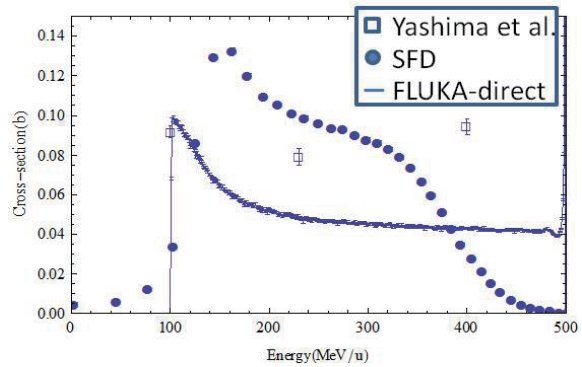


Fig.6 Excitation functions of  $^{56}\text{Fe}(\text{C},\text{x})^{54}\text{Mn}$  obtained by SFD, that directly calculated by FLUKA and cross-section data provided by Yashima *et al.*..

## II.B. Validation of SFD

In order to verify the SFD method, depth profiles of fragments were calculated by FLUKA-2008 and the SFD method was applied to the calculated fragment depth profiles. Thus obtained excitation functions of the fragmentation reactions (referred to as SFD cross-sections hereafter) were compared with the cross-sections directly calculated with the nuclear reaction models implemented in FLUKA (referred to as FLUKA-direct cross-section hereafter). The way to calculate SFD-cross-section is described below.

In the simulation, a carbon (density: 2.00 g/cm<sup>3</sup>) target with thickness of 10.5 cm assembled by 0.15 cm thick regions and 0.01 cm thick regions was irradiated by 500 MeV/u  $^{56}\text{Fe}$  ions ((the geometry is shown in Fig. 2). From 4.95 cm to 6.45 cm, fragments were scored with 0.01 cm thick regions because fragments with mass and charge close to those of projectiles are accumulated immediately beyond the range of the projectiles (4.95 cm). Nucleus-nucleus interaction model RQMD<sup>13</sup> was applied to simulate fragmentation reactions.

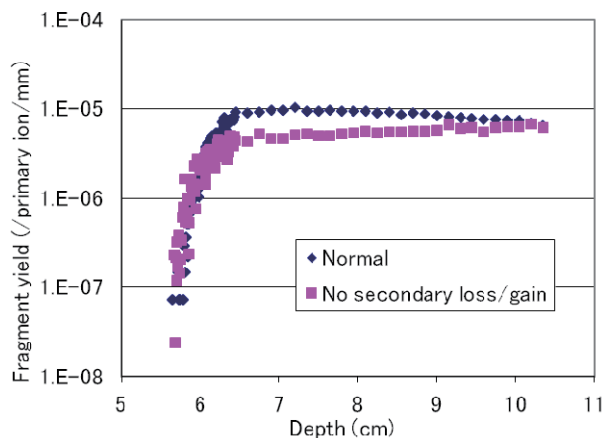


Fig.7  $^{24}\text{Na}$  depth profiles calculated by FLUKA with and without fragmentation reactions of fragmented projectile.

Because, in our scope, fragments in the target slices are measured by means of gamma spectrometry, radioactive projectile fragments in the target was calculated assuming 11.35 hours of irradiation period and 1 hour of cooling period to simulated residual nuclides in a practical experimental condition. In order to take into account the losses of the fragments by multiple fragmentation reactions, fragment density was corrected for the secondary reaction losses by substituting the total fragmentation cross-section reported by Kox *et al*<sup>14</sup> as  $\sigma_{l, Af, Zf}(E)$  in Eq. (3). The fluence and the energy of the primary ion beam were calculated by FLUKA at various depths of the target. Obtained fluences were fitted by Eq. (4) while depth dependence of projectile energy was expressed as a delta function.

$$\phi(z) = \text{Exp}(a_0 + a_1 z + a_2 z^2 + a_3 z^3) \quad (4)$$

where  $a_0, a_1, a_2, a_3$  are fitting parameters and  $z$  is the distance from the upstream surface. The stopping power and the range of the fragments in the Eq. (2) were calculated by SPAR<sup>15</sup>. For simplification, the energy straggling and the range straggling of neither primary ions nor the fragments were taken into account.

### III. Results

The examples of SFD-cross-sections and FLUKA-direct cross-sections are shown in Figs. 3-6 together with experimental data by Yashima *et al*<sup>9</sup>.

Sharp drop of excitation functions at 100 MeV/u is unimportant because it correspond to the lower energy limit of RQMD model implemented in FLUKA.

### IV. Discussion

The shape of SFD-cross-sections agrees with FLUKA-direct cross-sections below 300 MeV/u, however, all the SFD-cross-sections decrease above 300 MeV/u whereas FLUKA-direct cross-sections are energy-independent. The discrepancies may be attributed to the effects unaccounted in SFD, which are discussed below.

- 1, Fragmentation reactions of the projectile fragments
- 2, Transverse momentum of fragmented projectiles
- 3, Energy loss in fragmentation reaction
- 4, Contribution of progenitors
- 5, Fusion of projectile participants and target nuclei

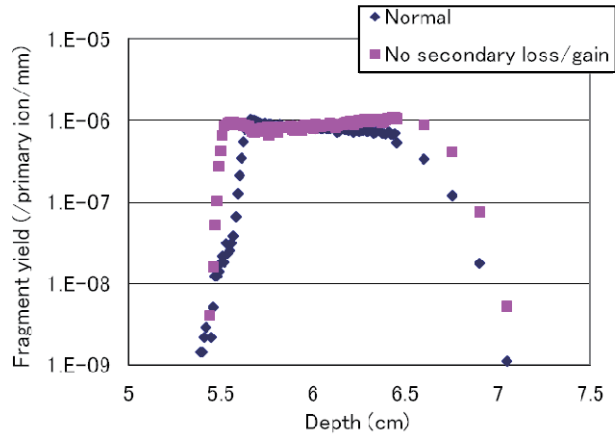


Fig.8 <sup>46</sup>Sc depth profiles calculated by FLUKA with and without fragmentation reactions of fragmented projectile.

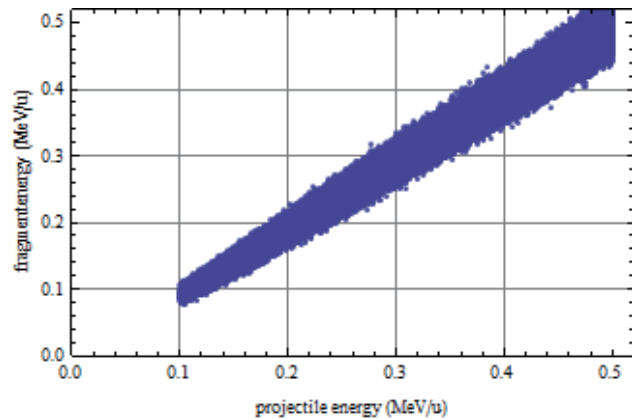


Fig.9 Two dimensional scatter plot of the fragment (<sup>24</sup>Na) energy and the projectile energy in the carbon target bombarded by 500 MeV/u <sup>56</sup>Fe ions calculated by FLUKA

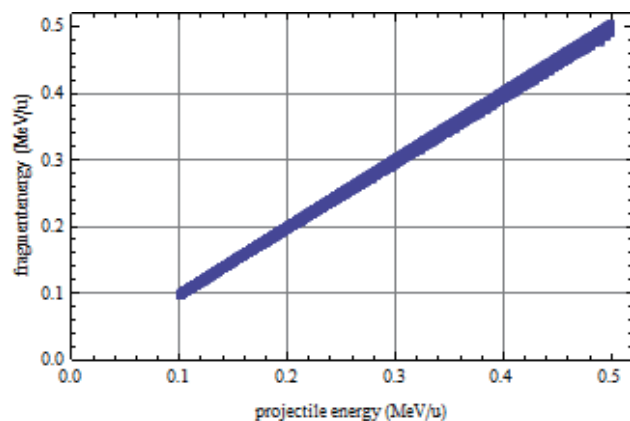


Fig.10 Two dimensional scatter plot of the fragment (<sup>54</sup>Mn) energy and the projectile energy in the carbon target bombarded by 500 MeV/u <sup>56</sup>Fe ions calculated by FLUKA

(1) Fragmentation reactions of the projectile fragments

Overestimation of light fragments (e.g.,  $^{24}\text{Na}$ ) is explained by fragmentation reactions of fragmented projectiles. The fragmented projectile may undergo another fragmentation reaction, which leads to an overestimation of light nuclei production cross-sections (e.g.,  $^{56}\text{Fe}(\text{C},\text{x})^{48}\text{V}$ ,  $^{48}\text{V}(\text{C},\text{x})^{24}\text{Na}$ ). Figure 7 shows  $^{24}\text{Na}$  depth profile and that without consideration for fragmentation reactions of the projectile fragments (i.e., produced fragments were transported to the end of their range without any reactions) calculated with FLUKA as “Normal” and “No secondary loss/gain”, respectively. The deviation between the two plots in Fig.7, in particular in the depth from 6 cm to 9 cm, indicates contribution from fragmentation of the projectile fragments.

Depth profiles of  $^{46}\text{Sc}$  calculated in the same manner as those in Fig. 7 is shown in Fig. 8. The fact is that the yields of “Normal” plot are not always lower than those of “No secondary loss/gain”. This also indicates contribution of multiple fragmentation reactions to produce  $^{46}\text{Sc}$ .

(2) Transverse momentum of fragmented projectiles

The momentum vectors of the fragments are deflected typically by a few degrees through fragmentation reactions though the fragments were assumed to travel in parallel with the beam axis in SFD. Five degrees of deflection<sup>16</sup>, for example, shorten the effective range by 0.3 %, which is too small to explain the reduction of fragments.

(3) Energy loss in fragmentation reaction

The projectile energy and fragment energy normalized by the number of the nucleons calculated with FLUKA are shown in Figs. 9 and 10. Generally, the lighter the fragment is, the greater the energy loss is. However, the energy loss is typically 10 - 20 MeV/u, which is rather small to explain the disagreement of the FLUKA-direct cross-sections and the SFD cross-sections.

(4) Contribution of progenitors

Another possible reason for the overestimation of cross-sections is the contribution from progenitor nuclides with short half-lives. For example,  $^{24}\text{Na}$  observed after 11.35 hours of irradiation and 1 hour of cooling is produced as  $^{24}\text{Na}$ ,  $^{24}\text{Ne}$ ,  $^{24}\text{F}$  or more unstable progenitor nuclides. The contribution of progenitor nuclides is estimated according to an empirical charge distribution<sup>17</sup> and listed in Table 1. This shows contribution of progenitors is not large enough to explain the deviations in Figs. 3-6.

Table.1 Contribution from progenitors (unit: %)

$^{22}\text{Na}$	$^{24}\text{Na}$	$^{42}\text{K}$	$^{44\text{m}}\text{Sc}$	$^{48}\text{Sc}$	$^{48}\text{V}$	$^{54}\text{Mn}$
16.5	19.5	< 0.1	0	< 0.1	0.8	0

(5) Fusion of projectile participants and target nuclei

It was assumed that only projectile spectators are ejected from the interaction of the target nucleus and the incident ion, however, target nuclei may fuse projectile participant (hereafter, fusion fragment) and move into the depth of the target. Given no nucleon emission backwards and no momentum distribution among nucleons inside the projectile, the maximum energy and range of the fusion fragments are calculated as Table 2.

Table 2 Maximum energy and range of fusion fragments and the primary ions

Nuclide	$^{22}\text{Na}$	$^{24}\text{Na}$	$^{42}\text{K}$	$^{43}\text{K}$	$^{44}\text{Sc}$	$^{46}\text{Sc}$	$^{47}\text{Sc}$	$^{48}\text{Sc}$	$^{48}\text{Cr}$	$^{54}\text{Mn}$	$^{56}\text{Fe}$
Energy (MeV/u)	227.2	250	357.1	360.4	363.6	369.5	372.3	375	375	388.8	500
Range (cm)	3.283	4.207	4.463	4.637	3.944	4.231	4.376	4.520	3.467	3.813	5.435

This shows fusion fragments do not go beyond the range of primary ions thereby fusion fragments are disregarded in SFD.

## V. CONCLUSIONS

An experimental technique, SFD, to measure excitation functions of nucleus-nucleus fragmentation reaction is proposed and validated against calculated results of FLUKA code. As a case study, bombardment of carbon target with 500 MeV/u  $^{56}\text{Fe}$  ions was simulated by FLUKA and excitation functions were obtained by applying SFD to the calculated residual nuclides distribution. SFD method is useful to determine the shape of

fragmentation cross-sections in limited energy range, however, SFD overestimates cross-section in most of energy range by a factor of three at maximum.

The overestimation is attributed to contribution of fragmentation reactions of fragmented projectiles. Essential improvement is necessary to measure excitation functions by this method.

## REFERENCES

1. A. Kitagawa, *et al.*, "Review on heavy ion radiotherapy facilities and related ion sources (invited)", *Rev. Sci. Instr.* **81**, 02B909, (2010).
2. G. D. Westfall, *et al.*, "Fragmentation of relativistic  $^{56}\text{Fe}$ ", *Phys. Rev. C*, **19**, 1309-1323 (1979).
3. N. T. Porile, *et al.*, "Nuclear reactions of silver with 25.2 GeV  $^{12}\text{C}$  ions and 300 GeV protons", *Phys. Rev. C*, **19**, 2288-2304 (1979).
4. J. R. Cummings, *et al.*, "Determination of the cross sections for the production of fragments from relativistic nucleus-nucleus interactions. I. Measurements", *Phys. Rev. C*, **42** 2508-2529, (1990).
5. J. Benlliure, *et al.*, "Production of medium-weight isotopes by fragmentation in 750 A MeV  $^{238}\text{U}$  on  $^{208}\text{Pb}$  collisions", *Euro. Phys. J. A*, **2** 193-198, (1998).
6. S. Cecchini, *et al.*, "Fragmentation cross sections of 158 A GeV Pb ions in various targets measured with CR-39 nuclear track detectors", *Nucl. Phys. A*, **707**, 513-524, (2002).
7. C. Scheidenberger, *et al.*, "Charge-changing interactions of ultrarelativistic Pb nuclei", *Phys. Rev. C*, **70**, 014902 (2004).
8. J. R. Cummings, *et al.*, "Determination of the cross-sections for the production of fragments from relativistic nucleus-nucleus interactions. II. Parametric fits", *Phys. Rev. C*, **42**, 6, 2530-2545 (1990).
9. H. Yashima, *et al.*, "Projectile dependence of radioactive spallation products induced in copper by high-energy heavy ions", *Phys. Rev. C*, **66** 044607, (2002).
10. R. Michel, *et al.*, "Cross sections for the production of residual nuclides by low- and medium-energy protons from the target elements C, N, O, Mg, Al, Si, Ca, Ti, V, Mn, Fe, Co, Ni, Cu, Sr, Y, Zr, Nb, Ba and Au", *Nucl. Instr. Meth. B*, **129**, 2, 153-193, (1997).
11. A. Ferrari, *et al.*, "FLUKA: a multi-particle transport code", CERN 2005-10, INFN TC 05/11, SLAC-R-773 (2005).
12. G. Battistoni, *et al.*, "The FLUKA code: Description and benchmarking", Proceedings of the Hadronic Shower Simulation Workshop 2006, 31-49, (2007).
13. V. Andersen, *et al.* "The FLUKA code for space applications: recent developments", *Advances in Space Research*, **34** 1302 (2004).
14. S. Kox, *et al.*, "Trends of total reaction cross sections for heavy ion collisions in the intermediate energy range", *Phys. Rev. C*, **35**, 5, 1678-1691, (1987)
15. T.W. Armstrong and K.C. Chandler, "Stopping powers and ranges for muons, charged pions, protons, and heavy ions", *Nuclear Instruments and Methods*, **113**, 2, 313-314, (1973)
16. J. Hufner, "Heavy fragments produced in proton-nucleus and nucleus-nucleus collisions at relativistic energies", *Phys. Rep.*, **125**, 4, 129-185 (1985)
17. H. Yashima *et al.*, "Cross sections for the production of residual nuclides by high-energy heavy ions", *Nucl. Instr. Meth. B*, **226**, 243-263 (2004)

## 19 Microscopic optical potentials for nucleon, deuteron, $^3\text{He}$ and $^4\text{He}$

Guo Hairui<sup>1,2</sup>, Han Yinlu<sup>2</sup>, Shen Qingbiao<sup>2</sup>, Yukinobu Watanabe<sup>1</sup>

<sup>1</sup>Department of Advanced Energy Engineering Science,  
Kyushu University, Kasuga, Fukuoka 816-8580, Japan

<sup>2</sup>China Institute of Atomic Energy, P. O. Box 275(41), Beijing 102413, China

Email: ghr@aees.kyushu-u.ac.jp

The microscopic optical potentials for nucleon, deuteron,  $^3\text{He}$  and  $^4\text{He}$  are obtained by Green function method. They are analyzed and used to calculate the total (for neutron), reaction cross sections and elastic scattering angular distributions for the target nuclei in mass range of  $6 \leq A \leq 209$  with incident energies per nucleon below 100 MeV. The theoretical results are compared with the experimental data. Good agreement is generally obtained.

### 1. Introduction

Optical model is one of the most fundamental theoretical models in nuclear reaction theory. It is applied widely in the nuclear reaction calculations. The phenomenological optical model potential includes some adjustable parameters, and is fixed by adjusting its parameters to fit large numbers of experimental data, while the microscopic optical potential (MOP) is generated theoretically based on the nucleon-nucleon interaction, which has no free parameters and does not depend on experimental data. The MOP has significant value in the study of the colliding systems for which the elastic scattering measurement is absent or difficult, such as in the case of neutron-rich or proton-rich  $\beta$ -unstable nuclei. Therefore, It can play an important role in many fields like nuclear data calculation, nuclear astrophysics, radioactive nuclear beam physics, and so on. In this work, the MOPs for nucleon [1], deuteron [2],  $^3\text{He}$  [3] and  $^4\text{He}$  [4] are systemically obtained.

### 2. Theoretical model and calculated results

From the view of the many-body theory, the nucleon optical potential is identified with the mass operator of the one-particle Green function. Thus, the mass operator can be used to calculate MOP. This approach, using the mass operator to get MOP, is called Green function method. Based on Skyrme nucleon-nucleon interaction, the first- and second-order mass operators of the one-particle Green function are obtained by expanding the Green function, performing Fourier transformation and finally comparing with Dyson equation under nuclear matter approximation. The real part of the nucleon MOP is denoted by the first-order mass operator of the one-particle Green function, and the imaginary part of the MOP is obtained from the imaginary part of the second-order mass operator of the Green function. Then the nucleon MOP for finite nuclei is obtained by local density approximation. The obtained microscopic optical potential shows that the potential depth, shape, relative contributions of

the surface and volume absorption parts, as well as the energy dependences are in reasonable agreement with the phenomenological optical potentials. The calculated results, such as the total and nonelastic cross sections and elastic scattering angular distributions can reproduce the experimental data [1]. The calculated neutron and proton elastic scattering angular distributions for  $^{56}\text{Fe}$  at incident neutron energies from 9.41 to 75.0 MeV and incident proton energies from 4.08 to 65.0 MeV are compared with experimental data [5–16] in Figs. 1 and 2, respectively. The theoretically calculated results are in reasonable agreement with the experimental data.

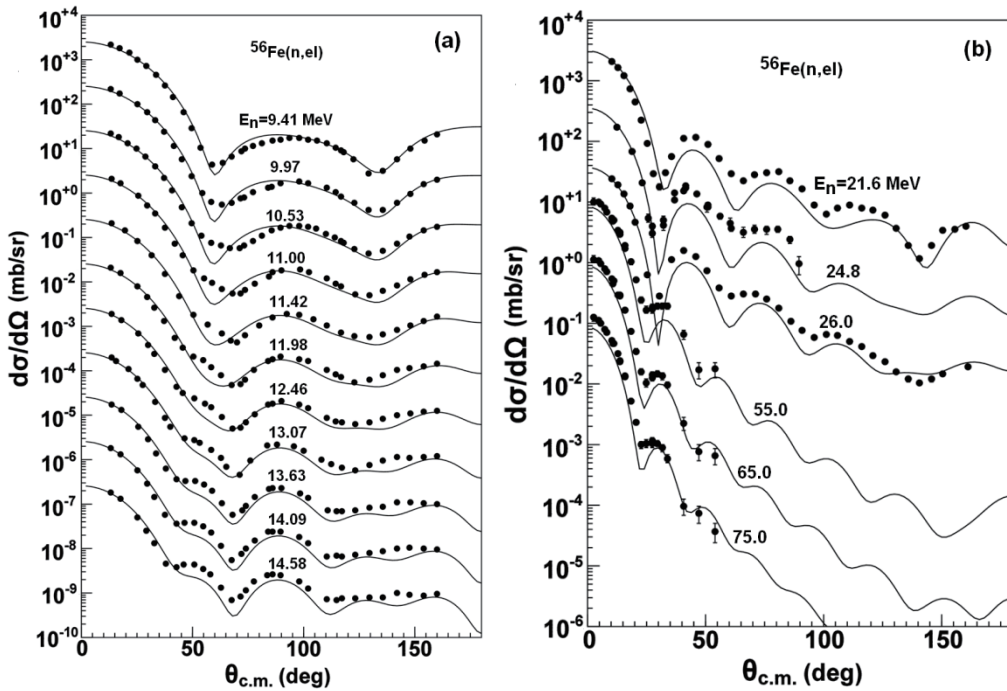


Fig.1 Calculated elastic scattering angular distributions (solid lines) compared with experimental data (symbols) for  $n+^{56}\text{Fe}$  reaction. The results are divided by  $10^0$ ,  $10^1$ ,  $10^2$ , and so on.

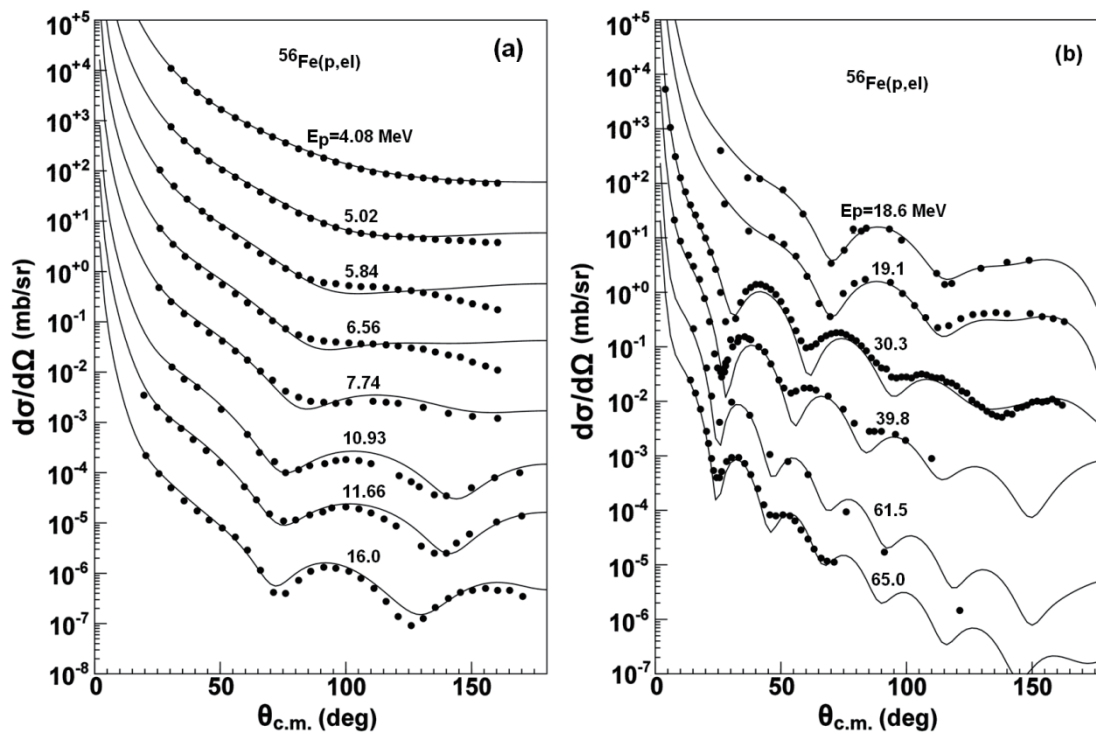


Fig.2 Calculated elastic scattering angular distributions (solid line) compared with experimental data (symbols) for  $p+^{56}\text{Fe}$  reaction. The results are divided by  $10^0$ ,  $10^1$ ,  $10^2$ , and so on.

The MOPs for deuteron,  $^3\text{He}$  and  $^4\text{He}$  are also obtained by Green function method. The real parts of MOPs are given by the first-order mass operators of two-, three- and four-particle Green functions, while the imaginary parts of MOPs are given by the imaginary parts of second-order mass operators. The radial dependence, the volume integral per nucleon and the root mean square (rms) radii of the microscopic optical potentials are calculated [2,3,4]. The reaction cross sections and elastic scattering angular distributions for target nuclei in the mass range  $6 \leq A \leq 209$  and the incident energy per nucleon up to 100 MeV are calculated, and the calculated results are compared with the experimental data.

For deuteron reaction cross sections, good agreement can be observed for some nuclei and discrepancy exists for some other nuclei. For the elastic scattering angular distribution, the calculated results are in good agreement with the experimental data [2]. Especially for the reaction cross sections for  $^{24}\text{Mg}$  and  $^{28}\text{Si}$ , the elastic scattering angular distribution for  $^{24}\text{Mg}$ ,  $^{40}\text{Ca}$ ,  $^{90}\text{Zr}$  and  $^{208}\text{Pb}$ , the calculated results are in good agreement with the experimental data. Furthermore, some elastic scattering angular distributions calculated by the deuteron microscopic optical potential are comparable to ones calculated by deuteron global optical potential [17] in fitting the experimental data, and some even better than the results calculated by some deuteron global optical potential in fitting the experimental data. The calculated elastic scattering angular distributions for  $^{24}\text{Mg}$  are compared with experimental data [18–20] in Fig. 3.

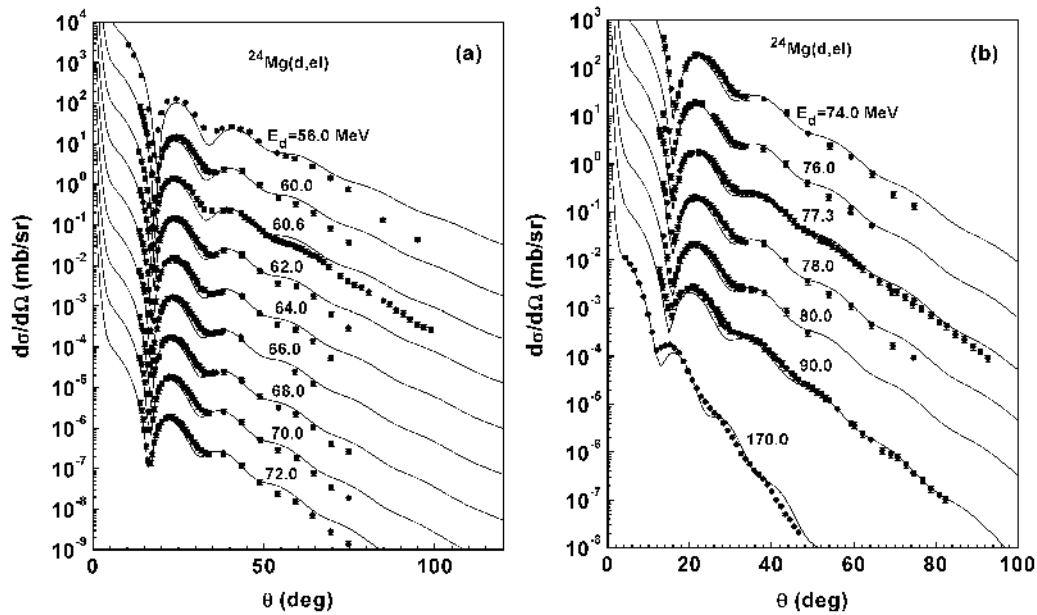


Fig.3 Calculated elastic scattering angular distributions (solid lines) compared with experimental data (symbols) for  $d+^{24}\text{Mg}$  reaction. The results are divided by  $10^0$ ,  $10^1$ ,  $10^2$ , and so on

The calculated results of reaction cross sections and elastic scattering angular distributions for helium-3 by the MOP are in reasonable agreement with the experimental data in most cases [3]. Figure 4 shows the comparison of the calculated results of elastic scattering angular distributions for the elastic scattering of 29 MeV  $^3\text{He}$  from different target nuclei with experimental data [21].

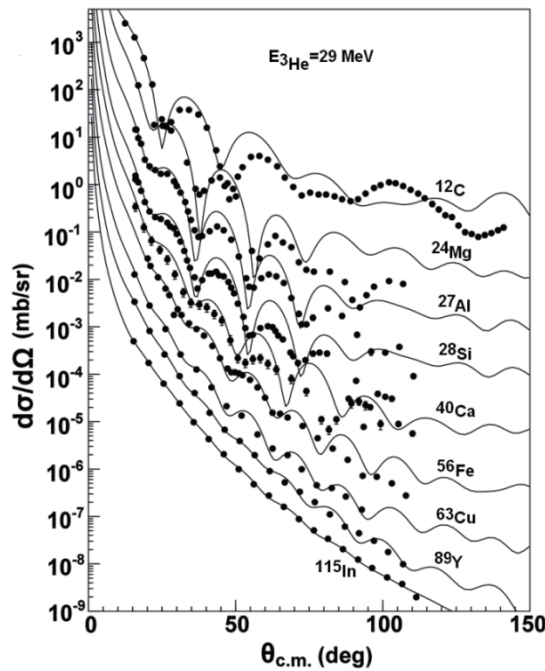


Fig.4 Calculated elastic scattering angular distributions (solid lines) compared with experimental data (symbols) for different target nuclei at incident  $^3\text{He}$  energy of 29 MeV. The results are divided by  $10^0$ ,  $10^1$ ,  $10^2$ , and so on.

The calculated results of reaction cross sections and elastic scattering angular distributions for  $^4\text{He}$  by the MOP can generally well reproduce the experimental data [4]. Figure 5 shows the comparison of the calculated results of differential cross sections relative to Rutherford cross sections for  $^{209}\text{Bi}$  at different incident energies with experimental data [22-24].

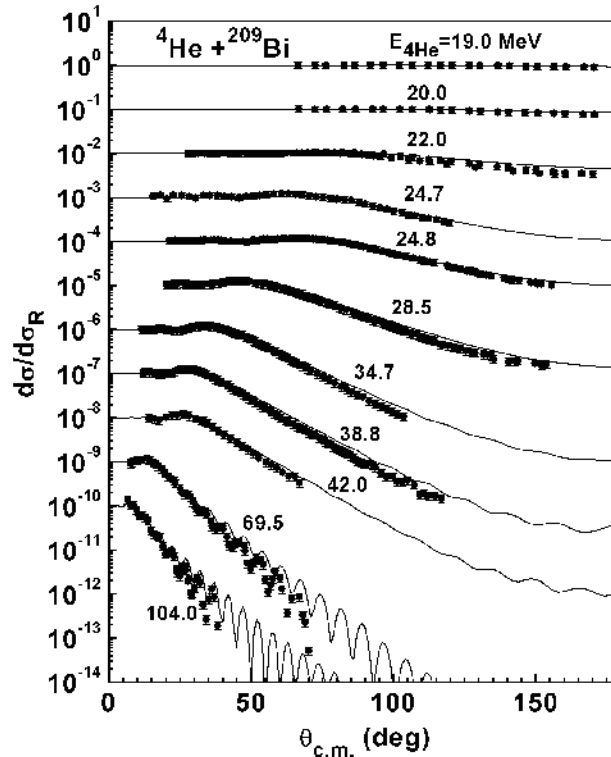


Fig.5 Calculated results of differential cross sections relative to Rutherford cross sections (solid lines) compared with experimental data (symbols) for  $^4\text{He}+^{209}\text{Bi}$  reaction. The results are divided by  $10^0$ ,  $10^1$ ,  $10^2$ , and so on.

### 3. Summary

The microscopic optical potentials for nucleon, deuteron and  $^3\text{He}$  and  $^4\text{He}$  are obtained by Green function method through nuclear matter approximation and local density approximation based on the Skyrme interaction. The calculated results of total cross section (for neutron), nonelastic cross sections and elastic scattering angular distributions by the microscopic optical potentials are compared with the experimental data. Good agreement is generally obtained for elastic scattering angular distributions. And for the reaction cross sections, good agreement is obtained for some nuclei.

### REFERENCES

- [1] Qingbiao Shen, Yinlu Han and Hairui Guo. Phys. Rev. C80: 024604 (2009).
- [2] Hairui Guo, Yongli Xu, Yinlu Han, and Qingbiao Shen. Phys. Rev. C81: 044617 (2010).
- [3] Hairui Guo, Yue Zhang, Yinlu Han, and Qingbiao Shen. Phys. Rev. C79: 064601 (2009).

- [4]Hairui Guo, Yongli Xu, Haiying Liang, Yinlu Han and Qingbiao Shen. Phys. Rev. C83: 064618 (2011).
- [5]N. Olsson, B. Trostell, E. Ramstroem and B. Holmqvist, Nucl. Phys. A472: 237 (1987).
- [6]T. P. Stuart, J. D. Anderson and C. Wong, Phys. Rev. 125: 276 (1962).
- [7]S. Mellema, R. W. Finlay, F. S. Dietrich and F. Petrovich, Phys. Rev. C28: 2267 (1983).
- [8]F. E. Bertrand and R. W. Peelle, Phys. Rev. C8: 1045 (1973).
- [9]N. Boukharouba, C. E. Brient, S. M. Grimes, V. Mishra and R. S. Pedroni, Phys. Rev. C46: 2375 (1992).
- [10]J. Benveniste, A. C. Mitchell, B. Buck and C. B. Fulmer, Phys. Rev. 133: 323 (1964).
- [11]R. Varner, Phys. Reports 201: 57 (1991).
- [12]P. Kossanyi-Demay, R. De Swiniarski, C. Glashausser, Nucl. Phys. A94: 513 (1967).
- [13]S. F. Eccles, H. F. Lutz and V. A. Madsen, Phys. Rev. 141: 1067 (1966).
- [14]B. W. Ridley and J. F. Turner, Nucl. Phys. 58: 497 (1964).
- [15]M. K. Brussel and J. H. Williams, Phys. Rev. 114: 525 (1959).
- [16]R. De Leo and H. Akimune et al., Phys. Rev. C53: 2718 (1996).
- [17]Yinlu Han, Yuyang Shi and Qingbiao Shen, Phys. Rev. C74: 044615 (2006).
- [18]K. Hatanaka et al., Nucl. Phys. A340: 93 (1980).
- [19]A. Kiss et al., Nucl. Phys. A262: 1 (1976).
- [20]C. Baeumer et al., Phys. Rev. C63: 037601 (2001).
- [21] D. J. Baugh, G. J. B. Pyle, P.M. Rolph, and S.M. Scarrott, Nucl. Phys. A95: 115 (1967).
- [22]A. R. Barnett and J. S. Lilley, Phys. Rev. C 9: 2010 (1974).
- [23]P. Singh, A. Chatterjee, S. K. Gupta, and S. S. Kerekatte, Phys. Rev. C 43: 1867 (1991).
- [24]A. Budzanowski *et al.*, Phys. Lett. 11: 74 (1964).

## 20 Low-Energy Nuclear Reactions of Light Nuclei

Masayuki Aikawa<sup>1</sup>, Yoshiharu Hirabayashi<sup>2</sup> and Kiyoshi Katō<sup>3</sup>

<sup>1</sup>Nuclear Reaction Data Centre (JCPRG), Hokkaido University, Sapporo 060-0810, Japan

<sup>2</sup>Information Initiative Center, Hokkaido University, Sapporo 060-0811, Japan

<sup>3</sup>Graduate School of Science, Hokkaido University, Sapporo 060-0810, Japan

e-mail: aikawa@sci.hokudai.ac.jp

It is important to understand low-energy nuclear reactions of light nuclei not only from basic research interests but also from application points of view. We propose a study of low-energy nuclear reactions of light nuclei based on cluster structures in the energy region around the threshold of the compound nucleus to decay into two particles as same as incident and target nuclei, respectively. We review our studies to describe nuclear structures and reactions in the frameworks of the continuum-discretized coupled channels (CDCC) method and the complex scaling method (CSM).

### 1. Introduction

Low-energy nuclear reactions of light nuclei are very important for basic researches and applications. Unlike nuclear reactions of heavy nuclei, the reactions of light nuclei show independent characteristics for each target nucleus, incident particle and energy. It is difficult to describe them within statistical approaches. Therefore it is necessary to investigate the reactions of light nuclei individually.

We here propose a study of low-energy nuclear reactions of light nuclei based on cluster structures in the energy region around the threshold of the compound nucleus to decay into two particles as same as incident and target nuclei, respectively. The threshold energy rule proposed by Ikeda et al. [1] has been shown successfully to play a useful guiding role in nuclear cluster structures of light nuclei. Most of those nuclear cluster structures have been studied in connection with nuclear reactions. Many useful methods to describe both nuclear cluster structures and reactions have been developed. Based on these studies, we try to describe nuclear structures and reactions in the frameworks of the continuum-discretized coupled channels (CDCC) method [2] and the complex scaling method (CSM) applying to the multi-cluster model [3]. In this paper, we review our studies about triple alpha,  $^{17}\text{O}(n,\gamma)^{18}\text{O}$ , and  $^{6,7}\text{Li}+n$  reactions.

### 2. $3\alpha \rightarrow ^{12}\text{C}$

Since the two-alpha system,  $^8\text{Be}$ , is not bound, the triple-alpha reaction is considered as a typical three-body reaction and closely related with  $3\alpha$  cluster structure in  $^{12}\text{C}$ . Kurokawa et al. [3] investigated the  $3\alpha$  resonant states in  $^{12}\text{C}$  within the correct boundary condition for three-body resonant states. In the study,

they applied the CSM, which is available for solving many-body resonant states and obtaining not only the resonance energy but also the total decay width with the same accuracy. Their result shows that many observed states above the  $3\alpha$  threshold energy are well reproduced, and also predicts a broad  $0^+$  resonant state ( $\Gamma = 1.48$  MeV) above the Hoyle ( $0^+_{2}$ ) state (Fig. 1). This  $0^+_{3}$  state contributes to have a large cross section of  $3\alpha \rightarrow {}^{12}\text{C}$ .

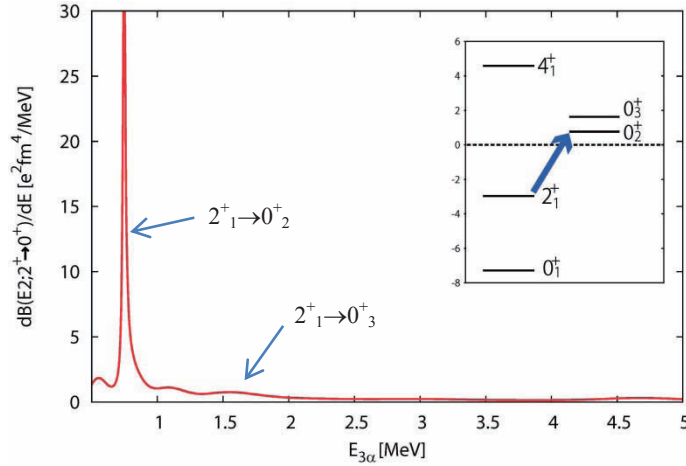


Fig. 1: E2 transition strength from  $2^+_{1}$  to  $0^+$  and energy levels. The transition strengths to  $0^+_{2}$  and  $0^+_{3}$  are indicated by arrows.

### 3. ${}^{17}\text{O}(n,\gamma){}^{18}\text{O}$

The reaction cross section of  ${}^{17}\text{O}(n,\gamma){}^{18}\text{O}$  is very crucial for the synthesis path from  ${}^{16}\text{O}$  to Ne isotopes in the nucleosynthesis of the very metal deficient stars [4]. In spite of its importance, we have no experimental data for this reaction since the natural  ${}^{17}\text{O}$  abundance among O isotopes is very small. A reliable theoretical estimation for the cross section and the reaction rate of the  ${}^{17}\text{O}(n,\gamma){}^{18}\text{O}$  reaction is desirable for the nuclear reaction network calculation.

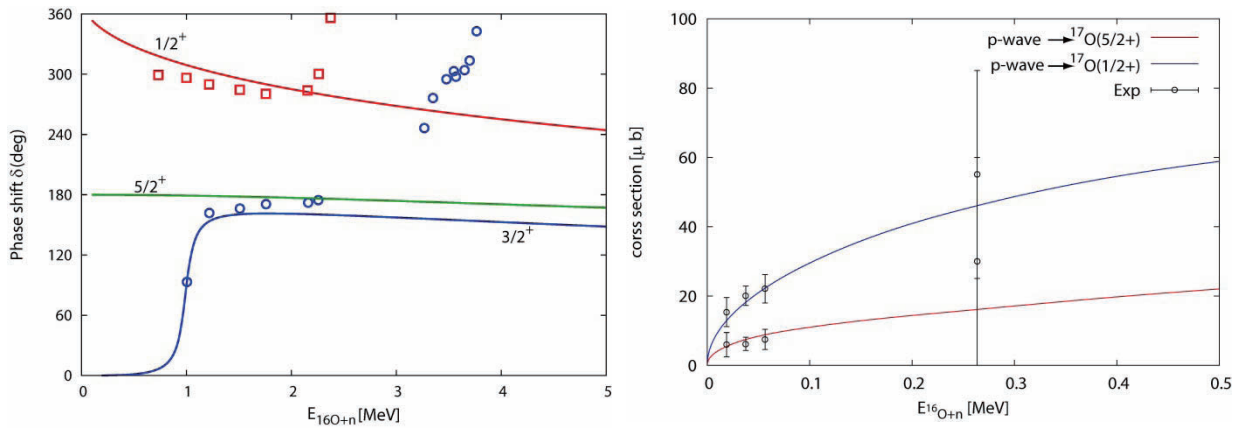


Fig. 2: Phase shift (left panel) and cross section (right panel) of  ${}^{16}\text{O}(n,\gamma){}^{17}\text{O}$ . Experimental data is derived from the references [5,6].

In order to study the  $^{17}\text{O}(n,\gamma)^{18}\text{O}$  reaction, an  $^{16}\text{O}+n+n$  model is promising. For this purpose, it is indispensable to examine the reliability of the  $^{16}\text{O}+n$  model. To explain the reaction cross section of  $^{16}\text{O}(n,\gamma)^{17}\text{O}$ , Yamamoto et al. [4] applied  $^{16}\text{O}+n$  model and the complex scaling method with the Lippmann-Schwinger solution for the complex-scaled Green's operator. This procedure is very powerful to analyze the reactions in the lower-energy region. Their result shows very good agreement with experimental data of the phase shift and the cross section, as shown in Fig. 2. According to the successful reproduction of the  $^{16}\text{O}(n,\gamma)^{17}\text{O}$  reaction, the method is being applied to the  $^{17}\text{O}(n,\gamma)^{18}\text{O}$  reaction.

#### 4. $^{6,7}\text{Li}+n$

The elastic and inelastic scattering of  $^{6,7}\text{Li}+n$  have been calculated [7,8]. The CDCC method is applied to calculate elastic and inelastic cross sections including the breakup channels. The CDCC method has advantages to obtain not only elastic and inelastic cross sections but also neutron spectra within the same framework. The  $^{6,7}\text{Li}$  nuclei are described by alpha plus deuteron and triton, respectively. In the references [7,8],  $^{6}\text{Li}+n$  scattering at the incident energies between 7 and 24 MeV has been analyzed. Once the calculated cross section for the elastic scattering is fitted with the experimental data, the inelastic cross section and neutron spectra (Fig. 3) are well reproduced simultaneously.

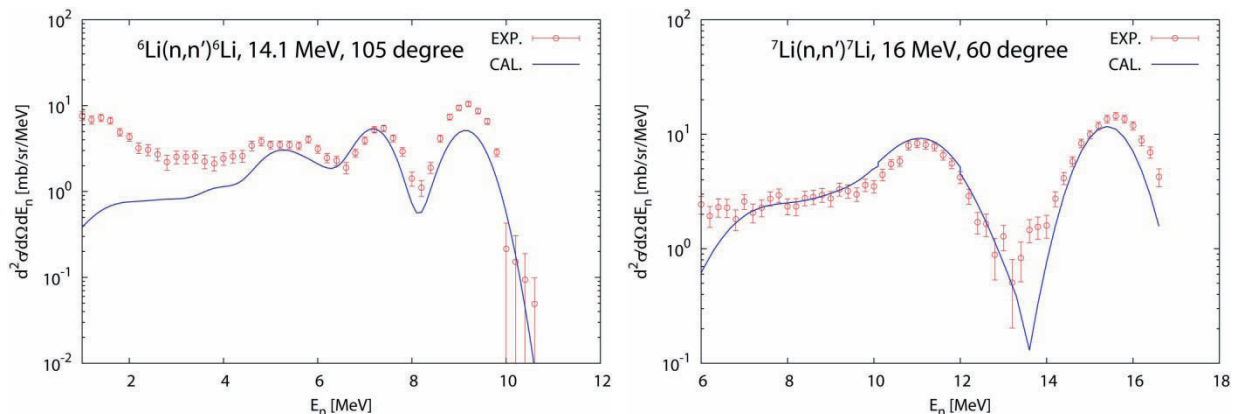


Fig. 3: Neutron spectra at 105 degree of  $^6\text{Li}+n$  at 14.1 MeV (left panel) and at 60 degree of  $^7\text{Li}+n$  at 16 MeV (right panel).  $E_n$  is the energy of outgoing neutrons. The experimental data are taken from the references [9,10].

#### 5. Summary

Nuclear reactions in low-energy regions are very important for basic researches and applications. The theoretical calculation using reliable frameworks is desirable. We review our theoretical works based on the continuum-discretized coupled channels (CDCC) method and the complex scaling method (CSM). The first application is the triple-alpha reaction for  $^{12}\text{C}$  production. The second one is the reaction rate of  $^{17}\text{O}(n,\gamma)^{18}\text{O}$ . The third one is elastic and inelastic scattering of  $^{6,7}\text{Li}+n$ . We are planning to extend these calculations to the rearrangement reactions.

## Acknowledgement

We would like to thank Dr. K. Yamamoto and Ms. D. Ichinkhorloo for their valuable supports.

## References

- [1] K. Ikeda, N. Takigawa and H. Horiuchi: Prog. Theor. Phys. Suppl. Ext., 464 (1968).
- [2] M. Kamimura, M. Yahiro, Y. Iseri, Y. Sakuragi, H. Kameyama and M. Kawai: Prog. Theor. Phys. Suppl., 89, 1 (1986).
- [3] C. Kurokawa and K. Kato: Nucl. Phys., A792, 87 (2007).
- [4] K. Yamamoto, H. Masui, K. Kato, T. Wada and M. Ohta: Prog. Theor. Phys., 121, 375 (2009).
- [5] C. H. Johnson and J. L. Fowler: Phys. Rev., 162, 890 (1967).
- [6] M. Igashira, Y. Nagai, K. Masuda, T. Ohsaki and H. Kitazawa: Astrophys. J., 441, L89 (1995).
- [7] T. Matsumoto, D. Ichinkhorloo, Y. Hirabayashi, K. Kato, and S. Chiba: Phys. Rev. C, 83, 064611 (2011).
- [8] D. Ichinkhorloo, T. Matsumoto, Y. Hirabayashi, K. Kato and S. Chiba: Jour. Nucl. Sci. Tech., 48, 1357 (2011).
- [9] S. Chiba, et al.: Phys. Rev. C, 58, 2205 (1998).
- [10] S. Chiba, M. Baba, N. Yabuta, T. Kikuchi, M. Ishikawa, N. Hirakawa, and K. Sugiyama: "Measurement of neutron-induced neutron-producing cross sections of  $^6\text{Li}$  and  $^7\text{Li}$  at 18.0 MeV," Proc. Int. Conf. on Nuclear Data for Science and Technology, 1988, Mito, Japan, p.253 (1988, Saikon Publishing).

## 21 Measurement of Neutron and Gamma-ray Yields on Thick Targets Bombarded with 12 MeV Protons

Masayuki HAGIWARA<sup>1)</sup>, Toshiya SANAMI<sup>1)</sup>, Yosuke IWAMOTO<sup>2)</sup>, Norihiro MATSUDA<sup>2)</sup>, Yukio SAKAMOTO<sup>2)</sup>, Yoshihiro NAKANE<sup>2)</sup>, Hiroshi NAKASHIMA<sup>2)</sup>, Kazuyoshi MASUMOTO<sup>1)</sup>, Yoshitomo UWAMINO<sup>3)</sup>

<sup>1)</sup>High Energy Accelerator Research Organization, KEK, Oho 1-1, Tsukuba-shi, Ibaraki-ken 305-0801

<sup>2)</sup>Japan Atomic Energy Agency, Shirakata-shirane 2-4, Tokai-mura, Naka-gun, Ibaraki-ken 319-1184

<sup>3)</sup>RIKEN, Hirosawa 2-1, Wako-shi, Saitama-ken 351-0198

e-mail: hagi@post.kek.jp

Differential thick target yields (TTYs) of neutrons and  $\gamma$ -rays induced by 12 MeV protons have been measured at six laboratory angles between  $0^\circ$  and  $120^\circ$  using several targets ( $^9\text{Be}$ ,  $\text{H}_2^{18}\text{O}$  and  $\text{H}_2^{\text{nat}}\text{O}$ ), in order to assess the nuclear data libraries and calculation codes for the proton-induced reaction at low energies. NE213 scintillators of 5.08 cm diameter and 5.08 cm length were employed with pulse-shape-discrimination technique for separation of neutron and  $\gamma$ -ray events. The neutron and  $\gamma$ -ray events were analyzed by a time-of-flight (TOF) method and an unfolding technique, respectively. The measured TTYs were compared with calculation results on the basis of the several nuclear data libraries and physical models.

### 1. Introduction

Nuclear data on proton-induced neutron and  $\gamma$ -ray production in the energy range from 10 to 20 MeV are important to execute the shielding design and to estimate activation of low-energy accelerator facilities such as medical-purpose accelerators for production of radiopharmaceuticals in positron emission tomography (PET) and a neutron source of boron neutron capture therapy (BNCT). The energy and angular distribution of neutrons produced through interactions between incident protons and accelerator components (target, beam stop, collimator and etc.) should be estimated for radiation safety as well as clearance of wastes from a facility. However, the experimental data on the energy and angular distribution for production of neutrons as well as  $\gamma$ -rays are very scarce especially for proton energies ranging from 10 to 20 MeV<sup>1)</sup>. So far, estimation of shielding and activation of such facilities was performed using nuclear data libraries and calculation codes such as ENDF/B-VII.0<sup>2)</sup>,

PHITS<sup>3)</sup>, and MCNPX<sup>4)</sup>. The accuracy of these codes and nuclear data library for such a low energy region should be checked by experimental data, because most of physical models for proton-induced reactions implemented in the codes were developed to describe reactions of high-energy particles. Therefore, we had measured differential thick target yield (TTY) data on proton-induced neutron and  $\gamma$ -ray production for various targets ( $^9\text{Be}$ ,  $^{\text{nat}}\text{C}$ ,  $^{27}\text{Al}$ ,  $^{\text{nat}}\text{Cu}$ ,  $^{181}\text{Ta}$  and  $\text{H}_2^{18}\text{O}$ ) at the incident energy of 18 MeV<sup>5)</sup>. In this paper, we describe the measurements of neutron and  $\gamma$ -ray energy spectra from  $^9\text{Be}$ ,  $\text{H}_2^{18}\text{O}$  and  $\text{H}_2^{\text{nat}}\text{O}$  targets induced by 12 MeV protons, and comparisons between the experimental data and calculation results.

## 2. Experiment

The experiment was carried out using the AVF cyclotron (K=110) at the Takasaki Ion Accelerators for Advanced Radiation Application (TIARA) facility of Japan Atomic Energy Agency (JAEA). A schematic view of the experimental apparatus is illustrated in Fig.1. A proton beam accelerated by the cyclotron was transported to HB-1 beam course, which is equipped with a 60-cm diameter vacuum chamber. Neutron detectors were set at six laboratory angles (0, 15, 30, 60, 90 and 120°) with distances of 2.0 – 5.0 m from the target. The beam transported to the target was thinned by lowering the beam frequency with a beam chopper in order to obtain TOF spectra down to a lower energy region by avoiding the frame-overlap effect. In the present experiment, the beam chopper was operated at 1/6 and the resultant beam frequency was 2.78 MHz. A detailed description of the target room is given in ref. 6.

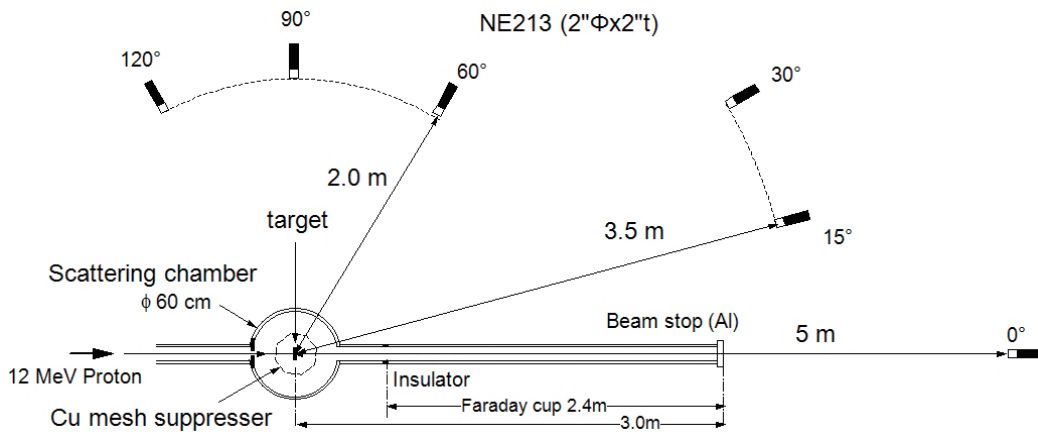


**Fig. 1.** Illustration of experimental setup at the HB-1 course in TIARA (horizontal view)

The thickness of each target (2 mm, 6.5 mm and 13 mm for  $^9\text{Be}$ ,  $\text{H}_2^{18}\text{O}$  and  $\text{H}_2^{\text{nat}}\text{O}$ , respectively) was determined to be thicker than the range of 12 MeV protons using the SRIM code<sup>7)</sup>. The water targets ( $\text{H}_2^{18}\text{O}$  [98 atm% enriched in  $^{18}\text{O}$ ] and  $\text{H}_2^{\text{nat}}\text{O}$ ) were prepared by

filling a 2.0-cm-diameter  $\times$  0.2-cm-thick Cu container covered with a 10  $\mu\text{m}$ -thick HAVAR foil. The size of the water targets in the Cu container was 1.6 cm in diameter. The targets were set on a remote-controlled target holder together with a beam viewer and a blank target in the vacuum chamber. The target holder was insulated from the ground and served as a Faraday cup to read the beam current. To measure an accurate number of incident protons, a copper mesh biased to -400 V was installed around the target to suppress secondary electron emission from the target.

Neutrons and  $\gamma$ -rays emitted from the target were detected with organic liquid scintillators (5.08-cm-diameter  $\times$  5.08-cm-thick NE213) equipped with an electric circuit for pulse-shape discriminations (PSD) and time-of-flight (TOF) methods<sup>6)</sup>. The beam current was measured using a current integrator connected to the target. These digital data were collected with the CAMAC system event by event using the Kakuken on-line data acquisition system (KODAQ) for off-line analysis<sup>8)</sup>.

### 3. Data analysis

Neutron TOF spectra were obtained by gating the events with the two light output data (total component and slow component) on the two-dimensional graphical plots after removing random background events. The pulse height distribution of the total light output was calibrated with  $\gamma$ -rays from a  $^{241}\text{Am-Be}$ ,  $^{60}\text{Co}$  and  $^{137}\text{Cs}$  source with energies of 4.43 MeV, 1.173 and 1.333 MeV and 0.662 MeV, respectively. The detector bias was set at 1.3 MeV for neutrons. The TOF spectra were converted into neutron energy spectra, according to the Lorentz conversion<sup>6)</sup>. The energy spectrum data were normalized by dividing with the detector solid angle, an integrated charge of the incident beam. The detection efficiency was calculated using the Monte Carlo code SCINFUL-R<sup>9)</sup>.

Experimental uncertainties were estimated on the basis of systematic error propagation. Statistical uncertainties were generally below 5% but increased to above 5% at the highest energy. The uncertainty of detector efficiency with the SCINFUL-R code was estimated to be 5%<sup>9)</sup>. The uncertainties of beam current measurements were estimated to be 5%.

The energy spectrum of prompt  $\gamma$ -rays was measured with the same NE213 scintillator of 5.08 cm thickness and diameter. After discriminating the  $\gamma$ -ray events from those of neutrons by the PSD method<sup>6)</sup>, the energy spectrum of  $\gamma$ -rays emitted within 50 ns around the prompt  $\gamma$ -ray peak was obtained with the unfolding technique using the FERDOU code<sup>10)</sup>. The response functions of  $\gamma$ -rays for the incident energies up to 20 MeV were calculated by the EGS4 code<sup>11)</sup>.

### 4. Results

The TTYs of neutrons for each emission angle and the TTY of  $\gamma$ -rays for 15° are

shown in Figs.2 and 3 with the corresponding calculation results obtained with MCNPX ver. 2.5 using the ENDF/B-VII.0 nuclear data library. The neutron energy spectra obtained in this experiments covered from 1.5 MeV up to 10 MeV. The highest energy was consistent with each reaction Q-value, e.g. (-1.85 MeV) of the  ${}^9\text{Be}(p,n){}^9\text{B}$  reaction. The calculation result generally well reproduces the measured energy spectra, though the calculation results underestimate the neutron spectra in the high energy region in comparison with the measured ones. For the  $\gamma$ -ray spectrum, the calculated peak energy is higher than measured one, but the calculation reproduces the measurement in yield. TTYs of neutrons for each emission angle and the TTY of  $\gamma$ -rays obtained from  $\text{H}_2{}^{18}\text{O}$  and  $\text{H}_2{}^{\text{nat}}\text{O}$  targets are shown in Figs. 4, 5, 6, and 7 with the corresponding calculation results obtained with MCNPX ver. 2.5. The highest energy of measure neutron spectra was consistent with each reaction Q-value, e.g. (-2.44 MeV) of the  ${}^{18}\text{O}(p,n){}^{18}\text{F}$  reaction. We performed the MCNPX calculation based on the nuclear data libraries of ENDF/B-VII.0, TENDL-2009<sup>12)</sup>, and the implemental models of intranuclear cascade (Bertini<sup>13)</sup>) and evaporation (Dresner<sup>14)</sup>). The calculation results with nuclear data library (ENDF/B-VII.0 and TENDL-2009) underestimate the measured spectra for neutrons and  $\gamma$ -rays, but the calculation with the Bertini + Dresner models generally well reproduce the measured energy spectra for the  $\text{H}_2{}^{18}\text{O}$  target, considering that these models are initially intended for use in the high-energy nuclear reaction with energies above 100 MeV.

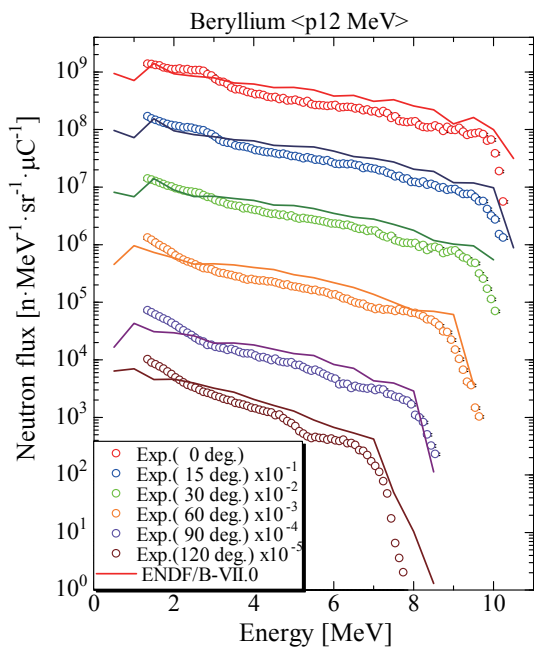


**Fig.2** Measured TTY of neutrons from p-Be reaction for 12 MeV in comparison with ENDF/B-VII.0

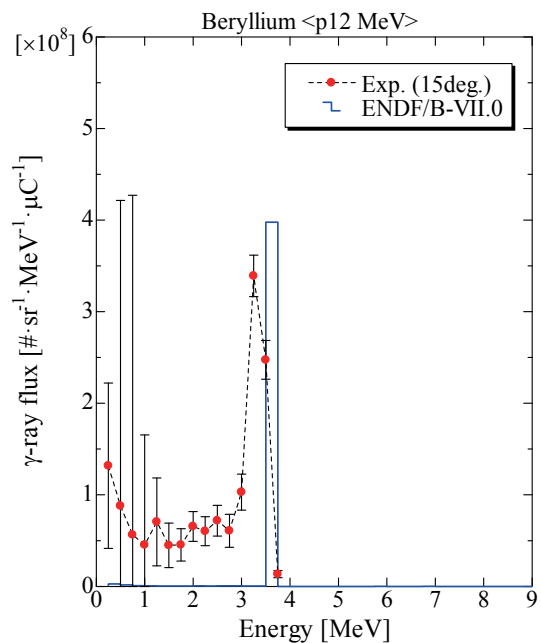


**Fig.3** Measured TTY of  $\gamma$ -rays from p-Be reaction for 12 MeV in comparison with ENDF/B-VII.0

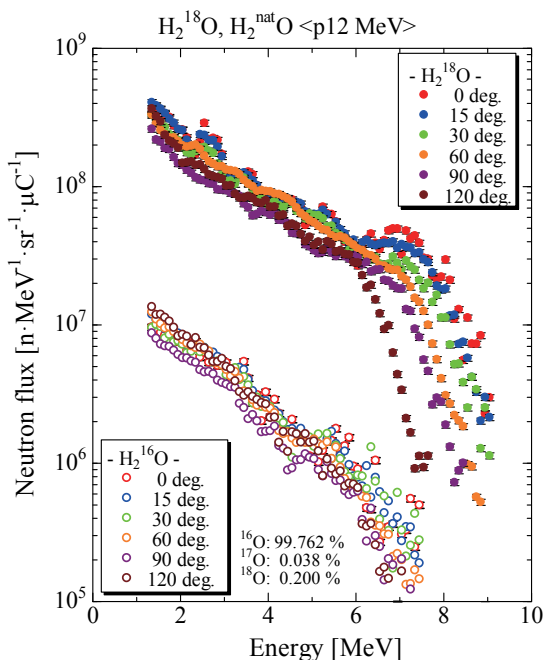


**Fig.4** Comparison of measured TTYs of neutrons between  $H_2^{18}O$  and  $H_2^{nat}O$  targets

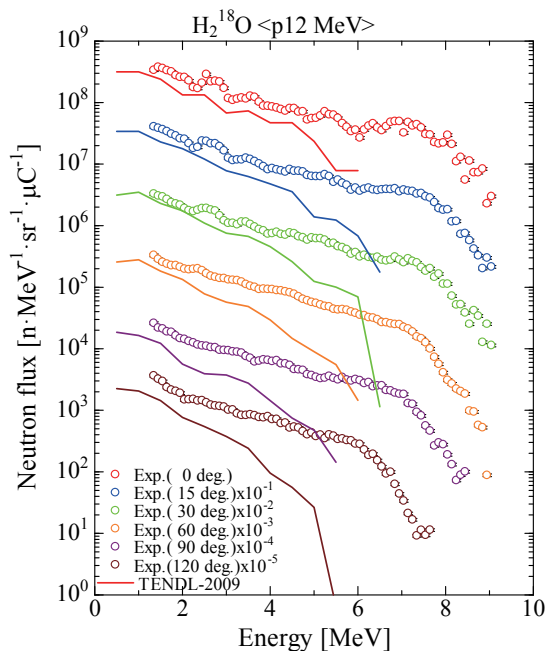


**Fig.5** Measured TTY of neutrons from  $p-H_2^{18}O$  reaction for 12 MeV in comparison with TENDL-2009

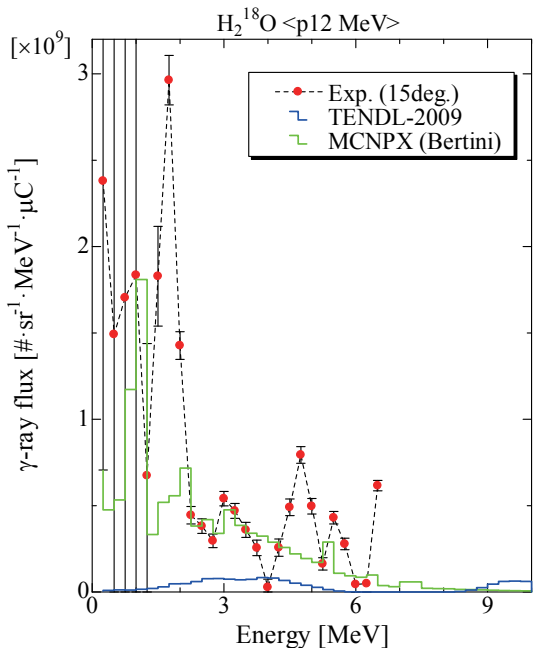


**Fig.6** TTY of  $\gamma$ -rays from  $p-H_2^{18}O$  reaction for 12 MeV in comparison between measurement and calculations

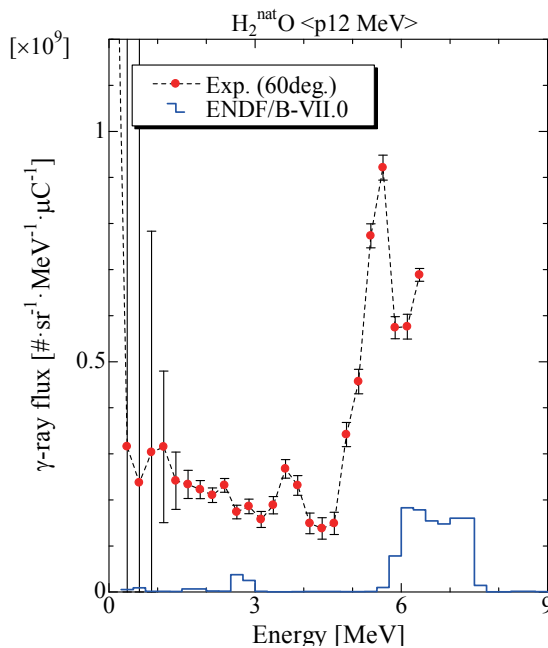


**Fig.7** Measured TTY of  $\gamma$ -rays from  $p-H_2^{nat}O$  reaction for 12 MeV in comparison with ENDF/B-VII.0

### 5. Summary

We measured double-differential TTYs of neutrons and  $\gamma$ -rays from several thick

targets at six laboratory angles (0, 15, 30, 60, 90 and 120°). The incident beam was 12 MeV protons and fully stopped in the target. The experimental TTY data were obtained at energies above 1.5 MeV for neutrons and 0.6 MeV for  $\gamma$ -rays. The neutron spectra have high-energy neutrons up to 10 MeV. The measured TTYs were compared with calculations of the MCNPX code based on the ENDF/B-VII.0, TENDL-2009, and Bertini + Dresner models. For the neutron energy spectra, the calculated results agreed fairly well with the experimental data, except underestimation of spectra at high energies. The MCNPX calculation of  $\gamma$ -ray spectrum result generally well reproduces the measured energy spectra only in the case of the H<sub>2</sub><sup>18</sup>O target using the Bertini + Dresner models.

## REFERENCES

- [1] R. Méndez, M. P. Iñiguez, J. M. Martí-Climent, I. Peñuelas, H. R. Vega-Carrillo and R. Barquero, *Phys. Med. Biol.*, **50**, 5141-5152 (2005).
- [2] M.B. Chadwick, P. Obložinský, M. Herman, et al., “ENDF/B-VII.0: Next Generation Evaluated Nuclear Data Library for Nuclear Science and Technology,” *Nucl. Data Sheets*, **102**, 2931-3059 (2006).
- [3] K. Niita, N. Matsuda, Y. Iwamoto, H. Iwase, T. Sato, H. Nakashima, Y. Sakamoto and L. Sihver, JAEA-Data/Code 2010-022 (2010).
- [4] M. B. Chadwick, P. G. Young, S. Chiba, S. C. Frankle, G. M. Hale, H. G. Hughes, A. J. Koning, R. C. Little, R. E. MacFarlane, R. E. Prael, and L. S. Waters, *Nucl. Sci. Eng.*, **131**, 293 (1999).
- [5] M. Hagiwara, T. Sanami, Y. Iwamoto, et al., JAEA-Conf 2010-02, 119-124 (2010).
- [6] Y. Iwamoto, Y. Sakamoto, N. Matsuda, Y. Nakane, K. Ochiai, H. Kaneko, K. Niita, T. Shibata and H. Nakashima, *Nucl. Instr. and Meth. A*, **598**, 687-695 (2009).
- [7] J. F. Ziegler, J. P. Biersack, U. Littmark, *The Stopping and Range of Ions in Solids* Pergamon Press, New York (1984).
- [8] K.Omata and Y.Hujita, INS-Rep-884, Institute for Nuclear Study, University of Tokyo, 1991.
- [9] S. Meigo, *Nucl. Instrum. Methods in Physics Research A* **401** 365 (1997)
- [10] K. Shin, Y. Uwamino and T. Hyodo, *Nucl. Technol.*, **53** (1981) 78.
- [11] W.Nelson, H.Hirayama, D.W.O.Rogers, “The EGS4 Code System” SLAC-265, Stanford University, Stanford (1985).
- [12] A.J. Koning, D. Rochman, TENDL-2009: consistent TALYS-based Evaluated Nuclear Data Library including covariance data, OECD/NEA JEF/DOC-1310, November 2009, <http://www.talys.eu/tendl-2009>.
- [13] H. W. Bertini, *Phys. Rev.*, **188**, 1711 (1969)
- [14] L. Dresner, ORNL-TM-196, Oak Ridge National Laboratory (1962).

## 22 Study on the Neutron Capture Cross Sections and Capture Gamma-ray Spectra of $^{93}\text{Nb}$ , $^{103}\text{Rh}$ and $^{115}\text{In}$

Taihei MATSUHASHI, Hiroyuki TSUDA, Kazushi TERADA,  
Tatsuya KATABUCHI and Masayuki IGASHIRA

*Research Laboratory for Nuclear Reactors, Tokyo Institute of Technology,  
2-12-1-N1-26 O-okayama, Meguro-ku, Tokyo 152-8550, Japan*

E-mail: matsuhashi.t.aa@m.titech.ac.jp

The neutron capture cross sections and gamma-ray spectra of  $^{93}\text{Nb}$ ,  $^{103}\text{Rh}$  and  $^{115}\text{In}$  were calculated based on the statistical model using the computer code CCONE. Model parameters such as level density parameter and gamma-ray strength function were optimized to reproduce available experimental data of neutron-induced reactions of these nuclides. Measurement of the capture cross sections and gamma-ray spectra in the neutron energy range from 15 to 100 keV was done. Time-of-flight method was utilized by means of anti-Compton NaI(Tl) spectrometer and pulsed neutron beam via the  $^7\text{Li}(p,n)^7\text{Be}$  reaction.

### 1. Introduction

The neutron capture reactions of  $^{93}\text{Nb}$ ,  $^{103}\text{Rh}$  and  $^{115}\text{In}$  are important for the design of nuclear reactors.  $^{93}\text{Nb}$  is used in structural materials of nuclear reactors and an element of superconductor alloys in fusion reactors.  $^{103}\text{Rh}$  is produced in fast reactors as fission products at a high cumulative fission yield of several percent. The neutron capture reaction by  $^{103}\text{Rh}$  decreases the neutron economy of such a reactor as a neutron poison.  $^{115}\text{In}$  is an important material for the control rods of thermal reactors.

The neutron capture cross sections of these nuclides have been measured by many research groups, but capture gamma-ray spectrum has not been measured well. The present status of capture gamma-ray spectrum data for those nuclides is very poor both in quality and quantity. The capture gamma-ray spectrum plays a very important role in determining the gamma-ray strength function that is used for theoretical calculation of capture cross section.

From this point of view, we have been studying the neutron capture gamma-ray spectra and capture cross sections of  $^{93}\text{Nb}$ ,  $^{103}\text{Rh}$  and  $^{115}\text{In}$ , theoretically and experimentally. In this contribution, we present the calculated and preliminary experimental results.

### 2. Calculation

Capture cross sections and gamma-ray spectra of  $^{93}\text{Nb}$ ,  $^{103}\text{Rh}$  and  $^{115}\text{In}$  were calculated based on the statistical model using the computer code CCONE [1]. Preequilibrium and direct processes were also taken into account in the calculation. Model parameters were optimized to reproduce available experimental data of neutron-induced reactions ( $(n,\text{tot})$ ,  $(n,n)$ ,  $(n,n')$ ,  $(n,\gamma)$ ,  $(n,2n)$ ,  $(n,3n)$ ,  $(n,p)$ ,  $(n,d)$ ,  $(n,t)$ ,  $(n,\alpha)$ ,  $(n,n\alpha)$ ) of these nuclides. Optical model potentials developed by Kunieda et al. [2] were adjusted to reproduce available experimental data for total and elastic scattering cross sections. Level density parameter was adjusted to reproduce nuclear discrete level data taken from the Reference Input Parameter Library RIPL-2[3]. The

constant temperature form was used for lower excitation energies, and the Fermi-gas form was used for higher excitation energies. The generalized Lorentzian form was employed for the gamma-ray strength function for E1 radiation. A pigmy resonance was added in accordance with experimental data of capture cross sections and capture gamma-ray spectra.

2-1.  $^{93}\text{Nb}$

Figure 1 shows the calculated neutron capture gamma-ray spectrum of  $^{93}\text{Nb}$ . The gamma-ray strength function was determined based on experiment data of capture gamma-ray spectrum [4]. A pigmy resonance was added in the gamma-ray strength function for E1 because calculated capture gamma-ray spectrum could not reproduce experimental data with only giant dipole resonance. The adopted parameters i.e., position, width and intensity parameter of the pigmy resonance ( $E, \Gamma, \sigma$ ) in Lorentzian, were 6.76MeV, 2.30MeV, and 3.70mb, respectively. Figure 2 shows the calculated neutron capture cross sections of  $^{93}\text{Nb}$  with available experimental data. The calculated result reproduces the past experimental data well.

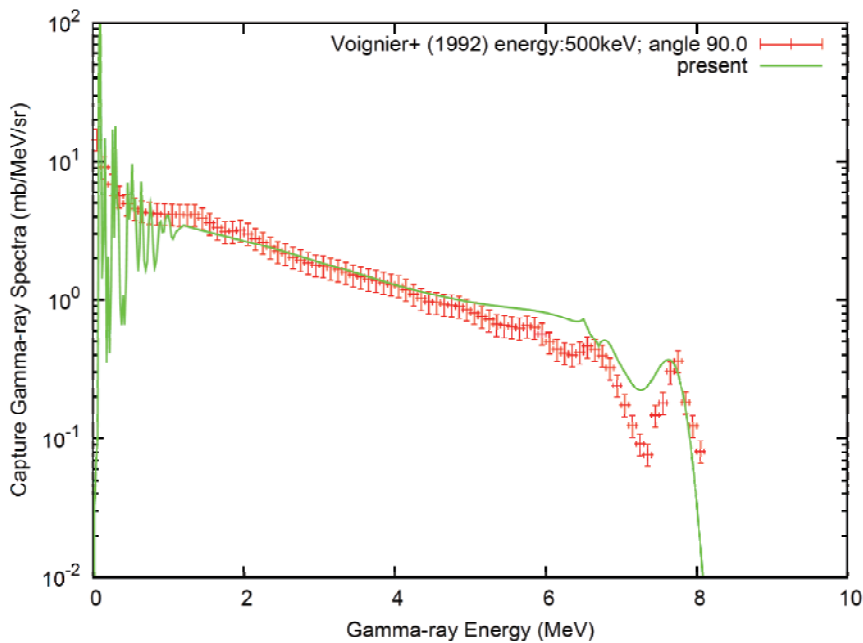


Fig. 1 Neutron capture gamma-ray spectrum of  $^{93}\text{Nb}$

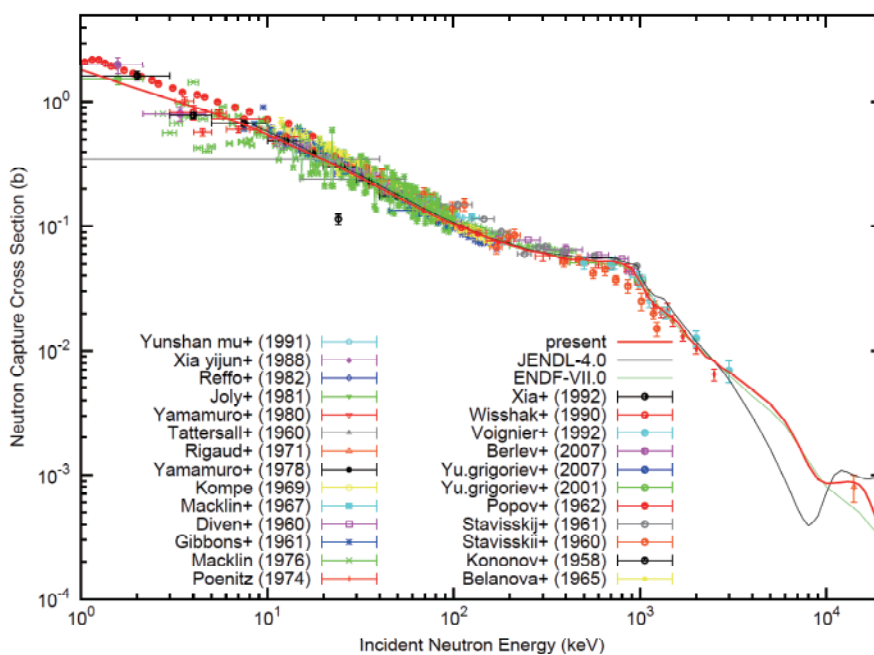


Fig. 2 Neutron capture cross sections of <sup>93</sup>Nb

2-2. <sup>103</sup>Rh

Figure 3 shows the calculated neutron capture cross sections of <sup>103</sup>Rh with available experimental data. The gamma-ray strength function was tentatively determined to reproduce experiment capture cross section data in the 10-100 keV region, where the cross section changes smoothly, because there is no experimental data of gamma-ray spectrum for <sup>103</sup>Rh. The calculated result of capture cross section reproduces the past experimental data well.

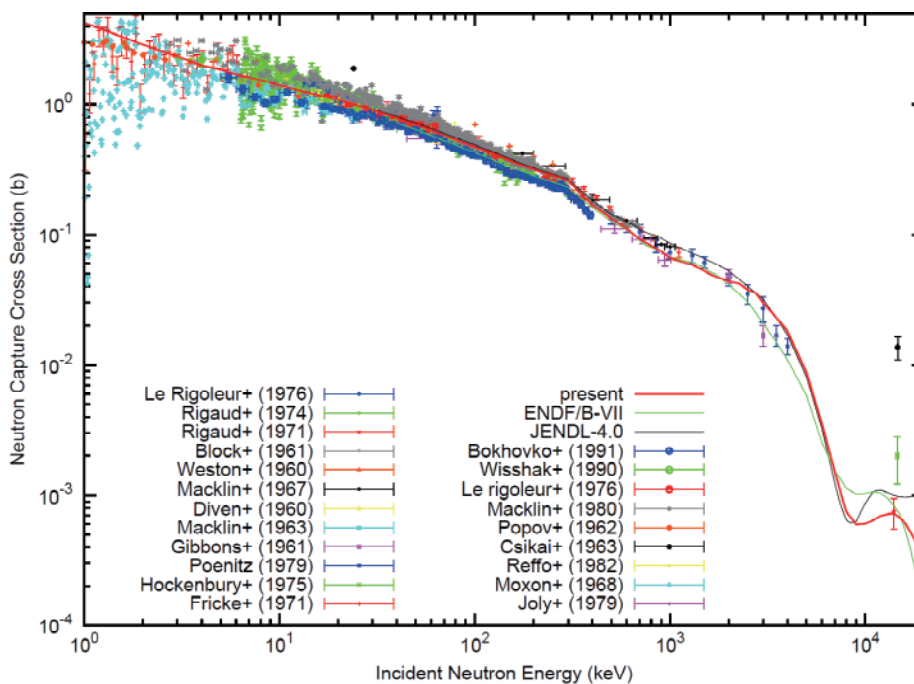


Fig. 3 Neutron capture cross sections of <sup>103</sup>Rh

2-3.  $^{115}\text{In}$

Figure 4 shows the neutron capture cross sections of  $^{115}\text{In}$ . The gamma-ray strength function was tentatively determined in the same way as  $^{103}\text{Rh}$  because of no experimental data. The calculated result reproduces the past experimental data of the capture cross section well.

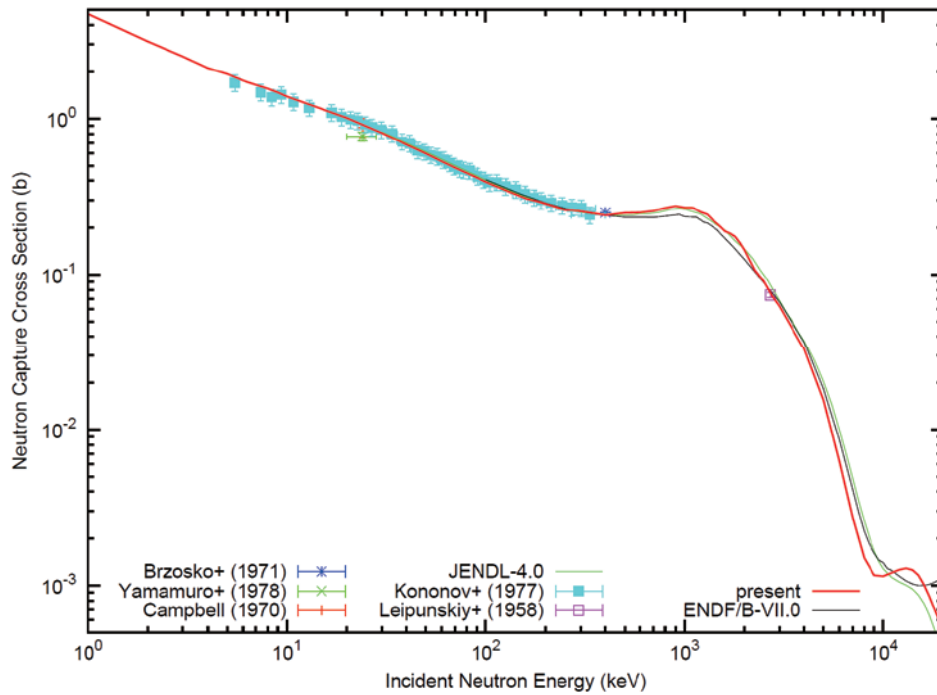


Fig. 4 Neutron capture cross sections of  $^{115}\text{In}$

3. Measurement

The characteristics of the samples is shown in Table 1. All the samples were natural abundance material.  $^{93}\text{Nb}$  and  $^{115}\text{In}$  were metal plate with a diameter of 20 mm.  $^{103}\text{Rh}$  was metal powder, which was cased in a carbon container with an inner diameter of 15 mm and wall thickness of 1 mm.

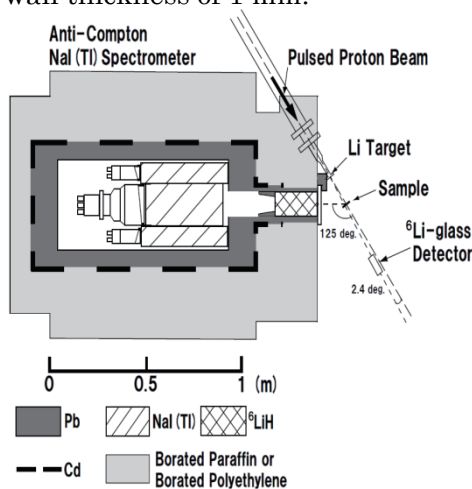


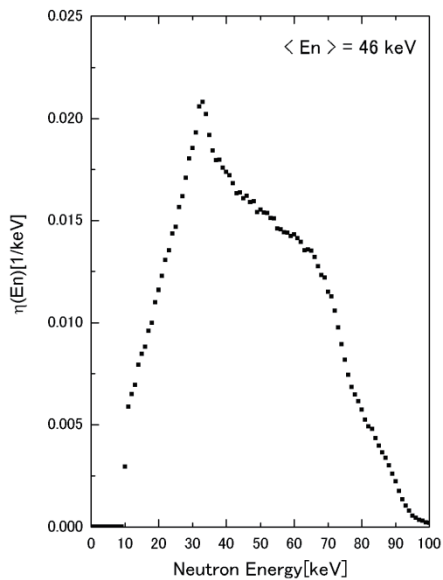
Fig. 5 Experiment setup

Table 1 Characteristics of the samples

sample	Nb-93	Rh-103	In-115	Au-197
Isotopic Purity [%]	100	100	95.7	99.9
Weight [g]	2.69	1.01	1.14	3.50/6.01
Diameter [mm]	20	15	20	15/20
Thickness [mm]	1.0	2.0	0.75	1.0

The capture cross sections and gamma-ray spectra in the neutron energy region from 15 to 100 keV were measured at the Tokyo Institute of Technology. **Figure 5** shows the experimental setup. Pulsed neutrons were produced by the  ${}^7\text{Li}(p,n){}^7\text{Be}$  reaction with a pulsed proton beam (width:1.5 ns, repetition rate:4MHz, average beam current 7-10  $\mu\text{A}$ ) from the 3-MV Pelletron accelerator. The incident neutron energy spectrum on a capture sample was measured by using a time-of-flight (TOF) method with a  ${}^6\text{Li}$ -glass detector located at a flight length of 30 mm. **Figure 6** shows the incident neutron energy spectrum in the  ${}^{93}\text{Nb}$  measurements. Neutrons at energies less than 100 keV were produced. The average neutron energy was 46 keV. Capture gamma-rays were detected with an anti-Compton NaI(Tl) spectrometer by using TOF method. The flight length from neutron source to the sample was 12 cm. **Figure 7** shows TOF spectra of the NaI(Tl) spectrometer in the  ${}^{93}\text{Nb}$  measurements. A broad bump around 460 ch is capture events in the sample. A sharp peak at 640 ch is the  ${}^7\text{Li}(p,g){}^8\text{Be}$  reaction from the neutron source.

The neutron capture cross sections are derived by the pulse-height weighting technique. The capture cross section of  ${}^{197}\text{Au}$  was used as standard of cross section. Data analysis to derive capture cross sections and capture gamma-ray spectra is currently underway.



**Fig. 6** Incident neutron energy spectrum in the  ${}^{93}\text{Nb}$  measurement

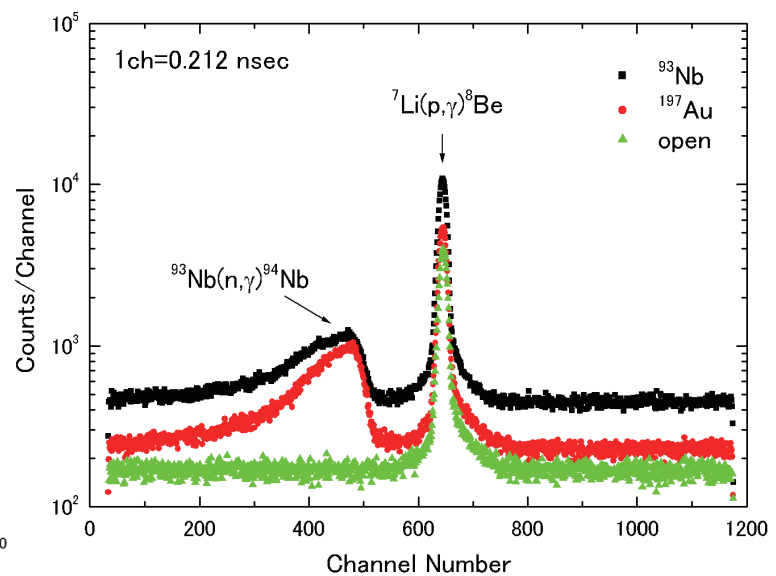


**Fig. 7** NaI(Tl) TOF spectra in the  ${}^{93}\text{Nb}$  measurement

#### 4. Summary

We performed theoretical calculation of capture gamma-ray spectra and capture cross section of  ${}^{93}\text{Nb}$ ,  ${}^{103}\text{Rh}$  and  ${}^{115}\text{In}$ . The model parameters were adjusted to reproduce the available experimental data. Only one experimental data of capture gamma-ray spectrum is available for  ${}^{93}\text{Nb}$ . No experimental capture gamma-ray data exists for  ${}^{103}\text{Rh}$  and  ${}^{115}\text{In}$ . In according to this experimental data situation, tentatively-determined gamma-ray strength functions were used in the theoretical calculation.

In order to improve the current data situation, we carried out measurement of the neutron capture cross section and capture gamma-ray spectrum for  ${}^{93}\text{Nb}$ ,  ${}^{103}\text{Rh}$  and  ${}^{115}\text{In}$ . Measurement was made using a pulsed neutron source and the time-of-flight method. Data analysis to derive capture cross section and capture gamma-ray spectrum is currently underway. The derived capture cross sections and capture gamma-ray spectra will be used to

adjust the model parameters in the theoretical calculation. In particular, gamma-ray strength function must be improved. We will provide the theoretical calculation of the capture cross section using the refined model parameters in a wide neutron energy range.

### Reference

- [1]O. Iwamoto, ‘ Development of a comprehensive code for nuclear data evaluation, CCONE, and validation using neutron-induced cross sections for uranium isotopes ’, J. Nucl. Sci. Technol. 44[5], 687 (2007).
- [2]S. Kunieda *et al.*, ‘Coupled-channels Optical Model Analyses of Nucleon-induced Reactions for Medium and Heavy Nuclei in the Energy Region from 1 keV to 200MeV’, J. Nucl. Sci. Technol. 44[6], 838 (2007).
- [3]T. Belgya, O. Bersillon, R. Capote et al., Handbook for Calculations of Nuclear Reaction Data, RIPL-2, IAEA-TECDOC-1506, International Atomic Energy Agency (IAEA) (2006).
- [4]J. Voignier, S. Joly, and G. Grenier, ‘ Capture cross sections and gamma-ray spectra from the interaction of 0.5 to 3.0 MeV neutron with nuclei in the mass range A=63 to 209 ’, J. Nucl. Sci. Eng. 112, 87 (1992).

## **23 Analysis of Radioactivity of the Ground Surface Measured at the Fukushima-Daiichi Nuclear Power Plant Site**

Go CHIBA

Graduate School of Engineering, Hokkaido University

Sapporo, Hokkaido, 060-8628

e-mail: [go\\_chiba@eng.hokudai.ac.jp](mailto:go_chiba@eng.hokudai.ac.jp)

Radioactivity of the ground surface at the Fukushima-daiichi nuclear power plant site has been continuously measured by several organizations. The present paper focuses on a time dependence of radioactivity ratios between an isotope having short half-life and another one having longer half-life. Through observation of this time dependence, it is confirmed that the radioactivity of the nuclides having short half-lives, such as Cs-134, Cs-136, Te-132 and Sr-89, has been monotonically decreasing after the accident. Numerical calculations yield consistent results with the measured data if appropriate fission yield data are employed.

### **1. Introduction**

There was quite a strong earthquake on March 11 in 2011 around the East Japan and the following Tsunami caused severe damages to the Fukushima-daiichi nuclear power plant (NPP) units 1, 2, 3 and 4. All the AC powers and the ultimate heat sinks were completely lost in these units, and nuclear fuels were melted in the units 1, 2 and 3. Although possibility of recriticality in these units is considered quite low, it cannot be zero. It has been confirmed that these units are not in a critical state by continuous measurements of the plant observable data, such as coolant temperature and radioactivity level.

Radioactivity of the ground surface of the Fukushima-daiichi NPP site has been continuously measured and the results have been reported on the web site of the Tokyo Electric Power Company (TEPCO). In the present study, we observe a time dependence of radioactivity ratios between different isotopes, and see whether radioactivity of the nuclides having short half-lives has been monotonically decreasing or not after the accident. By doing this, we can confirm that there is no recriticality with a high power in the reactor cores and no severe radioactivity leakage from them. Furthermore, we perform numerical calculations under some assumptions and compare the results with the measured data.

### **2. Time dependence of radioactivity ratio between different isotopes**

Radioactivity of several nuclides has been measured for the ground surface of the Fukushima-daiichi NPP site and the measured results have been reported. Here we observe a time dependence of the radioactivity of nuclides having short half-lives. Since absolute values of the measured radioactivity significantly depend on a measurement condition, we take a ratio of radioactivity of an isotope having short half-life to that of a different isotope having longer half-life. Since chemical behaviors of different isotopes are considered same, dependence on a measurement

condition can be cancelled out in a radioactivity ratio. Radioactivity ratios considered in the present study are Cs-134/Cs-137 (its effective half-life is 2.22 years), Cs-136/Cs-137 (13.18 days), Sr-89/Sr-90 (50.53 days) and Te-132/Te-129m (3.5 days).

We use measured data reported on a web site of TEPCO from April 6 to December 16 [1]. The measured data for radioactivity ratios are fitted to an exponential function with effective half-life by the least square method. **Figures 1 to 4** show a time dependence of measured radioactivity ratios with fitted functions. It is confirmed through observing these figures that radioactivity of nuclides having short half-lives has been monotonically decreasing after the accident. Radioactivity ratios at a time of a reactor shutdown are also estimated from the fitted curves.

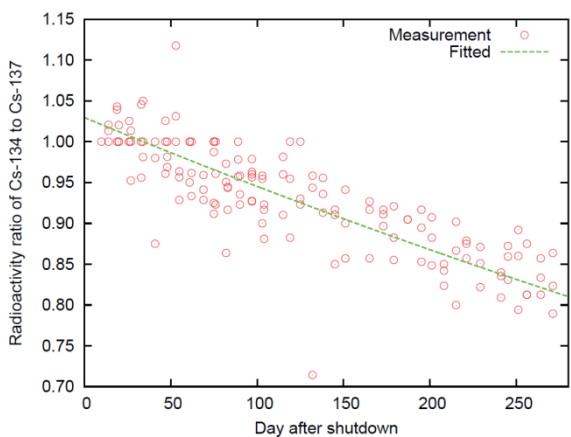


Fig. 1 Measured radioactivity ratio Cs-134/Cs-137

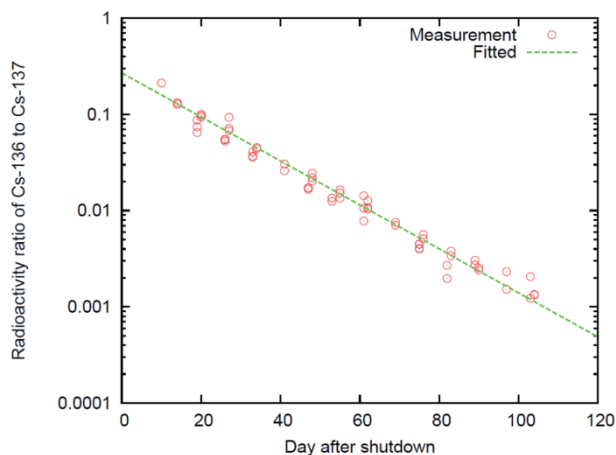


Fig. 2 Measured radioactivity ratio Cs-136/Cs-137

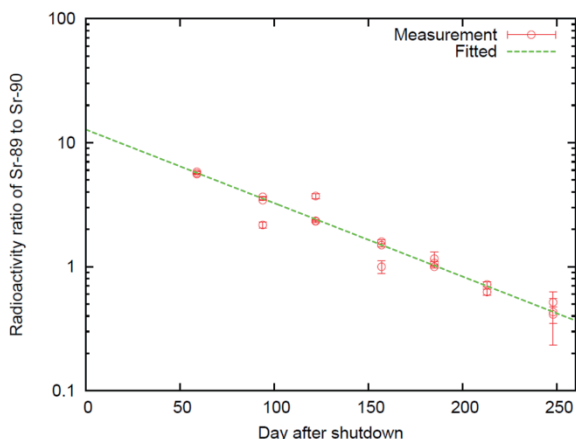


Fig. 3 Measured radioactivity ratio Sr-89/Sr-90

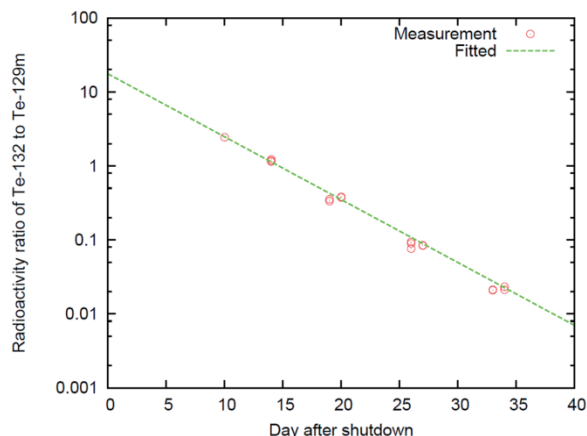


Fig. 4 Measured radioactivity ratio Te-132/Te-129m

### 3. Comparison with numerical result

In this section, we perform numerical calculations under several assumptions and compare the results with the measurement-based ones estimated in the preceding section.

For numerical calculations we use two light water reactor fuel pin cells: a UO<sub>2</sub> cell (STEP-III) and a MOX cell (plutonium content of 8%). Detailed information of fuel compositions and geometric data of these fuel cells are taken from Ref. [2]. We assume that a void fraction in a coolant region is 40% and a linear power density is 175 W/cm. In order to see a dependence of calculated radioactivity ratios on these parameters, additional calculations with a different linear power density of 200 W/cm or with a different void fraction of about 70% in a coolant region are carried out for the UO<sub>2</sub> cell.

All the calculations are performed with an in-house reactor physics calculation code system. A 107-group cross section library based on JENDL-4.0 [3] is used, and 107-group effective cross sections are calculated by the equivalence theory with the Dancoff factor. Eigenvalues and neutron fluxes are calculated with the collision probability method. Fuel burnup is treated with a nuclide chain model of the SRAC2006 code [4], which is composed of 40 heavy nuclides and about 200 fission products. JENDL-3.3 is used only for fission product yield data.

Numerical results are shown in **Figs. 5 to 8**, where a straight line indicates radioactivity ratios at the reactor shutdown estimated in the preceding section. Radioactivity ratio Cs-134/Cs-137 seems to be a linear function to the time. Detail investigation to this quantity can be found elsewhere [5]. We observe a large discrepancy between a numerical result and a measurement-based result in a radioactivity ratio Cs-136/Cs-137 if the MOX cell is used. Thus it is probable that the origin of the radioactivity emitted to the environment is a UO<sub>2</sub> fuel. It is also interesting to see that calculation conditions such as a linear power density and a void fraction do not affect a time dependence of a radioactivity ratio Sr-89/Sr-90. So a burnup period can be roughly estimated at about 900 days for the UO<sub>2</sub> fuel. On the other hand, a radioactivity ratio Cs-134/Cs-137 depends on calculation conditions. If we assume that a burnup period is 900 days, it is suggested that a linear power density or a void fraction should be larger. A numerical result for a radioactivity ratio Te-132/Te-129m significantly differs from a measurement-based result. Since this radioactivity ratio is determined mainly by the fission product yield, we take different cumulative yield data for Te-132 and Te-129m from different nuclear data libraries and re-do numerical calculations for the UO<sub>2</sub> cell. **Table 1** shows the fission yield data for Te-129m and Te-132 from various nuclear data libraries. There is a large difference in the fission yield data for Te-129m among different nuclear data libraries. **Figure 9** shows a numerical result. The result agrees with the measurement-based result much better if the JEFF-3.1.1 data is employed. This result suggests that a re-evaluation of the fission yield data for Te-129m of the JENDL library is required.

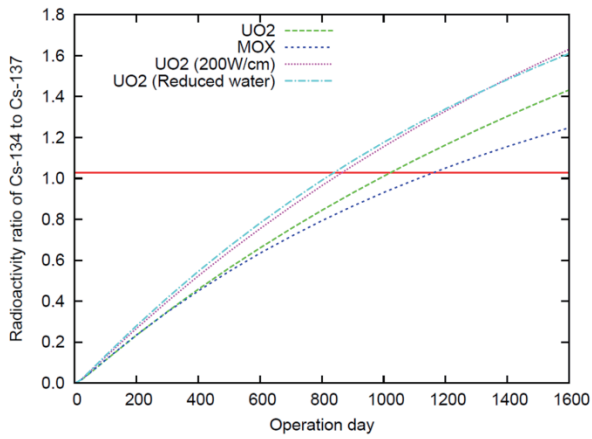


Fig. 5 Calculated radioactivity ratio Cs-134/Cs-137

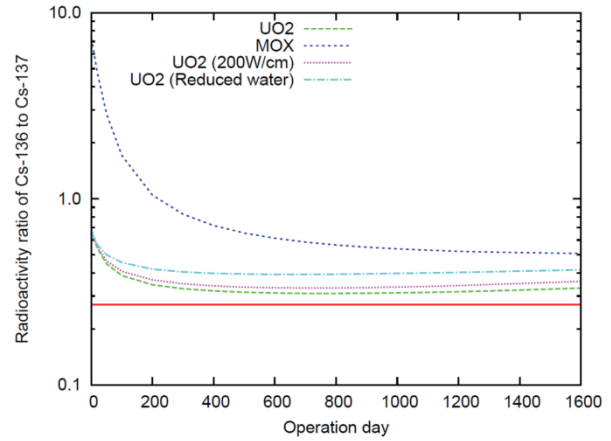


Fig. 6 Calculated radioactivity ratio Cs-136/Cs-137

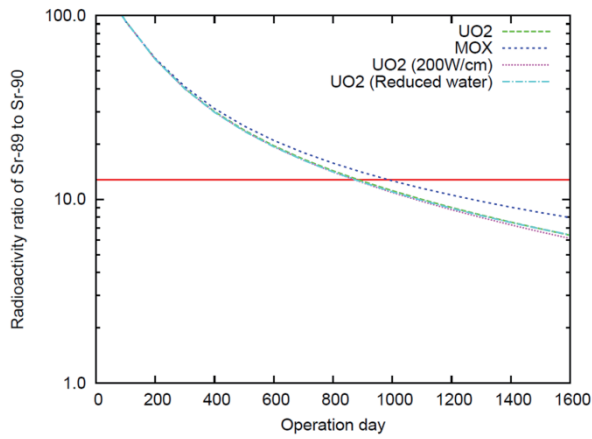


Fig. 7 Calculated radioactivity ratio Sr-89/Sr-90

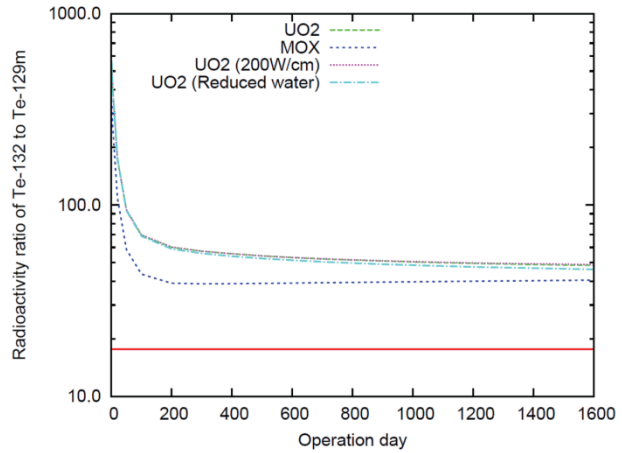


Fig. 8 Calculated radioactivity ratio Te-132/Te-129m

Table 1 Fission yields of Te-129m and Te-132 of various nuclear data files

Fissile	Library	Te-129m	Te-132	(Te-132/Te-129m)
U-235 (Thermal)	JENDL-3.3	7.199e-4	4.283e-2	59.5
	JENDL-4.0	4.771e-4	4.289e-2	89.9
	JEFF-3.1.1	2.771e-3	4.276e-2	15.4
	ENDF/B-VII.0	9.021e-4	4.295e-2	47.6
Pu-239 (Thermal)	JENDL-3.3	1.567e-3	5.202e-2	33.2
	JENDL-4.0	1.095e-3	5.139e-2	46.9
	JEFF-3.1.1	5.652e-3	5.095e-2	9.0
	ENDF/B-VII.0	2.280e-3	5.139e-2	22.5

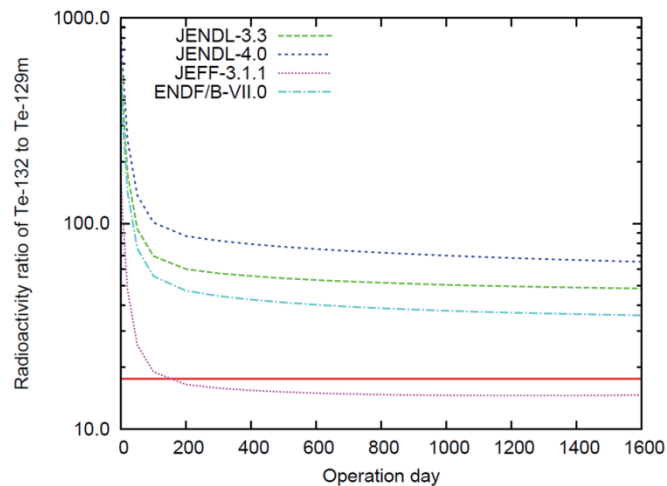


Fig.9 Radioactivity ratio Te-132/Te-129m calculated with various fission yield data

#### 4. Conclusion

The radioactivity of the ground surface at the Fukushima-daiichi NPP site has been continuously measured and reported. The present paper focuses on a time dependence of radioactivity ratios between different isotopes. Through observation of this time dependence, it is confirmed that the radioactivity of nuclides having short half-lives, such as Cs-134, Cs-136, Te-132 and Sr-89, has been monotonically decreasing after the accident. Numerical calculations yield consistent results with the measured data when appropriate fission yield data are utilized for numerical calculations.

#### References

- [1] <http://www.tepco.co.jp/cc/press/index-j.html>
- [2] J. Katakura, et al., A set of ORIGEN2 cross section libraries based on JENDL-3.3 library: ORLIBJ33, JAERI-Data/Code 2004-015, Japan Atomic Energy Research Institute (2004).[in Japanese]
- [3] K. Shibata, et al., JENDL-4.0: a new library for nuclear science and engineering, J. Nucl. Sci. Technol., 48[1], p.1-30 (2011).
- [4] K. Okumura, et al., SRAC2006: a comprehensive neutronics calculation code system, JAEA-Data/Code 2007-004, Japan Atomic Energy Agency (2007).
- [5] T. Endo, Estimation of average burnup of damaged fuels loaded in Fukushima Dai-ichi reactors by using the Cs-134/Cs-137 ratio method, (this proceeding).

**Appendix**

For readers' conveniences, cumulative fission yield data for Cs-134, Cs-136, Cs-137 and those for Sr-89 and Sr-90 are shown in **Tables 2** and **3**.

Table 2 Fission yields of Cs-134, Cs-136 and Cs-137 of various nuclear data files

Fissile	Library	Cs-133	Cs-136	Cs-137
U-235 (Thermal)	JENDL-3.3	6.689e-2	5.472e-5	6.269e-2
	JENDL-4.0	6.702e-2	5.529e-5	6.175e-2
	JEFF-3.1.1	6.596e-2	5.838e-5	6.221e-2
	ENDF/B-VII.0	6.699e-2	5.538e-5	6.188e-2
Pu-239 (Thermal)	JENDL-3.3	7.016e-2	8.134e-4	6.727e-2
	JENDL-4.0	6.976e-2	9.742e-4	6.605e-2
	JEFF-3.1.1	6.995e-2	7.601e-4	6.588e-2
	ENDF/B-VII.0	7.016e-2	9.743e-4	6.607e-2

Table 3 Fission yields of Sr-89 and Sr-90 of various nuclear data files

Fissile	Library	Sr-89	Sr-90	(Sr-89/Sr-90)
U-235 (Thermal)	JENDL-3.3	4.725e-2	5.772e-2	0.82
	JENDL-4.0	4.885e-2	5.904e-2	0.83
	JEFF-3.1.1	4.690e-2	5.729e-2	0.82
	ENDF/B-VII.0	4.733e-2	5.782e-2	0.82
Pu-239 (Thermal)	JENDL-3.3	1.722e-2	2.103e-2	0.82
	JENDL-4.0	1.712e-2	2.101e-2	0.81
	JEFF-3.1.1	1.689e-2	2.013e-2	0.84
	ENDF/B-VII.0	1.723e-2	2.104e-2	0.82

## **24 Design and Construction of A Thermal Column Using An Am-Be Neutron Source for BNCT Studies**

Kazuyuki HARADA\*, Isao MURATA

Division of Electrical, Electronic and Information Engineering, Osaka University

Yamada-oka 2-1, Suita, Osaka, 565-0871 Japan

\*E-mail: kharada@ef.eie.eng.osaka-u.ac.jp

At present, accelerator-based neutron sources are under development worldwide for spread of boron neutron capture therapy (BNCT). In the accelerator-based neutron source, the neutron energy spectrum becomes distorted. We are now developing various devices for BNCT. The objective of the present study is thus to develop thermal and epithermal columns for basic experimental studies for the new measuring devices. In the present paper, details of design and construction of a thermal column are described using an Am-Be neutron source.

### **1. Introduction**

Boron neutron capture therapy (BNCT) is a strong cancer therapy which becomes popular recent years. However, there are only two experimental nuclear reactors which can be utilized for BNCT. More recently, accelerator-based neutron sources are under development for spread of BNCT. In case of the accelerator-based neutron source compared with a nuclear reactor, it is known that the neutron energy spectrum of the former source becomes distorted. Measuring the neutron flux intensity and spectrum is thus indispensable. The authors' group is developing a new spectrometer based on a proportional counter, which aims at realization of precise measurement of thermal and epithermal neutron spectra for BNCT.[1]

BNCT is a radiation therapy which destroys tumor cells, suppressing influence against healthy cells. However estimation of the treatment effect is known to be difficult in real time, because it is quite hard to know the exact neutron flux intensity and boron concentration in real time during irradiation. The author's group is developing a SPECT system for BNCT to monitor the treatment effect during the BNCT irradiation.[2]

These new devices for BNCT should be tested very carefully before practical applications using a standard neutron field. The objective of our research is to develop thermal and epithermal columns for various basic experiments for BNCT studies.

### **2. Thermal Column Design**

#### **2.1 Design requirement for thermal column**

We designed a suitable thermal column for basic experiments for BNCT using an Am-Be neutron source. In

the OKTAVIAN facility of Osaka University, there are 4 Am-Be sources which were used for a subcritical assembly in the past, the intensity of which is about  $10^6$  n/sec. The design requirement of the thermal column is as follows:

- ① Thermal neutron flux intensity should be larger than  $1 \times 10^3$  n/cm<sup>2</sup>/sec taking into account detector calibration experiments.
- ② Cd ratio should be larger than 10 to decrease effect of epi-thermal neutrons.
- ③ Gamma-ray dose should be kept to be as low as possible simultaneously suppressing direct contribution of a 4.44 MeV gamma-ray emitted from the Am-Be source.(Fig. 1)

We examined moderator/reflector/gamma-ray shielding material for basic experiments for BNCT to meet the above-mentioned conditions with a Monte Carlo N-Particle Code, MCNP5 with an evaluated nuclear data library, ENDF/B-6.

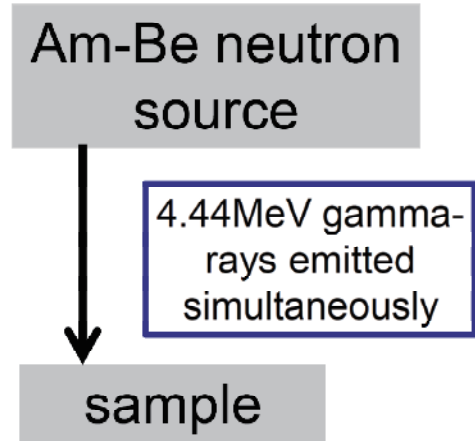


Fig. 1. 4.44 MeV gamma-rays emitted from Am-Be neutron source

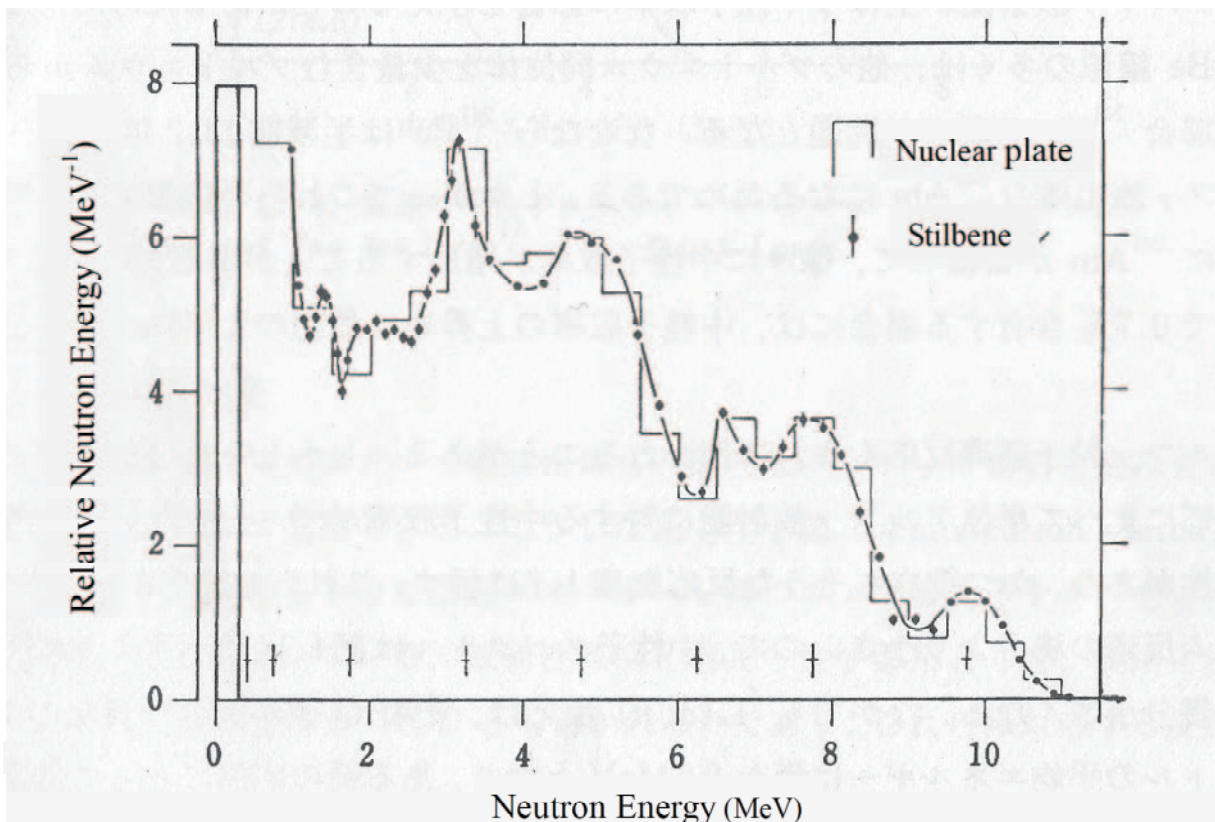


Fig. 2. Measured value of the energy spectrum of the neutron generated from <sup>239</sup>Pu-Be neutron source

## 2.2. Design calculation

We designed a thermal column of about 1 meter cubic with Be, heavy water, polyethylene, graphite and lead.

Beryllium plays a neutron multiplier role in the thermal column in case of using an Am-Be neutron source. Heavy water and polyethylene are moderators. Graphite is a reflector and lead shields gamma-rays. We carried out precise neutron and gamma-ray transport calculations with MCNP5 and optimized the thermal column so as to achieve a reasonable thermal neutron flux intensity, Cd ratio and gamma-ray dose, and so on described in the previous section. In the present calculations we used a source neutron spectrum of  $^{239}\text{Pu}$ -Be instead of Am-Be as shown in Fig. 2 [3]. According to our calculations, 15 cm thick heavy water and 5 cm thick polyethylene are the best configuration for the moderator to achieve a proper neutron flux. 40 cm graphite is an optimized thickness for the reflector. Finally, we designed a thermal neutron column as in Fig. 3. The calculated neutron and gamma-ray spectra are shown in Fig. 4.

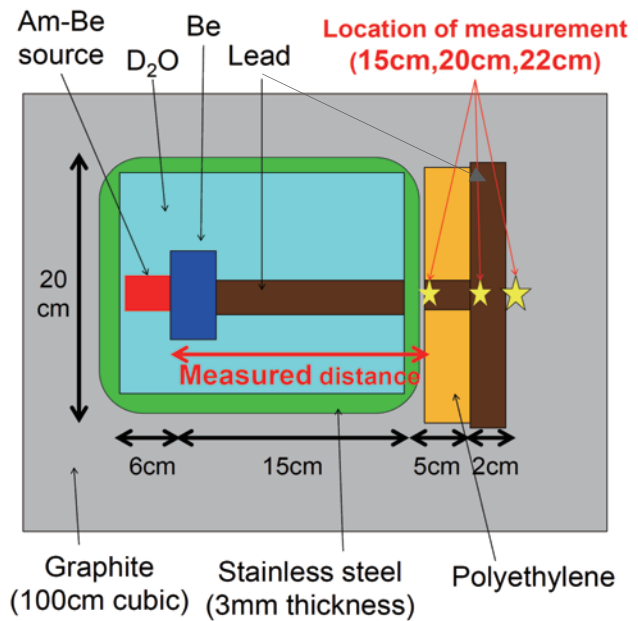


Fig. 3. Side view of the thermal column

According to our calculations, 15 cm thick heavy water and 5 cm thick polyethylene are the best configuration for the moderator to achieve a proper neutron flux. 40 cm graphite is an optimized thickness for the reflector. Finally, we designed a thermal neutron column as in Fig. 3. The calculated neutron and gamma-ray spectra are shown in Fig. 4.

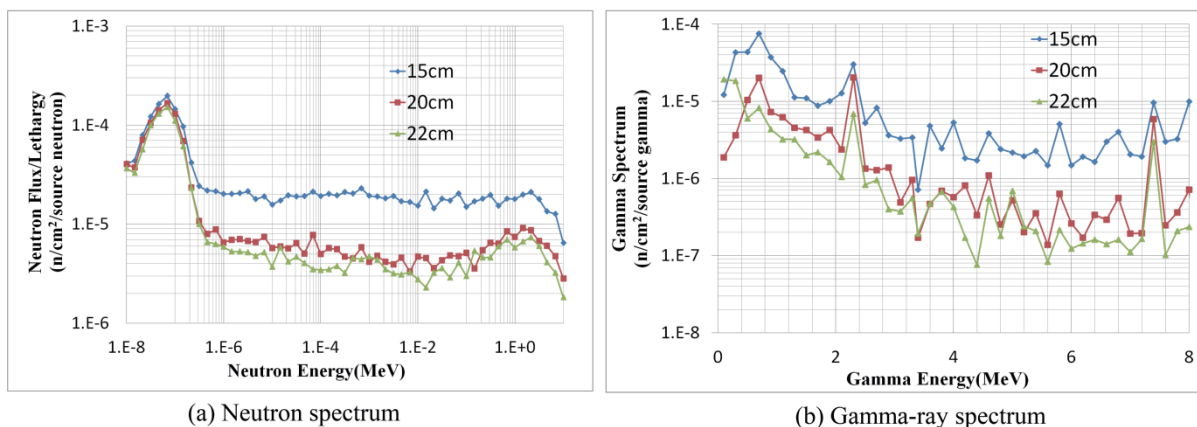


Fig.4. MCNP calculation results for thermal column (distances:15cm,20cm,22cm)

## 3. Characteristic Measurement Of The Optimized Thermal Column

### 3.1. Experimental method

#### (a) Measurement of the neutron flux

We constructed the optimized thermal column at the OKTAVIAN facility of Osaka University using an Am-Be

source of 46.3 GBq, which is equivalent to the neutron intensity of  $2.4 \times 10^6$  n/sec. The inside photo of the actual experiment system is shown in Fig. 5. We set a naked gold foil and a gold foil covered with a Cd sheet to the location of measurement described in the figure. After one or two day irradiation, we measured the gamma-ray intensity using a HpGe detector to evaluate the thermal neutron intensities and Cd ratios at 15 cm, 20 cm and 22 cm from the source.

(b) Measurement of gamma-ray dose

We measured gamma-ray dose using a gamma-ray survey meter by the following procedures.

- ① Measure gamma-ray dose in the column at 15 cm, 20 cm and 22 cm from the source.
- ② Measure 4.44 MeV gamma-ray dose outside the column with the same lead shield as used in the column, which is positioned between the source and the detector. Measurements are conducted at 15 cm, 20 cm and 22 cm from the source.
- ③ Same as ②, but without the lead shield.

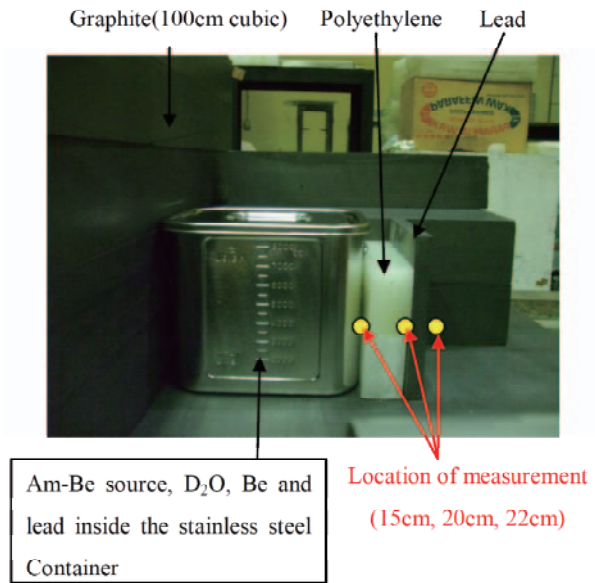


Fig. 5. Side view of experimental system

3.2. Results and discussion

(a) Results of the neutron flux measurement

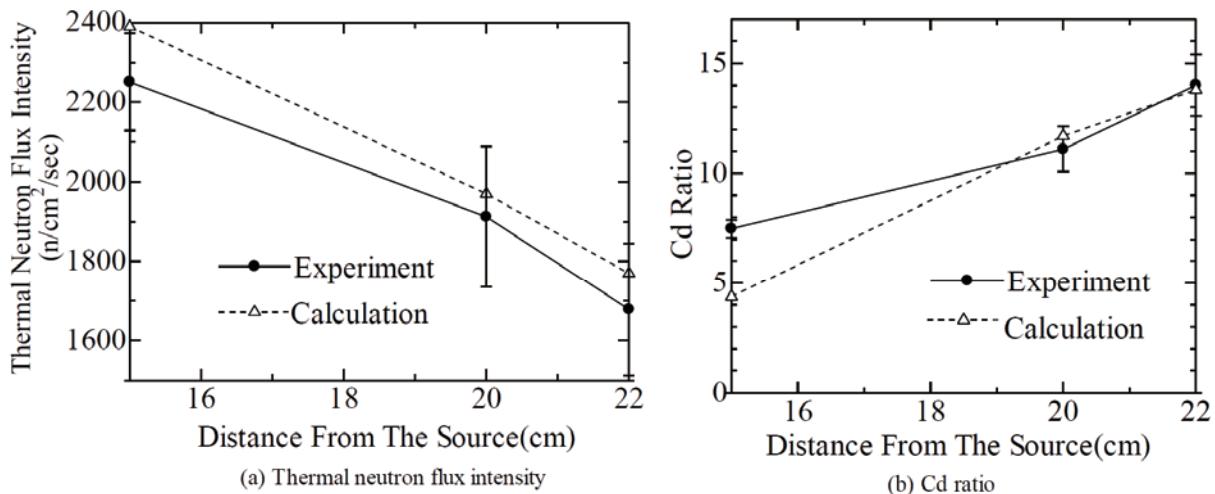


Fig. 6. Comparison of experimental results of neutron flux measurement with MCNP5 calculation

Comparison of experimental and calculated values of thermal neutron flux intensity and Cd ratio is described in Fig. 6. At all the three positions, measured thermal neutron flux intensities were larger than  $1 \times 10^3$  n/cm<sup>2</sup>/sec,

and Cd ratios at measured distances of 20 and 22 cm were 11.1 and 14.0, respectively, being larger than 10. We could obtain good results of thermal neutron flux intensity and Cd ratio. Comparing the experimental and calculated values of the thermal neutron intensity and Cd ratio, a fairly good agreement was obtained.

(b) Results of the gamma-ray dose measurement

Results of experimental values of gamma-ray dose are described in Fig. 7. Curves of black circles, triangles and squares are for ①, ② and ③, respectively. From the results of all gamma-ray and Am-Be + lead gamma-ray, the effect of decaying the 4.44 MeV gamma-ray of a lead shield has been confirmed to be sufficient. Moreover, it has been found that the gamma-ray intensity of 4.44 MeV became quite small compared with other results as seen in the result of MCNP of Fig. 4.

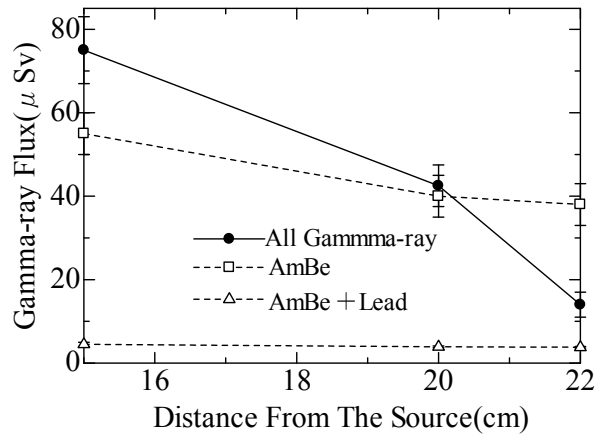


Fig. 7. Comparison of experimental results of Gamma-ray dose with MCNP5 calculation

4. Future Works

In recent years, it is said that epithermal neutrons are a more efficient option for BNCT to treat deep seated tumors such as Glioblastoma multiforme. Epithermal neutrons are moderated down to thermal energy after passing through normal brain tissues. The author’s group is developing a new spectrometer based on a proportional counter, which aims at realization of precise measurement of thermal and epithermal neutron spectra for BNCT. For this purpose, we are now developing an epithermal neutron source.

We are carrying out precise neutron and gamma-ray transport calculations with MCNP5 to optimize an epithermal neutron column for basic experiments so as to achieve a reasonable epithermal neutron flux intensity and gamma-ray dose. We preliminarily

designed an epithermal column of about 80 cm cubic with Be, AlF<sub>3</sub>, Ti, graphite and lead as shown in Fig. 8. The calculated results of neutron and gamma-ray spectra are shown in Fig. 9. It is planned to construct the designed epithermal column and measure the neutron flux and gamma-ray dose soon

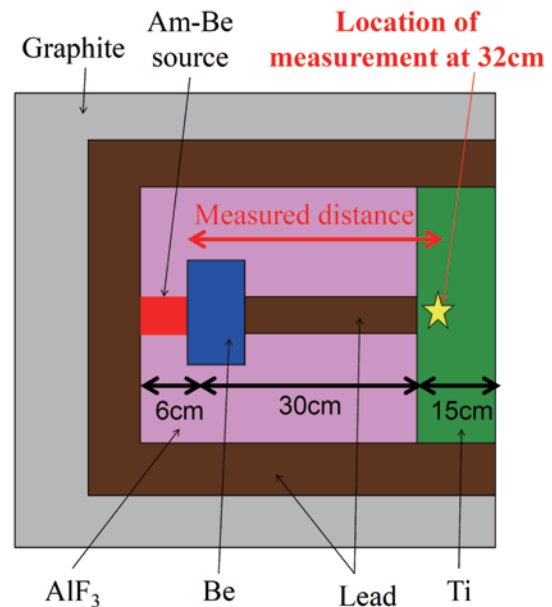


Fig. 8. Side view of the epithermal column

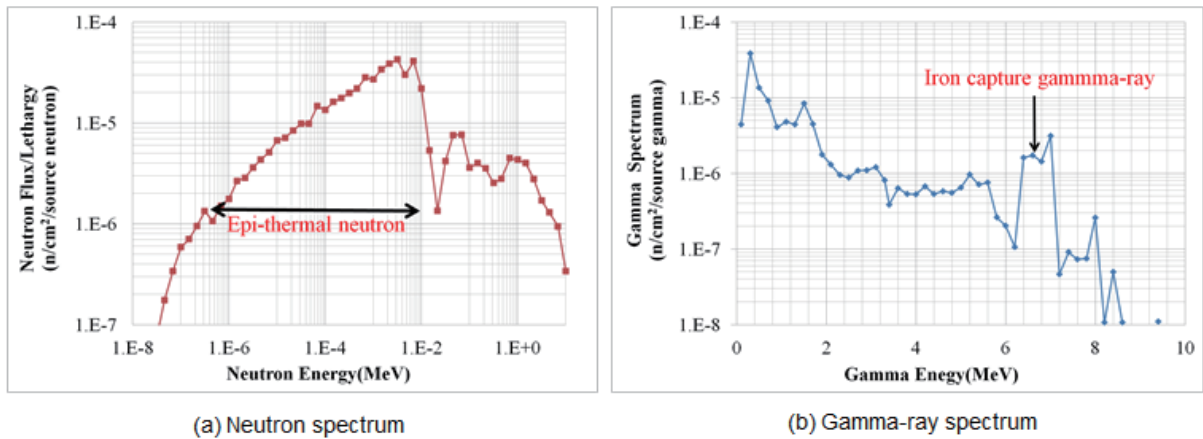


Fig. 9. MCNP calculation results for epithermal column

## 5. Conclusion

We have designed an optimized thermal column using an Am-Be neutron source so as to achieve a reasonable thermal neutron flux intensity, Cd ratio and gamma-ray dose by MCNP5 especially for basic researches of BNCT. We then constructed the optimized thermal column and measured the thermal neutron flux and Cd ratio thereafter. Compared with calculations, it was confirmed the constructed thermal column had an acceptable performance as obtained by the design calculation.

In the next phase, we will construct an optimized epithermal column and measure the neutron flux and gamma-ray dose.

## References

- [1] M. Ito, I. Murata, "Thermal / epi-thermal neutron spectrometer with a  $^3\text{He}$  position sensitive proportional counter," *Proc. 2010 Annual Symposium on Nucl. Data*, pp. 95-100, Nov. 25-26, 2010, C-CUBE, Chikushi Campus, Kyushu University (2011).
- [2] I. Murata, T. Mukai, S. Nakamura, H. Miyamaru, I. Kato, "Development of A Thick CdTe Detector for BNCT-SPECT," *Appl. Radiat. Isotopes*, 69, pp. 1706-1709 (2011).
- [3] G. F. Knoll, "Radiation Detection and Measurement, Second Ed.," John Wiley and Sons, Inc. (1989).

## 25 Measurement of $\gamma$ -ray-Production Double-Differential Cross Sections for 290 MeV/u Oxygen Ion Incidence

\*Haruhiko UEHARA<sup>a</sup>, Daisuke MORIGUCHI<sup>a</sup>, Tsuyoshi KAJIMOTO<sup>a</sup>  
 Keiichi HIRABAYASHI<sup>a</sup>, Hidetaka HIRANO<sup>a</sup>, Tomoya NISHIZAWA<sup>a</sup>  
 Nobuhiro SHIGYO<sup>a</sup>, Yusuke UOZUMI<sup>a</sup>, Daiki SATOH<sup>b</sup>, Toshiya SANAMI<sup>c</sup>  
 Yusuke KOBAYASHI<sup>d</sup>, Masashi TAKADA<sup>d</sup>, Naruhiro MATSUFUJI<sup>d</sup>

<sup>a</sup>*Department of Applied Quantum Physics and Nuclear Engineering Kyushu University  
 744 Motoooka, Nishi-ku, Fukuoka 819-0395, Japan*

<sup>b</sup>*Japan Atomic Energy Agency  
 2-4 Shirakatashirane, Tokai, Naka-gun, Ibaraki 319-1184, Japan*

<sup>c</sup>*High Energy Accelerator Research Organization  
 1-1 O-ho, Tsukuba, Ibaraki 305-0801, Japan*

<sup>d</sup>*National Institute of Radiological Sciences  
 4-9-1 Anagawa, Inage-ku, Chiba 263-8555, Japan*

*email : u.haruhiko@kune2a.nucl.kyushu-u.ac.jp*

$\gamma$ -ray-production double-differential cross sections for 290 MeV/u oxygen ion incidence on a carbon target which was 1.5 cm thick were measured with NE213 liquid organic scintillators. The scintillators 12.7 cm in diameter and 12.7 cm thick were placed in the directions of 15°, 30°, 45°, 60°, 75° and 90°. The measurement was carried out using a time-of-flight (TOF) method since the neutrons energies were also measured simultaneously. For measurement of background, measurement without target was practiced. We analyzed the prompt- $\gamma$ -rays data which was emitted within several nsec from incidence of the oxygen ions into the target. The  $\gamma$ -ray energy spectra were acquired from unfolding the integrated charge spectra as the scintillation light output ones using the response functions of the scintillators. The response functions were calculated by the EGS5 code and the unfolded energy spectra were derived using the FORIST code. The cross sections were obtained for  $\gamma$ -ray energy above 1 MeV, and compared with the calculation data of the PHITS2 code.

### 1. Introduction

The heavy-ion radiotherapy has advantages to be able to expect not only patient's return to society after treated but also the improvement of quality of life. As increasing the number of patients enrolled in the heavy-ion radiotherapy, the potential risk of radiation-induced second cancers has become a serious issue, especially for young patients [1, 2]. To investigate contribution of the secondary particles with simulation codes is expected. Some charged particles and neutrons production double-differential cross sections (DDXs) on biological elements, which is the experimental data to improve the accuracy of calculation codes, have been measured. Evaluation about the exposure to secondary  $\gamma$ -ray is not carried out until now since Relative Biological Effectiveness (RBE)

of a  $\gamma$ -ray is about 1, which has been considered that there is no influence in a human body. These days, however, to assess the amount of production of the  $\gamma$  ray is seemed to be important when making a treatment precise. The evaluation of the secondary  $\gamma$ -rays from the nuclear reactions induced by the carbon ions in the body is required. Especially, oxygen contained in the human body in the largest numbers after hydrogen is the second most important among the biological elements.

Since hydrogen have the difficulty in preparation as a target, we measured  $\gamma$ -ray-production double-differential cross sections for 290 MeV/u oxygen ions incidence on a carbon target. In addition, since it is also difficult to arrange a oxygen target, we performed the  $C(^{16}O, x\gamma)$  DDXs measurement to conduct inverse reaction analysis. The experimental data are compared with calculated results by the PHITS2 code [3].

## 2. Experimental procedure

The experiment was carried out at the PH2 beam line at the heavy ion accelerator facility HIMAC of the National Institute of Radiological Sciences, Chiba, Japan. A schematic view of the experimental setup is illustrated in Fig. 1. The  $\gamma$ -rays produced from a carbon target which was 1.5 cm thick and placed at an angle of  $45^\circ$  to the beam line were detected using the NE213 liquid organic scintillators, having the dimension of 12.7 cm in diameter and 12.7 cm thick, and the measurement was carried out using a time-of-flight (TOF) method since the neutrons energies were also measured simultaneously [4]. The NE213 detectors were placed to measure angular distributions at  $15^\circ$ ,  $30^\circ$ ,  $45^\circ$ ,  $60^\circ$ ,  $75^\circ$  and  $90^\circ$ .

A 0.5 mm thick plastic scintillator (beam pickup scintillator), made of NE102A

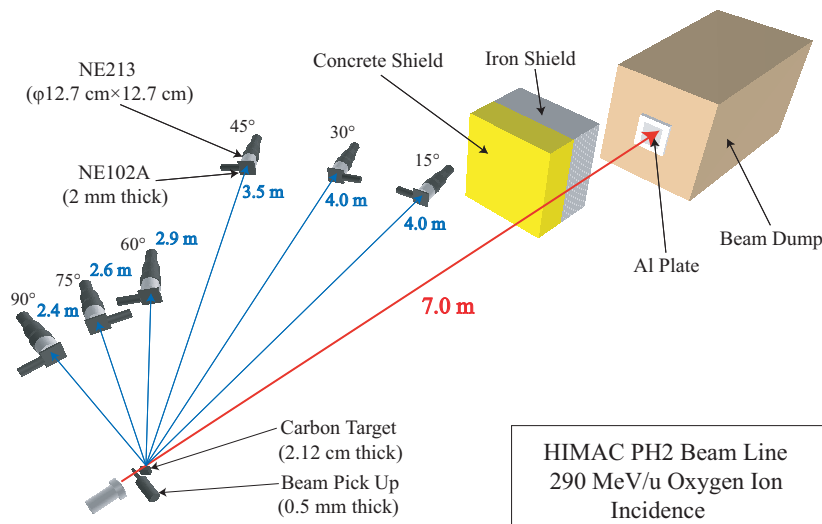


Fig. 1: Illustration of experimental setup

plastic scintillator, was set upstream of the target to measure the number of incident particles and to discriminate single incident particle events from multiple ones. Since the synchrotron was operated in a pulse mode (0.3 Hz repetition cycle) and incident oxygen beam intensity was very weak in level of  $10^4 \sim 10^5$  particles/3.3 sec, the number of incident oxygens can be individually counted. In measurement, we used an inverse TOF, defined as the time difference between the signal of the trigger in the NE213 detectors and the delayed beam pickup scintillator. A veto detector,  $150 \times 150 \times 2 \text{ mm}^3$ , made of NE102A plastic scintillator, was set in front of each NE213 scintillator to eliminate charged particle events. In order to reduce  $\gamma$ -rays from the beam dump, a couple of an iron of 63 cm thick and a concrete of 50 cm thick shields was placed between the detectors and beam dump. To estimate the background  $\gamma$ -rays, the measurement without a target was carried out.

### 3. Data analysis

In order to determine the number of incident carbon ions, beam pickup scintillator monitored them. The beam pickup scintillator, however, detected not only the events induced to single incident ion but also plural incident ions as one ion. As clearly shown in Fig. 2, when two or three projectiles pass through the beam pickup scintillator coincidentally, the pulse heights seem to be twice or three times higher than that of single projectile. The analysis was gone on with only the events induced to single incident ion, and the number of projectiles was corrected with the ratio of the single events to the all events. In this work, we analyzed using the prompt- $\gamma$ -rays data which was emitted within several nsec from incidence of the oxygen ions into the target [5].

The energy calibration curve was given by fitting the Compton edges of standard  $\gamma$ -ray sources,  $^{60}\text{Co}$  and Am-Be, below a few MeV region. In the energy region above a few MeV, the calibration was performed using signal charge for the recoil protons. The neutron energy was determined from the time differences between prompt- $\gamma$ -rays and neutrons. The results of energy calibrations in the energy regions below and above a few MeV are shown in Fig. 3 and Fig. 4, respectively. After these data were connected, the neutron energy was transformed into the  $\gamma$ -ray energy.

In order to obtain the  $\gamma$ -ray production spectra, measured charge spectra were unfolded. Unfolding was carried out by the FORIST code [6]. Fig. 5 indicates the response functions of NE213 detectors calculated by the EGS5 code [7], where energy resolutions of the detectors were considered.

$\gamma$ -ray production DDXs were obtained by subtracting the results of the background measurement from those of the foreground, after normalization with the number of incident oxygens.

### 4. Results and discussion

The  $\gamma$ -ray-production double-differential cross sections are indicated in Fig. 6 for

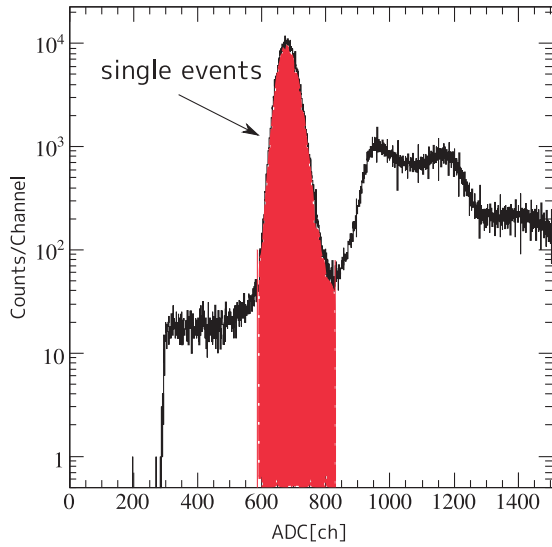


Fig. 2: Pulse-height spectrum of the beam pick up detector

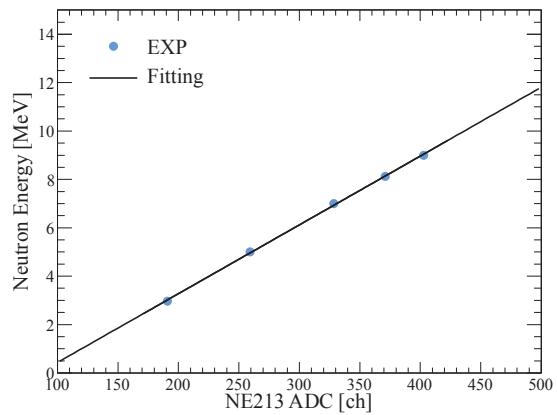


Fig. 3: Energy calibration in the energy region below about 10 MeV

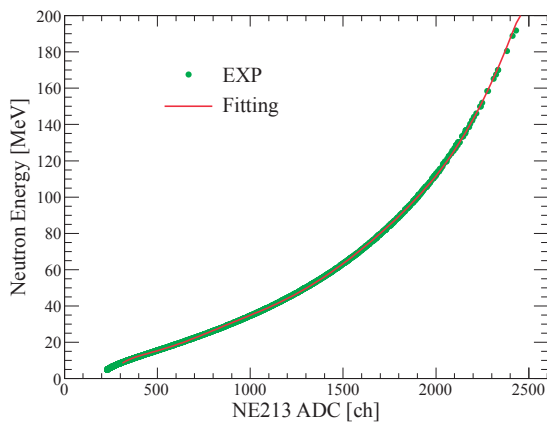


Fig. 4: Energy calibration in the energy region above about 10 MeV

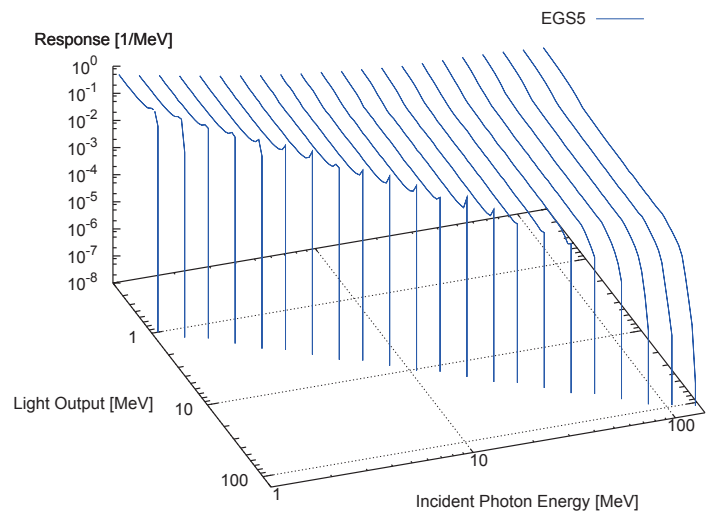


Fig. 5: Response functions of the NE213

incident oxygen energies of 290 MeV/u on C. The only statistical error was taken into account. The  $\gamma$ -ray production DDXs were obtained for  $\gamma$ -ray energy region between 1MeV and 60MeV. The experimental results were compared with the calculation data of the PHITS2 code. Although differences between the experimental values and the calculated values are not so large, the PHITS2 code overestimates the experimental data below 25 MeV, while it underestimates them above 25 MeV.

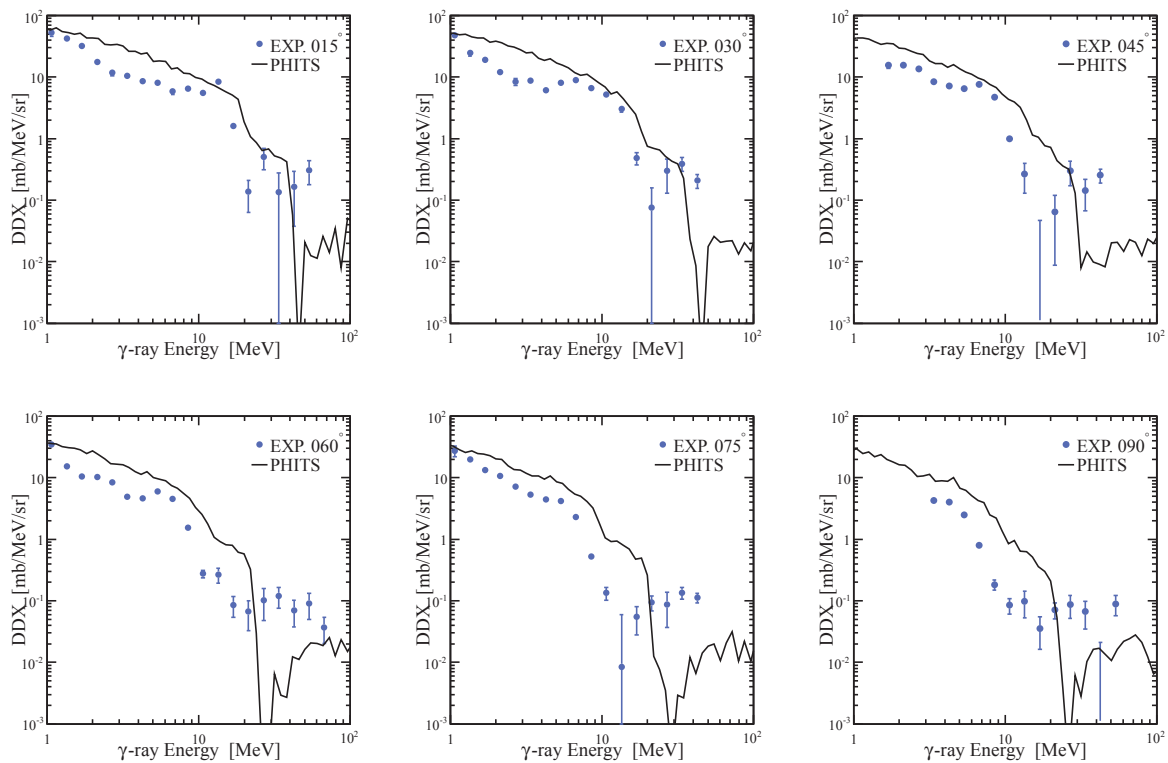


Fig. 6: Comparison the experimental and the calculated values with the PHITS2 code for the  $\gamma$ -ray-production double-differential cross sections for the  $C(O, x\gamma)$  reaction at the incident oxygen energy of 290 MeV/u on C

## 5. Summary

We measured the double-differential cross sections for  $C(O, x\gamma)$  reaction to conduct inverse reaction analysis for the  $O(C, x\gamma)$  reaction. The 290 MeV/u oxygen ions were used as incident particles. An NE102A plastic scintillator and six NE213 liquid organic scintillators were employed to monitor the number of incident oxygen particles and to detect produced  $\gamma$ -rays, respectively. The energy calibration was performed using the Compton edges of standard  $\gamma$ -ray sources and neutron energy obtained from recoil protons. Unfolding was carried out by the FORIST code. The response functions of NE213 detectors were calculated by the EGS5 code. The cross sections were obtained for  $\gamma$ -ray energy region between 1MeV and 60MeV. The PHITS2 code overestimates the experimental data below 25 MeV, while it underestimates them above 25 MeV.

## Acknowledgement

We are grateful to Dr. T. Murakami and staffs of the HIMAC for their generous support of our experiments. This work was supported by Grant-in-Aid for Scientific Research (B) 22360406.

## References

- [1] C. Z. Jarlskog, and H. Paganetti, "Risk Developing Second Cancer from Neutron Dose in Proton Therapy as Function of Field Characteristics, Organ, and Patient Age," *Int. J. Radiation Oncology Biol. Phys.*, **72**, 228(2008).
- [2] E. J.Hall, "Intensity-Modulated Radiation Therapy, Protons, and Risk of Second Cancers," *Int. J. Radiation Oncology Biol. Phys.*, **65**, 1(2006).
- [3] K. Niita, N. Matsuda, Y. Iwamoto, H. Iwase, T. Sato, H. Nakashima, Y. Sakamoto, and L. Sihver, "PHITS: Particle and Heavy Ion Transport code System, Version 2.23," JAEA-Data/Code 2010-022, Japan Atomic Energy Agency, (2010).
- [4] D. Satoh, D. Moriguchi, T. Kajimoto, H. Uehara, N. Shigyo, M. Ueyama, M. Yoshioka, Y. Uozumi, T. Sanami, Y. Koba, M. Takada, N. Matsufuji, "Measurement of neutron-production double-differential cross-sections on carbon bombarded with 290MeV/nucleon carbon and oxygen ions," *Nucl. Instr. and Meth. A*, **644**, 1(2011), 59.
- [5] K. Iga, K. Ishibashi, N. Shigyo, K. Maehata, N. Matsufuji, T. Nakamoto, M. Numajiri, S. Meigo, H. Takada, S. Chiba, "Measurement of Gamma-Ray Production Double-Differential Cross-Sections for 1.5GeV  $\pi^+$  Meson Incidence on Iron," *Journal of Nuclear Science and Technology*, **37**, 3(2000), 211.
- [6] R. H. Johnson, D. T. Ingersoll, B. W. Wehring, and J. J. Dorning, "NE-213 neutron spectrometry system for measurements from 1.0 to 20 MeV," *Nucl. Instrum. Methods*, **145** (1977), 337.
- [7] H. Hirayama, Y. Namito, A. F. Bielajew, S. J. Wilderman, and W. R. Nelson, "The EGS5 Code System," SLAC-R-730, (2005).

## 26 Identification of High-Energy Levels in $^{147}\text{Ce}$ with a Total Absorption Clover Detector

Yosuke Shima<sup>1\*</sup>, Yasuaki Kojima<sup>2</sup>, Michihiro Shibata<sup>2</sup>,  
Hiroaki Hayashi<sup>3</sup>, Akihiro Taniguchi<sup>4</sup>

<sup>1</sup>*Graduate School of Engineering, Nagoya University*

<sup>2</sup>*Radioisotope Research Center, Nagoya University*

<sup>3</sup>*Institute of Health Biosciences, The University of Tokushima Graduate School*

<sup>4</sup>*Research Reactor Institute, Kyoto University*

\*E-mail: shima.yosuke@g.mbox.nagoya-u.ac.jp

By using a total absorption clover detector having almost  $4\pi$  solid angle, a decay scheme of fission product  $^{147}\text{La}$  ( $Q_{\beta} = 5366$  keV) separated by an on-line mass separator was proposed up to high energy region about 3500 keV. In measured spectra with the detector, sum peaks were strongly observed owing to large coincidence summing effects and those correspond to excited levels. Fifty six levels and a hundred sixty  $\gamma$ -rays of daughter nucleus  $^{147}\text{Ce}$  were preliminarily identified. To determine  $\gamma$ -ray intensities properly, a correction method using a Monte Carlo simulation for coincidence summing effects was also proposed.

### 1. Introduction

Decay schemes are fundamental information as nuclear data. In particular,  $\beta$ -branching ratios are important for studies on nuclear structure and calculations of decay heat. These values reflect spins and parities of excited levels and average energies of  $\beta$ -rays are needed for the calculations of decay heat. The  $\beta$ -branching ratio to each level is deduced from the imbalance between  $\gamma$ -ray intensities populating and depopulating each level. Therefore, the cascade relation of  $\gamma$ -rays and the  $\gamma$ -ray intensities is necessary. For unstable nuclei far off the  $\beta$ -stability line, it is difficult to identify the cascade relation and the  $\gamma$ -ray intensities from high-energy levels because unstable nuclei far off the  $\beta$ -stability line have large  $\beta$ -decay energies ( $Q_{\beta}$  values), then, there are many  $\gamma$ -rays and complicated cascade relation, and some of the  $\gamma$ -ray intensities are weak. In this study, we propose an effective method using a total absorption clover detector having both large volume Ge crystals and large solid angle to identify high-energy levels and cascade relation of  $\gamma$ -rays and to determine the  $\gamma$ -ray intensities. We applied the method to fission product  $^{147}\text{La}$  and identified level structure of the daughter nucleus  $^{147}\text{Ce}$  including high-energy excited levels. The  $Q_{\beta}$  value of  $^{147}\text{La}$  was reported to be 5366 keV [1]; nevertheless the excited levels in  $^{147}\text{Ce}$  have been reported only up to 924.3 keV [2]. It is expected that  $^{147}\text{Ce}$  has much higher levels.

## 2. A total absorption clover detector, and identification of high-energy levels and cascade $\gamma$ -rays with the detector

Figure 1 shows a schematic drawing of the total absorption clover detector. The detector is composed of four large Ge crystals ( $80 \text{ mm}^\Phi \times 90 \text{ mm}^L \times 4$ ). Along the central axis of the detector, there is a through hole ( $15 \text{ mm}^\Phi \times 165 \text{ mm}^L$ ). An inner window of the hole is made by  $0.4 \text{ mm}^t$  aluminum. Radioactive sources can be put into the through hole with a large solid angle of 98%. Energy signals and the corresponding time information of the four Ge crystals were recorded in the event-by-event mode. Obtained list mode data are analyzed by two modes: singles and add-back mode. In the singles mode, four individual spectra of Ge crystals were summed and stored in the singles spectrum. In the add-back mode, energy signals from the different crystals corresponding to coincident events, for example, incidence of cascade  $\gamma$ -rays and Compton scattering between the crystals, were summed and stored in the add-back spectrum. Figure 2 shows experimentally determined full energy peak efficiencies and simulated ones using the Monte Carlo simulation code GEANT4 [3]. A solid line, a dashed line and a dot line indicate the efficiencies in the add-back mode, in the singles mode and of one Ge crystal, respectively. Open circles indicate experimental efficiencies obtained using  $^{203}\text{Hg}$ ,  $^{137}\text{Cs}$  and  $^{54}\text{Mn}$ . The efficiency in the add-back mode is six times higher than that of the singles mode with one Ge crystal because energies of scattered photons are summed and reconstructed in the add-back mode.

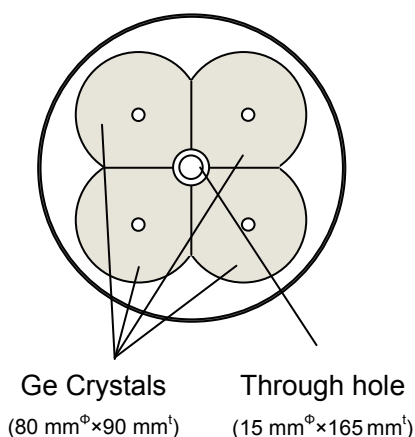


Fig. 1 A schematic drawing of the total absorption clover detector.

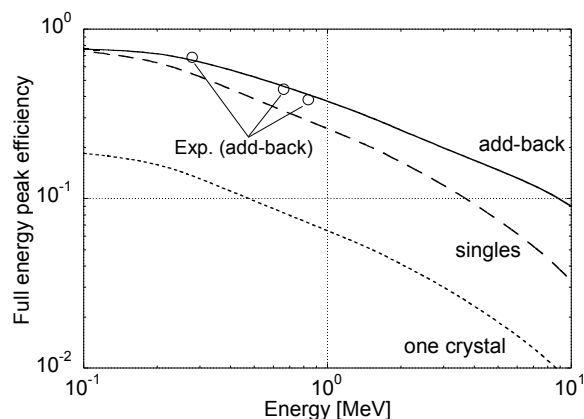


Fig. 2 Full energy peak efficiencies of the total absorption clover detector. A solid line, a dashed line and a dot line indicate the simulated efficiencies in the add-back mode, in the singles mode and of one Ge crystal, respectively. Open circles indicate the experimental efficiencies in the add-back mode using  $^{203}\text{Hg}$ ,  $^{137}\text{Cs}$  and  $^{54}\text{Mn}$ .

Here, we consider measurement of the radioactive nucleus having a schematic decay scheme as shown in Fig. 3. Solid lines and arrows indicate identified levels and  $\gamma$ -rays, respectively. On the other hand, dashed lines and arrows indicate missing levels and  $\gamma$ -rays, respectively. In the add-back mode, cascade  $\gamma$ -rays are effectively absorbed due to the large coincidence effects and those energies are summed. Summed  $\gamma$ -rays (thick arrows) are strongly observed as sum peaks in the add-back spectrum and those correspond to excited levels. Therefore, excited levels can be identified. In this data acquisition system, sum peaks are composed of the coincident events and can be decomposed into individual Ge signals. Thus,  $\gamma-\gamma$ ,  $\gamma-\gamma-\gamma$  or  $\gamma-\gamma-\gamma-\gamma$  cascade relation can be identified.

### 3. Experiments

The total absorption clover detector was installed at the Kyoto University Research Reactor (KUR). The  $^{147}\text{La}$  isotope was produced with the neutron-induced fission reaction of  $^{235}\text{U}$ . The 93% enriched  $\text{UF}_4$  of 50 mg was irradiated by a thermal neutron flux of  $3 \times 10^{12} \text{ n/cm}^2/\text{s}$ . The isotope was mass-separated by the on-line isotope separator (ISOL) [4]. Figure 4 shows a schematic drawing of the experimental setup at KUR-ISOL. The mass-separated isotopes were collected on an aluminized Mylar tape and periodically transported to the measurement position. The collecting and the measuring times are set at 8.0 and 8.0 s, respectively. The tape was sandwiched between a pair of semi-cylindrical plastic  $\beta$ -ray stoppers of 7 mm thick. Gamma-rays following the decay of  $^{147}\text{La}$  were measured for 24 hours. The detector was shielded with lead blocks of 5 or 10 cm thick and boron doped polyethylene blocks of 5 cm thick.

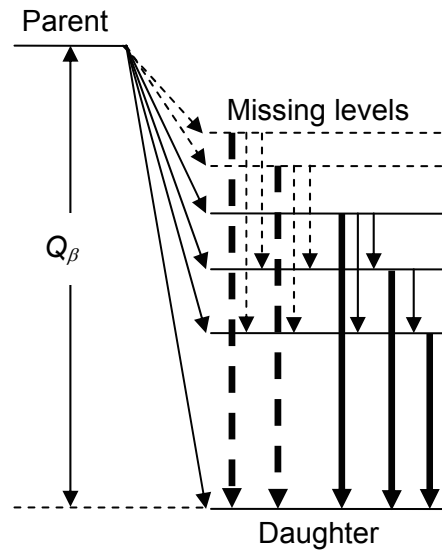


Fig. 3 A schematic decay scheme. Solid lines and arrows indicate identified levels and  $\gamma$ -rays, respectively. Dashed lines and arrows indicate missing levels and  $\gamma$ -rays, respectively. Summed  $\gamma$ -rays (thick arrows) in the add-back mode correspond to excited levels.

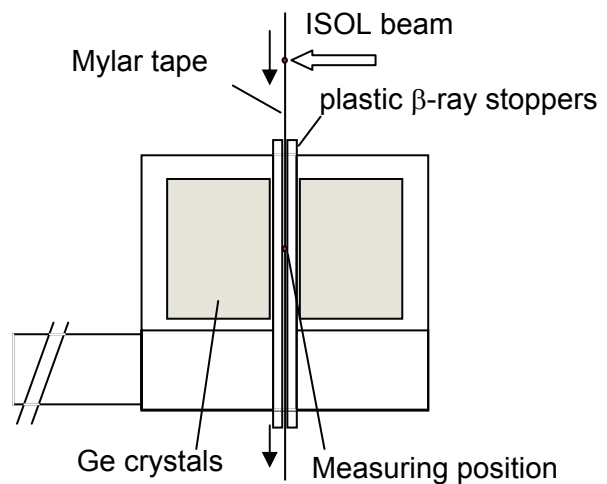


Fig. 4 A schematic drawing of the experimental setup at KUR-ISOL.

#### 4. Results and discussion

A singles and an add-back spectrum were obtained using an off-line sorting program. Figure 5 shows a part of the singles (dashed line) and add-back (solid line) spectrum in the decay of  $^{147}\text{La}$ . The closed circles correspond to sum peaks of newly identified levels in  $^{147}\text{Ce}$ . It shows that sum peaks are strongly observed in the add-back spectrum compared to those in the singles one. In the preliminary analysis, 56 levels from 1000 to 3500 keV were identified for the first time, as shown in Fig. 6.

In the data acquisition system in this experiment, add-back spectra can be decomposed into coincident events. Cascade relation of  $\gamma$ -rays in the newly identified levels in  $^{147}\text{Ce}$  is investigated with decomposition process. For example, Fig. 7 shows a decomposed spectrum of the 3509 keV sum peak. Peaks in this spectrum indicate cascade  $\gamma$ -rays which de-excite from the 3509 keV level. The nine  $\gamma$ -rays were found by the decomposition of the level. In this way, a partial decay scheme was constructed as shown in the inset of Fig. 7. These cascade  $\gamma$ -rays were also observed in  $\gamma-\gamma$  or  $\gamma-\gamma-\gamma$  coincidence measurements vice versa. Preliminarily, 160  $\gamma$ -rays in  $^{147}\text{Ce}$  were observed.

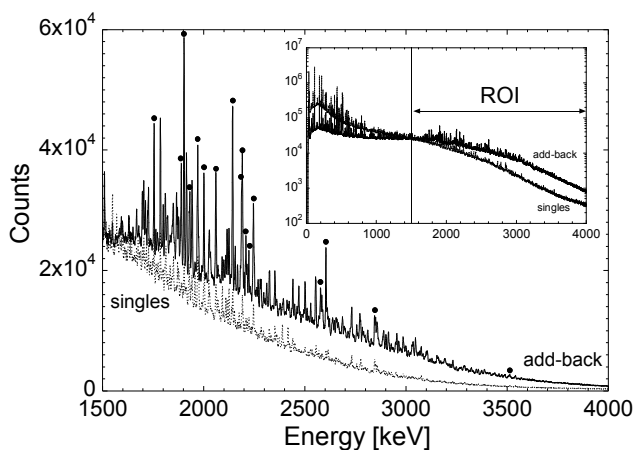


Fig. 5 A singles and an add-back spectra in the decay of  $^{147}\text{La}$ . The inset shows overall spectra and a region of interest (ROI). Closed circles indicate some of newly observed excited levels in  $^{147}\text{Ce}$ .

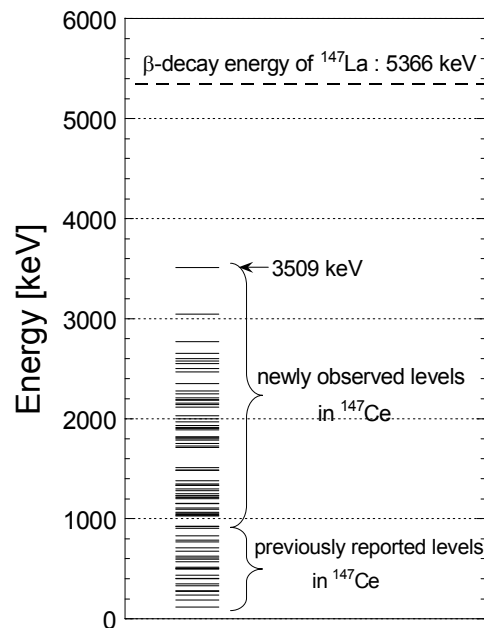


Fig. 6 Newly observed and previously reported levels in  $^{147}\text{Ce}$ .



## 5. Conclusions

By using a total absorption clover detector, a method to identify high-energy levels and cascade relation of  $\gamma$ -rays was proposed. The decay of fission product  $^{147}\text{La}$  was measured with the detector. As a result, 56 levels and 160  $\gamma$ -rays in  $^{147}\text{Ce}$  were preliminarily identified. A coincidence summing correction method using Monte Carlo calculation was also proposed for the determination of  $\gamma$ -ray intensities. Experimental  $\gamma$ -ray intensities of  $^{134}\text{Cs}$  were properly corrected by the method. Further analyses for  $^{147}\text{Ce}$  are in progress.

## Acknowledgments

This study is partially supported by “Study on nuclear data by using a high intensity pulsed neutron source for advanced nuclear system” entrusted to Hokkaido University by the Ministry of Education, Culture, Sports, Science and Technology of Japan (MEXT). The measurements of high-energy levels in  $^{147}\text{Ce}$  were carried out under the Research Collaboration Program of the Research Reactor Institute, Kyoto University.

## References

- [1] H. Hayashi *et al.*, Nucl. Instrum. Meth. A **606** (2009) 484.
- [2] J. D. Robertson *et al.*, Phys. Rev. **40** (1989) 2804.
- [3] S. Agostinelli *et al.*, Nucl. Instrum. Meth. A **506** (2003) 250.
- [4] A. Taniguchi *et al.*, Nucl. Instrum. Meth. A **351** (1994) 378.
- [5] N. Nica, Nucl. Data Sheets **110** (2009) 749.

## 27 Neutron Capture Cross Section of Palladium-107 in the Thermal-Neutron Energy Region

Shoji.NAKAMURA<sup>1</sup>, Masayuki OHTA<sup>1,†</sup>, Masumi OSHIMA<sup>1</sup>, Fumito KITATANI<sup>1</sup>,  
Atsushi KIMURA<sup>1</sup>, Tadahiro KIN<sup>1</sup>, Mitsuo KOIZUMI<sup>1</sup>, Shinji GOKO<sup>1,‡</sup>, Yosuke TOH<sup>1</sup>,  
Kaoru Y.HARA<sup>1</sup>, Hideo HARADA<sup>1</sup>, Kentaro HIROSE<sup>1</sup>, Kazuyoshi FURUTAKA<sup>1</sup>,  
Masayuki IGASHIRA<sup>2</sup>, Tatsuya KATABUCHI<sup>2</sup>, Motoharu MIZUMOTO<sup>2</sup>,  
Koichi KINO<sup>3</sup>, Yoshiaki KIYANAGI<sup>3</sup>,  
Jun-ichi HORI<sup>4</sup>, Koichi TAKAMIYA<sup>4</sup>, Satoshi FUKUTANI<sup>4</sup>, and Toshiyuki FUJII<sup>4</sup>

<sup>1</sup> Nuclear Science and Engineering Directorate, Japan Atomic Energy Agency

<sup>2</sup> Research Laboratory for Nuclear Reactors, Tokyo Institute of Technology

<sup>3</sup> Faculty of Engineering, Hokkaido University

<sup>4</sup> Research Reactor Institute, Kyoto University

Present address: <sup>†</sup> Fusion Research and Development Directorate, Japan Atomic Energy Agency

<sup>‡</sup> Storage and Transport Safety Evaluation Gr., Japan Nuclear Energy Safety Organization

E-mail: nakamura.shoji@jaea.go.jp

The neutron capture cross section of <sup>107</sup>Pd in the thermal-neutron energy region has been measured relative to the <sup>10</sup>B(n,αγ) reaction cross section by the neutron time-of-flight (TOF) method. The relative cross section was normalized to the average value calculated by the SAMMY code with JENDL-4.0 at the three energy points: 6.8 eV of <sup>107</sup>Pd, 11.8 eV of <sup>105</sup>Pd, and 33 eV of <sup>108</sup>Pd. Neutron-capture γ rays were measured with a large Ge detector array called “4πGe spectrometer”, which is one component of the Accurate Neutron-Nucleus Reaction measurement Instrument (ANNRI) installed at the neutron Beam Line No.4 (BL04) of the Materials and Life science experimental Facility (MLF) in the Japan Proton Accelerator Research Complex (J-PARC). This paper presents new findings on resonance assignments of <sup>107</sup>Pd, and the preliminary cross section.

### 1. Introduction

Production of long-lived fission products (LLFPs) in nuclear reactors has caused the problems of fuel handling, reprocessing, and waste disposal. Neutron absorption in LLFPs has an important effect on their net production. This caused a demand for improved neutron capture cross sections of LLFPs. Seven nuclei were listed up as the most important LLFPs[1], namely <sup>79</sup>Se, <sup>93</sup>Zr, <sup>99</sup>Tc, <sup>107</sup>Pd, <sup>126</sup>Sn, <sup>129</sup>I, and <sup>135</sup>Cs.

Palladium-107 is considered to be of importance because of its extremely long half-life ( $6.5 \times 10^6$  year [2]) and not so small cumulative fission yield (3 % [3] for <sup>239</sup>Pu). In spite of the demand for the accurate cross-section data for <sup>107</sup>Pd, there exist only a few experimental data available. One of the reasons is that an activation method is not applicable for <sup>107</sup>Pd because its daughter nucleus is stable. Singh *et al.* [4] measured the cross section of <sup>107</sup>Pd, and obtained the level parameters for 34 resonances below 700 eV with the Rensselaer Polytechnic Institute (RPI) Gaertner Laboratory electron linear accelerator. Macklin [5] made neutron capture measurements at the Oak Ridge Electron Linear Accelerator (ORELA)

time-of-flight facility, and analysed one hundred thirty resonance peaks up to 3.5 keV. In these past measurements, they did not pay attention for the cross-section behaviour in the thermal energy region, and therefore there was only the evaluated value for the thermal-neutron capture cross-section ( $\sigma_0$ ) of  $^{107}\text{Pd}$ . Recently, one of the authors determined the thermal-neutron capture cross section of  $^{107}\text{Pd}$  with a prompt  $\gamma$ -ray spectroscopic method, and reported the value of  $9.16 \pm 0.27$  b [6], which was about five times larger than the evaluated one (1.8 b) [7]. It was necessary to examine carefully the behaviour of the cross sections of  $^{107}\text{Pd}$  in the thermal energy region. In this paper, the preliminary results of  $^{107}\text{Pd}$  are reported.

## 2. Experiment

A  $^{107}\text{Pd}$  enriched pellet was supplied by the Nuclear Research and consultancy Group (NRG) of Netherlands. The same Pd sample as used to make the  $^{107}\text{Pd}$  pellet was analyzed in detail with a Thermal Ionization Mass Spectrometer (TIMS) at the Kyoto University Research Reactor Institute. The isotopic abundances of Pd isotopes in the sample are summarized in **Table 1** in comparison with the natural abundances. The abundance of  $^{107}\text{Pd}$  was precisely obtained as  $15.3 \pm 0.1$  %.

**Table 1** Isotopic abundances (%) of the Pd sample analyzed by TIMS

Mass	102	104	105	106	107	108	109
Sample	0.0	$1.6 \pm 0.4$	$48.8 \pm 0.8$	$23.1 \pm 0.3$	$15.3 \pm 0.4$	$8.7 \pm 0.3$	$2.6 \pm 0.3$
Natural	1.0	11.1	22.3	27.3	0.0	26.5	11.7

The  $^{107}\text{Pd}$  enriched pellet was 137.37 mg in weight, 4.523 mm in diameter and 0.917 mm in thickness. The pellet was encapsulated in an aluminium container, which was 229.76 mg in weight, 9.077 mm in diameter and 1.86 mm in thickness. Another aluminium container without the pellet was prepared for background measurements. A piece of natural boron was used for the neutron-flux measurement at the irradiation position, and a crystal of NaCl sample, which was irradiated with neutrons, was also used for a  $\gamma$ -ray energy calibration source. The boron and NaCl samples were packed in Teflon bags, respectively.

The measurements were performed using Accurate Neutron-Nucleus Reaction measurement Instrument (ANNRI), which is installed at the neutron Beam Line No.4 (BL04) of the Materials and Life Science Experimental Facility (MLF) in the Japan Proton Accelerator Research Complex (J-PARC). The ANNRI has a large Ge detectors array called “ $4\pi\text{Ge}$  spectrometer”, which consists of two cluster-Ge detectors, eight coaxial Ge detectors and BGO Compton-suppression detectors. **Figure 1** shows the  $4\pi\text{Ge}$  spectrometer. In this study, we used only the two cluster-Ge detectors and BGO detectors. The  $4\pi\text{Ge}$  spectrometer is placed at a distance of 21.5 m from the Japan Spallation Neutron Source in MLF. The pulsed-neutron beam was produced through the spallation reaction in Hg target bombarded by 3-GeV proton beam. The proton accelerator was operated at 120-kW power, and its repetition rate was 25 Hz. The proton beams are supplied in the double-bunched mode; they consist of two bunches, and each bunch has a width of 0.1  $\mu\text{s}$  and an interval of 0.6  $\mu\text{s}$ . Each sample was set at the center of the spectrometer. The neutron beam was collimated into a diameter of 3 mm at the irradiation position using a rotary collimator system [8]. A 37.5 mm Pb filter was placed to suppress the  $\gamma$  flash at the upstream of the BL04.

The signals from the cluster-Ge crystals were processed using a data acquisition system [9] in event-by-event mode as a two-dimensional data of  $\gamma$ -ray pulse height and Time-of-Flight.

Neutron-capture  $\gamma$  rays emitted from the sample were measured with the  $4\pi$  Ge spectrometer using the TOF method. The measurement time was about 31 hours for the  $^{107}\text{Pd}$  sample. Its counting rate was about 13k events/sec. To estimate the background, a measurement with the empty aluminum container was also done. A small plate of boron piece containing  $^{10}\text{B}$  was used for the neutron-flux measurement at the irradiation position [10].

### 3. Data Analysis

The TOF spectrum corresponding to the flux of neutrons was derived by gating on the 478-keV  $\gamma$  ray emitted through the  $^{10}\text{B}(n,\alpha\gamma)^7\text{Li}$  reaction. The energy dependence of flux of neutrons was deduced from the gated TOF spectrum and the neutron capture cross section of  $^{10}\text{B}$  in JENDL-3.3[7].

The background subtraction from TOF spectra of  $^{107}\text{Pd}$  was performed using the TOF spectra from the empty aluminum container. The normalization of the background TOF spectrum was performed with yields of the prompt  $\gamma$ -rays emitted from the neutron capture reaction of  $^{27}\text{Al}$ .

Dead time changes depending on time in the whole detection system, and changes largely under the influence of huge resonances of the samples and the  $\gamma$  flash. For making a dead-time correction[11], external random-timing pulses made with a random pulse generator (Berkeley Nucleonics, DB-2) were fed into every pre-amplifier of Ge crystal during measurements. The average pulse rate of the random pulse generator was 1 kHz. The dead-time correction factor was obtained by comparing the counts of input pulses with actually stored pulses.

The neutron self-shielding and multi-scattering effects were calculated with the Monte Carlo simulation code MCNP [12]. The size, shape, weight, and the isotope abundances of the samples were taken into account. The intensity distribution in radial of collimated neutron beam was also considered in the calculation. The details for these corrections are given in Ref.[13].

The neutron capture cross sections involving the contributions of both  $^{107}\text{Pd}$  and other Pd isotopes were derived in the energy range from 0.01 eV to 300 eV from the obtained TOF spectra relative to the cross sections of  $^{10}\text{B}$ . The relative cross sections were normalized to the values calculated by the SAMMY code[14] with JENDL-4.0[15] at the three energy points: 6.8 eV of  $^{107}\text{Pd}$ , 11.8 eV of  $^{105}\text{Pd}$ , and 33 eV of  $^{108}\text{Pd}$ .

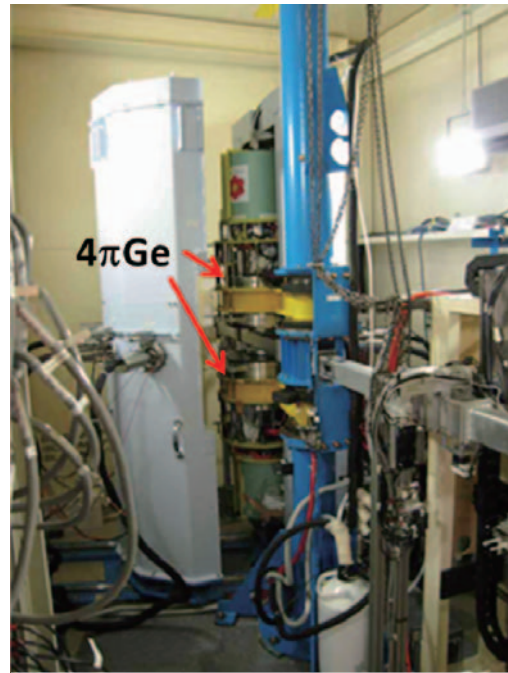


**Fig.1** A photo of the  $4\pi\text{Ge}$  spectrometer installed at the ANNRI in J-PARC / MLF.

### 4. Results and Discussion

Figure 2 shows the present result in the neutron energy ranging from 1 eV to 100 eV. In the present analyses, some new information was obtained for the resonances at 2.9 eV, 3.9 eV, and 5.2 eV. The identified nuclides are shown with parentheses in Fig.2. The first resonance peak of  $^{108}\text{Pd}$  at 2.9 eV is too small compared to that of JENDL-4.0[15]. The neutron width  $\Gamma_n$  of the 2.9-eV resonance was obtained as  $0.0018 \pm 0.0001$  meV by peak-fitting of the present data with the SAMMY code. On the other hand, the value of  $\Gamma_n$  in JENDL-4.0 is 0.01 meV, which is about five times larger than the present result.

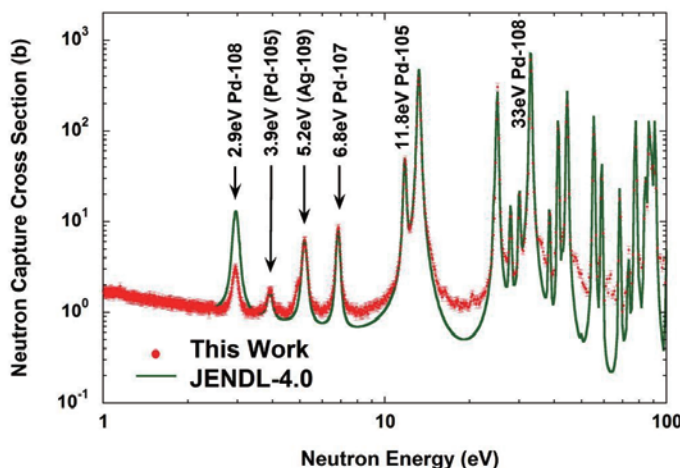


Fig.2 Present result of the cross section in the energy region ranging from 1 eV to 100 eV.

It was examined whether the 3.9-eV and 5.2-eV resonances were surely originated to  $^{107}\text{Pd}$  or not. Prompt  $\gamma$ -ray spectra were extracted by gating on the 3.9-eV and 5.2-eV resonance peaks, respectively. The prompt  $\gamma$ -ray spectra were obtained as shown in Figures 3a) and 3b). As shown in Fig.3 a), we observed only the prompt  $\gamma$ -rays originated from the neutron capture reaction of  $^{105}\text{Pd}$ . This shows that the 3.9-eV resonance is not originated to  $^{107}\text{Pd}$  but  $^{105}\text{Pd}$ . Since we use the Ge detectors, we can precisely distinguish which resonance is due to what kind of isotope.

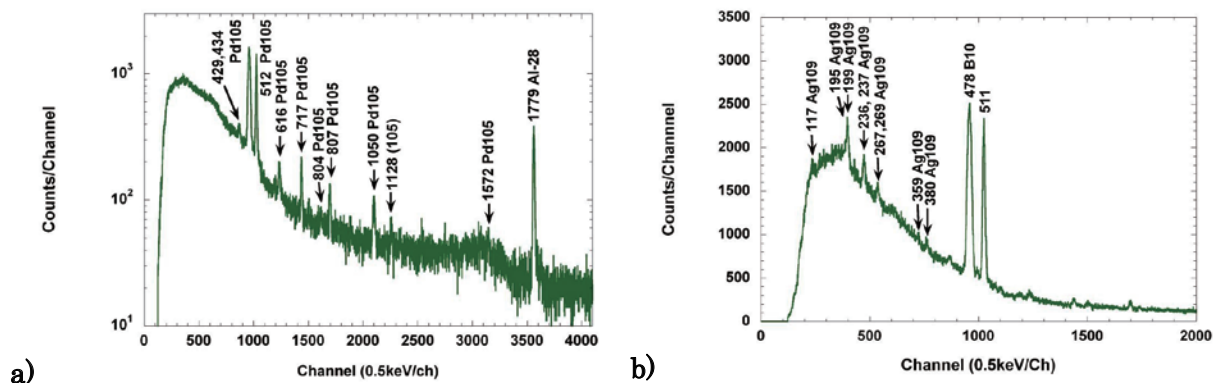
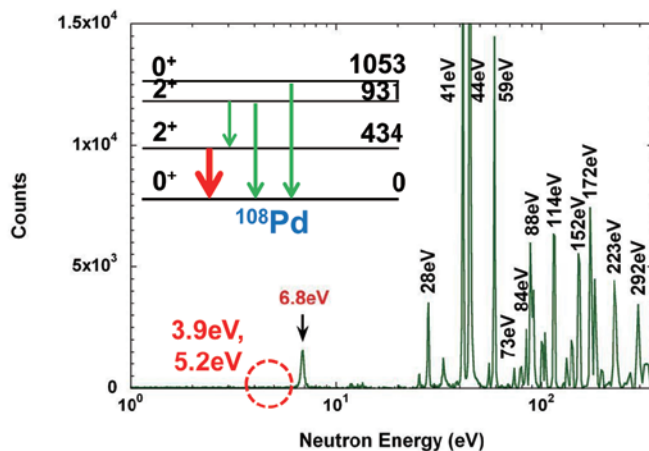


Fig.3 Gamma-ray spectra obtained by gating a) on the 3.9-eV resonance peak, and b) on the 5.2-eV one in the TOF spectrum, respectively.

As shown in Fig.3 b), only the prompt  $\gamma$ -rays due to the  $^{109}\text{Ag}$  were observed by gating on the 5.2-eV resonance peak. It seems that  $^{109}\text{Ag}$  was contained as a contaminant in the  $^{107}\text{Pd}$  sample. Since the first resonance of  $^{109}\text{Ag}$  at 5.2 eV has huge cross section as 20,000 b, the first resonance only appeared in the TOF spectrum. The abundance of  $^{109}\text{Ag}$  was found to be only 0.025 % by fitting the experimental data to the calculated values by SAMMY. Thus trace element analysis would be possible by using ANNRI.

To confirm those resonance peaks do not originate in  $^{107}\text{Pd}$ , the TOF spectrum was examined by gating at the 434-keV ground-state transition  $\gamma$  ray in the  $^{107}\text{Pd}(n,\gamma)$  reaction. **Figure 4** shows the gated TOF spectrum. There remained only a few counts around the energies of 3.9 eV and 5.2 eV. From the above observations, we found that both the 3.9-eV and 5.2-eV resonances do not belong to  $^{107}\text{Pd}$ . Since the past experiment [4] was carried out with the transmission technique, the 3.9-eV and 5.2-eV resonances would be misidentified in lack of the isotope identification with prompt  $\gamma$  rays. The incorrect piece of information has been reported up to now.



**Fig.4** A TOF spectrum obtained by gating on the 434-keV  $\gamma$ -ray peak.

The cross sections of  $^{107}\text{Pd}$  in the low energy region were derived as follows: Firstly, the cross sections of Pd isotopes except for  $^{107}\text{Pd}$  was calculated with the resonance parameters in JENDL-4.0. In this calculation, the adjusted parameter for 2.9-eV resonance of  $^{108}\text{Pd}$  was used. Since the cross sections of  $^{105}\text{Pd}$  have been examined [16], the evaluated data of  $^{105}\text{Pd}$  were considered to be reliable and also used. Secondly, the cross-section components for those Pd isotopes were subtracted from the result shown in Fig.2. The remained components are due to  $^{107}\text{Pd}$ . Finally, the remained components were divided by the abundance of  $^{107}\text{Pd}$  in the sample listed in Table 1; the cross sections of  $^{107}\text{Pd}$  were derived at its abundance of 100 %. The preliminary result is given in **Figure 5** together with the  $\sigma_0$  measured by a prompt  $\gamma$ -ray spectroscopy [6]. The evaluated values of JENDL-4.0 are also plotted in comparison with the present result. The obtained cross-section curve in the thermal energy region supports the previous result of  $\sigma_0$  [6]. From the behavior of the cross sections at 25.3 meV, the value of  $\sigma_0$  for  $^{107}\text{Pd}$  was found to be  $\sim 10$  b.

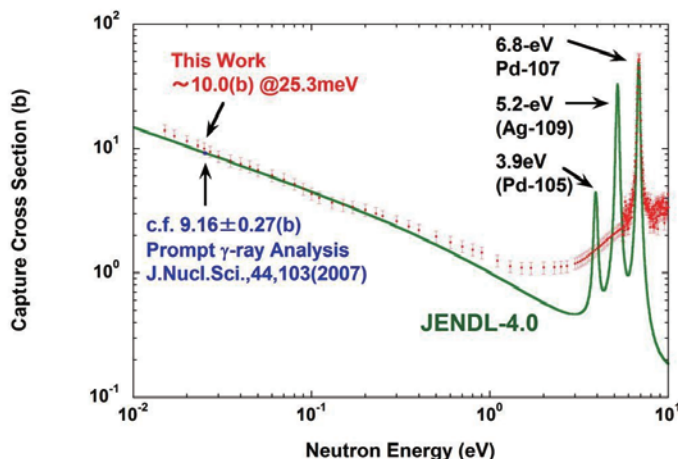


**Fig.5** Preliminary result of neutron capture cross sections of  $^{107}\text{Pd}$  together with the evaluated data of JENDL-4.0. Broadening effects are taken into account.

## 5. Summary

We measured the cross section of  $^{107}\text{Pd}$  in the thermal-neutron energy region with the “ $4\pi$  Ge spectrometer” installed at the ANNRI in the MLF at the J-PARC. It was also found that two resonances at 3.9 eV and 5.2 eV are not due to  $^{107}\text{Pd}$ . From the behavior of the cross

section of  $^{107}\text{Pd}$ , the value of  $\sigma_0$  was found to be  $\sim 10$  b. In near future, final result for the  $^{107}\text{Pd}$  cross section will be published.

## Acknowledgments

The present study includes the results of “Study on nuclear data by using a high intensity pulsed neutron source for advanced nuclear system” entrusted to Hokkaido University by the Ministry of Education Culture, Sports, Science and Technology of Japan (MEXT). This work was also supported by KAKENHI (22226016).

## References

- [1] H. Harada, *et al.*, “Plan of LLFP neutron cross section measurements for nuclear transmutation,” *J. Nucl. Sci. Technol.*, Suppl. **2**, 366 (2002).
- [2] V.S.Shirley, *et al.*, “Table of Isotopes, 8<sup>th</sup> ed.”, John Wiley and Sons, New York (1995).
- [3] K.Tasaka, *et al.*, “JNDC Nuclear Data Library of Fission Products”, JAERI-1320 (1990).
- [4] U.N.Singh, *et al.*, “Neutron capture and transmission measurements on fission product palladium-107”, *Nucl.Sci.Eng.*, **67**, 54 (1978).
- [5] R.L.Macklin, “Neutron capture and transmission measurements on fission product  $^{107}\text{Pd}$ ,” *Nucl. Sci. Eng.*, **89**, 79 (1985).
- [6] S. Nakamura, *et al.*, “Thermal neutron capture cross section of Palladium-107,” *J. Nucl. Sci. Technol.*, **44**, 2, 103 (2007).
- [7] K.Shibata, *et al.*, “Japanese Evaluated Nuclear Data Library Version 3 Revisoin-3: JENDL-3.3,” *J. Nucl. Sci. Technol.*, **39**, 1125 (2002).
- [8] K.Kino, *et al.*, “Measurement of energy spectra and special distributions of neutron beams provided by the ANNRI beam line for capture cross-section measurements at the J-PARC/MLF,” *Nucl. Instrum. Meth.*, **A 626-627**, 58 (2011).
- [9] A.Kimura, *et al.*, “Performance of a high speed and high density data acquisition system for multiple gamma-ray detection,” *Conference Record of IEEE NSS/MIC/RTDS 2008*, Article Number: N30-68 (2008).
- [10] M.Ohta, *et al.*, “Measurement of Neutron Spectrum at BL04 of J-PARC/MLF”, *2009 Fall meeting of AESJ*, J15 (2009) . (in Japanese).
- [11] A.Kimura, *et al.*, “A Dead-Time Correction Method for Multiple Gamma-ray Detection,” *Conference Record of IEEE MSS/MIC 2009*, Article Number: N07-03 (2009).
- [12] J.F.Briesmeister (Ed.), “MCNP-A General Monte Carlo N-Particle Transport Code, Version 4C”, LA-13709-M (2000).
- [13] S.Nakamura, *et al.*, “Measurements of neutron-capture cross sections of palladium isotopes at the J-PARC/MLF/ANNRI”, *Journal of the Korean Physical Society*, **59**, No.2, p.1772(2011).
- [14] N.M.Larson, *Updated Users’ Guide for SAMMY: Multilevel R-Matrix Fits to Neutron Data Using Bayes’ Equations*, ORNL/TM-9179/R7, Oak Ridge National Laboratory(2006).
- [15] K. Shibata, *et al.*, “JENDL-4.0: A New Library for Nuclear Science and Engineering,” *J. Nucl. Sci. Technol.*, **48**, 1 (2011).
- [16] D.A.Smith *et al.*, “Neutron resonance spectroscopy of  $^{104}\text{Pd}$ ,  $^{105}\text{Pd}$ , and  $^{110}\text{Pd}$ ”, *Physical Review C* **65**, 024607 (2002).

## 28 Study on neutron spectrometer for thermal to epithermal energy regions with an advanced multi-activation-foil method

Hiroyuki KANASUGI\*, Isao MURATA

Division of Electronic and Information Engineering, Osaka University

Yamada-oka 2-1, Suita, Osaka, 565-0871 Japan

\*E-mail: hkanasugi@ef.eie.eng.osaka-u.ac.jp

At present, measurement of energy spectrum for thermal and epi-thermal neutrons becomes crucial for application of neutron capture therapy, as well as physical applications. In the present paper, we described the preliminary result of ongoing development of thermal and epi-thermal neutron spectrometer using the multi-activation-foil method to measure energetic neutrons up to keV region. We designed and constructed a thermal/epithermal neutron column with a DT neutron source and carried out a test measurement with it. From the result, the developed spectrometer was confirmed to be feasible as a thermal/epithermal neutron spectrometer.

### 1. Introduction

Spectrum measurement of thermal and epi-thermal neutrons becomes crucial recently considering possible applications such as boron neutron capture therapy (BNCT). But there is no direct technique to measure the low-energy neutron spectrum. In the low-energy neutron measurement, there are some conventional ways. One way used frequently is to measure neutrons directly with a gas counter such as  $\text{BF}_3$ ,  $^3\text{He}$  and fission chamber. However, they have too large Q-values compared with the incident neutron energy to detect the energy correctly. Another way is the foil activation method, in which several types of foils and unfolding code should be used to estimate the neutron spectrum. This method is available only by off-line analysis and the unfolding process which contains many uncertainties. If the neutron source is pulsed, the time-of-flight method can be used. It needs a complicated technique in processing detector signals with electronic modules. However, the accuracy of the method is known to be commonly high.

In BNCT facilities, the major problem in the neutron spectrum measurement is how precisely the energy could be determined. So the author's group started development of a spectrometer which aimed at measuring thermal and epithermal neutron spectra precisely[1]. In this paper, we applied the multi-activation-foil method to measurement of the energy in keV region as an alternative technique. By increasing the number of resonance-foils covering epithermal energy as well as thermal energy region, the neutron spectrum measurement up to epi-thermal region would be realized by a simple unfolding process using the Bayes' theorem without an

initial guess.

The neutron spectrum can be derived by unfolding the measured number of counts of gamma rays emitted from activation-foils with the evaluated response function. In this work, we measured gamma rays emitted from the foils which are activated by thermal and epithermal neutrons in a graphite column created by a DT neutron source. The graphite column was designed by MCNP5[2] and constructed for the present test measurement. In this paper, the details of the detection method are presented and ongoing test measurement results are briefly summarized.

## 2. Experimental data analysis

### 2.1 Principle of neutron flux determination

The method of the present neutron spectrum measurement is a similar to the commonly used one, which includes a procedure of selecting several foils that have strong resonance peaks in their reaction cross sections around thermal energy region. In this study, by increasing the number of resonance foils covering even epithermal energy, the neutron spectrum measurement up to epi-thermal region would be realized by an unfolding process based on the Bayes' theorem even without an initial guess.

### 2.2 Spectrum derivation

There is no direct method to measure the low energy neutron spectrum as mentioned before. Hence, in this work, we employed an unfolding technique with reaction rates of several activation foils.

So-called inverse problem could be solved as follows:

$$x = \mathbf{R}^{-1} \cdot y$$

where,

$\mathbf{R}$  : Response matrix of reaction rates for activation foils,

$x$  : Neutron energy spectrum, and

$y$  : Measured count number of gamma-rays emitted from foils

By solving this, the neutron spectrum  $x(=\mathbf{R}^{-1} \cdot y)$  can be derived. We used an unfolding procedure based on the Bayes' theorem. By increasing the number of foils, we are aiming at an initial guess free solution

Response matrix ( $\mathbf{R}$ ) can theoretically be deduced with help of MCNP5 calculations as;

$$\mathbf{R} = \begin{pmatrix} a_1 & & & & \\ & \ddots & & & \\ & & a_i & & \\ & & & \ddots & \\ & & & & a_N \end{pmatrix} \begin{pmatrix} \sigma \end{pmatrix}$$

where,

$\sigma$ : Average cross section,

$a_i$ : Other factors for each foil, and

N: Number of foils

Other factors,  $a_i$ , are calculated as in the following equation:

$$a_i = N_0(1 - e^{-\lambda t_0})e^{-\lambda t_1}(1 - e^{-\lambda(t_2 - t_1)})E_{\text{eff}}\phi_0 f_h f_n f_g$$

where,

$N_0$ : Number of atoms

$\lambda$ : Decay constant (1/sec)

$t_0$ : Irradiation time (sec)

$t_1$ : Cooling time (sec)

$t_2$ :  $t_1$  plus measuring time (sec)

$E_{\text{eff}}$ : Detection efficiency

$\phi_0$ : Neutron flux intensity (n/sec/cm<sup>2</sup>)

$f_h$ : Relative intensity of gamma-ray

$f_n$ : Neutron self-absorption correction factor

$f_g$ : Gamma-ray self-attenuation correction factor

### 2.3 Selection of activation foils

In the present method, it is necessary to measure gamma rays emitted from activation-foils as a sufficient number of counts within a reasonable measuring time. Therefore, we have to select suitable activation foils based on the following criteria.

- (1) Activation cross section should be larger than about 0.05 barn.
- (2) Half-lives of residual nuclei should be longer than several minutes and shorter than several days.
- (3) Decayed gamma rays emitted from the residual nuclei should have suitable energies and enough high emission probabilities for measurement.

We finally chose the following 14 foils accordingly; Eu-151, In-115, Au-197, Sb-121, Mo-98, W-186, Sn-122, Cd-114, Cu-65, Zr-96, Te-130, Ge-74, Se-80 and Pr-141.

### 3. Experiment

In order to test the present spectrometer performance, we performed a test measurement with activation-foils.

We first designed a graphite thermal/ epi-thermal column with a DT neutron source by MCNP5 as in Fig. 1. The designed thermal/epi-thermal neutron column was constructed at OKTAVIAN facility of Osaka University as shown in Fig. 2.

The DT neutron source intensity is  $6 \times 10^9$  n/sec and the irradiation time is 2 hours. Activities of the foils were measured with an HpGe semiconductor detector.

The measuring time and cooling time for each foil are different from each other because the half-life of each foils is different. The measurement conditions are summarized in Table 1.

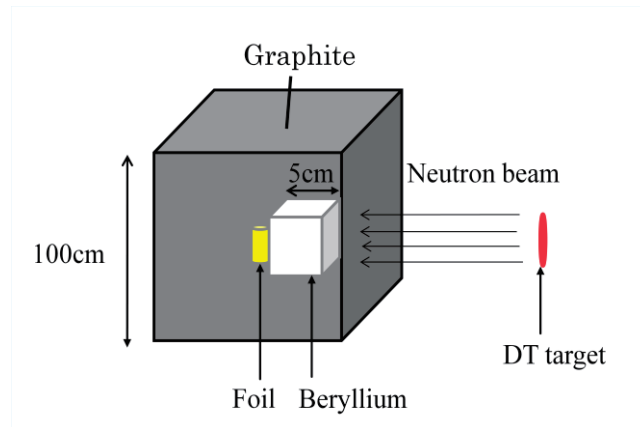


Figure 1 Schematic figure of the designed neutron column.

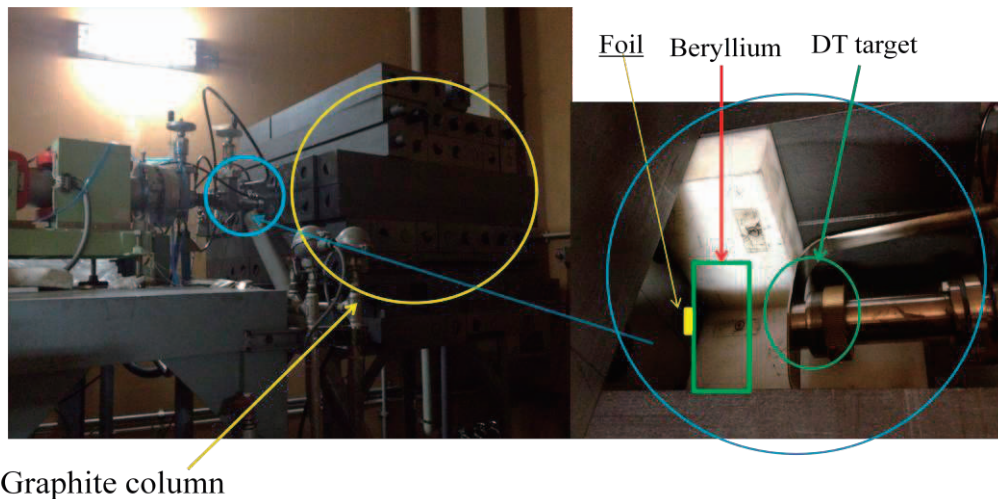


Figure 2 the irradiation room(left) and the DT target(right).

#### 4. Results and Discussion

After the irradiation, gamma-rays emitted from each foil were counted. The result is summarized in Table 1. The measured number of counts for all the foils were unfolded to derive the neutron energy spectrum. For the unfolding process, we adopted the Bayes theorem developed by Iwasaki[3]. As an initial guess, a uniform distribution was used.

Figures 3 and 4 are the measured neutron spectrum and the calculated neutron spectrum with MCNP5. Vertical and horizontal axes of each figure correspond to neutron flux ( $n/sec/cm^2$ ) and Energy (keV), respectively. Comparing the two spectra, although there are some discrepancies, the agreement is acceptable. In Fig. 3, we confirm two hollows. It is presumed that small number of counts of gamma-rays for Cu-65, Zr-96, Se-80 may cause this. In the next experiment, we will examine whether the problem could be improved by regulating the condition for increasing the number of counts and the number of foils at the same time.

Table 1 Experimental conditions and obtained results for each foil.

Activation-foil	Eu-151	In-115	Au-197	Sb-121	Mo-98	W-186	Sn-122	Cd-114	Cu-65	Zr-96	Te-130	Ge-74	Se-80	Pr-141
Number of counts	10480	738371	33859	1075501	101432	82585	29220	22278	2727	4056	21158	44543	992	2975
Measuring time(s)	3591	3359	3600	61138	72894	53963	7214	53985	903	72022	5714	10008	5287	10615
Energy of resonance position (eV)	0.5	1.5	5	6	10	20	100	100	200	300	1000	3000	20000	100000
Cross section (barn)	20000	6000	7000	500	8	2000	1	40	3	20	0.1	0.7	1	30
Half-life (s)	33480	3246	232934.4	231552	237672	86040	2406	192240	306	60840	1500	4920	1110	69120
Gamma-ray energy (keV)	344.31	416.86	411	564.24	140.51	685.73	160.32	336.24	1039.2	743.36	149.72	264.6	275.93	1575.6

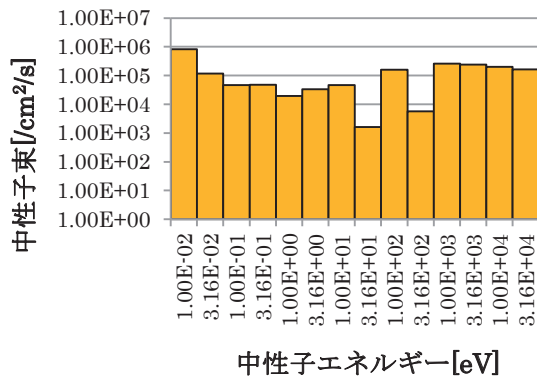


Figure 3 Measured neutron spectrum.

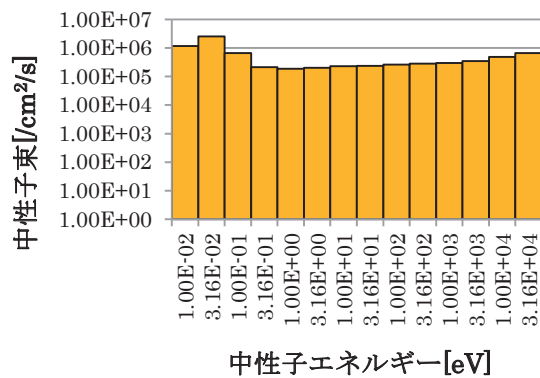


Figure 4 Calculated neutron spectrum by MCNP5.

### 5. Future Work

In the present study, we confirmed basic applicability to measure thermal/epithermal neutron spectrum for BNCT. However, there are discrepancies seen between experiment and calculation. We will improve the accuracy of this technique by searching more suitable activation foils, and increasing the number of foils.

As the next step, the performance of detecting low energy neutrons will be compared with other spectrometers like Bonner Ball counter.

In the future, the present technique will be applied to the spectrum measurement in the actual BNCT scene.

### 6. Conclusion

We carried out the series studies concerning the thermal/epithermal spectrum measurement especially for BNCT facilities. In the present study, by increasing the number of resonance-foils covering epithermal energy as well as thermal energy region, the neutron spectrum measurement up to epi-thermal region was realized by a simple unfolding process using the Bayes' theorem even without an initial guess.

For the test measurement, a neutron field with a DT neutron source was designed by MCNP5 calculation and constructed at the OKTAVIAN facility of Osaka University. From the result, enough number of counts for gamma-rays for each foil was obtained and the neutron spectrum was successfully estimated by unfolding the measured number of counts with the response function of the activation foils.

### References

- [1] M. Ito, I. Murata, “Thermal / epi-thermal neutron spectrometer with a  $^3\text{He}$  position sensitive proportional counter,” *Proc. 2010 Annual Symposium on Nucl. Data*, pp. 95-100, Nov. 25-26, 2010, C-CUBE, Chikushi Campus, Kyushu University (2011).
- [2] X-5 Monte Carlo Team: MCNP-A General Monte Carlo N-Particle Transport Code, 2003 X-5 Monte Carlo Team: MCNP—A general Monte Carlo N-particle transport code, version 5, Los Alamos National Laboratory, Los Alamos, New Mexico, USA, April 2003.
- [3] S.Iwasaki: “A new approach for unfolding PHA problems based only the Bayes’ Theorem”, *Proc. 9<sup>th</sup> International Symposium on Rector Dosimetry*, Prague, Chezk Republic, pp. 245-252 (1996).

## 29 Systematic Study on keV-neutron Capture Cross Sections and Capture Gamma-ray Spectra of Pd Isotopes

K. Terada, M. Igashira, T. Matsushashi, T. Katabuchi, T. A. Tran

*Research Laboratory for Nuclear Reactors, Tokyo Institute of Technology,  
2-12-1 Ookayama, Meguro-ku, Tokyo 152-8550*

E-mail: terada.k.aa@m.titech.ac.jp

### Abstract

The capture cross sections and capture gamma-ray spectra of  $^{104,105}\text{Pd}$  were measured in the neutron energy region of 15-100 keV as part of a systematic series of measurements. A neutron time-of-flight method was utilized by means of an anti-Compton NaI(Tl) spectrometer and a nsec pulsed neutron source via the  $^7\text{Li}(p,n)^7\text{Be}$  reaction. The capture yields were obtained by applying a pulse-height weighting technique to the net capture gamma-ray pulse-height spectra. The capture cross sections of  $^{104,105}\text{Pd}$  were derived with errors of less than 5%, using the standard capture cross sections of  $^{197}\text{Au}$ . The capture gamma-ray spectra of  $^{104,105}\text{Pd}$  were also derived by unfolding the respective observed capture gamma-ray pulse-height spectra. Additionally, the theoretical calculation was made by means of the CCONE computer code.

## 1 Introduction

The nuclear transmutation of long-lived fission products (LLFPs) into stable or short-lived nuclides by neutron capture reaction is expected to reduce the impact on the environment by nuclear waste disposal, and it has been studied thoroughly. Palladium-107 (half life:  $6.5 \times 10^6$  y) is one of the most important LLFPs, and its neutron capture cross sections are important for the study of LLFP transmutation systems. Additionally, the capture cross sections of stable Pd isotopes also affect the performance of a transmutation system if it lacks isotope separation. Therefore, their capture cross sections as well as those of  $^{107}\text{Pd}$  are important for the R&D of nuclear transmutation systems. Moreover, capture gamma-ray spectra contain much information on important physical quantities such as gamma-ray strength function, and the information is quite useful for theoretical calculation of neutron capture cross sections of Pd isotopes, especially  $^{107}\text{Pd}$ . From the viewpoint mentioned above, we started a systematic series of studies on keV-neutron capture cross sections and capture gamma-ray spectra of Pd isotopes ( $^{104,105,106,108,110}\text{Pd}$  and  $^{107}\text{Pd}$ ), using a time-of-flight method with a pulsed  $^7\text{Li}(p,n)^7\text{Be}$  neutron source and a large anti-Compton NaI(Tl) gamma-ray spectrometer. We completed measurement for  $^{104,105}\text{Pd}$  in the neutron energy of 15-100 keV. Additionally, the theoretical calculation of capture cross sections and capture gamma-ray spectra were made by using the CCONE<sup>1)</sup> computer code.

## 2 Experimental Procedure and Analysis

The keV-neutron capture cross sections and capture gamma-ray spectra were measured in the neutron energy region of 15-100 keV by means of the 3 MV Pelletron accelerator at the Research Laboratory for Nuclear Reactors of the Tokyo Institute of Technology.

Pulsed proton beams from the accelerator produce a 1.5 nsec pulsed neutron beam via the  ${}^7\text{Li}(p,n){}^7\text{Be}$  reaction.

We used isotopically enriched Pd and standard  ${}^{197}\text{Au}$  samples. The distance between the neutron source and the sample was 12 cm. The capture gamma-rays emitted from the sample were measured with an anti-Compton NaI(Tl) spectrometer. The signals from the spectrometer were accumulated event by event as time-of-flight (TOF) and Pulse Height(PH) data. The incident neutron energy spectra were measured by a time-of-flight method with a  ${}^6\text{Li}$ -glass scintillation detector.

The  ${}^{104}\text{Pd}$  and  ${}^{105}\text{Pd}$  samples were enriched metal powder with masses of 700 mg and 495 mg, respectively. Both of the samples had chemical purities of higher than 99.97% and isotopic purities of higher than 98%. The  ${}^{104}\text{Pd}$  sample was formed into a disk by using a pressing machine and was then sealed with a Mylar film. The  ${}^{105}\text{Pd}$  sample was sealed in a graphite case. Two standard Au samples which respectively matched the dimensions of the Pd samples were also used.

We carried out the measurements cyclically for the Pd sample, the Au sample, and a "no sample" scenario (a blank run), in order to average experimental conditions.

The incident neutron energy spectra were obtained from the TOF spectra measured with a  ${}^6\text{Li}$ -glass detector from the no sample measurement. Four neutron energy regions were set in the incident neutron energy spectrum, and average capture cross sections were derived for these neutron energy regions, respectively.

Four gates, corresponding to the four neutron energy regions, were set in the foreground region of the TOF spectra measured with the NaI(Tl) spectrometer, and one gate was set in the time-independent background region in the TOF spectra. Then the foreground and background PH spectra were obtained from the Pd and Au measurements.

A pulse height weighting technique<sup>2)</sup> was applied to the net PH spectra in order to obtain the capture yields of Pd and Au. Finally, the capture cross sections of  ${}^{104,105}\text{Pd}$  were derived with the standard capture cross sections<sup>3)</sup> of  ${}^{197}\text{Au}$ . Moreover, the capture gamma-ray spectra were derived by unfolding the net capture gamma-ray PH spectra with the FERDOR computer code<sup>4)</sup> and the response matrix of the NaI(Tl) spectrometer.

### 3 Theoretical Calculation

Theoretical calculations were performed by using the CCONE<sup>1)</sup> computer code. First, coupled channel optical calculation was applied to reproduce the total cross sections and elastic scattering angular distribution for natural palladium, and the neutron transmission coefficients were obtained which are used in statistical model calculations by CCONE. Next, the calculation of capture cross sections and capture gamma-ray spectra for palladium isotopes were made by using CCONE code based on the Hauser-Feshbach statistical model.

The generalized Lorentzian was used as the gamma-ray strength functions in order to obtain the neutron capture cross sections and capture gamma-ray spectra of  ${}^{104,105}\text{Pd}$ . The data of discrete level and decay branching ratio were adopted from Reference Input Parameter Library for Calculation of Nuclear Reactions and Nuclear Data Evaluations (RIPL-3)<sup>5)</sup>. The nuclear level density was derived from the constant temperature model and Fermi-Gas model that is predicated on the systematics of Mengoni-Nakajima.

## 4 Results and Discussion

### 4.1 Capture Cross sections

The capture cross sections of  $^{104,105}\text{Pd}$  were derived with errors of less than 5% in the neutron energy region of 15-100 keV. **Figure 1** shows the present experimental results together with previous measurements, evaluated values, calculation results. The present results are plotted at the average neutron energies. Horizontal bars show the neutron energy region corresponding to the four regions described above. The calculation parameters were adjusted to reproduce the experimental results.

For  $^{104}\text{Pd}$ , there are two previous measurements: those of Macklin<sup>6)</sup> and Cornelis *et al.*<sup>7)</sup>. Their measurements are in good agreements with the present measurements. The evaluations of JENDL-4.0<sup>8)</sup> and ENDF/B-VII.0<sup>9)</sup> are also in good agreement with the present measurements.

For  $^{105}\text{Pd}$ , there are four previous measurements: Ro *et al.*<sup>10)</sup>, Cornelis *et al.*<sup>7)</sup>, Macklin<sup>6)</sup>, and Hockenbury *et al.*<sup>11)</sup>. Comparing the previous measurements with the present results, the previous measurements are larger than the present measurements by 10-20%. The evaluations of JENDL-4.0 and ENDF/B-VII.0 are also larger than the present results by 6-10%.

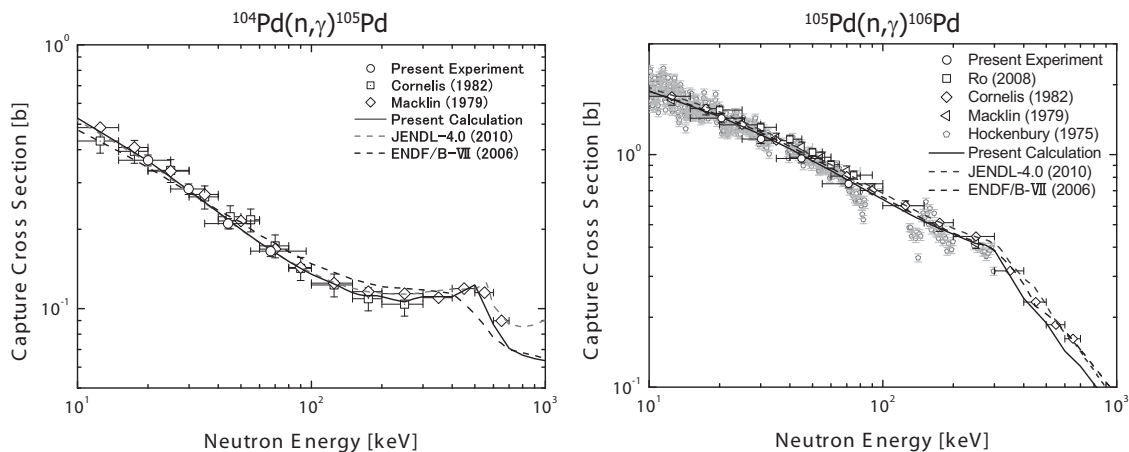


Figure 1: The keV-neutron capture cross sections of  $^{104}\text{Pd}$  and  $^{105}\text{Pd}$ . Open circles indicate the present measurements. Those are plotted at the average neutron energies, and the horizontal bars indicate the neutron energy regions. Solid lines indicate the calculation results by means of the CCONE computer code. Dashed lines indicate the evaluations of JENDL-4.0 and ENDF/B-VI.8

### 4.2 Capture Gamma-ray Spectra

The keV-neutron capture gamma-ray spectra of  $^{104,105}\text{Pd}$  were derived from the present measurements. **Figure 2** shows the present results for  $^{104,105}\text{Pd}$ , respectively. **Fig. 2**, low-lying levels of  $^{105}\text{Pd}$  and  $^{106}\text{Pd}$  are shown as vertical bars, respectively.

For  $^{104}\text{Pd}$ , the primary transition from the neutron capture state to the ground state was weak in **Fig. 2**. The multiplicity of capture gamma-rays was  $2.69 \pm 0.064$  gamma-rays/capture from the measurements. The calculations of the gamma-ray strength functions were made by using the Giant Dipole Resonance (GDR) parameters of RIPL-3. Above 4.5 MeV, there was a discrepancy between measurements and calculations due to underestimation of the gamma-ray strength functions.

For  $^{105}\text{Pd}$ , the primary transition from the neutron capture state to the ground and first excited states of  $^{106}\text{Pd}$  were observed around 9.6 and 9.1 MeV, respectively. The multiplicity of capture gamma-rays was  $3.85 \pm 0.03$  gamma-rays/capture from the measurements. Above 7.8 MeV, the calculation underestimated the measurements.

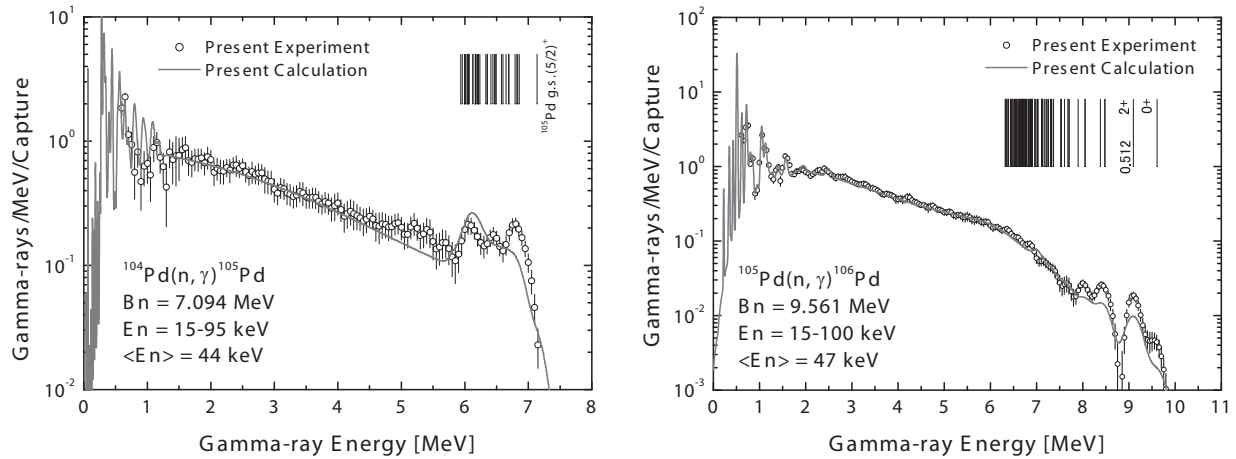


Figure 2: The keV-neutron capture gamma-ray spectra of  $^{104}\text{Pd}$  and  $^{105}\text{Pd}$ . Open circles indicate the present measurements. Solid lines indicate the calculation results. The vertical bars show low-lying levels of the residual nucleus.

## 5 Conclusion

We have measured the keV-neutron capture cross sections and capture gamma-ray spectra of  $^{104,105}\text{Pd}$  in the neutron energy region of 15-100 keV. The neutron capture cross sections of  $^{104,105}\text{Pd}$  have been derived with errors of less than 5%. In the case of  $^{104}\text{Pd}$ , the previous measurements were in good agreement with the present results. On the other hand, in the case of  $^{105}\text{Pd}$ , discrepancy between the present results and the previous measurements was found. The keV-neutron capture gamma-ray spectra of  $^{104,105}\text{Pd}$  were derived for the first time. In addition, a calculation of capture cross sections and capture gamma-ray spectra has been performed to reproduce the present results.

## Acknowledgments

This work was supported by KAKENHI (22226016).

## References

- 1) O. Iwamoto, *J. Nucl. Sci. Technol.*, **44**, 687-697 (2007).
- 2) R. L. Macklin and J. H. Gilbbons, *Phys. Rev.*, **159**, 1007-1012 (1967).
- 3) “JENDL-4.0 data file for  $^{197}\text{Au}$  (MAT=7925),” evaluated by N. Iwamoto, (2010).
- 4) H.Kendrick *et al*, *Gulf Radiation Technology*, **GA-9882**, (1970).

- 5) R. Capote *et al.*, Reference Input Parameter Library (RIPL-3), <http://www-nds.iaea.org/RIPL-3>, (2009)
- 6) R. L. Macklin, *Nucl. Sci. Eng.*, **71**, 181-191 (1979).
- 7) E.Cornelis *et al.*, *Conf. on Nucl. Cross-Sect. and Techn., Antwerp*, **2**, (1982).
- 8) K. Shibata *et al.*, *J. Nucl. Sci. Technol.*, **48**, 1-30 (2011).
- 9) M. B. Chadwick *et al.*, (CSEWG collaboration), *Nucl. Data Sheets*, **102**, 2931-3060 (2006).
- 10) T. I. Ro *et al.*, *Journal of the Korean Physical Society*, **5**, 1598-1603, (2007).
- 11) R.W.Hockenbury *et al.*, *Conf. on Nucl. Cross-Sect. and Techn., Washington*, **2**, (1975).

This is a blank page.

### 30 Characterization Test of CdTe Detector Element Designed and Developed for BNCT-SPECT

Soichiro Nakamura, Taiki Mukai, Masanobu Manabe, Isao Murata,

Division of Electrical, Electronic and Information Engineering, Graduate School of Engineering, Osaka University, Yamada-oka 2-1, Suita, Osaka 565-0871, Japan

E-mail: snakamura@ef.eie.eng.osaka-u.ac.jp

BNCT is the radiation therapy which can destroy only tumor cells and will not damage healthy cells compared with other radiation therapy. One severe BNCT problem exists that it is difficult to determine the neutron irradiation time. For solving the problem, we are studying the development of BNCT-SPECT to monitor the BNCT effect in real time. In the present study, we produced a trial CdTe detector for the BNCT-SPECT, measured the characterization and confirmed it could meet the requirements of the BNCT-SPECT.

#### 1. Introduction

Boron neutron capture therapy (BNCT) is a promising radiation therapy which can kill tumor cells very efficiently. The principle of BNCT is in the following:  $^{10}\text{B}$  is locally concentrated in the tumor cells. Thereafter, low-energy neutrons such as thermal neutrons are irradiated from outside. As the result, only the tumor cells including boron are selectively destroyed by charged particles emitted from  $^{10}\text{B}(n,\alpha)^7\text{Li}$  reaction. Produced  $\alpha$  particle and  $^7\text{Li}$  have path lengths of several  $\mu\text{m}$ . Since it is comparable to a cell diameter, only the tumor cells are killed and the effect to normal tissues can be suppressed substantially. This is an essential and specific advantage compared with other radiation therapies.

However, it is known that there are some problems in BNCT. One severe problem exists that it is difficult to determine the suitable irradiation time beforehand. This is caused by the fact that exact boron concentration and neutron flux intensity in the tumor cells cannot be known easily. To solve the problem, we measure 478 keV prompt gamma-rays emitted from  $^{10}\text{B}(n,\alpha)^7\text{Li}$  reaction in BNCT. Three dimensional treatment effect of BNCT can thus be estimated with a Single photon emission computed tomography (SPECT) system by measuring 478 keV gamma-rays. The SPECT system for BNCT is called BNCT-SPECT in this paper. Researches of the BNCT-SPECT have been carried out by some researchers. Though utilization of scintillators and semiconductor detectors has been investigated for years, BNCT-SPECT is not in practical use yet even as a prototype one.[1~4]

In the present study, a CdTe detector was selected as a basic device to detect 478 keV gamma-rays.[5,6] Design of an array type CdTe detector is underway now and a test detector element was produced to

examine the characterization for checking the suitability for BNCT-SPECT. Measuring the detection efficiency and energy resolution of standard gamma-ray sources, we evaluated and checked the performance of the trial CdTe detector.

## 2. Detector Design of BNCT-SPECT

### 2.1 Principle of Measurement

94 % of produced  ${}^7\text{Li}$  is in an excited state, from which 478 keV gamma-ray is emitted by a transition from the first excited state to the ground state almost simultaneously. If the position and intensity of the gamma-ray emission are measured, the information is directly related to the  $(n,\alpha)$  reaction distribution in the tumor, which becomes the three dimensional dose distribution in BNCT. Reproduction of the three dimensional dose distribution could be realized by a so-called SPECT system as shown in Fig.1 schematically. In this way, the three dimensional BNCT effectiveness can be visualized in real time.

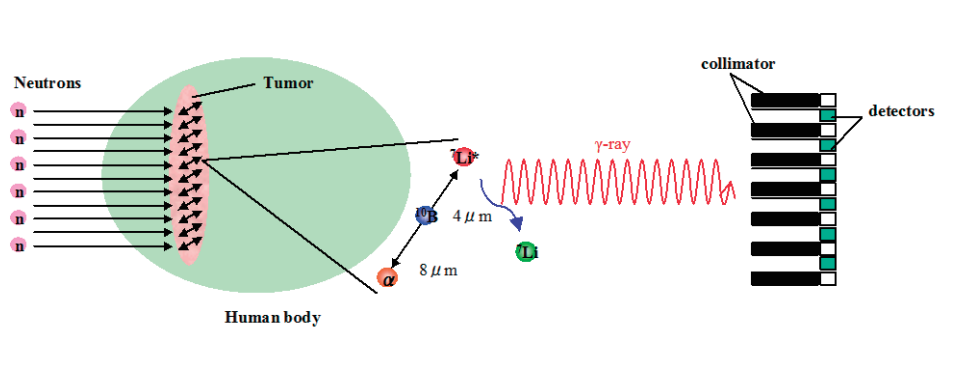


Fig.1 Conceptual figure of BNCT-SPECT

### 2.2 Difficulty in BNCT-SPECT development

It is difficult, however, to realize the 478 keV gamma-ray measurement in BNCT. In case of a normal SPECT measurement, no radiations exist except those used for acquiring a tomography image. However, in the case of BNCT-SPECT, the thermal neutron intensity used reaches  $\sim 10^9\text{ n/sec/cm}^2$  around the tumor. The cross section of  ${}^{10}\text{B}(n,\alpha){}^7\text{Li}$  reaction is quite large. However the  ${}^{10}\text{B}$  concentration is about 10 ppm in the tumor. Hence, the intensity of 478 keV gamma-rays emitted from  ${}^{10}\text{B}(n,\alpha){}^7\text{Li}$  reaction becomes much smaller than that of secondary gamma-rays emitted by various  $(n,\gamma)$  reactions and direct signals in the CdTe detector directly produced by incident neutrons. Thus it becomes quite hard for a conventional SPECT to selectively measure 478 keV gamma-rays in a strong radiation field including a lot of background gamma-rays.

### 2.3 Requirements for BNCT-SPECT

The requirements to achieve BNCT-SPECT are summarized as follows:

- (1) Measuring time should be around 30 minutes, because most clinical irradiations are completed in less than 1 hour.

- (2) Spatial resolution should be less than several mm.
- (3) Statistical accuracy should be less than several %, meaning one detector should measure about 1000 counts under conditions of (1) and (2).
- (4) Energy resolution should be less than 30 keV to separately measure 478 keV gamma-rays and 511 keV annihilation gamma-rays.

#### **2.4 Present Status of BNCT-SPECT**

A CdTe detector seems to be the best candidate to meet the above requirements. Previously, we evaluated the pulse height spectrum to be measured in an actual BNCT spot by using MCNP5 (Monte Carlo N-Particle transport) code. As a result, we successfully estimated suitable dimensions of an elemental device of CdTe so that the total count of 478 keV gamma-ray would be larger than 1000 in 30 minutes, that is, our design target of (1)~(3).

As a result of the above calculations, the detector should be small and should have an enough large sensitivity. We thus employed a CdTe device as an elemental detector for the BNCT-SPECT, which has an enough thickness and a small entrance surface area. For this purpose, we used an electrode surface as a side surface to keep its thickness. This is acceptable because the gamma-ray energy of interest is enough high, that is, 478 keV.

Now we are producing various CdTe crystals and testing them to determine the elemental detection device for the BNCT-SPECT, with which an array type detector would be designed.

### **3. Experiment**

We measured gamma-rays with a trial CdTe elemental detector to examine the performance. The best performance in the design calculation is found in a  $1.5 \times 2 \times 30$  mm crystal. However, because it is made from a little thick wafer, the wafer is not yet produced. Though it is a little smaller than this, we used a  $1.5 \times 2 \times 25$  mm one and examined the performance, that is, whether it would really meet the design targets of (1) ~ (4).

With some standard gamma-ray sources we measured the detection efficiency and energy resolution of the elemental CdTe detector of  $1.5 \times 2 \times 25$  mm as shown in Fig.2. The distance between the CdTe detector and the gamma-ray source is 4cm.

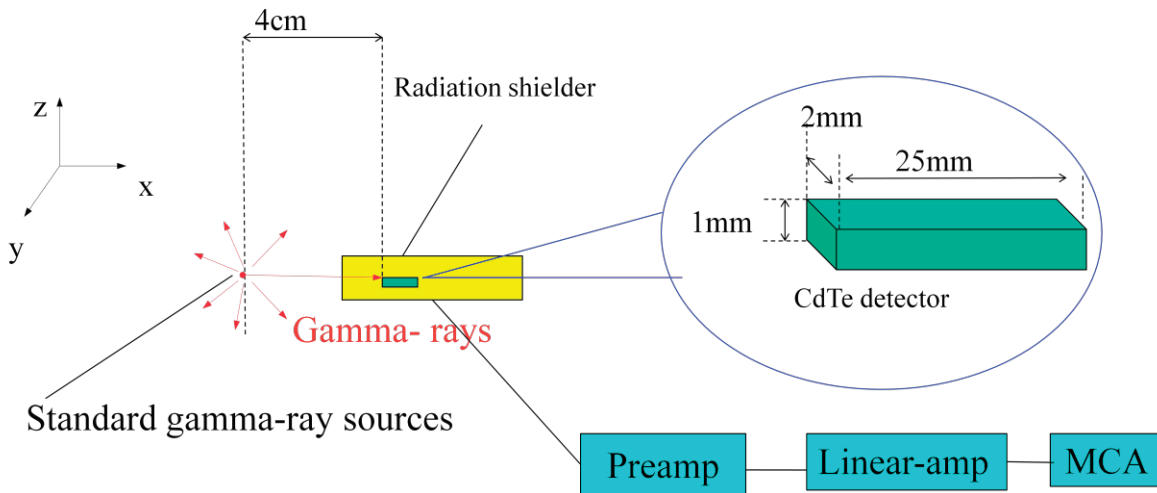


Fig.2 Experiment model using experiment model

#### 4. Results and Discussion

Figure 3 shows the measured energy resolution of the CdTe detector. The energy resolution at 478 keV estimated by measured values of standard gamma-ray sources of  $^{243}\text{Am}$  (60 keV),  $^{133}\text{Ba}$  (356 keV) and  $^{137}\text{Cs}$  (661 keV) is 15.3 keV which is shown by a bold solid line in the figure. Figure 4 describes the absolute photopeak efficiency of it. Solid line is the experimental result and dashed line is the calculation result. From the experimental absolute efficiency curve, the estimated value at 478 keV is 10%.

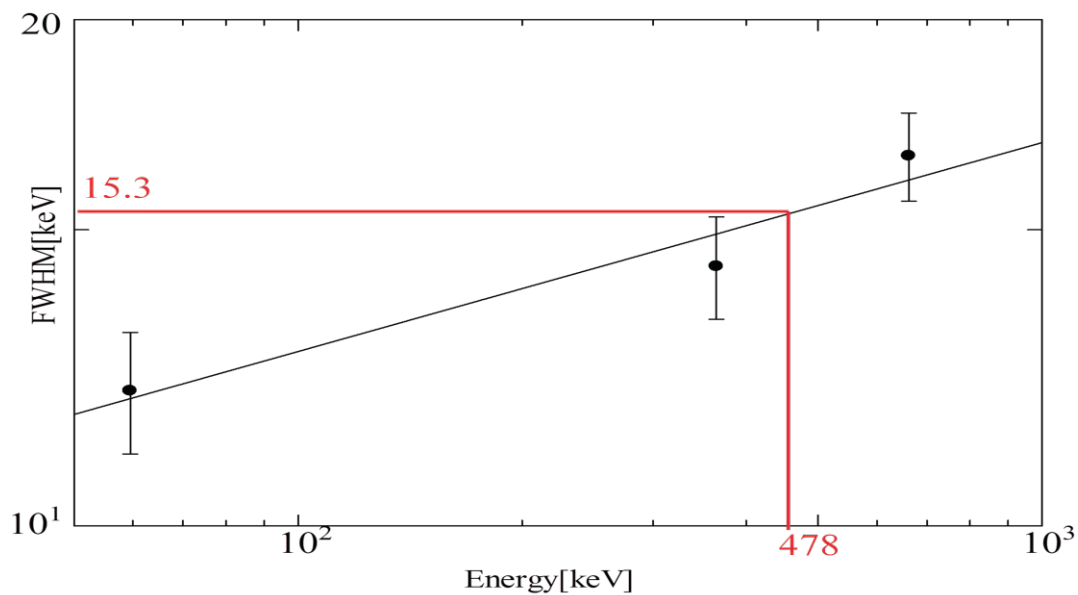


Fig3. Energy Resolution

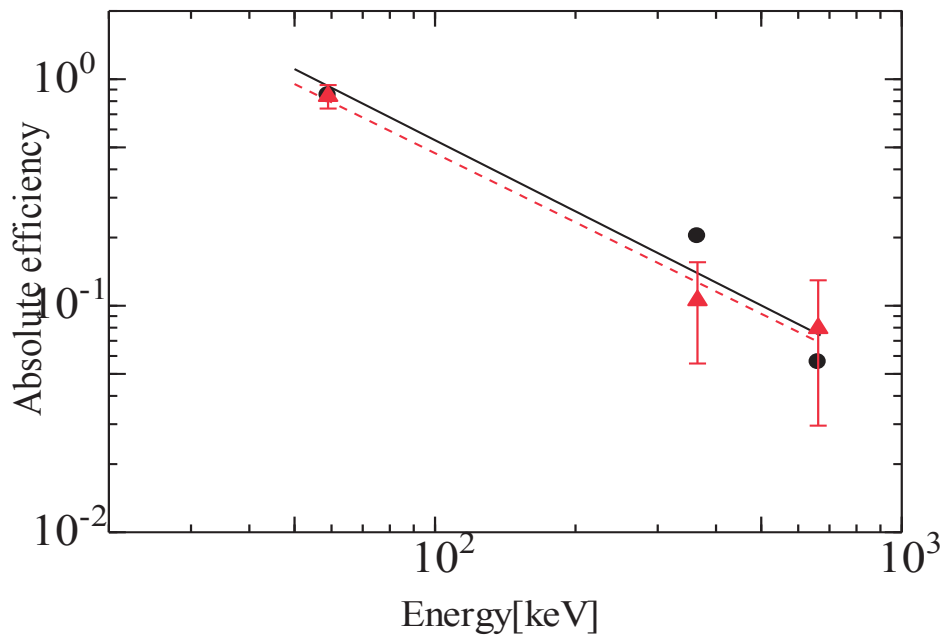


Fig4. Absolute photopeak efficiency(Solid line is the experimental result and dashed line is the calculation result)

As for the energy resolution, 15 keV at 478 keV was found to be enough narrow to confirm that adjacently existing 511 keV annihilation gamma-ray, which was expected to become a troublesome background in a real BNCT scene, could separately be measured even if taking into account the Doppler broadening of the 478 keV peak. For the absolute efficiency, the experiment data are higher than the calculation by about 1%, showing the optimum CdTe( $1.5 \times 2 \times 30$  mm) designed previously has a potential ability for the BNCT-SPECT. The reason is in the following: The presently produced CdTe element is surely a little smaller. However, the calculation procedure was verified by the present comparison. The larger CdTe element of  $1.5 \times 2 \times 30$  mm is thus expected to meet the requirements because the experimental value is higher than the calculation by 1 %.

## 5. Future Work

We will produce an elemental CdTe detector of  $1.5 \times 2 \times 30$  mm which would be expected to meet the requirements of (1)~(4) by calculations. Then, we will test the larger CdTe element. Following it, the detection performance of 478 keV gamma-rays will be checked by a phantom experiment using a neutron source of Osaka University. Next a test measurement will be done in a real BNCT scene in hospitals under the collaboration with the Department of Dentistry, Osaka University. Finally an array type CdTe detector will be produced as an elemental detection device for BNCT-SPECT.

## 6. Conclusion

We measured absolute detection efficiencies and energy resolutions with standard gamma-ray sources for a thick CdTe detector of  $1 \times 2 \times 25$  mm. From the result, the energy resolution at 478 keV was found to be about 15 keV and the absolute efficiency was estimated to be 10%. The energy resolution is sufficiently large to discriminate 478 keV and 511 keV gamma-rays. The absolute efficiency is in good agreement with the calculation result. So the result shows indirectly that a larger CdTe detector element of  $1.5 \times 2 \times 30$  mm could meet the requirements for BNCT-SPECT.

## References

- [1] Kobayashi T. et al., “A noninvasive dose estimation system for clinical BNCT based on PG-SPECT – Conceptual study and fundamental experiments using HPGe and CdTe semiconductor detectors ” *Med. Phys.*, 27(9), 2124-2132 (2000).
- [2] Minsky D.M. et al., “Experimental feasibility studies on a SPECT tomograph for BNCTdosimetry” *Appl Radiat Isot.* 67(7-8), S179-82(2000).
- [3] Munck af Rosenschöld P. et al., “Prompt gamma tomography during BNCT – A feasibility study” *J. Instrum.* 1, 1–10(2006).
- [4] Verbakel W. et al., “ $\gamma$ -ray telescope for online measurements of low boron concentrations in a head phantom for BNCT. *Nucl. Instrum*” *Methods Phys. Res. Sect. A* 394 (1–2), 163–172(1997),
- [5] I. Murata, T. Mukai, M. Ito, H. Miyamaru, S. Yoshida, “Feasibility study on BNCT-SPECT using a CdTe detector,” *Progress in Nucl. Sci. Technol.*, 1, pp. 267-270 (2011).
- [6] T. Mukai, I. Murata, M. Ito, H. Miyamaru, “Development of CdTe detector for BNCT-SPECT,” *Proc. of the 2009 Annual Symposium on Nucl. Data*, Nov. 26-27, 2009, RICOTTI, Tokai-mura, Ibaraki-ken, Japan, JAEA-Conf 2010-005, pp.75-80 (2010).

## 31 Critical Experiment with Thorium at KUCA

Takashi FUJII<sup>1)</sup>, Kazuhiro WADA<sup>1)</sup>, Vu Thanh Mai<sup>1)</sup>, Takanori KITADA<sup>1)</sup>, Akinori YAMAGUCHI<sup>2)</sup>,  
Hiroki WATANABE<sup>2)</sup>, Naoyuki TAKAKI<sup>2)</sup>, and Hironobu UNESAKI<sup>3)</sup>

1) Osaka University, 2-1 Yamada-oka, Suita-shi, Osaka, Japan, 565-0871

2) Tokai University, 4-1-1, kitakaname, Hiratsuka-shi, Kanagawa, Japan, 259-1292

3) Kyoto University Research Reactor Institute, 2-1010 Asashiro-Nishi, Kumatori-cho, Sennan-gun, Osaka, Japan, 590-049

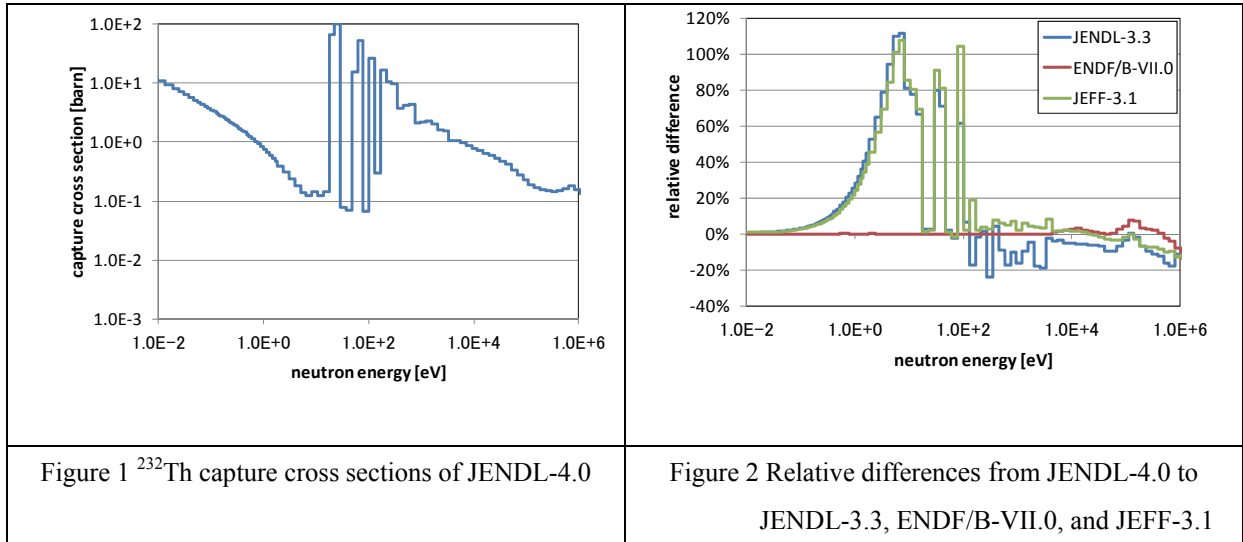
E-mail: t-fujii@ne.see.eng.osaka-u.ac.jp

Thorium cross sections show relatively large differences among recent libraries compared with other major nuclides such as Uranium and Plutonium. In order to check the validity of cross section data, a series of critical experiments with Thorium at Kyoto University Critical Assembly (KUCA) has been performed since 1985. In these experiments, the purpose is to get the criticality property of nine cores of which  $H/^{235}U$  and/or  $Th/^{235}U$  values are different. Seven of the nine cores have been assembled. This experimental purpose is to obtain the experimental results for Thorium cores with different composition which have never been assembled at the KUCA:  $H/^{235}U=150$  and  $Th/^{235}U=15.2$ . In this experiment, approach to criticality, control rod calibration, and measurement of sample worth for Thorium were performed. Comparing the experimental sample worth to calculation results by continuous energy Monte Carlo code MVP by JENDL-4.0, JENDL-3.3 ENDF/B-VII.0, and JEFF-3.1, there are about 10% difference. And there is also difference between libraries.

However the experimental results are based on delayed neutron fraction which is calculated by SRAC, so it's necessary to assess the impact of delayed neutron fraction by using different libraries.

### 1. Introduction

Thorium is an attractive fuel element generating  $^{233}U$  efficiently, and many researches have been performed. However, the capture cross sections of Thorium have large ambiguity even in the recent evaluated nuclear data libraries. Figure 1 shows  $^{232}Th$  capture cross sections of JENDL-4.0[1], and Figure 2 shows relative difference of  $^{232}Th$  capture cross section of JENDL-3.3[2], ENDF/B-VII.0[3], and JEFF-3.1[4] based on JENDL-4.0. The difference is more than 50% in the neutron energy range from 1 to 100 eV.



Then, a series of critical experiment with Thorium has been performed at KUCA since 1985. In the series, seven experiments of cores composed of different  $^{232}\text{Th}/^{235}\text{U}$  and/or  $\text{H}/^{235}\text{U}$  values have been performed, but there are two never assembled cores with the unit fuel cell containing Thorium plates. By considering these facts, the experiment has been performed to obtain the complete set of experimental results for Thorium cores with the unit fuel cell composed of different  $^{232}\text{Th}/^{235}\text{U}$  and/or  $\text{H}/^{235}\text{U}$  values, and to check the validity of the cross sections data of Thorium by comparing the measured sample worth and calculated results. The two experiments were done in August and November 2011. This time, the experiment on August is reported.

## 2. Experiment

### 2.1 Approach to Criticality

Approach to criticality was performed to ascertain that the neutronic property of the assembled core meets the design constraints. The composition fraction in this experiment is that  $^{232}\text{Th}/^{235}\text{U}=15.2$ ,  $\text{H}/^{235}\text{U}=140$ . This core composed of fuel rods called

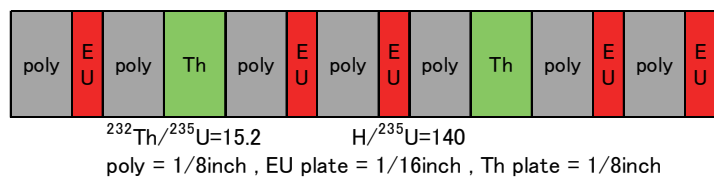


Fig.3 Unit fuel cell

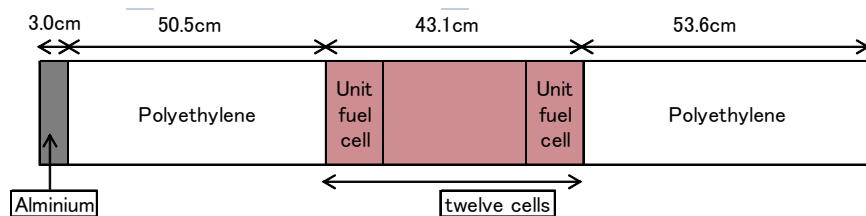
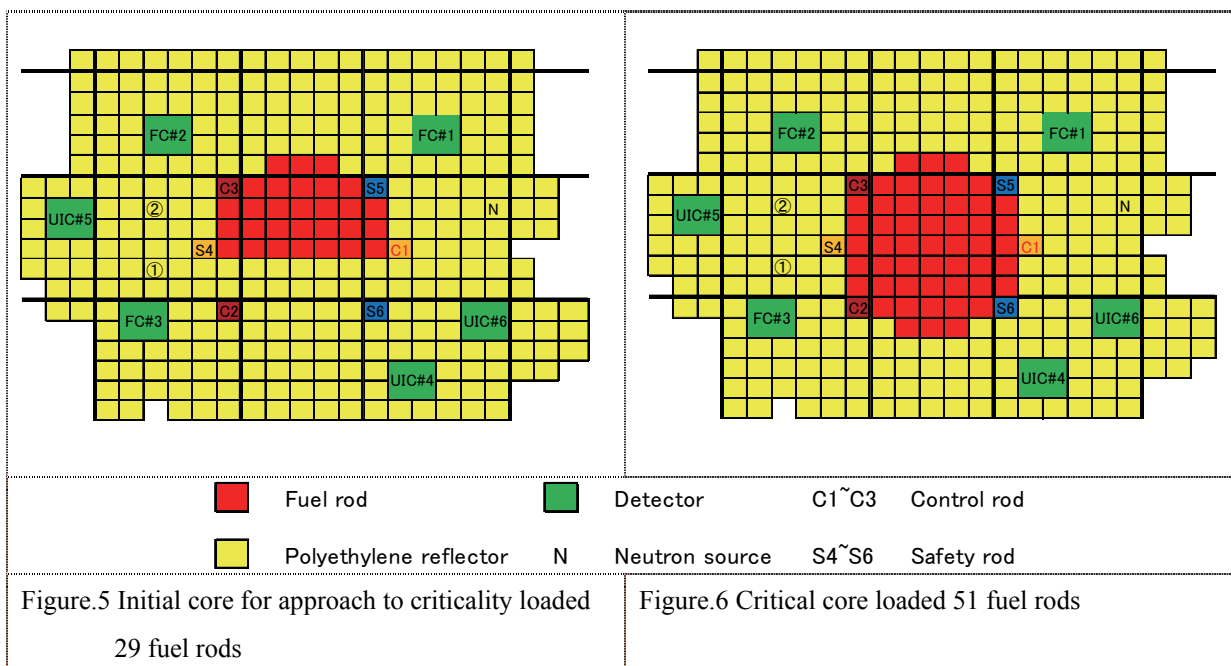


Fig.4 B7/8''PETEETEE fuel rod

B7/8''PETEETEE has never been assembled. Figure 3 shows the unit fuel cell of the core, and Figure 4 the fuel rod. Initially the experiment was performed with 29 fuel rods. Figure 5 illustrates the initial core for approach to criticality. Added the number of fuel rods, finally the core loaded 51fuel rods has been critical. The critical core is showed in Fig. 6.



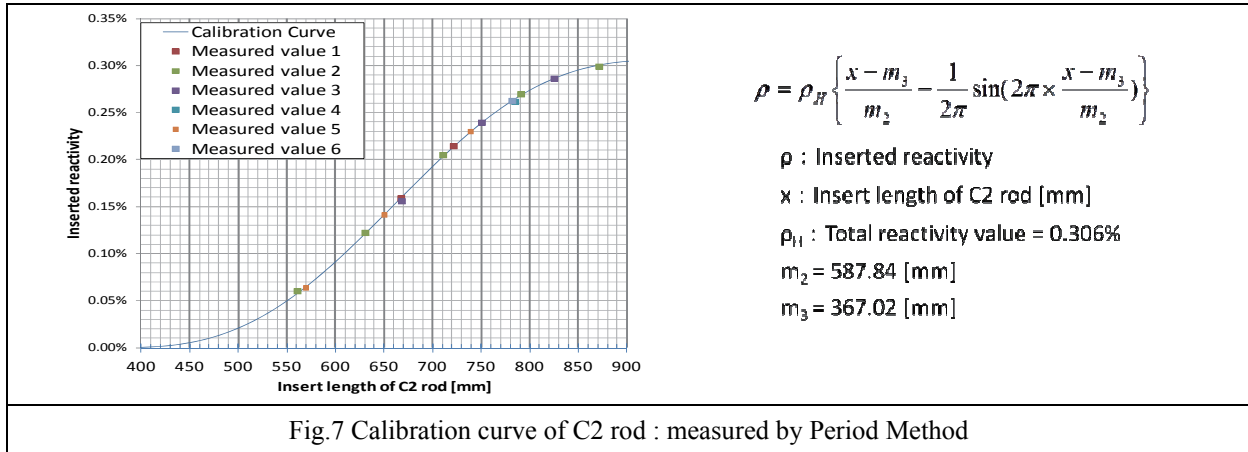
### 2.2 Control Rod Calibration

Control rod worth was measured by two methods: Rod Drop Method and Period Method. Table 1 lists control rods worth of the critical core shown in Fig. 5 measured by Rod Drop Method. These values satisfy the constraints of KUCA. The constraints are that the value of the largest control rod worth is lower than one third of the whole control rod worth, and the whole control rod worth is between 1 and 4%.

Table.1 Reactivity worth of Control rods

	Reactivity Worth [ $\Delta k/k$ ]
C1 rod	0.31%
C2 rod	0.32%
C3 rod	0.32%
Whole control rod	1.90%

On the other hand, inserted worth of C2 rod was measured by Period Method. The measurement was repeated six times with changing inserted length of C2 rod. Moreover the integral control rod calibration curve of C2 rod has been plotted using following equation. Figure 7 shows the inserted worth of C2 rod and the calibration curve of C2 rod. The calibration curve represents the reactivity as the inserted length of C2 rod. The formula of the calibration curve is shown beside the Fig. 7.



The calibration curve was fitted to the measured values. Using the calibration curve, reactivity worth can be found by only monitoring the inserted length of C2 rod without measurement by Period Method.

### 2.3 Measurement of Sample Worth for Thorium

In this experiment, sample worth of replacement from Thorium plates to Aluminum plates was measured. Figure 8 shows the configuration of the core for measurement of Thorium sample worth. For the measurement of the sample worth for Thorium plate, the excess reactivity of three types of cores was measured.

- The core for no Thorium plate replaced
- The core for two Thorium plates replaced to Aluminum
- The core for four Thorium plates replaced to Aluminum

To prevent the excess reactivity from exceeding the constraint of KUCA when Thorium plates are replaced to Aluminum plates, two fuel rods were replaced to partial length fuel rods. Figure 9 shows Partial length fuel rod.

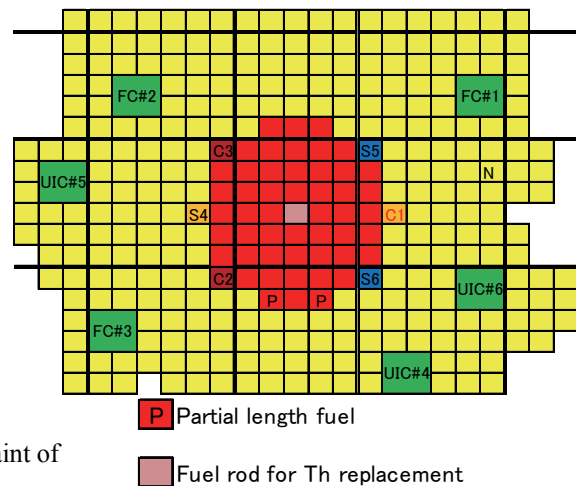


Fig.8 Core configuration for measurement of Thorium sample worth

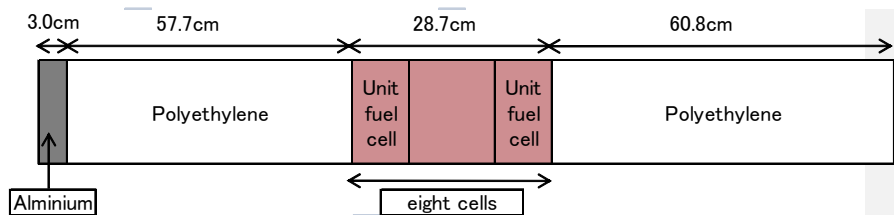


Fig.9 Partial length fuel rod

To get the reproducibility of measured results, following works were repeated four times.

- I. Measurement of excess reactivity of the core for no replacement was performed.
- II. Central four Thorium plates of the center fuel rod were replaced to Aluminum plates, and the excess reactivity of the core was measured.

- III. Two plates which were either end of four Aluminum plates replaced from Thorium plates on Experiment II were replaced to Thorium plates, and the excess reactivity of the core was measured.
- IV. The remaining two Aluminum plates were replaced to Thorium plates, and excess reactivity of the core was measured.

The measurements of excess reactivity were performed using the calibration curve of C2 rod shown in Figure 7. Although it's thought that the figure of the calibration curve changes if Thorium plates are replaced, it's assumed that the difference is small enough. The results are shown in Table 2.

Table.2 Excess reactivity of three types of core for Thorium sample worth

Core configuration	Excess reactivity[ $\Delta k/k$ ]	Standard deviation
No Th plates replaced	4.35E-04	3.06E-06
Two Th plates replaced	1.43E-03	3.59E-06
Four Th plates replaced	2.44E-03	1.11E-05

As the results, replacement worth of one Thorium plate to Aluminum plate is  $5.01 \times 10^{-4}$ , and the standard deviation is  $6.30 \times 10^{-6}$ .

### 3. Comparison with Calculation by MVP

To compare the results of the experiment, the calculation by continuous energy Monte Carlo code MVP[5] by JENDL-4.0 was performed. The history number is  $20,000 \times (50,000+50)$  : The number of neutron history is 20,000, batch is 50,000, 50 batches are abandoned. From the results, the replacement worth of one Thorium plate of each library was calculated. They are showed in Table 3.

Table.3 Replacement worth of one Thorium by MVP calculation

	JENDL-4.0	JENDL-3.3	ENDF/B-VII.0	JEFF-3.1
<b>Replacement worth</b>	4.46.E-04	4.43.E-04	4.37.E-04	4.60.E-04
<b>Error</b>	4.2%	4.2%	4.3%	4.1%
<b>Relative difference from experimental value</b>	-12.3%	-13.0%	-14.6%	-8.9%

The replacement worth of these libraries has about 5% difference each other. It can be thought the difference of libraries causes it. Above the relative difference of each library from experimental value are about 10%. It indicates possibility that the experimental value is wrong. It is based on delayed neutron fraction which is calculated by SRAC, so it's necessary to assess the impact of delayed neutron fraction by using different libraries.

### Future Works

It was ascertained not only that there was difference of replacement worth for one Thorium plate between libraries but that the experimental results had inaccuracy because of delayed neutron fraction. So, impact of delayed neutron fraction of different libraries will be assessed.

Moreover the rest core which has the unit cell of  $^{232}\text{Th}/^{235}\text{U}=15.2$  and  $\text{H}/^{235}\text{U}=210$ , was assembled at KUCA in November 2011. The neutron spectrum is softer than the above core, and the same replacement worth

experiment is planned to check the impact of neutron spectrum change on the replacement worth. The detailed comparison among the libraries and the validation of libraries are also planned to be performed by using MVP and sensitivity analysis code.

## References

- [1] K. Shibata, O. Iwamoto, T. Nakagawa, N. Iwamoto, A. Ichihara, S. Kunieda, S. Chiba, K. Furutaka, N. Otuka, T. Ohsawa, T. Murata, H. Matsunobu, A. Zukeran, S. Kamada, and J. Katakura: "JENDL-4.0: A New Library for Nuclear Science and Engineering," *J. Nucl. Sci. Technol.* 48(1), 1-30 (2011)
- [2] K. Shibata, T. Kawano, T. Nakagawa, O. Iwamoto, J. Katakura, T. Fukahori, S. Chiba, A. Hasegawa, T. Murata, H. Matsunobu, T. Ohsawa, Y. Nakajima, T. Yoshida, A. Zukeran, M. Kawai, M. Baba, M. Ishikawa, T. Asami, T. Watanabe, Y. Watanabe, M. Igashira, N. Yamamuro, H. Kitazawa, N. Yamano and H. Takano: "Japanese Evaluated Nuclear Data Library Version 3 Revision-3: JENDL-3.3," *J. Nucl. Sci. Technol.* 39, 1125 (2002).
- [3] M. B. Chadwick, P. Oblozinsky, M. Herman, N. M. Greene, R. D. McKnight et al., "ENDF/B-VII.0: Next generation evaluated nuclear data library for nuclear science and technology," *Nucl. Data Sheets*, 102, 2931 (2006).
- [4] A. Koning, R. Forrest, M. Kellett, R. Mills, H. Henriksson, Y. Rugama (Ed.) "The JEFF-3.1 nuclear data library", JEFF Report 21 (2006).
- [5] Y. Nagaya, K. Okumura, T. Mori et al., "MVP/GMVP Version 2 : General Purpose Monte Carlo Codes for Neutron and Photon Transport Calculations based on Continuous Energy and Multigroup Methods", JAERI 1348 (2005).

## 32 Benchmark Test of JENDL-4.0 with TOF Experiments at Osaka Univ./OKTAVIAN

Yoshinari KATO<sup>1)</sup>, Kentaro OCHIAI<sup>2)</sup>, Kosuke TAKAKURA<sup>2)</sup>,  
Satoshi SATO<sup>2)</sup>, Chikara KONNO<sup>2)</sup>

1) Tokai University, Kitakaname 4-1-1, Hiratsuka-shi, Kanagawa-ken 259-1292

2) Japan Atomic Energy Agency, Shirakata-shirane 2-4, Tokai-mura, Naka-gun,  
Ibaraki-ken 319-1184

E-mail: 0barm001@mail.tokai-u.jp

JENDL-4.0, the latest version of Japanese Evaluated Nuclear Data Library (JENDL), was released in May 2010. In order to validate JENDL-4.0, we have analyzed TOF experiments at Osaka University OKTAVIAN with JENDL-4.0 and the Monte Carlo N-Particle transport code MCNP5. And for comparison, older version JENDL-3.3 and other recent nuclear data libraries ENDF/B-VII.0 and JEFF-3.1 have also been used. As a result, the followings have been found out: (1) Si, As, Se, Mo, W: Calculation results with JENDL-4.0 agreed with the experimental ones better than those with JENDL-3.3. (2) Cr, Mn, Nb: Calculation results with JENDL-4.0 were partially better and partially worse than those with JENDL-3.3.

### 1. Introduction

The latest version of Japanese Evaluated Nuclear Data Library (JENDL), JENDL-4.0 [1], was released in May 2010. It is important to validate JENDL-4.0 through analyses of integral benchmark experiments. From 1984 to 1988, sphere pile integral benchmark experiments were carried out with DT neutrons of OKTAVIAN in Osaka University [2]. Thus we have analyzed these experiments with JENDL-4.0 as one of benchmark tests of JENDL-4.0.

### 2. Overview of TOF Experiments at OKTAVIAN

Leakage neutron spectra from spherical piles were carried out with the time-of-flight (TOF) technique at the DT neutron source facility OKTAVIAN in Osaka University. The piles were made by filling spherical vessels with sample powder or flakes of LiF, CF<sub>2</sub>, Al, Si, Ti, Cr, Mn, Co, Cu, As, Se, Zr, Nb, Mo and W. Neutrons were produced in the (d,t) reaction by bombarding a 370 GBq tritium target placed at the center of the pile with 250 keV deuteron

beam. A cylindrical liquid organic scintillator NE-218 was used as a neutron detector, which was located at about 11 m from the tritium target in direction of 55 deg. with respect to the deuteron beam axis, surrounded by concrete or heavy concrete. A pre-collimator made of polyethylene-iron multi-layers was set between the pile and the detector in order to reduce the background neutrons. The experimental arrangement is shown in Fig. 1. The total error was estimated to be about 10 % in this study.

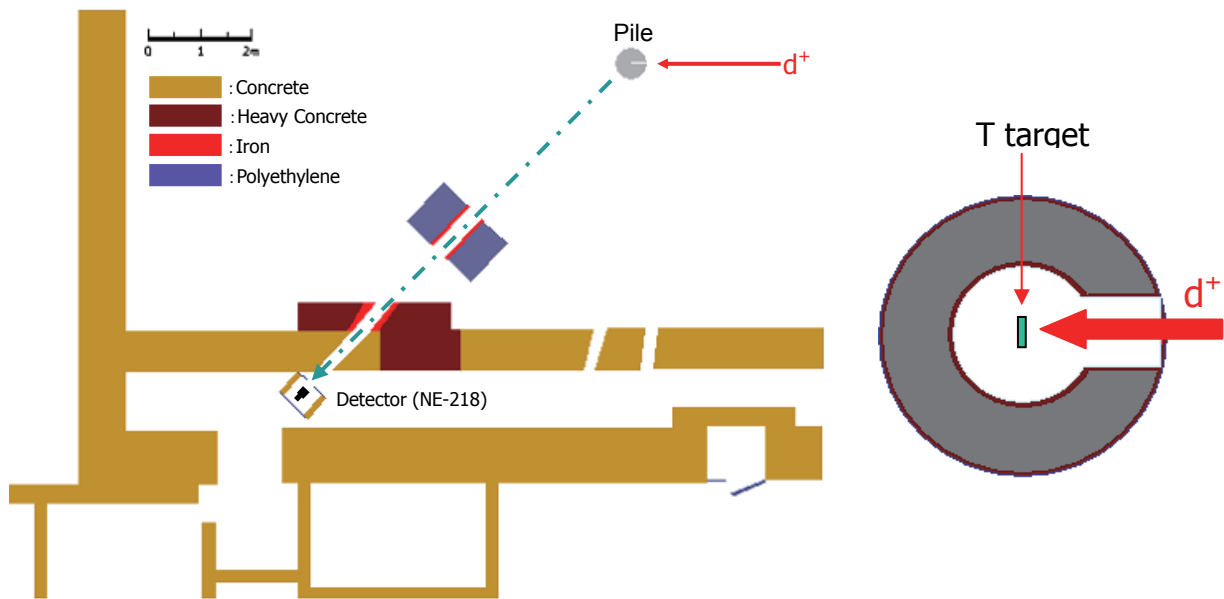


Fig. 1 Experimental arrangement.

### 3. Analysis

The Monte Carlo code MCNP-5 [3] and ACE file FSXLIB-J40 generated from JENDL-4.0 have been used for the analysis. Calculations with the ACE files of the following nuclear data libraries have also been carried out for comparison.

- JENDL-3.3 (ACE file : FSXLIB-J33) [4]
- ENDF/B-VII.0 (ACE file : endf70 in MCNP Data) [5]
- JEFF-3.1 (ACE file : MCJEFF3.1) [6]

Experiments for lithium fluoride and aluminum piles have not been analyzed in this work because these nuclear data were not revised in JENDL-4.0.

For more detailed investigation, we have compared reaction cross section data (MF=3) and angular distribution data (MF=4), energy spectrum data (MF=5) or energy-angle distribution data (MF=6) of emitted particle and replaced them in selected reactions of JENDL-3.3 by those of JENDL-4.0. ACE files have been produced with NJOY99.336 [7] and patch for JENDL-4.0.

#### 4. Results and Discussion

Measured and calculated spectra are shown in Figs. 2 - 9. As a result, we have found out the followings:

- 1) Silicon, Arsenic, Selenium, Molybdenum: Calculation results with JENDL-4.0 agreed with the experimental ones better than those with other 3 libraries.
- 2) Tungsten: Calculation results with JENDL-4.0 agreed with the experimental ones better than those with JENDL-3.3 and JEFF-3.1.
- 3) Chromium, Manganese: Calculation results with JENDL-4.0 were partially better and partially worse than those with other 3 libraries.
- 4) Niobium: Calculation results with JENDL-4.0 were partially better and partially worse than those with JENDL-3.3.
- 5) Polytetrafluoroethylene (CF<sub>2</sub>), Titanium, Cobalt, Copper, Zirconium: Calculation results with JENDL-4.0 were comparable to those with JENDL-3.3.

Next we have investigated reasons of differences between calculations with JENDL-4.0 and JENDL-3.3 for arsenic, selenium, niobium and tungsten by comparing reaction cross section data and double differential cross section (DDX) data. We have specified that the followings caused the differences.

- 1) Arsenic : DDX data of the  $^{75}\text{As}(n, 2n)^{74}\text{As}$  and  $^{75}\text{As}(n, n')^{75m}\text{As}$  reactions are improved (calculated with POD code) in JENDL-4.0.
- 2) Selenium : Reaction cross section data and DDX data of the  $^{78}\text{Se}(n, n')^{78m}\text{Se}$  and  $^{80}\text{Se}(n, n')^{80m}\text{Se}$  reactions to the continuum state are improved (calculated with POD code) in JENDL-4.0.
- 3) Tungsten : Reaction cross section data and DDX data of the  $^{183}\text{W}(n, 2n)^{182}\text{W}$ ,  $^{184}\text{W}(n, 2n)^{183}\text{W}$  and  $^{186}\text{W}(n, 2n)^{185}\text{W}$  reactions are improved (calculated with CCONE code) in JENDL-4.0.
- 4) Niobium : DDX data of the  $^{93}\text{Nb}(n, 2n)^{92}\text{Nb}$  reaction and the  $^{93}\text{Nb}(n, n')^{93m}\text{Nb}$  reaction to the continuum state are revised (taken from JENDL fusion file). DDX data of these reactions are improved below 1 MeV in JENDL-4.0, while those are worsen above 1 MeV.

#### 5. Conclusion

We have benchmarked JENDL-4.0 with TOF experiments at Osaka University OKTAVIAN. The followings have been found out:

- 1) Silicon, Arsenic, Selenium, Molybdenum, and Tungsten : Calculation results with JENDL-4.0 agree with the experimental ones better than those with JENDL-3.3.
- 2) Polytetrafluoroethylene (CF<sub>2</sub>), Titanium, Cobalt, Copper, Zirconium : Calculation

results with JENDL-4.0 are comparable to those with JENDL-3.3.

- 3) Chromium, Manganese, Niobium : Calculation results with JENDL-4.0 are partially better and partially worse than those with JENDL-3.3.

## References

- [1] K. Shibata, O. Iwamoto, T. Nakagawa *et al.*, JENDL-4.0: A New Library for Nuclear Science and Engineering, *J. Nucl. Sci. Technol.* 48(1) (2011), pp. 1-30.
- [2] F. Maekawa, J. Yamamoto, C. Ichihara *et al.*, *Collection of experimental data for fusion neutronics benchmark*, JAERI-M 94-014, Japan Atomic Energy Research Institute, (1994).
- [3] X-5 Monte Carlo Team, *MCNP - A General Monte Carlo N-Particle Transport Code, Version 5*, LA-UR-03-1987 Revised, Los Alamos National Laboratory, (2008).
- [4] K. Shibata, T. Kawano, T. Nakagawa *et al.*, Japanese Evaluated Nuclear Data Library Version 3 Revision-3: JENDL-3.3, *J. Nucl. Sci. Technol.* 39(2002), pp.1125-1136.
- [5] M.B. Chadwick, P. Oblozinsky, M. Herman *et al.*, ENDF/B-VII.0: next generation evaluated nuclear data library for nuclear science and technology, *Nucl. Data sheets* 107(2006), pp. 2931-3059.
- [6] A. Koning, R. Forrest, M. Kellett *et al.*, *The JEFF-3.1 Nuclear Data Library*, JEFF Report 21, OECD Nuclear Energy Agency, (2006).
- [7] R.E. MacFarlane, D.W. Muir, *The NJOY Nuclear Data Processing System, Version 91*, LA-12740-M, Los Alamos National Laboratory, (1994).

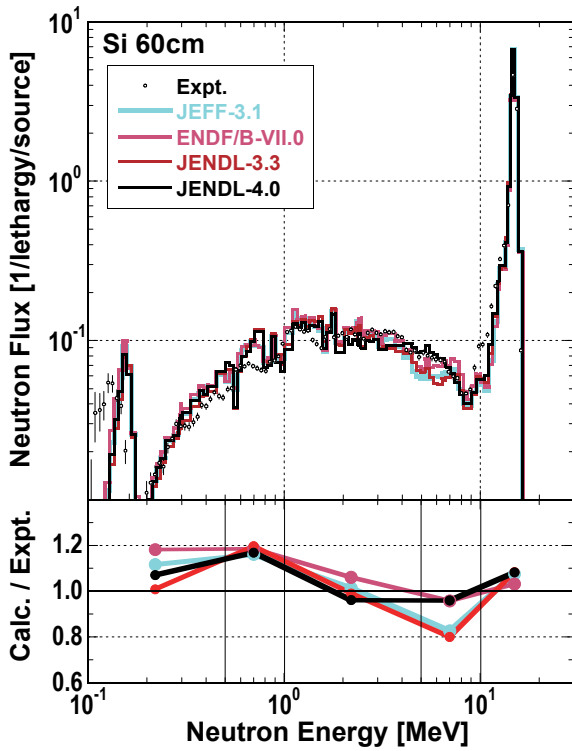


Fig. 2 Experimental and calculated spectra from Si 60 cm pile.

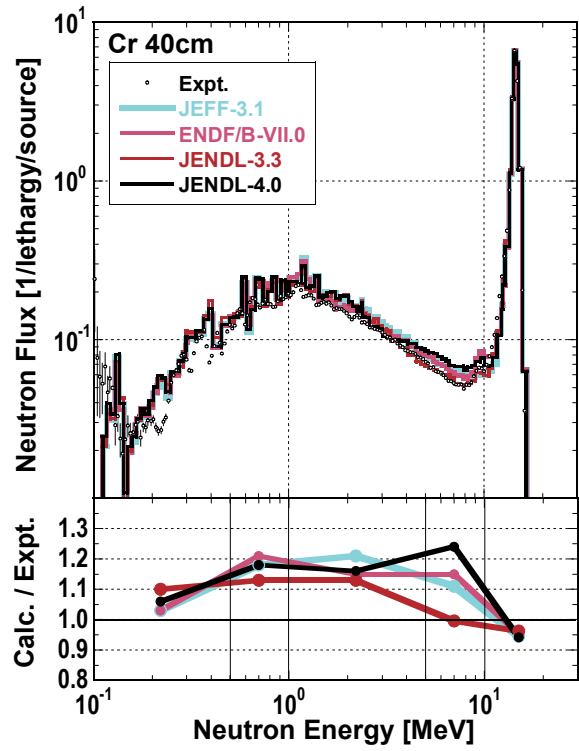


Fig. 3 Experimental and calculated spectra from Cr 40 cm pile.

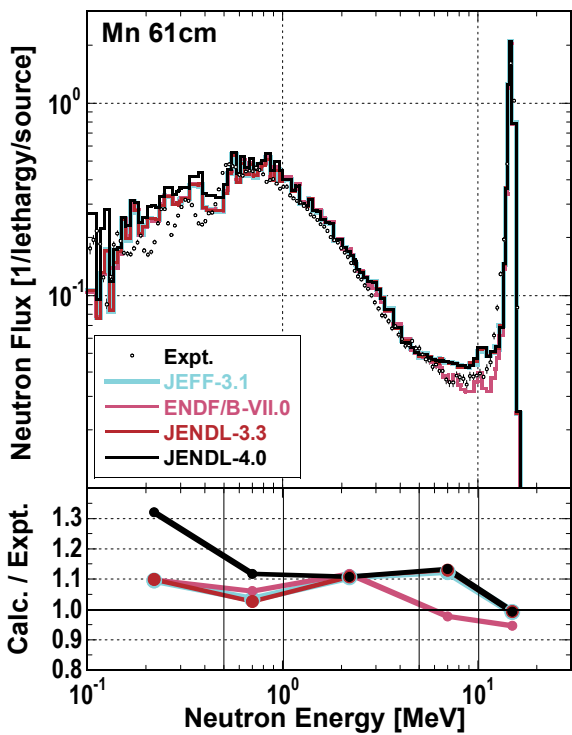


Fig. 4 Experimental and calculated spectra from Mn 61 cm pile.

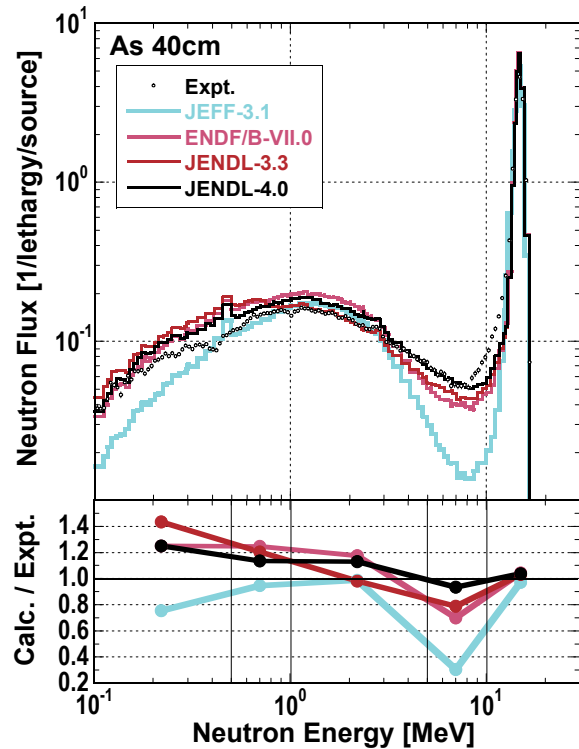


Fig. 5 Experimental and calculated spectra from As 40 cm pile.

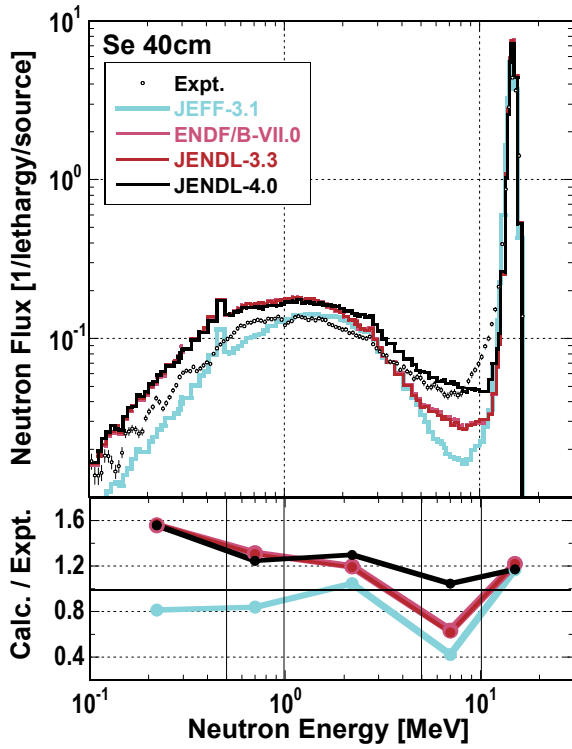


Fig. 6 Experimental and calculated spectra from Se 40 cm pile.

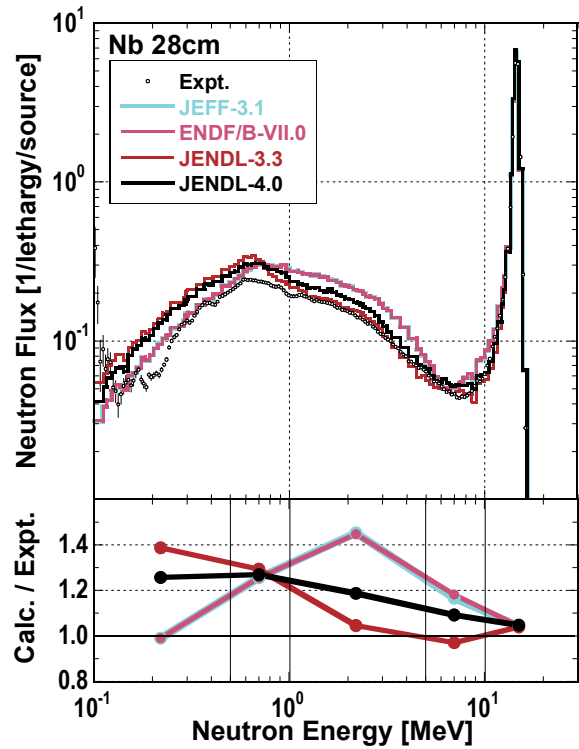


Fig. 7 Experimental and calculated spectra from Nb 28 cm pile.

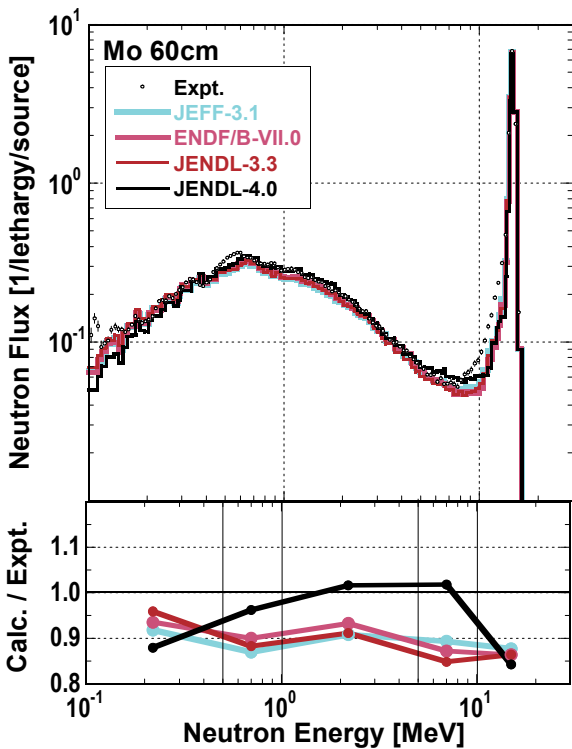


Fig. 8 Experimental and calculated spectra from Mo 60 cm pile.

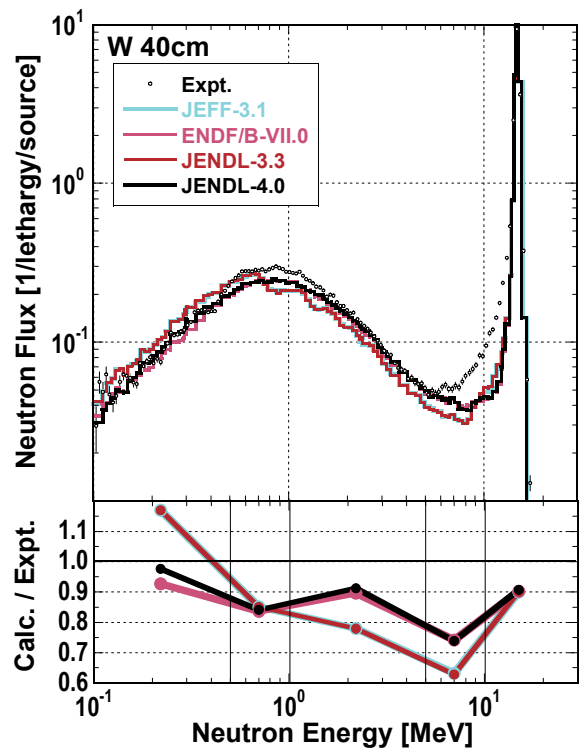


Fig. 9 Experimental and calculated spectra from W 40 cm pile.

### 33 Self-shielding effect in unresolved resonance data in JENDL-4.0

Chikara Konno<sup>1</sup>, Yoshinari Kato<sup>2</sup>, Kosuke Takakura<sup>1</sup>, Kentaro Ochiai<sup>1</sup>, and Satoshi Sato<sup>1</sup>

<sup>1</sup>Fusion Research and Development Directorate, Japan Atomic Energy Agency  
Tokai-mura, Naka-gun, Ibaraki-ken 319-1195 Japan  
e-mail : konno.chikara@jaea.go.jp

<sup>2</sup>Tokai University  
1117 Kitakaname, Hiratsuka-shi, Kanagawa-ken 259-1292 Japan

At International Conference on Nuclear Data for Science and Technology in 2007 we pointed out that most of unresolved resonance data in JENDL-3.3 have a problem related to self-shielding correction. Here with a simple calculation model we have investigated whether the latest JENDL, JENDL-4.0, was improved for the problem or not. The results suggest that unresolved resonance data in JENDL-4.0 have no problem, but it seems that self-shielding effects for the unresolved resonance data in JENDL-4.0 are too large. New benchmark experiments for unresolved resonance data are strongly recommended in order to verify unresolved resonance data.

#### 1. Introduction

At International Conference on Nuclear Data for Science and Technology in 2001, we pointed out that the leakage neutron spectrum from a niobium sphere of 0.5 m in radius with a 20 MeV neutron in the center, which was calculated with ANISN [1], MCNP4C [2] and JENDL-3.3 [3], had a large strange bump around 100 keV as shown in Fig. 1 [4].

At International Conference on Nuclear Data for Science and Technology in 2007, we specified that too large self-shielding correction around the maximum energy of the unresolved resonance region shown in Fig. 2 caused the large strange bump around 100 keV in the leakage neutron spectrum from the niobium sphere and that most (139 nuclei) of unresolved resonance data in JENDL-3.3 had the same problem [5].

JENDL-4.0 [6], the newest JENDL, tried to improve this problem by increasing the maximum energy of the unresolved resonance region. Note that nuclei with unresolved resonance data in JENDL-4.0 (291 nuclei) are more than those in JENDL-3.3 (210 nuclei), e.g. <sup>55</sup>Mn.

In this paper we have examined the unresolved resonance data in JENDL-4.0 and their self-shielding effects with a simple calculation model.

## 2. Method

We adopted a simple calculation model, where neutron spectra were calculated inside a natural element sphere of 1 m in radius with a 20 MeV neutron source in the center. Pure manganese, arsenic and niobium were selected as the natural material because the self-shielding effects were expected to be larger owing to the unique stable isotope.

The Monte Carlo code MCNP4C and the official ACE file FSXLIB-J40 [7] of JENDL-4.0 were used for this analysis. We performed both analyses with and without the probability table for unresolved resonance data. Analyses with the official ACE file FSXLIB-J33 [8] of JENDL-3.3 were also carried out for comparison.

For check of self-shielding correction, self-shielding corrected and uncorrected cross sections were deduced from the official MATXS file MATXSLIB-J33 [8] and MATXSLIB-J40 [7] of JENDL-3.3 and JENDL-4.0, respectively, with the TRANSX-2.15 [9] code.

## 3. Results and discussion

Figure 3 shows the neutron spectra at 60 cm from the center of natural manganese sphere of 1 m in radius with a 20 MeV neutron source in the center. The unresolved resonance region is 125 keV - 1 MeV in  $^{55}\text{Mn}$  of JENDL-4.0, while  $^{55}\text{Mn}$  in JENDL-3.3 has no unresolved resonance data. The spectra with JENDL-4.0 without unresolved resonance data and JENDL-3.3 are almost the same in the unresolved resonance region. There is no strange bump around the maximum energy of the unresolved resonance region in the neutron spectrum with JENDL-4.0 with unresolved resonance data. However it seems that the self-shielding effect is too large. Figure 4 shows the self-shielding corrected and uncorrected total cross section data of  $^{55}\text{Mn}$ . It is clear that the self-shielding correction for the unresolved resonance data is very large, particularly around the minimum energy of the unresolved resonance region, compared with that for the resolved resonance data.

Figure 5 shows the neutron spectra at 60 cm from the center of natural arsenic sphere of 1 m in radius with a 20 MeV neutron source in the center. The unresolved resonance region is 9.7 keV - 500 keV in  $^{75}\text{As}$  of JENDL-4.0, while it is 9.7 keV - 100 keV in  $^{75}\text{As}$  of JENDL-3.3. There is no strange bump, which appears in the neutron spectrum with JENDL-3.3, around the maximum energy of the unresolved resonance region in the neutron spectrum with JENDL-4.0 with unresolved resonance data. As well as  $^{55}\text{Mn}$ , it seems that the self-shielding effect is too large. Figure 6 shows the self-shielding corrected and uncorrected total cross section data of  $^{75}\text{As}$ . The self-shielding correction for the

unresolved resonance data is very large, particularly around the minimum energy of the unresolved resonance region, compared with that for the resolved resonance data.

Figure 7 shows the neutron spectra at 60 cm from the center of natural niobium sphere of 1 m in radius with a 20 MeV neutron source in the center. The unresolved resonance region is 7 keV - 600 keV in  $^{93}\text{Nb}$  of JENDL-4.0, while it is 7 keV - 100 keV in  $^{93}\text{Nb}$  of JENDL-3.3. There is no strange bump, which appears in the neutron spectrum with JENDL-3.3, around the maximum energy of the unresolved resonance region in the neutron spectrum with JENDL-4.0 with unresolved resonance data. As well as  $^{55}\text{Mn}$  and  $^{75}\text{As}$ , it seems that the self-shielding effect is too large. Figure 8 shows the self-shielding corrected and uncorrected total cross section data of  $^{93}\text{Nb}$ . The self-shielding correction is comparable with that for the resolved resonance data, particularly around the minimum energy of the unresolved resonance region.

The results suggest that unresolved resonance data in JENDL-4.0 have no problem, but it seems that self-shielding effects for the unresolved resonance data in JENDL-4.0 are too large. So far unresolved resonance data have not been verified with experiments. New integral experiments for benchmarking unresolved resonance data are strongly recommended.

#### 4. Summary

We investigated unresolved resonance data in JENDL-4.0 and their self-shielding effects for  $^{55}\text{Mn}$ ,  $^{75}\text{As}$  and  $^{93}\text{Nb}$  with a simple calculation model. It suggests that unresolved resonance data in JENDL-4.0 have no problem, but it seems that self-shielding effects of the unresolved resonance data in the neutron spectrum are too large. New benchmark experiments for unresolved resonance data in JENDL-4.0 are strongly recommended in order to verify unresolved resonance data.

#### References

- [1] C. Konno, Y. Ikeda, MATXS Files Processed from JENDL-3.2 and -3.3 for Shielding, *J. Nucl. Sci. Technol. Suppl. 2* (2002), pp. 1037-1041.
- [2] *DOORS3.2a : One, Two- and Three-Dimensional Discrete Ordinates Neutron/Photon Transport Code System*, RSICC CODE PACKAGE CCC-650, Oak Ridge National Laboratory, (2007).
- [3] J.F. Briesmeister (Ed.), *MCNP - A General Monte Carlo N-Particle Transport Code, Version 4C*, LA-13709-M, Los Alamos National Laboratory, (2000).
- [4] K. Shibata, et al., Japanese Evaluated Nuclear Data Library Version 3 Revision-3: JENDL-3.3, *J. Nucl. Sci. Tech.* 39 (2002), pp. 1125-1136.

- [5] C. Konno, et al., Problem on Unresolved Resonance Data in Recent Nuclear Data Libraries, *Proc. International Conference on Nuclear Data for Science and Technology 2007*, Nice, France, April 22-27, 2007, (2008) pp.713-716.
- [6] K. Shibata, et al., JENDL-4.0: A New Library for Nuclear Science and Engineering, *J. Nucl. Sci. Technol.*, 48 (2010), pp. 1-30.
- [7] K. Okumura, private communication (2010).
- [8] K. Kosako, et al., *The Libraries FSXLIB and MATXSLIB based on JENDL-3.3*, JAERI-Data/Code 2003-011, Japan Atomic Energy Research Institute, (2003).
- [9] R.E. MacFarlane, *TRANSX 2 : A Code for Interfacing MATXS Cross-Section Libraries to Nuclear Transport Codes*, LA-12312-MS, Los Alamos National Laboratory, (1993).

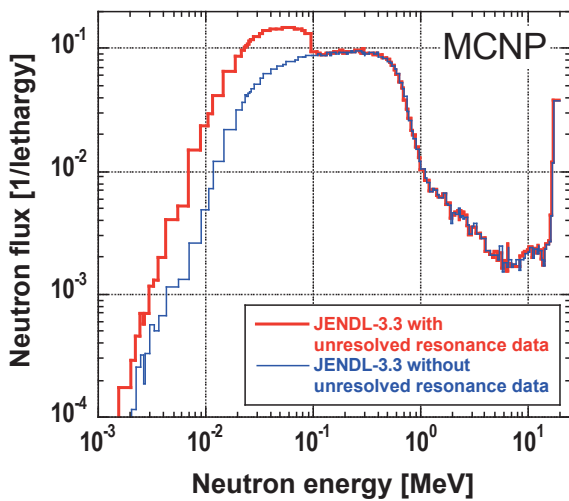


Fig. 1 Leakage neutron spectra from niobium sphere (MCNP).

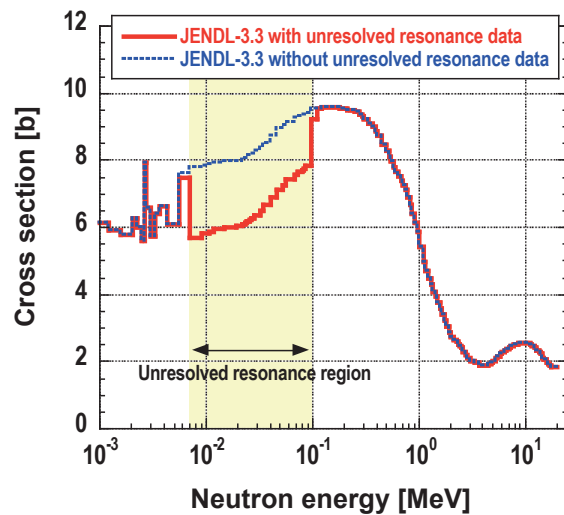


Fig. 2 Elastic cross section of <sup>93</sup>Nb in JENDL-3.3

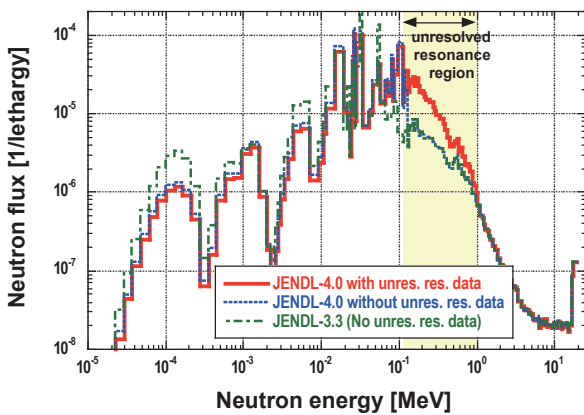


Fig. 3 Leakage neutron spectra from manganese sphere (MCNP).

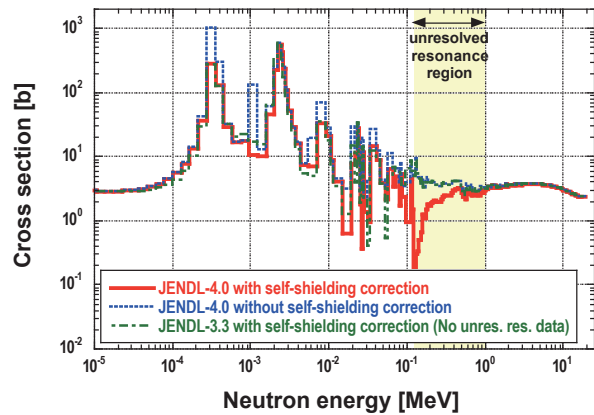


Fig. 4 Total cross section of <sup>55</sup>Mn.

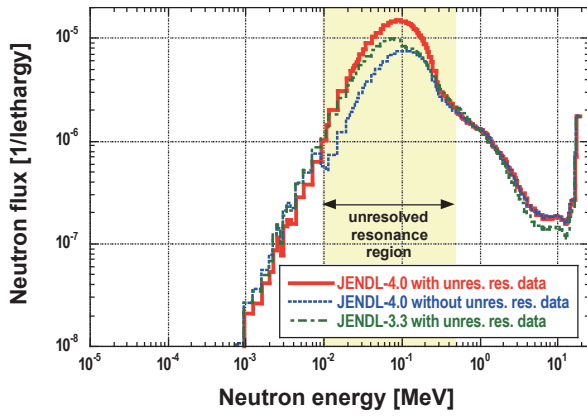


Fig. 5 Leakage neutron spectra from arsenic sphere (MCNP).

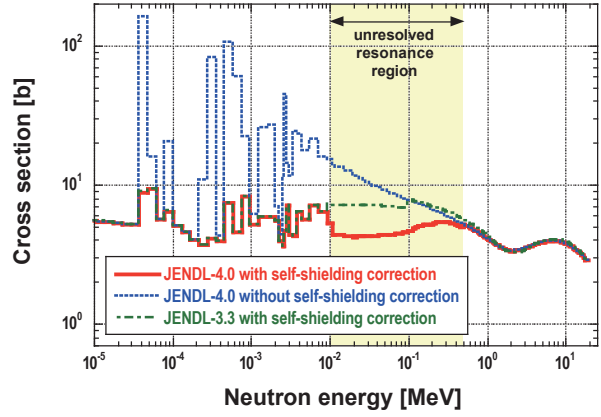


Fig. 6 Total cross section of  $^{75}\text{As}$ .

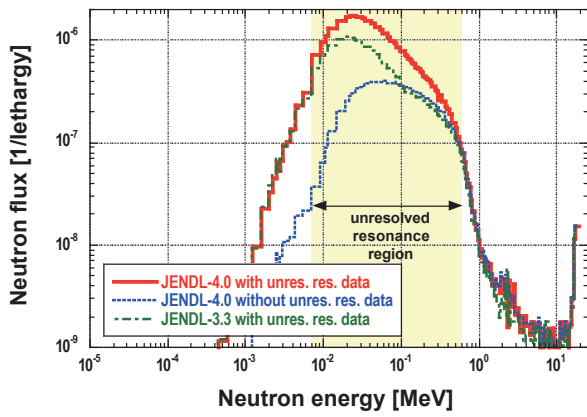


Fig. 7 Leakage neutron spectra from niobium sphere (MCNP).

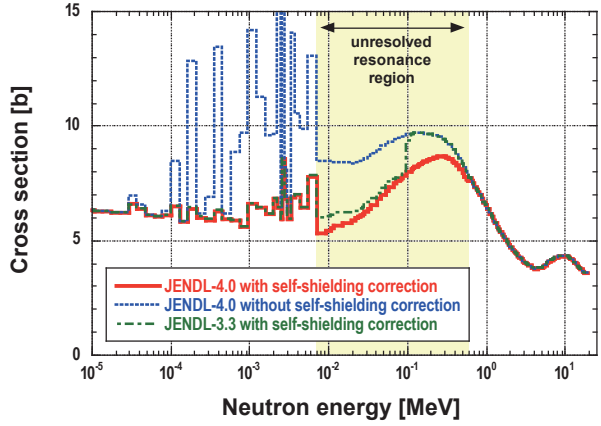


Fig. 8 Total cross section of  $^{93}\text{Nb}$ .

This is a blank page.

## 34 Angular distribution of light fragments for proton induced reaction at intermediate energies

T.Sanami, M.Hagiwara, H.Iwase

*Applied research laboratory, High energy accelerator research organization,*

*Oho 1-1, Tsukuba, Ibaraki 305-0801 JAPAN*

Email: toshiya.sanami@kek.jp

Angular distributions of light mass fragments for proton induced reaction at intermediate energies were obtained based on systematic experimental data of double differential cross sections measured using Bragg curve counter. For energy integration of the experimental data from threshold to upper energy, the data points were fitted using Maxwellian curve with considering coulomb barrier effect. The obtained angular distributions were compared with calculation results obtained by theoretical code that consists of intra-nuclear cascade model and general evaporation model. The comparison indicates that the calculation generally reproduces angular distribution of experimental data well.

### 1. Introduction

Energy and angular distribution of light mass fragment (LMF) produced by a nuclear reaction are one of key parameters to evaluate irradiation effect in a matter due to incidence of energetic particles at intermediate energies, since the effects depend on linear energy transfer that increases with Z number of ions. To simulate irradiation effect at this energy, a general reaction model that calculates reaction products, energy and angular distribution based on pictures of reaction mechanisms, should be established since the correlation of generated ions is indispensable for the evaluation. The picture and reaction model parameters should be examined for their predictions using systematic experimental data of double differential cross section (DDX). Our group has conducted series of experiments for DDX measurement of fragment production. Under this program, we developed a Bragg curve counter (BCC) with improving acceptable energy range to measure various LMFs in this energy range [1-3]. The DDXs of LMFs were obtained for C, N, O, Al, Ti, and Cu targets for 40 to 300 MeV proton incident energies at 30 to 120 degree emission angles [4-8]. The data set is useful not only as benchmark data for evaluation of existing reaction models and parameters but also for development of new models based on a picture of LMF production. Angular distribution of LMFs which could be deduced from energy integration of DDXs, provides an idea of reaction picture,

knock-on, pickup process or indirect statistical decay process, for instance. In this study, we deduced angular distribution of LMFs from DDX data points by Maxwellian curve fitting with considering coulomb barrier effect. The obtained angular distributions were compared with calculation results obtained by existing theoretical code that consists of intra-nuclear cascade model and general evaporation model.

## 2. Experimental

Details of experimental apparatus and procedure were described in references [1,2,6,7,8], thus only outline is described below. The experiments were performed using the NIRS 930 cyclotron in National Institute of Radiological Science (NIRS) for 40-80 MeV protons and the ring cyclotron in Research Center for Nuclear Physics (RCNP), Osaka University for 140-300 MeV protons. Figure 1

shows a picture of the experimental setup at RCNP. Proton beam was focused to 1 mm in diameter spot size on the target foil that was mounted on a target changer. The target changer mounts blank, ZnS viewer as well as less than 1  $\mu\text{m}$  in thickness C, Al, AlN, Al<sub>2</sub>O<sub>3</sub>, Ti, Cu and Ta targets. Al<sub>2</sub>O<sub>3</sub> and AlN were sputtered on a Ta foils for oxygen and nitrogen DDX measurement with subtracting Al and Ta contribution by separate runs. Fragments from the target were measured by the BCCs mounted on the 30, 60, 90 and 120° ports of the scattering chamber.

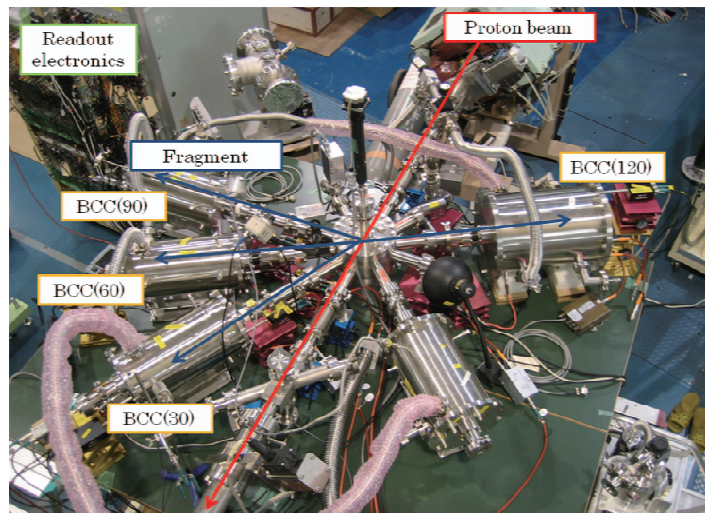


Figure 1 Picture of experimental setup at RCNP

Figure 2 shows schematic view of the BCC. The BCC is a parallel plate ionization chamber with a grid. The structure was contained in a stainless steel cylindrical chamber. The distances between cathode and grid, and grid and anode were 300 mm and 5 mm, respectively. The field shaping rings maintained uniformity of the electric field. High voltage was applied to the cathode, field shaping rings and

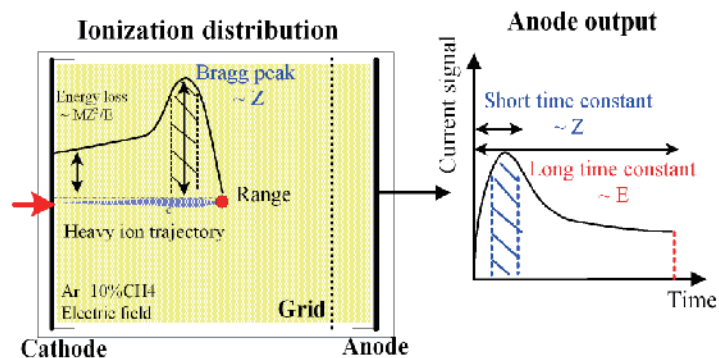


Figure 2 Schematic view of BCC(left) and its output signal.

grid electrodes to form electric field for electron drift. The cylindrical chamber was sealed using O-rings to keep low-pressure counting gas, 267 kPa (200 Torr) Ar+10% CH<sub>4</sub> gas, inside. The cathode side of the chamber had a hole of 20 mm in diameter covered with a thin entrance window, 0.5 μm thick SiN supported by window frame, to introduce fragments from the target. Fragments which entered the BCC stopped and produced electrons through ionization process. The number of electrons along its trajectory was proportional to the energy loss of the fragment, i.e, Bragg curve. The electrons drifted toward to the grid with keeping their distribution along the electric field between the cathode and grid. The grid potential was chosen to allow that all electrons reach to the anode with passing through the grid. Under this condition, time distribution of the anode signal had inverse shape of the original distribution of electrons that equal to Bragg curve. Thus, the energy and atomic number of the fragment could be deduced from integral and peak height of the anode signal. In addition to this, the events having too low energy to identify using the Bragg curve vs energy plot could be identified through the range-energy plot method [1]. The range was determined using the signal from the cathode electrode. On the other hand, for the events having too high energy to be stopped in BCC, the missed energy could be compensated through off-line analysis [2]. By using these two methods, the energy spectra could be obtained for each fragment over 0.5 MeV/nucleon to tens of MeV. The measured data were analyzed to obtain energy spectra for each fragment with Z, corrected for the effects of energy losses in sample and incident window, and normalized to solid angle, the number of target atoms and the number of incident protons. From the measurements, we have obtained DDX data of fragments for proton-induced reactions on C, N, O, Al, Ti and Cu at several beam energies between 40 and 300 MeV, and several laboratory angles between 30° and 120°. The absolute value of the experimental data was confirmed through comparison with existing data of the Al(p,Li) and Al(p,Be) measured by another group[8].

### 3. Fitting

For the resultant data of the experiments, the data points were fitted using Maxwellian curve with considering coulomb barrier effect to integrate over threshold to maximum energies. The set of equation as shown in the following was used [9].

$$f(E) = g(E) \cdot h(E)$$

$$g(E) = \frac{s}{2(\pi T)^{3/2}} \sqrt{E} \cdot \exp\left(-\frac{E}{T}\right)$$

$$h(E) = \frac{1}{1 + \exp\left[-\left(\frac{E - kB}{d}\right)\right]}$$

$$B = \frac{Z_f(Z_t - Z_f)e^2}{1.44(A_f^{1/2} + (A_t - A_f)^{1/2})}$$

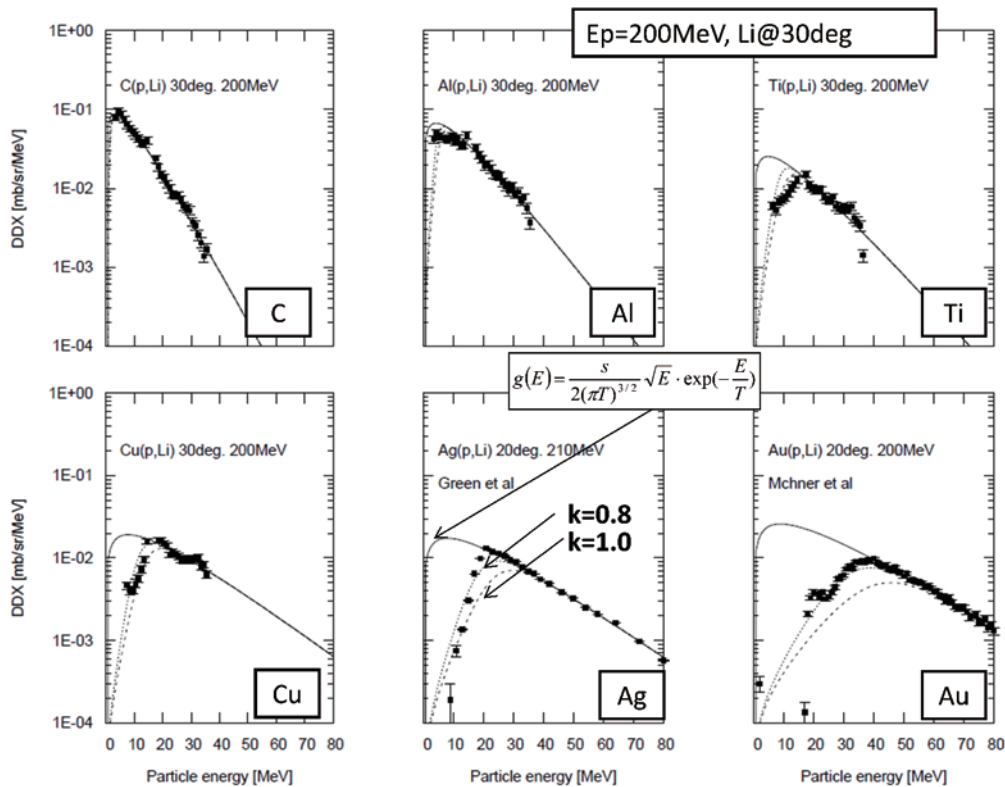


Figure 3 Fitting results of Lithium production at 30 degree laboratory angle for 200 MeV proton on various targets

The  $g(E)$  and  $h(E)$  stand for Maxwellian curve and coulomb barrier, respectively, where  $E$  is LMF energy,  $s$ ,  $T$  and  $k$  are fitting parameters.  $d$  is fixed as  $d=kB/5.5$ .  $Z_f$  and  $Z_t$  are atomic number of LMF and target,  $A_f$  and  $A_t$  mass numbers. Figure 3 shows example of fitting results of Lithium production at 30 degree laboratory angle for 200 MeV proton on various targets. Closed circles in this figure stand for experimental data [7,10,11], dotted and broken lines are  $g(E)$ ,  $f(E)$  with  $k=0.8$  and  $1.0$ . The fitting parameter of  $s$  and  $T$  for  $g(E)$  were determined using data points of the slopes at high energy side. The other slope at low energy side that is caused due to coulomb barrier between target and fragment could be reproduced using  $h(E)$  with fitting parameter  $k$ . As shown in equation  $h(E)$ , the parameter  $k$  stands for adjustable factor of  $B$  value, which corresponds to difference between target and precursor of fragment emission. In this study,  $k$  was chosen to give best fit with the  $s$  and  $T$  previously determined from high energy side slope. After the parameters determination, energy integration of the experimental data from threshold to upper energy was performed for each angle.

#### 4. Results

Figure 4 shows angular distribution of Li, Be, B, C for Al on 140, 200, 300 MeV protons. Closed circles in this figure stand for experimental data, dotted, broken and solid lines are results of theoretical calculation with ISOBAR+GEM, QMD+GEM and Bertin+GEM models [12], respectively.

As shown in this figure, the experimental data decrease monotonically with increasing emission angle. The slopes of the decrease are similar to one for calculation results, which attributes momentum of center-of-mass system. The fact indicates that dominant LMF production process has isotropic angular distribution on center-of-mass system. Thus the calculation model of reaction process to fragment emission, i.e, evaporation model, seems to be applicable to describe most of fragment production in this energy region. The absolute value of the fragment production, however, is underestimated by

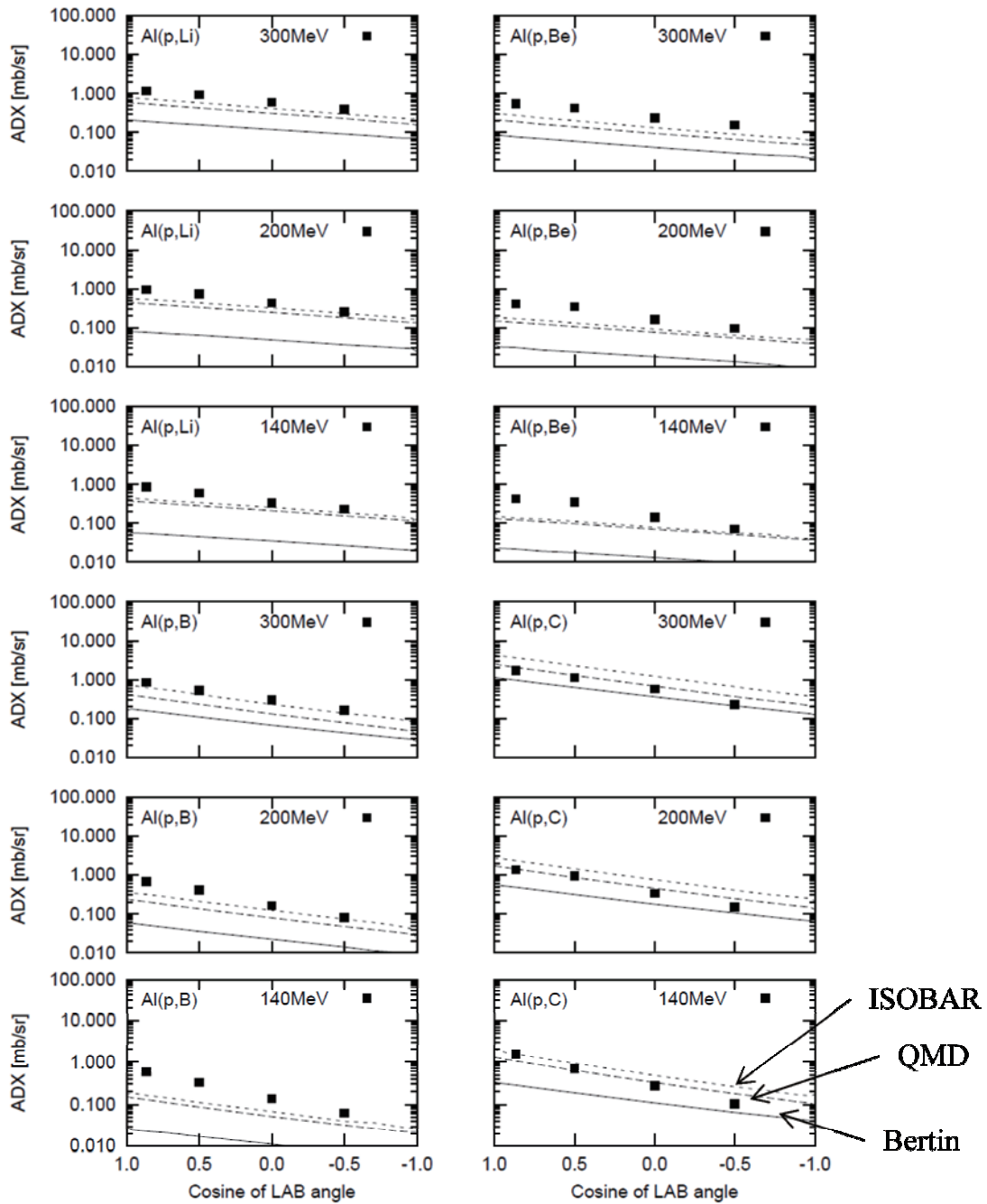


Figure 4 Angular distribution of Li, Be, B, C for Al on 140, 200, 300 MeV protons

Bertin-GEM model and in fairly agreement for ISOBAR-GEM and QMD-GEM models. Therefore, the intra-nuclear cascade models should be chosen carefully when we calculate fragment yield and local energy deposition even we choose right model for fragment production stage. For other target, Ti and Cu show same tendency. For C target, on the other hand, all the calculations overestimate experimental values. The differences between calculation and experiment increase with fragment Z-number, which means the calculation underestimates light charged particle production that is partner of LMF production.

### Acknowledgements

The authors wish to thank operators and supporting crew of NIRS cyclotron and RCNP for their help to perform beam experiment. The BCC was originally developed with support of Grant-in-aid of ministry of education "KAKENHI(15360499, M.Baba, Tohoku University)". A part of this study is the result of "Systematic measurement of fragments for intermediate energy proton induced reaction" carried out under the Strategic Promotion Program for Basic Nuclear Research by the Ministry of Education, Culture, Sports, Science and Technology of Japan.

### References

- [1] T.Sanami et al., *Nucl. Instrm. Meth.* **A589** 193 (2008)
- [2] M. Hagiwara et al., *Nucl. Instrm. Meth.* **A592** 73 (2008)
- [3] T.Sanami et al., *Nucl. Instrm. Meth.* **A610** 660 (2009)
- [4] M.Hagiwara et al., *Radiat Prot Dosimetry* **126** 104 (2007)
- [5] M. Hagiwara et al., "Measurements of Double Differential Fragment Production Cross Sections of Silicon for 70 MeV Protons", *Proc. 2005 Symp. Nucl. Data*, JAEA-Conf 2006-009 (2006)
- [6] T.Sanami et al., "Recent progress of fragment measurement from tens of MeV proton induced reaction using Bragg Curve Counter", *Proc. 2008 Symp. Nucl. Data*, JAEA-Conf 2009-004 (2009)
- [7] T.Sanami et al, "Fragment DDX measurement of proton induced reactions on light-medium nuclei for energy range from reaction threshold to a few hundred MeV ", *Journal of Korean Physics Society* **59**, 1805-1808 (2011)
- [8] T.Sanami et al., "Experimental studies of light fragment production cross section for nucleon induced reaction at intermediate energies", *Proc. 2010 Symp. Nucl. Data* (JAEA-Conf 2011-002) (2011)
- [9] G.D.Westfall et al., *Phys.Rev.***C17**, 1368 (1978)
- [10] R.Green et al., *Phys.Rev.***C22** 1594(1980)
- [11] H.Machner et al., *Phys.Rev.***C73**, 044606(2006)
- [12] K. Niita et al., "PHITS: Particle and Heavy Ion Transport code System, Version 2.23", JAEA-Data/Code 2010-022 (2010).

## 35 Sensitivity Analysis for Kyoto University Research Reactor Using JENDL-4.0

Tadafumi SANO\*, Ken NAKAJIMA, Hironobu UNESAKI

Division of Nuclear Engineering Science, Kyoto University Research Reactor Institute

Kumatori-cho, Sennan-gun, Osaka, 590-0494, Japan

E-mail : t-sano@rri.kyoto-u.ac.jp

Sensitivity analysis of effective multiplication factor ( $k_{\text{eff}}$ ) for Kyoto University Research Reactor (KUR) core is performed using JENDL-4.0 and JENDL-3.3. The  $k_{\text{eff}}$  is 1.0414 by SRAC/CITATION with JENDL-4.0. This value is  $6.00 \times 10^{-2} \%$ dk/k larger than that by JENDL-3.3.  $^{235}\text{U}$  capture cross section in energy range 1eV-10keV, and  $^{238}\text{U}$  capture cross section in energy range less than 10keV have main effects on  $k_{\text{eff}}$  change. The uncertainty of  $k_{\text{eff}}$  is evaluated by the sensitivity coefficients and cross section covariance. The uncertainty is 0.36%dk/k by JENDL-4.0. On the other hand, the uncertainty is 0.55%dk/k by JENDL-3.3. The reason is that the uncertainty of  $^{235}\text{U}$  capture cross section by JENDL-4.0 is remarkably reduced.

### 1. Introduction

KUR is light water moderated / cooled tank-type reactor (Fig.1). KUR attained to first criticality in 1964, and since then it is used for many experimental studies on physics, chemistry, engineering, material science, biology and so on. In addition, the neutron beam from KUR core is used for Boron Neutron Capture Therapy in recent years. The operation of KUR with high enriched uranium (HEU) fuel was ended in February 2006. KUR with low enriched uranium (LEU) fuel core has been successful achievement of first criticality on April 15, 2010. KUR has two kinds of fuel elements. The one is standard fuel element having 18 fuel plates. On the other hand, the special fuel element, in which the control rod is inserted, consists of 9 fuel plates. The  $^{235}\text{U}$  enrichment of LEU fuel is about 20wt% and the uranium density is  $3.2\text{gU/cm}^3$ . The composition of fuel



Fig.1 Kyoto University Research Reactor

meat in LEU fuel is  $U_3Si_2-Al$ . In this paper, we perform the sensitivity analysis of  $k_{eff}$  for KUR core by using JENDL-4.0<sup>[1]</sup> and JENDL-3.3<sup>[2]</sup>. In addition, the cross section uncertainty of  $k_{eff}$  for KUR core is evaluated.

## 2. Calculational model

To analyze the neutronics characteristics in KUR core (Fig.2), the 107-group cross section set processed by using SRAC code system<sup>[3]</sup> with JENDL-4.0 was utilized. The core calculations were performed using SRAC/CITATION with XYZ model. The sensitivity coefficients with respect to each cross section were calculated using the generalized perturbation theory code SAGEP<sup>[4]</sup>. The fuel loading position is shown in Fig.3.

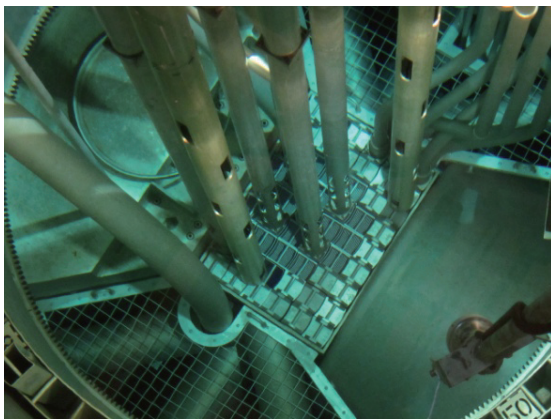


Fig.2 KUR core

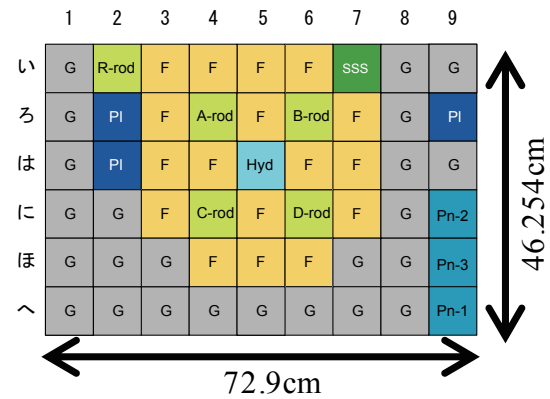


Fig.3 Fuel loading position

F: Standard fuel, G: Graphite reflector,  
 PI: Water plug, A-D: Special fuel for Shim rods,  
 R: Special fuel for Regulation rod  
 Hyd,SSS: irradiation hole, Pn: Pneumatic tube

## 3. Numerical result

### 3.1 Sensitivity coefficient of effective cross section

The core calculation is performed by SRAC/CITATION with JENDL-4.0, and the  $k_{eff}$  is 1.0414. Compared with a result by JENDL-3.3, the  $k_{eff}$  is increased by  $6.00 \times 10^{-2} \%dk/k$ .

The difference of  $^{238}U$  effective capture cross section is shown in Fig.4. We can see the large difference in the resonance and thermal region. The effect of  $k_{eff}$  change by difference in group constant from JENDL-4.0 and JENDL-3.3 is defined by Eq.(1).

$$\Delta R^g = S^g \times \frac{\Delta \sigma^g}{\sigma^g}, \quad (1)$$

where  $S^g$  is the sensitivity coefficient for  $k_{eff}$  and  $\Delta \sigma^g$  is the difference of effective cross section between JENDL-4.0 and JENDL-3.3. Figure 5 shows the sensitivity coefficient with

respect to  $^{238}\text{U}$  effective capture cross section and the effect of  $k_{\text{eff}}$  change by difference in group constant. In the resonance region, that cross section has large sensitivity coefficient. Thus, the difference of nuclear data library in this energy region has large effect for  $k_{\text{eff}}$  change.

Figure 6 shows the difference of  $^{235}\text{U}$  effective capture cross sections between JENDL-4.0 and JENDL-3.3. Figure 7 shows that the sensitivity coefficient of  $^{235}\text{U}$  effective capture cross section in the energy region of 450eV-2.6keV is so small. However, the cross section in 450eV-2.6keV is decreased by about 50% from JENDL-3.3. Therefore, the difference of cross section has large effect for  $k_{\text{eff}}$ .

Table 1 shows the effect of difference in group constants from JENDL-4.0 and JENDL-3.3 on the  $k_{\text{eff}}$  change. The main effects of  $k_{\text{eff}}$  change come from the change of  $^{235}\text{U}$  capture cross section in energy range 1eV-10keV, and  $^{238}\text{U}$  capture cross section in resonance and thermal energy regions.

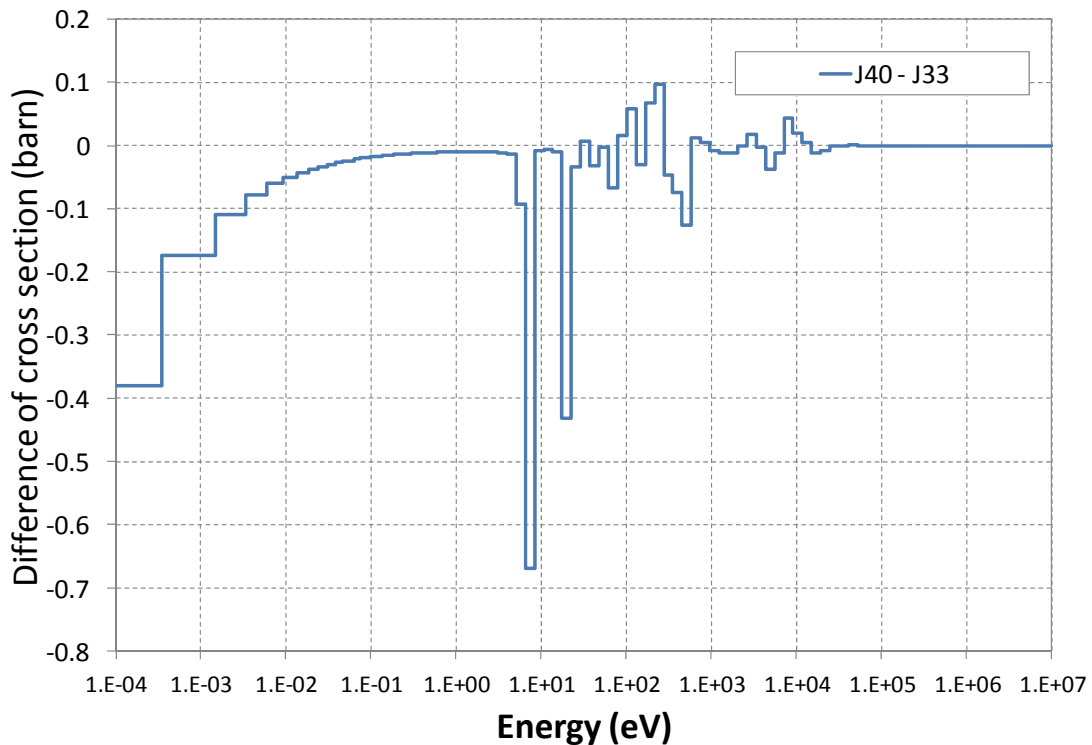


Fig.4 Difference of  $^{238}\text{U}$  effective capture cross section between JENDL-4.0 and JENDL-3.3

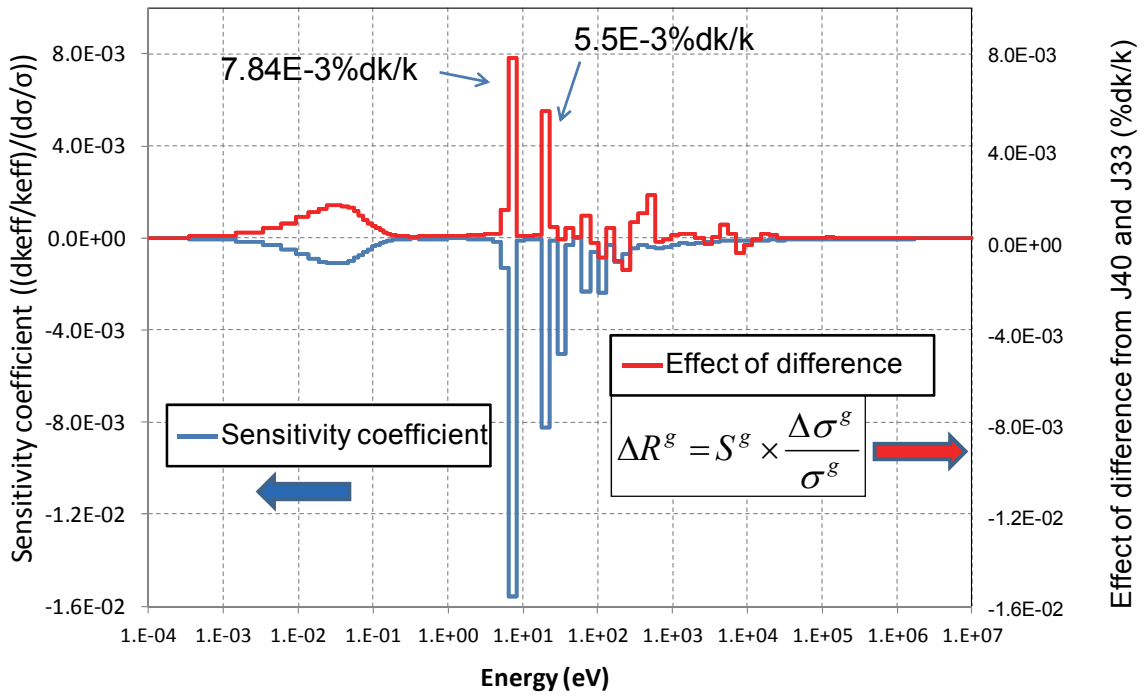


Fig.5 Sensitivity coefficient of  $k_{eff}$  with respect to  $^{238}\text{U}$  effective capture cross section

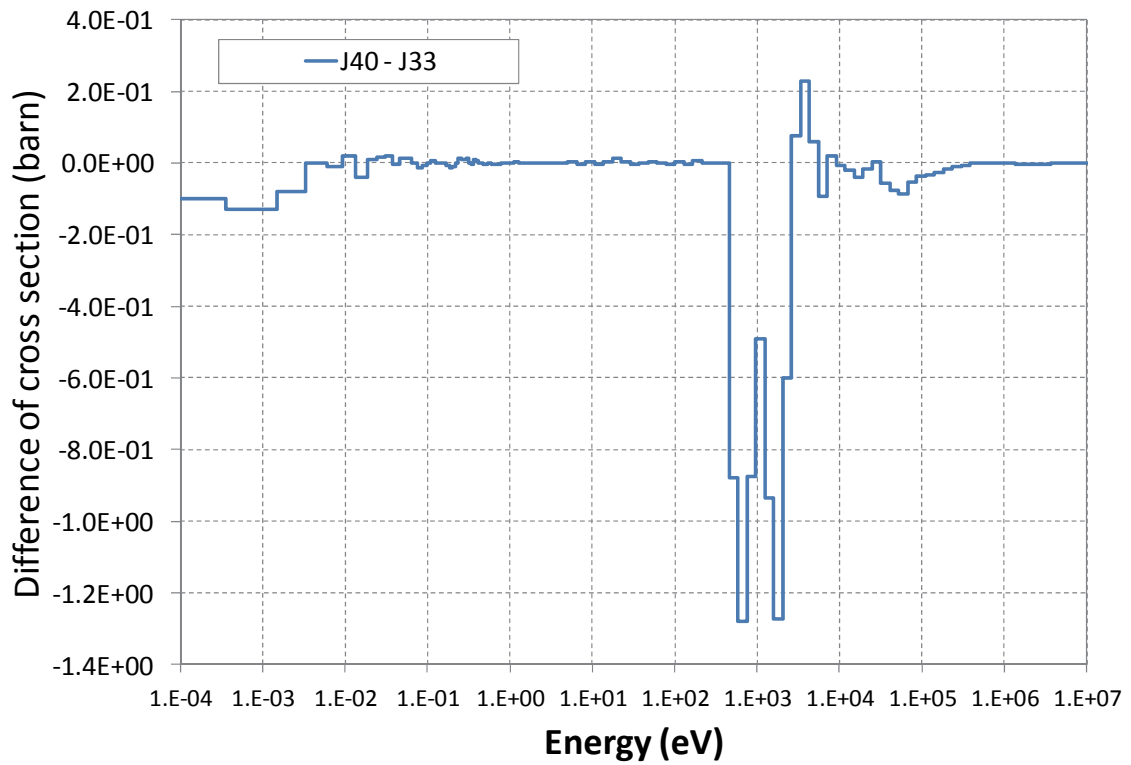


Fig.6 Difference of  $^{235}\text{U}$  effective capture cross section between JENDL-4.0 and JENDL-3.3

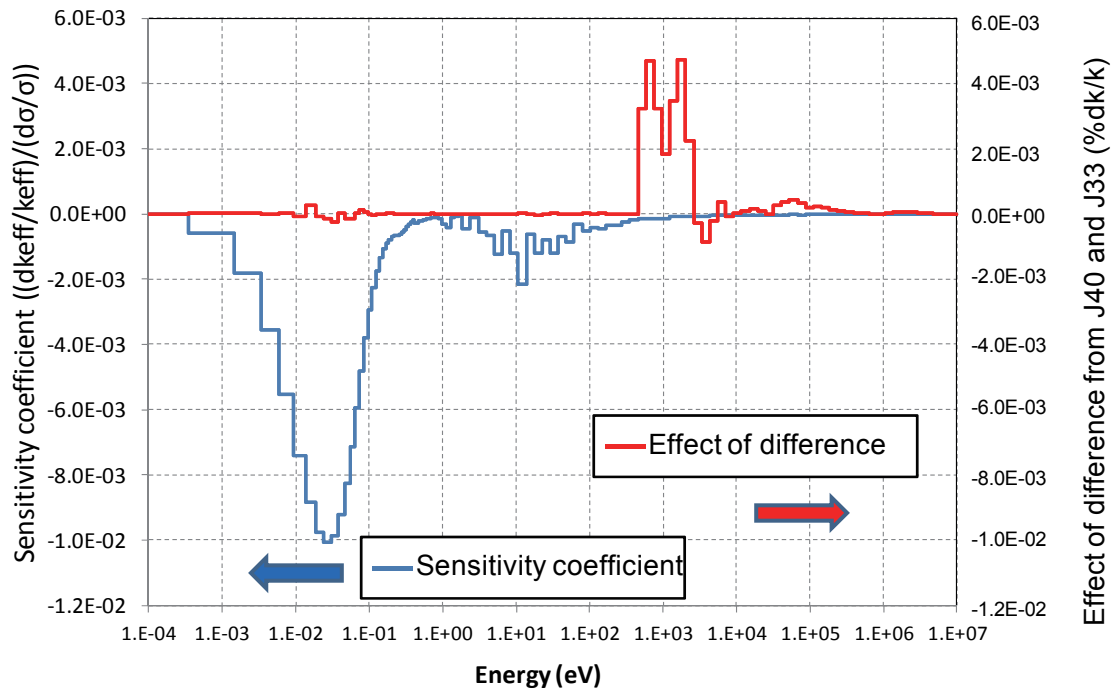


Fig.7 Sensitivity coefficient of  $k_{eff}$  with respect to  $^{235}\text{U}$  effective capture cross section

Table 1 Effect of difference in group constants from JENDL-4.0 and JENDL-3.3

Energy region	Cross section		
	U238 capture	U235 fission	U235 capture
10keV <	$-1.79 \times 10^{-5} \%dk/k$	$-6.31 \times 10^{-3} \%dk/k$	$2.89 \times 10^{-3} \%dk/k$
1eV – 10keV	$1.85 \times 10^{-2} \%dk/k$	$-6.91 \times 10^{-4} \%dk/k$	$2.23 \times 10^{-2} \%dk/k$
< 1eV	$1.69 \times 10^{-2} \%dk/k$	$7.38 \times 10^{-3} \%dk/k$	$-3.55 \times 10^{-4} \%dk/k$
Total	$3.54 \times 10^{-2} \%dk/k$	$3.49 \times 10^{-4} \%dk/k$	$2.48 \times 10^{-2} \%dk/k$

### 3.2 Uncertainty reduction of $k_{eff}$

We evaluate the uncertainty of  $k_{eff}$  for KUR core by cross section error. Figure 8 shows the components of the uncertainty. The uncertainty of  $k_{eff}$  is evaluated by the sensitivity coefficients and cross section covariance. The uncertainty is 0.36%dk/k by JENDL-4.0. On the other hand, the uncertainty is 0.55%dk/k by JENDL-3.3. The reason is that the uncertainty of  $^{235}\text{U}$  capture cross section by JENDL-4.0 is remarkably reduced.

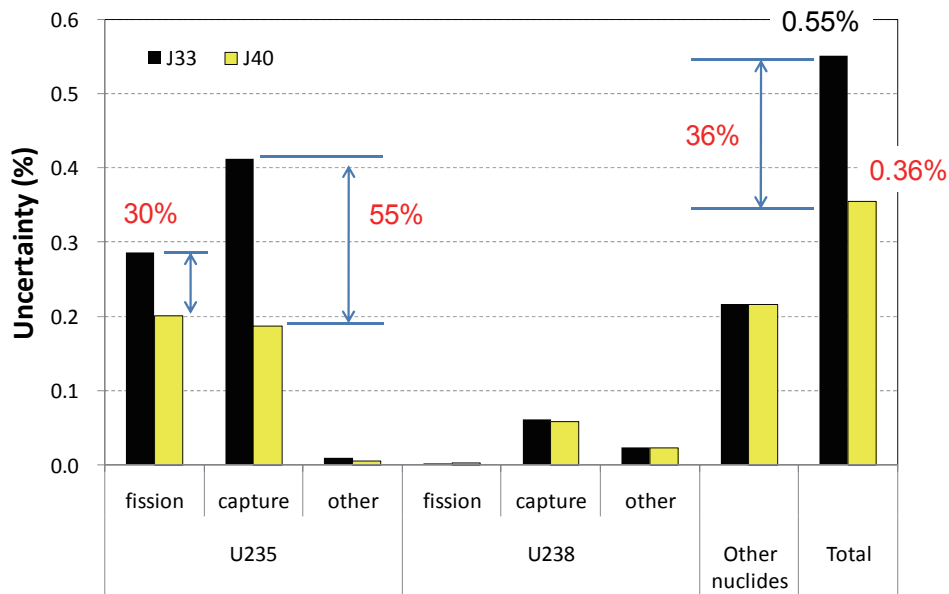


Fig.8 Nuclide-wise contribution to uncertainty of  $k_{eff}$  for KUR LEU core

#### 4. Conclusion

The sensitivity analysis of  $k_{eff}$  for KUR core is performed using JENDL-4.0. The  $k_{eff}$  is increased by  $6.00 \times 10^{-2} \%dk/k$  compared with the result by JENDL-3.3. The main effects of  $k_{eff}$  change are due to the changes of  $^{235}\text{U}$  capture cross section in energy range 1eV-10keV, and  $^{238}\text{U}$  capture cross section in resonance and thermal energy regions. In addition, the uncertainty of  $k_{eff}$  by JENDL-4.0 was reduced, because the uncertainty of  $^{235}\text{U}$  capture cross section was remarkably reduced.

#### References

- [1] K. Shibata, *et al.*, "JENDL-4.0: A New Library for Nuclear Science and Engineering," J. Nucl. Sci. Technol. 48(1), 1-30 (2011).
- [2] K. Shibata, *et al.*, "Japanese Evaluated Nuclear Data Library Version3 Revision-3 : JENDL-3.3," J. Nucl. Sci. and Technol., 39, 1125, (2002).
- [3] K. Okumura, *et al.*, "SRAC2006: A Comprehensive Neutronics Calculation Code System," JAEA-Data/Code, 2007-004, (2007).
- [4] A. Hara, T. Takeda *et al.*, "SAGEP: Two-Dimensional Sensitivity Analysis Code Based on Generalized Perturbation Theory," JAERI-M 84-065, (1984), [in Japanese].

# 国際単位系 (SI)

表1. SI基本単位

基本量	SI基本単位	
	名称	記号
長さ	メートル	m
質量	キログラム	kg
時間	秒	s
電流	アンペア	A
熱力学温度	ケルビン	K
物質	モル	mol
光	カンデラ	cd

表2. 基本単位を用いて表されるSI組立単位の例

組立量	SI基本単位	
	名称	記号
面積	平方メートル	m <sup>2</sup>
体積	立方メートル	m <sup>3</sup>
速度	メートル毎秒	m/s
加速度	メートル毎秒毎秒	m/s <sup>2</sup>
波数	数メートル	m <sup>-1</sup>
密度, 質量密度	キログラム毎立方メートル	kg/m <sup>3</sup>
面積密度	キログラム毎平方メートル	kg/m <sup>2</sup>
比体積	立方メートル毎キログラム	m <sup>3</sup> /kg
電流密度	アンペア毎平方メートル	A/m <sup>2</sup>
磁界の強さ	アンペア毎メートル	A/m
量濃度 <sup>(a)</sup> , 濃度	モル毎立方メートル	mol/m <sup>3</sup>
質量濃度	キログラム毎立法メートル	kg/m <sup>3</sup>
輝度	カンデラ毎平方メートル	cd/m <sup>2</sup>
屈折率 <sup>(b)</sup>	(数字の) 1	1
比透磁率 <sup>(b)</sup>	(数字の) 1	1

(a) 量濃度 (amount concentration) は臨床化学の分野では物質濃度 (substance concentration) ともよばれる。  
 (b) これらは無次元量あるいは次元1をもつ量であるが、そのことを表す単位記号である数字の1は通常は表記しない。

表3. 固有の名称と記号で表されるSI組立単位

組立量	SI組立単位			
	名称	記号	他のSI単位による表し方	SI基本単位による表し方
平面角	ラジアン <sup>(b)</sup>	rad	1 <sup>(b)</sup>	m/m
立体角	ステラジアン <sup>(b)</sup>	sr <sup>(c)</sup>	1 <sup>(b)</sup>	m <sup>2</sup> /m <sup>2</sup>
周波数	ヘルツ <sup>(d)</sup>	Hz	1	s <sup>-1</sup>
力	ニュートン	N		m kg s <sup>-2</sup>
圧力, 応力	パスカル	Pa	N/m <sup>2</sup>	m <sup>-1</sup> kg s <sup>-2</sup>
エネルギー, 仕事, 熱量	ジュール	J	N m	m <sup>2</sup> kg s <sup>-2</sup>
仕事率, 工率, 放射	ワット	W	J/s	m <sup>2</sup> kg s <sup>-3</sup>
電荷, 電気量	クーロン	C		s A
電位差 (電圧), 起電力	ボルト	V	W/A	m <sup>2</sup> kg s <sup>-3</sup> A <sup>-1</sup>
静電容量	ファラド	F	C/V	m <sup>-2</sup> kg <sup>-1</sup> s <sup>4</sup> A <sup>2</sup>
電気抵抗	オーム	Ω	V/A	m <sup>2</sup> kg s <sup>-3</sup> A <sup>-2</sup>
コンダクタンス	ジーメンズ	S	A/V	m <sup>-2</sup> kg <sup>-1</sup> s <sup>3</sup> A <sup>2</sup>
磁束密度	ウェーバ	Wb	Vs	m <sup>2</sup> kg s <sup>-2</sup> A <sup>-1</sup>
磁束	テスラ	T	Wb/m <sup>2</sup>	kg s <sup>-2</sup> A <sup>-1</sup>
インダクタンス	ヘンリー	H	Wb/A	m <sup>2</sup> kg s <sup>-2</sup> A <sup>-2</sup>
セルシウス温度	セルシウス度 <sup>(e)</sup>	°C		K
光照射度	ルーメン	lm		cd sr <sup>(c)</sup>
放射線核種の放射能 <sup>(f)</sup>	ベクレル <sup>(d)</sup>	Bq		s <sup>-1</sup>
吸収線量, 比エネルギー分与, カーマ	グレイ	Gy	J/kg	m <sup>2</sup> s <sup>-2</sup>
線量当量, 周辺線量当量, 方向性線量当量, 個人線量当量	シーベルト <sup>(g)</sup>	Sv	J/kg	m <sup>2</sup> s <sup>-2</sup>
酸素活性	カタール	kat		s <sup>-1</sup> mol

(a) SI接頭語は固有の名称と記号を持つ組立単位と組み合わせても使用できる。しかし接頭語を付した単位はもはやコヒーレントではない。  
 (b) ラジアンとステラジアンは数字の1に対する単位の特別な名称で、量についての情報をつたえるために使われる。実際には、使用する時には記号rad及びsrが用いられるが、習慣として組立単位としての記号である数字の1は明示されない。  
 (c) 測光学ではステラジアンという名称と記号srを単位の表し方の中に、そのまま維持している。  
 (d) ヘルツは周期現象についてのみ、ベクレルは放射性核種の統計的過程についてのみに使用される。  
 (e) セルシウス度はケルビンの特別な名称で、セルシウス温度を表すために使用される。セルシウス度とケルビンの単位の大きさは同一である。したがって、温度差や温度間隔を表す数値はどちらの単位で表しても同じである。  
 (f) 放射性核種の放射能 (activity referred to a radionuclide) は、しばしば誤った用語で"radioactivity"と記される。  
 (g) 単位シーベルト (PV,2002,70,205) についてはCIPM勧告2 (CF-2002) を参照。

表4. 単位の中に固有の名称と記号を含むSI組立単位の例

組立量	SI組立単位		
	名称	記号	SI基本単位による表し方
粘着力	パスカル秒	Pa s	m <sup>-1</sup> kg s <sup>-1</sup>
力のモーメント	ニュートンメートル	N m	m <sup>2</sup> kg s <sup>-2</sup>
表面張力	ニュートン毎メートル	N/m	kg s <sup>-2</sup>
角速度	ラジアン毎秒	rad/s	m m <sup>-1</sup> s <sup>-1</sup> =s <sup>-1</sup>
角加速度	ラジアン毎秒毎秒	rad/s <sup>2</sup>	m m <sup>-1</sup> s <sup>-2</sup> =s <sup>-2</sup>
熱流密度, 放射照度	ワット毎平方メートル	W/m <sup>2</sup>	kg s <sup>-3</sup>
熱容量, エントロピー	ジュール毎ケルビン	J/K	m <sup>2</sup> kg s <sup>-2</sup> K <sup>-1</sup>
比熱容量, 比エントロピー	ジュール毎キログラム毎ケルビン	J/(kg K)	m <sup>2</sup> s <sup>-2</sup> K <sup>-1</sup>
比エントロピー	ジュール毎キログラム	J/kg	m <sup>2</sup> s <sup>-2</sup>
熱伝導率	ワット毎メートル毎ケルビン	W/(m K)	m kg s <sup>-3</sup> K <sup>-1</sup>
体積エネルギー	ジュール毎立方メートル	J/m <sup>3</sup>	m <sup>-1</sup> kg s <sup>-2</sup>
電界の強さ	ボルト毎メートル	V/m	m kg s <sup>-3</sup> A <sup>-1</sup>
電荷密度	クーロン毎立方メートル	C/m <sup>3</sup>	m <sup>-3</sup> s A
電表面積電荷	クーロン毎平方メートル	C/m <sup>2</sup>	m <sup>-2</sup> s A
電束密度, 電気変位	クーロン毎平方メートル	C/m <sup>2</sup>	m <sup>-2</sup> s A
誘電率	ファラド毎メートル	F/m	m <sup>-2</sup> kg <sup>-1</sup> s <sup>4</sup> A <sup>2</sup>
透磁率	ヘンリー毎メートル	H/m	m kg s <sup>-2</sup> A <sup>-2</sup>
モルエネルギー	ジュール毎モル	J/mol	m <sup>2</sup> kg s <sup>-2</sup> mol <sup>-1</sup>
モルエントロピー, モル熱容量	ジュール毎モル毎ケルビン	J/(mol K)	m <sup>2</sup> kg s <sup>-2</sup> K <sup>-1</sup> mol <sup>-1</sup>
照射線量 (X線及びγ線)	クーロン毎キログラム	C/kg	kg <sup>-1</sup> s A
吸収線量	グレイ毎秒	Gy/s	m <sup>2</sup> s <sup>-3</sup>
放射強度	ワット毎ステラジアン	W/sr	m <sup>3</sup> m <sup>-2</sup> kg s <sup>-3</sup> =m <sup>2</sup> kg s <sup>-3</sup>
放射輝度	ワット毎平方メートル毎ステラジアン	W/(m <sup>2</sup> sr)	m <sup>2</sup> m <sup>-2</sup> kg s <sup>-3</sup> =kg s <sup>-3</sup>
酵素活性濃度	カタール毎立方メートル	kat/m <sup>3</sup>	m <sup>-3</sup> s <sup>-1</sup> mol

表5. SI接頭語

乗数	接頭語	記号	乗数	接頭語	記号
10 <sup>24</sup>	ヨタ	Y	10 <sup>1</sup>	デシ	d
10 <sup>21</sup>	ゼタ	Z	10 <sup>2</sup>	センチ	c
10 <sup>18</sup>	エクサ	E	10 <sup>3</sup>	ミリ	m
10 <sup>15</sup>	ペタ	P	10 <sup>6</sup>	マイクロ	μ
10 <sup>12</sup>	テラ	T	10 <sup>9</sup>	ナノ	n
10 <sup>9</sup>	ギガ	G	10 <sup>12</sup>	ピコ	p
10 <sup>6</sup>	メガ	M	10 <sup>15</sup>	フェムト	f
10 <sup>3</sup>	キロ	k	10 <sup>18</sup>	アト	a
10 <sup>2</sup>	ヘクト	h	10 <sup>21</sup>	ゼプト	z
10 <sup>1</sup>	デカ	da	10 <sup>24</sup>	ヨクト	y

表6. SIに属さないが、SIと併用される単位

名称	記号	SI単位による値
分	min	1 min=60s
時	h	1 h=60 min=3600 s
日	d	1 d=24 h=86 400 s
度	°	1°=(π/180) rad
分	'	1'=(1/60)°=(π/10800) rad
秒	"	1"=(1/60)'=(π/648000) rad
ヘクタール	ha	1ha=1hm <sup>2</sup> =10 <sup>4</sup> m <sup>2</sup>
リットル	L, l	1L=11=1dm <sup>3</sup> =10 <sup>3</sup> cm <sup>3</sup> =10 <sup>-3</sup> m <sup>3</sup>
トン	t	1t=10 <sup>3</sup> kg

表7. SIに属さないが、SIと併用される単位で、SI単位で表される数値が実験的に得られるもの

名称	記号	SI単位で表される数値
電子ボルト	eV	1eV=1.602 176 53(14)×10 <sup>-19</sup> J
ダルトン	Da	1Da=1.660 538 86(28)×10 <sup>-27</sup> kg
統一原子質量単位	u	1u=1 Da
天文単位	ua	1ua=1.495 978 706 91(6)×10 <sup>11</sup> m

表8. SIに属さないが、SIと併用されるその他の単位

名称	記号	SI単位で表される数値
バール	bar	1 bar=0.1MPa=100kPa=10 <sup>5</sup> Pa
水銀柱ミリメートル	mmHg	1mmHg=133.322Pa
オングストローム	Å	1 Å=0.1nm=100pm=10 <sup>-10</sup> m
海里	M	1 M=1852m
バイン	b	1 b=100fm <sup>2</sup> =(10 <sup>-12</sup> cm) <sup>2</sup> =10 <sup>-28</sup> m <sup>2</sup>
ノット	kn	1 kn=(1852/3600)m/s
ネーパ	Np	SI単位との数値的な関係は、 対数量の定義に依存。
ベベル	B	
デジベル	dB	

表9. 固有の名称をもつCGS組立単位

名称	記号	SI単位で表される数値
エル	erg	1 erg=10 <sup>-7</sup> J
ダイン	dyn	1 dyn=10 <sup>-5</sup> N
ポアズ	P	1 P=1 dyn s cm <sup>-2</sup> =0.1Pa s
ストークス	St	1 St=1cm <sup>2</sup> s <sup>-1</sup> =10 <sup>-4</sup> m <sup>2</sup> s <sup>-1</sup>
ストルブ	sb	1 sb=1cd cm <sup>-2</sup> =10 <sup>-4</sup> cd m <sup>-2</sup>
フォト	ph	1 ph=1cd sr cm <sup>-2</sup> 10 <sup>4</sup> lx
ガリ	Gal	1 Gal=1cm s <sup>-2</sup> =10 <sup>-2</sup> ms <sup>-2</sup>
マクスウェル	Mx	1 Mx=1G cm <sup>2</sup> =10 <sup>8</sup> Wb
ガウス	G	1 G=1Mx cm <sup>-2</sup> =10 <sup>4</sup> T
エルステッド <sup>(c)</sup>	Oe	1 Oe ≡ (10 <sup>3</sup> /4π)A m <sup>-1</sup>

(c) 3元系のCGS単位系とSIでは直接比較できないため、等号「≡」は対応関係を示すものである。

表10. SIに属さないその他の単位の例

名称	記号	SI単位で表される数値
キュリー	Ci	1 Ci=3.7×10 <sup>10</sup> Bq
レントゲン	R	1 R=2.58×10 <sup>-4</sup> C/kg
ラド	rad	1 rad=1cGy=10 <sup>-2</sup> Gy
レム	rem	1 rem=1cSv=10 <sup>-2</sup> Sv
ガンマ	γ	1 γ=1 nT=10 <sup>-9</sup> T
フェルミ	fm	1 fm=10 <sup>-15</sup> m
メートル系カラット		1メートル系カラット=200 mg=2×10 <sup>-4</sup> kg
トル	Torr	1 Torr=(101 325/760) Pa
標準大気圧	atm	1 atm=101 325 Pa
カロリ	cal	1cal=4.1858J (「15°C」カロリ), 4.1868J (「IT」カロリ), 4.184J (「熱化学」カロリ)
マイクロン	μ	1 μ=1μm=10 <sup>-6</sup> m

